

## MAGNETISM OF PEROVSKITE-BASED TRANSITION METAL OXIDES

UNEXPECTED MAGNETIC PROPERTIES OF PEROVSKITE-BASED TRANSITION  
METAL OXIDES

By

HEATHER LYNN CUTHBERT, B.Sc.(Hons.), M.Sc., B.Ed.

A Thesis

Submitted to the School of Graduate Studies

in Partial Fulfilment of the Requirements

for the Degree

Doctor of Philosophy

McMaster University

© Copyright by Heather Lynn Cuthbert, November 2008

DOCTOR OF PHILOSOPHY (2008)

McMaster University

(Chemistry)

Hamilton, Ontario

TITLE: Unexpected Magnetic Properties of Perovskite-Based Transition Metal  
Oxides

AUTHOR: Heather Lynn Cuthbert, B.Sc. (Hons.) (Brock University), M.Sc.  
(University of Western Ontario), B.Ed. (University of Western Ontario)

SUPERVISOR: Doctor John E. Greedan

NUMBER OF PAGES: xvii, 231

## Abstract

Various transition metal oxides with interesting magnetic properties (often based on the perovskite structure) were prepared using conventional solid-state methodologies and fully characterized using a variety of techniques such as powder X-ray diffraction, variable temperature neutron diffraction, SEM-EDS, TEM-EDS, SQUID magnetometry and heat capacity measurements.

One family of compounds that was investigated intensively were the ‘pillared perovskites’. In this structure type, perovskite-like layers of corner shared octahedra are separated by about 10 Å by diamagnetic edge-shared octahedral dimer ‘pillars’. Despite this long distance between layers, long-range order is present in both the  $\text{La}_5\text{Re}_3\text{CoO}_{16}$  and  $\text{La}_5\text{Re}_3\text{NiO}_{16}$  members. In fact, a new magnetic structure was discovered for the Ni compound consisting of ferromagnetically ordered layers, coupled antiferromagnetically.

In addition, for the first time, substitution of the 5+ ion within the layer was successful, yielding compounds with general formula,  $\text{La}_5\text{Re}_{3-x}\text{Ta}_x\text{BO}_{16}$  ( $B = \text{Mn, Fe, Co, Ni}$ ;  $x \sim 0.5$ ). Surprisingly, despite replacing about half of the magnetic ions within the perovskite layers with non-magnetic tantalum, the materials had the same ordering temperatures and magnetic structures as their unsubstituted analogues. This observation is evidence that the longer interlayer coupling pathway is the key to long-range ordering in this structure type.

The lanthanum rhenium oxide,  $\text{La}_3\text{Re}_2\text{O}_{10}$ , involves the edge-shared octahedral dimer ‘pillar’ unit from the pillared perovskite structure, but with one unpaired electron per dimer unit. Prepared for the first time by solid-state synthesis, and studied

magnetically in depth, long-range order was evident at 18 K. Theoretical investigations hinted that the magnetic structure consists of antiferromagnetically coupled chains of dimers, coupled antiferromagnetically.

The magnetic properties of the double perovskite, SrLaRuNiO<sub>6</sub>, were also explored for the first time. This study demonstrates the power of neutron diffraction at elucidating magnetic information, such as the ordering temperature and magnetic structure, despite the presence of a ferromagnetic impurity that dominated much of the measurements.

The candidate's examination of the magnetism of the rock-salt oxides, Na<sub>2</sub>Cu<sub>2</sub>TeO<sub>6</sub> and Na<sub>3</sub>Cu<sub>2</sub>SbO<sub>6</sub> has raised some controversy in the literature, as the exact nature of the one-dimensional order (either antiferromagnetic-antiferromagnetic or antiferromagnetic-ferromagnetic alternating linear chains) is uncertain. Again, theoretical calculations and comparison with other magnetic data can aid in the ultimate understanding of the overriding magnetism.

This thesis has focussed on the synthesis and study of transition metal oxides with interesting or unusual magnetic properties. In many cases, the compounds exhibited long-range magnetic order despite convoluted or non-existent magnetic superexchange pathways.

## **Acknowledgements**

Of course, I did not complete this research on my own. Many people have contributed both professionally and personally through the many years of research ups and downs, and I wish to acknowledge some of them here. Individuals that have contributed directly to the thesis (i.e. by collecting data) have been noted in the Chapter their involvement appears in.

First and foremost, I want to thank my supervisor, Dr. Greedan. Your humanity, knowledge, encouragement, dry wit, sense of humour and belief in me as a chemist has really helped me grow and blossom as a solid state chemist and as a person. I could never adequately thank you enough for your kindness and guidance.

I would also like to thank the members of the Greedan group and the Brockhouse Institute for Materials Research, past and present: Athena Safa-Sefat, Tomoko Aharen, Antonio Diego Lozano-Gorrin, Tetsuhiro Kazumata, Shahab Derakhshan, Farshid Ramezanipour, Jonathan Mitchell, Andrew Grosvenor, Hanna Dabkowska, Anton Dabkowski and Jim Garrett, for your invaluable help and friendship. I do not think that I would have completed a Ph.D. without you! Thanks to my committee members, Dr. Jacques Barbier, Dr. Bruce Gaulin and Dr. Yuriy Mozharivskyj, for your assistance, guidance, and for attending all those committee meetings. Special thanks to Dr. Ignacio Vargas-Baca, Dr. Emslie and Dr. Schrobilgen, for participating in my comprehensive exam as well as providing encouragement and support.

Some additional thanks to secretaries and staff, especially Anne Reynolds and Sheila Marsden, Lynda Fraser, Carol Dada, Barbra DeJean, Josie Petrie, Tammy Feher, Connie Carrabs, Christina Gulewitsch, Marlene Webb (and Newman) and Maureen Shaw for all your help figuring out such confusing things like administration, paperwork and fax machines!

I would also like to thank a few people who have helped me develop as a teacher and educator at McMaster University: Dr. Brian McCarry, Dr. Maggie Austen, Dr. Barbara Russer and Dr. Jeff Landry. An extra special thanks to my mentor and friend,

Dr. Pippa Lock, for listening, laughing, providing sage advice and helping me mature as an educator, and as a person.

On a more personal level, there are so many people here at McMaster whose friendship, humour, camaraderie and encouragement have provided a much-needed boost through the good times and the bad, that they are too numerous to list. However, there are a few of you who deserve special recognition: the Lounge Lunch Crowd, the Running Club, the TAN ladies – Tina Guenther, Amanda Donovan, Anika Louie, Christa Homenick, Janice Hickey, Bonnie Leung, Karen Lam – for all of the fun and hard work, my dearest friends – Jennilee Gavina, Christa Homenick, Bonnie Leung, Lindsey Brock, Erik Youngson, Jason Traer, Dave Brock, Babak Behnam Azad – for the many potlucks, hugs, surprise 30<sup>th</sup> birthday party, half marathon run, snowmen, pranks, cat pictures, shopping sprees, Pizza Hut lunch buffets, and rounds of golf. I love you all very dearly, and feel honoured to have you in my life.

I would also like to thank my family – Mom, Gram and Matt – for all of your love, caring and support. You have always been there for me, and I appreciate all that you do.

Finally, last but certainly not least, an extra special thank you to Michael. You are the love of my life, my soulmate, my partner. You have loved me, supported me and helped me unconditionally throughout this research, and I could never thank you enough for all that you have done for me. I am a better person with you in my life.

## Table of Contents

### Chapter 1 – Introduction

1.1 Thesis Outline .....	2
1.2 Perovskite Structure Type.....	4
1.3 Magnetism.....	9
1.4 Metamagnetism and Spin Flop .....	20
1.5 References.....	24

### Chapter 2 – Experimental Techniques

2.1 Structural Determination.....	26
2.2 Diffraction Theory .....	27
2.3 X-ray Diffraction .....	32
2.4 Neutron Diffraction.....	36
2.5 Magnetic Neutron Diffraction.....	41
2.6 Rietveld Refinement .....	46
2.7 DC SQUID Magnetometry .....	49
2.8 Heat Capacity Measurements .....	60
2.9 References.....	65

### Chapter 3 – Investigations of the Magnetic Properties and Structures of the Pillared

#### Perovskites, $\text{La}_5\text{Re}_3\text{MO}_{16}$ ( $M = \text{Co}, \text{Ni}$ )

3.1 Abstract .....	67
3.2 Introduction.....	68
3.3 Experimental .....	69
3.4 Results and Discussion .....	72
3.5 Summary and Conclusions .....	92
3.6 References.....	95

Chapter 4 – Synthesis, Structure and Magnetic Properties of the Pillared Perovskites,

$\text{La}_3\text{Re}_{3-x}\text{Ta}_x\text{BO}_{16}$  ( $B = \text{Mn, Fe, Co, Ni}$ )

4.1 Abstract.....	97
4.2 Introduction.....	98
4.3 Experimental.....	102
4.4 Results and Discussion .....	105
4.5 Conclusions.....	158
4.6 References.....	161
Appendix A.....	162

Chapter 5 – Synthesis, Structure and Unexpected Magnetic Properties of  $\text{La}_3\text{Re}_2\text{O}_{10}$

5.1 Abstract.....	165
5.2 Introduction.....	166
5.3 Experimental Methods.....	168
5.4 Results and Discussion .....	170
5.5 Conclusions.....	184
5.6 References.....	185

Chapter 6 – Synthesis, Structure and Magnetic Properties of the Double Perovskite,

$\text{SrLaRuNiO}_6$

6.1 Abstract.....	188
6.2 Introduction.....	188
6.3 Experimental.....	190
6.4 Results and Discussion .....	192
6.5 Conclusions.....	200
6.6 References.....	201

Chapter 7 – Magnetic Studies of the Ordered Rock Salt Oxides,  $\text{Na}_2\text{Cu}_2\text{TeO}_6$  and

$\text{Na}_3\text{Cu}_2\text{SbO}_6$

7.1 Abstract.....	204
7.2 Introduction.....	205
7.3 Experimental.....	209
7.4 Results and Discussion .....	210
7.5 Conclusions.....	221
7.6 References.....	223

Chapter 8 – Conclusions

8.1 Conclusions.....	225
8.2 Future Work.....	228
8.3 References.....	230

## List of Figures

### Chapter 1 - Introduction

1.1	Crystal structure of the ideal $ABO_3$ perovskite.....	5
1.2	Crystal structure of an ordered $A_2BB'O_6$ double perovskite.....	7
1.3	Crystal structure of a “pillared perovskite”, $Ln_5D_2ABO_{16}$ .....	8
1.4	Magnetic superexchange illustrated for $Mn^{3+} - O - Mn^{3+}$ with $180^\circ$ bonding angle and octahedral crystal field .....	15
1.5	Magnetic superexchange illustrated for $Mn^{2+} - O - Mn^{4+}$ with $180^\circ$ bonding angle and octahedral crystal field .....	15
1.6	Ferromagnetism .....	19
1.7	Antiferromagnetism .....	19
1.8	Ferrimagnetism .....	19
1.9	Spin flop graph of temperature versus field; magnetization versus field .....	23
1.10	Metamagnetism graph of temperature versus field; magnetization versus field .....	23

### Chapter 2 – Experimental Techniques

2.1	Bragg’s Law illustrated for a set of reflections from lattice planes separated by a distance, $d$ .....	28
2.2	Ewald’s Sphere for diffraction.....	28
2.3	Transmission geometry powder diffraction illustrating a Debye cone of scattering .....	31
2.4	Powder x-ray diffraction pattern of silicon.....	31
2.5	Neutron and X-ray coherent scattering lengths according to atomic number .....	33
2.6	Characteristic X-ray spectra for Mo and Cu radiation.....	33
2.7	Geometry of the Guinier-Hagg camera.....	35
2.8	Maxwell distribution of the speed of neutrons produced from different reactor sources, using different moderators .....	37
2.9	Geometry of a typical neutron experiment that involves elastic scattering .....	40

2.10	Neutron scattering geometry for a reactor source.....	40
2.11	Geometry of a magnetic neutron experiment.....	43
2.12	Susceptibility ( $\chi$ ) versus temperature plot for typical magnetic systems .....	51
2.13	Inverse susceptibility versus temperature plots for typical magnetic systems .....	51
2.14	Susceptibility ( $\chi$ ) multiplied by temperature (T) versus temperature plot .....	53
2.15	Fisher heat capacity (derivative of $\chi T$ with respect to T) for an antiferromagnet...53	
2.16	A typical magnetization curve for a ferromagnet .....	55
2.17	Sample translation inside the pick-up coils of a SQUID magnetometer and the voltage signal that is produced.....	57
2.18	Diagram of a RF SQUID, detailing the Josephson Junction and the LC circuit ....	59
2.19	Sample mount for the Oxford Instruments Heat Capacity probe .....	64

### Chapter 3 – Investigations of the Magnetic Properties and Structures of the Pillared

#### Perovskites, $\text{La}_5\text{Re}_3\text{MO}_{16}$ ( $M = \text{Co}, \text{Ni}$ )

3.1	Crystal structure of $\text{La}_5\text{Re}_3\text{MO}_{16}$ .....	71
3.2	ZFC/FC magnetic susceptibility measurements of $\text{La}_5\text{Re}_3\text{CoO}_{16}$ with applied fields of 0.05 T, 2.0 T and 5.0 T .....	75
3.3	$\chi T$ versus T plot of $\text{La}_5\text{Re}_3\text{CoO}_{16}$ using the ZFC data only .....	77
3.4	Isothermal magnetization versus applied field data for $\text{La}_5\text{Re}_3\text{CoO}_{16}$ .....	77
3.5	Heat capacity measurements of $\text{La}_5\text{Re}_3\text{CoO}_{16}$ with no field applied and in a 7.0 T field .....	79
3.6	Magnetic component of the heat capacity of $\text{La}_5\text{Re}_3\text{CoO}_{16}$ , in zero applied field and in a 7 T field .....	79
3.7	Powder neutron diffraction patterns of $\text{La}_5\text{Re}_3\text{CoO}_{16}$ at 5 K, 30 K and 50 K .....	81
3.8	Magnetic structure of $\text{La}_5\text{Re}_3\text{CoO}_{16}$ .....	81
3.9	Rietveld refinement of the low angle powder neutron diffraction data for $\text{La}_5\text{Re}_3\text{CoO}_{16}$ at 5 K .....	82
3.10	Temperature dependence of the magnetic peak indexed as $(1-1\ 1/2) / (1\ 1\ 1/2)$ in $\text{La}_5\text{Re}_3\text{CoO}_{16}$ .....	82

3.11	ZFC/FC magnetic susceptibility measurements of $\text{La}_5\text{Re}_3\text{NiO}_{16}$ with applied fields of 0.05 T, 2.0 T and 5.0 T .....	85
3.12	$\chi T$ versus T plot of $\text{La}_5\text{Re}_3\text{NiO}_{16}$ using the ZFC data only .....	86
3.13	Isothermal magnetization versus applied field data for $\text{La}_5\text{Re}_3\text{NiO}_{16}$ .....	86
3.14	Heat capacity measurements of $\text{La}_5\text{Re}_3\text{NiO}_{16}$ with no field applied and in a 7.0 T field .....	90
3.15	Magnetic component of the heat capacity of $\text{La}_5\text{Re}_3\text{NiO}_{16}$ , in zero applied field and in a 7 T field .....	90
3.16	Powder neutron diffraction patterns of $\text{La}_5\text{Re}_3\text{NiO}_{16}$ at 4 K and 50 K.....	91
3.17	Possible magnetic structure of $\text{La}_5\text{Re}_3\text{NiO}_{16}$ .....	91

#### Chapter 4 – Synthesis, Structure and Magnetic Properties of the Pillared Perovskites,

##### $\text{La}_5\text{Re}_{3-x}\text{Ta}_x\text{BO}_{16}$ ( $B = \text{Mn, Fe, Co, Ni}$ )

4.1	Crystal structure of a “pillared perovskite”, $\text{La}_5\text{Re}_{3-x}\text{Ta}_x\text{BO}_{16}$ .....	99
4.2	Comparison plot of the X-ray diffraction patterns of $\text{La}_5\text{Re}_{3-x}\text{Ta}_x\text{MnO}_{16}$ from 22-32° 2 $\theta$ , fired at three different temperatures .....	107
4.3	Comparison plot of the X-ray diffraction patterns of $\text{La}_5\text{Re}_{3-x}\text{Ta}_x\text{MnO}_{16}$ from 22-32° 2 $\theta$ , assuming full or half Ta substitution in the starting stoichiometry .....	107
4.4	Rietveld refinements of powder neutron diffraction data for $\text{La}_5\text{Re}_{3-x}\text{Ta}_x\text{BO}_{16}$ ....	109
4.5	SEM image of $\text{La}_5\text{Re}_{3-x}\text{Ta}_x\text{MnO}_{16}$ .....	111
4.6	SEM-EDS spectrum of the elemental composition of $\text{La}_5\text{Re}_{3-x}\text{Ta}_x\text{MnO}_{16}$ .....	111
4.7	TEM image of crystallites of $\text{La}_5\text{Re}_{3-x}\text{Ta}_x\text{MnO}_{16}$ .....	113
4.8	TEM diffraction pattern of a single crystal of $\text{La}_5\text{Re}_{3-x}\text{Ta}_x\text{MnO}_{16}$ .....	113
4.9	TEM-EDS spectrum of the elemental composition of $\text{La}_5\text{Re}_{3-x}\text{Ta}_x\text{MnO}_{16}$ .....	115
4.10	Rietveld refinement of powder X-ray diffraction data for $\text{La}_5\text{Re}_{3-x}\text{Nb}_x\text{MnO}_{16}$ .....	119
4.11	Comparison plot of the X-ray diffraction patterns of $\text{La}_5\text{Re}_{3-x}\text{Nb}_x\text{MnO}_{16}$ from 22-32° 2 $\theta$ , assuming full or half Nb substitution in the starting stoichiometry .....	119
4.12	SEM image of $\text{La}_5\text{Re}_{3-x}\text{Nb}_x\text{MnO}_{16}$ .....	121
4.13	SEM-EDS spectrum of the elemental composition of $\text{La}_5\text{Re}_{3-x}\text{Nb}_x\text{MnO}_{16}$ .....	121

4.14	TEM-EDS spectrum of the elemental composition of $\text{La}_5\text{Re}_{3-x}\text{Nb}_x\text{MnO}_{16}$ .....	122
4.15	TEM image of crystallites of $\text{La}_5\text{Re}_{3-x}\text{Nb}_x\text{MnO}_{16}$ .....	124
4.16	TEM diffraction pattern of a single crystal of $\text{La}_5\text{Re}_{3-x}\text{Nb}_x\text{MnO}_{16}$ .....	124
4.17	ZFC/FC magnetic susceptibility of $\text{La}_5\text{Re}_{3-x}\text{Ta}_x\text{MnO}_{16}$ .....	127
4.18	$\chi T$ versus temperature plot for $\text{La}_5\text{Re}_{3-x}\text{Ta}_x\text{MnO}_{16}$ .....	127
4.19	Magnetization curves recorded for $\text{La}_5\text{Re}_{3-x}\text{Ta}_x\text{MnO}_{16}$ .....	129
4.20	ZFC/FC magnetic susceptibility of $\text{La}_5\text{Re}_{3-x}\text{Ta}_x\text{FeO}_{16}$ .....	132
4.21	$\chi T$ versus temperature plot for $\text{La}_5\text{Re}_{3-x}\text{Ta}_x\text{FeO}_{16}$ .....	132
4.22	Magnetization curves recorded for $\text{La}_5\text{Re}_{3-x}\text{Ta}_x\text{FeO}_{16}$ .....	133
4.23	ZFC/FC magnetic susceptibility of $\text{La}_5\text{Re}_{3-x}\text{Ta}_x\text{CoO}_{16}$ .....	136
4.24	$\chi T$ versus temperature plot for $\text{La}_5\text{Re}_{3-x}\text{Ta}_x\text{CoO}_{16}$ .....	136
4.25	Magnetization curves recorded for $\text{La}_5\text{Re}_{3-x}\text{Ta}_x\text{CoO}_{16}$ .....	137
4.26	ZFC/FC magnetic susceptibility of $\text{La}_5\text{Re}_{3-x}\text{Ta}_x\text{NiO}_{16}$ .....	140
4.27	$\chi T$ versus temperature plot for $\text{La}_5\text{Re}_{3-x}\text{Ta}_x\text{NiO}_{16}$ .....	140
4.28	Magnetization curves recorded for $\text{La}_5\text{Re}_{3-x}\text{Ta}_x\text{NiO}_{16}$ .....	141
4.29	Critical field versus reduced temperature for the metamagnetic transitions of $\text{La}_5\text{Re}_{3-x}\text{Ta}_x\text{MO}_{16}$ ( $M = \text{Mn, Fe, Co, Ni}$ ) .....	143
4.30	$\chi T$ versus temperature plot for $\text{La}_5\text{Re}_{3-x}\text{Nb}_x\text{MnO}_{16}$ .....	146
4.31	Magnetization curves recorded for $\text{La}_5\text{Re}_{3-x}\text{Nb}_x\text{MnO}_{16}$ .....	146
4.32	Heat capacity data for $\text{La}_5\text{Re}_{3-x}\text{Ta}_x\text{CoO}_{16}$ .....	148
4.33	Heat capacity data for $\text{La}_5\text{Re}_{3-x}\text{Ta}_x\text{NiO}_{16}$ .....	149
4.34	Powder neutron diffraction pattern of $\text{La}_5\text{Re}_{3-x}\text{Ta}_x\text{MnO}_{16}$ taken at various temperatures.....	152
4.35	Rietveld refinements of low temperature powder neutron diffraction data for $\text{La}_5\text{Re}_{3-x}\text{Ta}_x\text{BO}_{16}$ .....	154
4.36	Intensity of the (0 0 1/2) and the (1 1 1/2)/(1 -1 1/2) reflection versus temperature for $\text{La}_5\text{Re}_{3-x}\text{Ta}_x\text{MnO}_{16}$ .....	155
4.37	Powder neutron diffraction pattern of $\text{La}_5\text{Re}_{3-x}\text{Ta}_x\text{NiO}_{16}$ at 4 K and room temperature .....	157

## Chapter 5 – Synthesis, Structure and Unexpected Magnetic Properties of $\text{La}_3\text{Re}_2\text{O}_{10}$

5.1	Rietveld refinement of the powder neutron diffraction data for $\text{La}_3\text{Re}_2\text{O}_{10}$ .....	172
5.2	Unit cell of $\text{La}_3\text{Re}_2\text{O}_{10}$ .....	172
5.3	ZFC/FC magnetic susceptibility of $\text{La}_3\text{Re}_2\text{O}_{10}$ .....	174
5.4	Fit of the ZFC magnetic susceptibility data from 200-300 K to the Curie-Weiss law .....	174
5.5	Fisher heat capacity of $\text{La}_3\text{Re}_2\text{O}_{10}$ .....	177
5.6	Isothermal magnetization curves for $\text{La}_3\text{Re}_2\text{O}_{10}$ collected at 10 and 30 K .....	177
5.7	Heat capacity of $\text{La}_3\text{Re}_2\text{O}_{10}$ , measured in the absence of a magnetic field .....	180
5.8	Comparison of the powder neutron diffraction patterns of $\text{La}_3\text{Re}_2\text{O}_{10}$ taken at 4 and 285 K .....	180
5.9	Re-Re bonding orbitals of $\text{Re}_2\text{O}_{10}\text{H}_8^-$ as calculated using DFT and spin density for $\text{Re}_2\text{O}_{10}\text{H}_8^-$ mapped over the total density isosurface .....	181

## Chapter 6 – Synthesis, Structure and Magnetic Properties of the Double Perovskite, $\text{SrLaRuNiO}_6$

6.1	ZFC/FC magnetic susceptibility of $\text{SrLaRuNiO}_6$ .....	196
6.2	$\chi T$ versus temperature plot for $\text{SrLaRuNiO}_6$ .....	196
6.3	Magnetization curves recorded for $\text{SrLaRuNiO}_6$ .....	198
6.4	Powder neutron diffraction data for $\text{SrLaRuNiO}_6$ at 4, 54, 80 and 283 K .....	199
6.5	Temperature dependence of the magnetic peak indexed as $(1/2\ 0\ 1/2) / (-1/2\ 0\ 1/2)$ in $\text{SrLaRuNiO}_6$ .....	199

## Chapter 7 – Magnetic Studies of the Ordered Rock Salt Oxides, $\text{Na}_2\text{Cu}_2\text{TeO}_6$ and

### $\text{Na}_3\text{Cu}_2\text{SbO}_6$

7.1	Edge-sharing octahedra in $\text{Na}_3\text{Cu}_2\text{SbO}_6$ .....	207
7.2	Schematic representation of the possible Cu–Cu interaction pathways in the <i>ab</i> plane of $\text{Na}_3\text{Cu}_2\text{SbO}_6$ .....	208
7.3	High temperature inverse magnetic susceptibility of $\text{Na}_2\text{Cu}_2\text{TeO}_6$ .....	211

7.4	ZFC magnetic susceptibility (from 5 to 600 K) and FC susceptibility (from 5 to 300 K) of $\text{Na}_2\text{Cu}_2\text{TeO}_6$ .....	211
7.5	ZFC magnetic susceptibility of $\text{Na}_2\text{Cu}_2\text{TeO}_6$ between 5 and 300 K.....	214
7.6	Comparison of the low temperature fits for the single dimer model ( $J_2/J_1 = 0$ ) and the alternating chain model ( $J_2/J_1 = 0.10(1)$ ).....	214
7.7	High temperature inverse magnetic susceptibility of $\text{Na}_3\text{Cu}_2\text{SbO}_6$ .....	217
7.8	ZFC magnetic susceptibility of $\text{Na}_3\text{Cu}_2\text{SbO}_6$ between 5 and 300 K.....	217

## List of Tables

### Chapter 1 - Introduction

1.1	Long-range Magnetic Order Possibilities for Lattice and Spin Dimensionality.....	17
-----	--	----

### Chapter 3 – Investigations of the Magnetic Properties and Structures of the Pillared Perovskites, $\text{La}_5\text{Re}_3\text{MO}_{16}$ ( $M = \text{Co}, \text{Ni}$ )

3.1	Unit Cell Parameters and Agreement Factors for the Structural Refinement of Diffraction Data for $\text{La}_5\text{Re}_3\text{CoO}_{16}$ and $\text{La}_5\text{Re}_3\text{NiO}_{16}$ .....	73
3.2	Magnetic Data for the $\text{La}_5\text{Re}_3\text{MO}_{16}$ Series .....	93

### Chapter 4 – Synthesis, Structure and Magnetic Properties of the Pillared Perovskites, $\text{La}_5\text{Re}_{3-x}\text{Ta}_x\text{BO}_{16}$ ( $B = \text{Mn}, \text{Fe}, \text{Co}, \text{Ni}$ )

4.1	Magnetic Data for the $\text{La}_5\text{Re}_3\text{BO}_{16}$ Series .....	100
4.2	Unit Cell Constants and Agreement Indices for the Rietveld Pattern Refinement of Powder Neutron Diffraction Data for $\text{La}_5\text{Re}_{3-x}\text{Ta}_x\text{BO}_{16}$ .....	108
4.3	SEM-EDS Analysis of $\text{La}_5\text{Re}_{3-x}\text{Ta}_x\text{MnO}_{16}$ and Calculated Atomic Percentages..	110
4.4	Diffraction Image Analysis of $\text{La}_5\text{Re}_{3-x}\text{Ta}_x\text{MnO}_{16}$ and Comparison with Pillared Perovskite Phase .....	114
4.5	TEM-EDS Analysis of $\text{La}_5\text{Re}_{3-x}\text{Ta}_x\text{MnO}_{16}$ and Calculated Atomic Percentages..	114
4.6	TEM-EDS Analysis of $\text{La}_5\text{Re}_3\text{NiO}_{16}$ and Calculated Atomic Percentages .....	116
4.7	Unit Cell Constants and Agreement Indices for the Rietveld Pattern Refinement of Powder X-ray Diffraction Data for $\text{La}_5\text{Re}_{3-x}\text{Nb}_x\text{MnO}_{16}$ .....	118
4.8	SEM-EDS Analysis of $\text{La}_5\text{Re}_{3-x}\text{Nb}_x\text{MnO}_{16}$ and Calculated Atomic Percentages .	120
4.9	TEM-EDS Analysis of $\text{La}_5\text{Re}_{3-x}\text{Nb}_x\text{MnO}_{16}$ and Calculated Atomic Percentages .	123
4.10	Diffraction Image Analysis of $\text{La}_5\text{Re}_{3-x}\text{Nb}_x\text{MnO}_{16}$ and Comparison with Pillared Perovskite Phase .....	125
4.11	Critical Fields for Metamagnetic Transitions Observed for $\text{La}_5\text{Re}_{3-x}\text{Ta}_x\text{BO}_{16}$ .....	142

4.12	Magnetic Data Comparison of the $\text{La}_5\text{Re}_{3-x}\text{Ta}_x\text{BO}_{16}$ and $\text{La}_5\text{Re}_3\text{BO}_{16}$ Series and $\text{La}_5\text{Re}_{3-x}\text{Nb}_x\text{MnO}_{16}$ .....	159
------	--	-----

Chapter 5 – Synthesis, Structure and Unexpected Magnetic Properties of  $\text{La}_3\text{Re}_2\text{O}_{10}$

5.1	Lattice Constants and Selected Interdimer Distances for $\text{La}_3\text{Re}_2\text{O}_{10}$ .....	173
5.2	$(\Delta e)^2$ for Some Magnetic Exchange Pathways (Intralayer and Interlayer) Between Various Dimers Calculated using the Spin Dimer Model .....	183

Chapter 6 – Synthesis, Structure and Magnetic Properties of the Double Perovskite,  $\text{SrLaRuNiO}_6$

6.1	Lattice Constants and Refinement Agreement Indices for $\text{SrLaRuNiO}_6$ .....	193
6.2	Atomic Parameters for $\text{SrLaRuNiO}_6$ .....	193

Chapter 7 – Magnetic Studies of the Ordered Rock Salt Oxides,  $\text{Na}_2\text{Cu}_2\text{TeO}_6$  and  $\text{Na}_3\text{Cu}_2\text{SbO}_6$

7.1	Possible Dimensionalities of the $\text{Cu}^{2+}$ Spin Correlations .....	206
7.2	Relative Strengths of Cu–Cu Exchange Pathways in <i>ab</i> Plane of $\text{Na}_2\text{Cu}_2\text{TeO}_6$ ....	212
7.3	Comparison of the Fitting Parameters for the Simple Dimer (Bleaney-Blowers) Model and the Alternating Chain Model .....	213
7.4	Obtained Values from the AF-AF Alternating Chain Model Fit to the ZFC Susceptibility Data of $\text{Na}_2\text{Cu}_2\text{TeO}_6$ and $\text{Na}_3\text{Cu}_2\text{SbO}_6$ .....	218
7.5	$(\Delta e)^2$ for the Various Exchange Pathways in $\text{Na}_2\text{Cu}_2\text{TeO}_6$ and $\text{Na}_3\text{Cu}_2\text{SbO}_6$ Calculated Using the Spin Dimer Model.....	219
7.6	Comparison of Observed and Calculated Weiss Constants ( $\theta$ ) for the AF-AF and AF-F Linear Chain Models for $\text{Na}_2\text{Cu}_2\text{TeO}_6$ and $\text{Na}_3\text{Cu}_2\text{SbO}_6$ .....	221

## **Chapter 1**

### **Introduction**

This chapter introduces key concepts that will be illustrated in the following chapters, including the perovskite structure type, magnetism and magnetic superexchange in particular, as well as metamagnetism and spin flop transitions.

## 1.1 Thesis Outline

Magnetism is an unusual natural phenomenon that has fascinated man since ancient times. Much research has focussed on experimental and theoretical investigations of magnetism and magnetic properties of materials. Interesting and useful properties such as superconductivity and colossal magnetoresistance have been discovered and are still being intensely researched.<sup>1,2</sup> In fact, the 2007 Nobel Prize in Physics was awarded to Prof. Albert Fert and Prof. Peter Grünberg, who each independently discovered the giant magnetoresistance phenomena.<sup>3</sup> However, despite an enormous body of research, there is currently no reliable method for predicting a compound's magnetic properties before it has been synthesized and magnetically characterized.

This Ph.D. thesis has focussed on the preparation and characterization of seemingly low-dimensional transition metal oxides (typically based on the perovskite structure type) that exhibit long-range order, despite large separation lengths between magnetic centres. It is structured as follows. Chapter One continues with a brief introduction of perovskites, general magnetism and magnetic superexchange in oxides. Each Chapter focuses on a unique research project within the scope of this thesis and has its own brief introduction. Chapter Two details the experimental methods (both theory and specific instrumentation) used by the author to synthesize and study these materials. Chapters Three through Seven describe the author's research in detail, while Chapter Eight is a general summary of the thesis research and conclusions.

Specifically, Chapter Three discusses the further investigation of the magnetic properties and magnetic structures of two "pillared" perovskites,  $\text{La}_5\text{Re}_3\text{MO}_{16}$  ( $M = \text{Co}$ ,

Ni). Long-range magnetic order is evident in these layered compounds, despite an interlayer distance of over 10 Å, and a completely different magnetic structure than the other series member was found for the Ni compound.<sup>4</sup> The focus of Chapters Four is the synthesis and complete magnetic characterization of a new series of “pillared” perovskites –  $\text{La}_5\text{Re}_{3-x}\text{Ta}_x\text{BO}_{16}$  ( $B = \text{Mn, Fe, Co, Ni; } x \sim 0.5$ ). The extent of tantalum(V) substitution was also investigated thoroughly, as the synthetic challenges in this system were not trivial. The substitution of non-magnetic tantalum(V) further dilutes the magnetic system, however, long-range order persists within this series of compounds. With critical temperatures within a few degrees from their all rhenium derivatives, it appears the interlayer connectivity pathway is the key to long-range magnetic order.

Chapter Five outlines the first polycrystalline synthesis and full magnetic characterization of  $\text{La}_3\text{Re}_2\text{O}_{10}$ , a compound with relatively isolated, magnetically active “dimer” units that unexpectedly orders at 18 K.<sup>5</sup> Chapter Six recounts the synthesis and magnetic investigation of the double perovskite,  $\text{SrLaRuNiO}_6$ . A case of pseudo-symmetry and a high degree of correlation between the two different magnetic moments made a single unique magnetic structure solution impossible to determine. However, this study did demonstrate the power of neutron diffraction in determining magnetic properties of a particular compound when bulk susceptibility data suffer from contamination by ferromagnetic impurities. Finally, Chapter Seven describes the author’s contribution to the magnetic characterization and understanding of the low-dimensional, ordered rock-salt oxides,  $\text{Na}_2\text{Cu}_2\text{TeO}_6$  and  $\text{Na}_3\text{Cu}_2\text{SbO}_6$ . In this case, the specific bond

lengths and angles between interacting magnetic centres plays a critical role in determining the overall magnetic properties of the system.<sup>6,7</sup>

## 1.2 Perovskite Structure Type

The perovskite structure type is one of the most prevalent and robust in transition metal oxide chemistry. The basic formula is  $ABO_3$  and the ideal structure is cubic ( $Pm\bar{3}m$ ), illustrated in Figure 1.1 for  $SrTiO_3$ . It can be described as a three-dimensional framework of corner-shared  $BO_6$  octahedra, with  $A$ -site cations occupying the 12 coordinate interstices.<sup>8</sup> Both the  $A$  and  $B$  cations form a cubic close packed lattice, and all of the atoms lie on special positions.

What makes the perovskite structure so versatile is that various distortions away from cubic symmetry are possible, while maintaining the same basic structure type. Three different distortions have been identified: distortions of the  $BO_6$  octahedra,  $B$ -site cation displacements and tilting of the  $BO_6$  octahedra. Octahedral tilting is the most common type of distortion, resulting in lower crystal symmetry. Glazer<sup>9</sup> and Woodward<sup>10,11</sup> have developed systems to describe the various tilting schemes that are possible and the space groups associated with them. The apparent driving force behind this type of distortion is the differences in size and charge of the ions on the  $A$  and  $B$  sites.

A “tolerance factor”<sup>12</sup> has been defined that roughly determines the stability of the perovskite structure in terms of the  $A$  and  $B$  cation sizes, as well as the oxygen radius:

$$t = \frac{r_A + r_O}{\sqrt{2}(r_B + r_O)} \quad 1.1$$

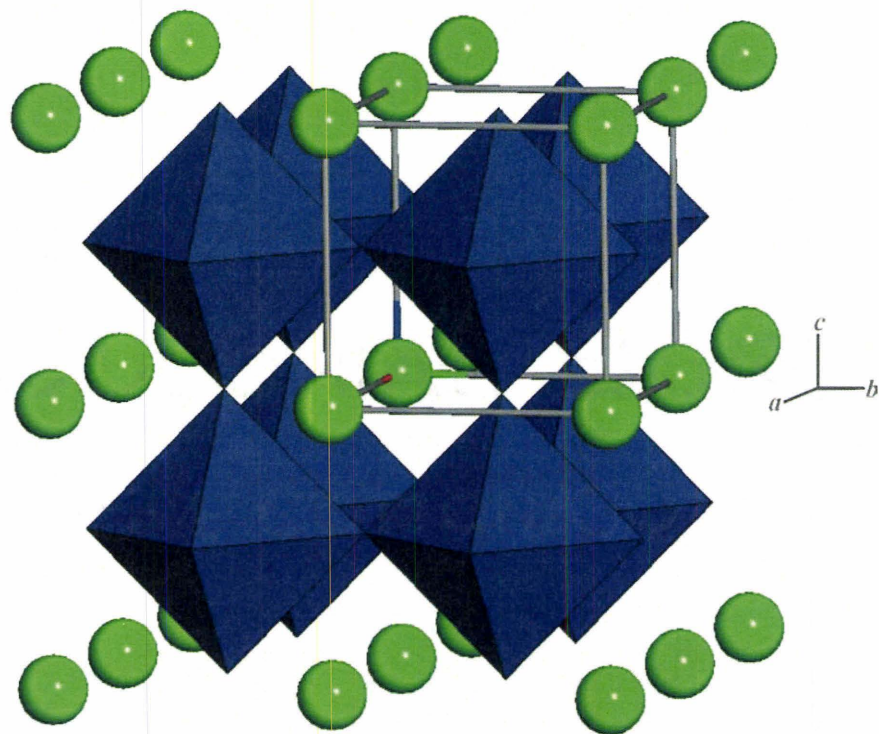


Figure 1.1. Crystal structure of the ideal  $ABO_3$  perovskite. The green spheres represent  $A$  site cations, the blue octahedra are  $B$ -site ions with oxygens located at corners of the polyhedra.

The perovskite structure is stable in the range  $0.8 \leq t \leq 1$ . Outside of this range, other phases, such as hexagonal  $ABO_3$  structures or pyroxenes, are more stable. The most stable perovskites have  $A$ -site cations that have larger radii than the  $B$ -site cations, and distortions away from cubic symmetry are noted when these ratios are not ideal (i.e.  $t \neq 1$ ).

Another remarkable feature of the perovskite structure is its tolerance for  $A$  and  $B$  site substitution. “Double perovskites”,  $AA'BB'O_6$  ( $A = A'$  or  $A \neq A'$ ;  $B \neq B'$ ), are formed when the  $B$ -site cations are occupied by two different elements. The  $A$  sites may contain all the same element or not. As with the ideal perovskites, distortions away from cubic geometry are common, as is octahedral tilting. However, depending on the charge and size difference between the  $B$  and  $B'$  cations, they may be randomly distributed or site ordered within the structure. If the  $B$  and  $B'$  ions are ordered, they each form a face-centred cubic lattice (Figure 1.2). Of course, if  $B$  and  $B'$  are magnetic, whether they are ordered or randomly distributed over the  $B$  sites plays a critical role in their observed magnetic behaviour.<sup>13-16</sup> Chapter Six describes the synthesis and subsequent magnetic characterization of one such double perovskite compound,  $SrLaRuNiO_6$ .

Finally, a relatively new structure type, derived from the basic perovskite structure, has been identified. The so-called “pillared perovskite” is pictured in Figure 1.3. The general formula is  $Ln_5D_2ABO_{16}$ , where  $Ln$  is a lanthanide ( $La^{3+}$ );  $D$  is a 4d or 5d transition metal such as  $Mo^{4+}$ ,  $Re^{5+}$  or  $Os^{5+}$ ; and  $A$  and  $B$  are a specific combination of 3d, 4d or 5d transition metals (such as  $Mo^{5+}$  with  $Mo^{4+}$  or  $Mn^{2+}$ ,  $Co^{2+}$ ,  $Mg^{2+}$  or  $Ni^{2+}$ )<sup>17-19</sup>; ( $Re^{5+}$  with  $Mn^{2+}$ ,  $Fe^{2+}$ ,  $Co^{2+}$ ,  $Ni^{2+}$  or  $Mg^{2+}$ )<sup>4,20-22</sup>; or ( $Os^{5+}$  with  $Mn^{2+}$ )<sup>23</sup>.

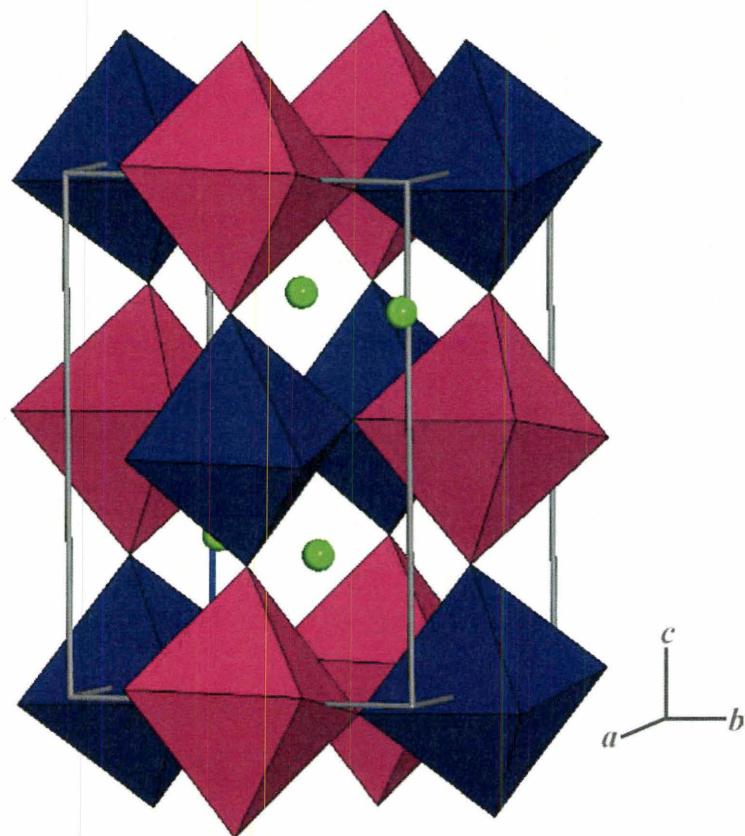


Figure 1.2. Crystal structure of an ordered  $A_2BB'O_6$  double perovskite. The green spheres are the  $A$  site ions; the pink and blue octahedra are the  $B$  and  $B'$  ions, respectively with oxygens located on the corners of the polyhedra.

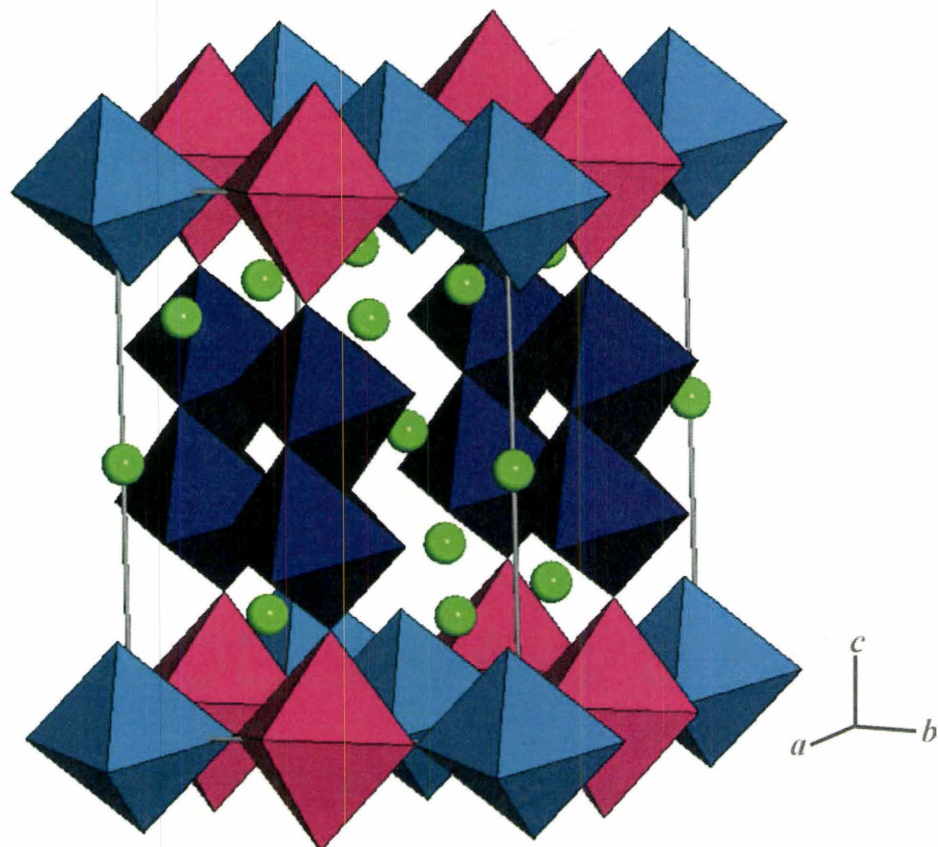


Figure 1.3. Crystal structure of a “pillared perovskite”,  $Ln_5D_2ABO_{16}$ . The Ln ions are green spheres; the  $D_2O_{10}$  dimer “pillar” is in dark blue; the ordered A and B-site cations are the light blue and pink octahedra, respectively, with oxygens located at the corners.

From the Figure, it is clear that the structure contains perovskite-like layers of corner-shared  $AO_6$  and  $BO_6$  octahedra that are usually charge-ordered. “Pillars”, consisting of edge-shared  $D_2O_{10}$  octahedral dimer units, separate the layers by about 10 Å, and only connect through the  $B$  site cations. Due to metal-metal bonding within the dimers, electrons are typically paired, and the “pillars” are diamagnetic. The lanthanide ions are contained in interstitial sites between the layers, and can also be non-magnetic.

Due to the lattice topology, where normally the only ions containing unpaired electrons reside within the perovskite layers, one would expect two-dimensional magnetic behaviour with only weak interactions (if any) between the planes. However, long-range order has been observed for most of these systems, with relatively high critical temperatures (160–180 K) in some cases.<sup>18-21</sup> Chapters Three and Four discuss further investigations of this interesting magnetic behaviour for some of these systems.

### 1.3 Magnetism

#### *Free Ion Magnetism*

All matter responds in some way to an applied magnetic field. Magnetic susceptibility ( $\chi$ ) is defined as the magnetization of a material in response to an applied magnetic field. Compounds react differently on the susceptibility scale, depending on how the electrons are arranged. Electrons paired in orbitals (such as “core electrons”) exhibit diamagnetism. Induced charge density currents act to oppose an applied magnetic field, and hence diamagnetism is negative. It is also temperature independent. The diamagnetic contribution to an atom’s overall magnetic susceptibility is typically a few

orders of magnitude smaller than any paramagnetic contribution, which is always positive.

Paramagnetism results from any unpaired electrons as well as their associated orbital angular momentum. If the coupling between the spin and the orbital angular momentum is negligible (typically the case for a transition metal), the total magnetic moment on a paramagnetic atom can be expressed by equation 1.2:

$$\tilde{\mu} = -\mu_B(\tilde{L} + g_s\tilde{S}) \quad 1.2$$

where  $\tilde{\mu}$  is the magnetic moment operator,  $\mu_B$  is the Bohr magneton,  $\tilde{L}$  is the orbital angular momentum operator,  $\tilde{S}$  is the spin angular momentum operator and  $g_s$  equals 2 (for a free ion). However, when spin-orbit coupling can not be ignored (i.e. for a lanthanide ion), the magnetic moment depends on the total angular momentum ( $\tilde{J}$ ):

$$\tilde{\mu} = -\mu_B g_J \tilde{J} \quad 1.3$$

where  $\tilde{J}$  is a combination of orbital and spin angular momentum and  $g_J$  is given by:

$$g_J = \frac{3}{2} + \frac{S(S+1) - L(L+1)}{2J(J+1)} \quad 1.4$$

These equations work for an isolated free ion, and do not account for crystal field effects or the interactions between magnetic ions. The next few sections discuss cooperative magnetic effects.

#### *Paramagnetism and the Curie Law*

Paramagnetism is a random arrangement of magnetic spins in space and time. It can consist of temperature dependent and independent parts. Several magnetic states can be accessed according to a Boltzmann distribution, which is weighted according to the

population of states. Applying Perturbation Theory results in the van Vleck equation, which describes the magnetic susceptibility ( $\chi$ ) of a material as a function of temperature,  $T$ :

$$\chi = \frac{\langle M \rangle}{H} = \frac{\sum_n \left( \frac{(E_n^{(1)})^2}{k_B T} - 2E_n^{(2)} \right) \exp(-E_n^0 / k_B T)}{\sum_n \exp(-E_n^0 / k_B T)} \quad 1.5$$

where  $\langle M \rangle$  is the average magnetization,  $H$  is the external applied magnetic field,  $E^0$  is the ground state energy and  $E^{(1)}$  and  $E^{(2)}$  are the first and second order Zeeman energies, respectively (which arise from the magnetic moment operator operating on the ground and excited state wavefunctions);  $k_B$  equals Boltzmann's constant, and the index,  $n$ , denotes accessible states. High temperature expansion of van Vleck's equation leads to the Curie Law, which describes temperature dependent paramagnetism with no interactions between moments:

$$\chi = \frac{C}{T} \quad 1.6$$

where  $C$  is the Curie constant. The Curie Law is valid for paramagnets with no thermally accessible states whose populations vary with changing temperature. If a temperature independent term is considered, it simply results in an additive term:

$$\chi = \frac{C}{T} + TIP \quad 1.7$$

The Curie constant can be defined in terms of the total angular momentum quantum number,  $J$ , which is a combination of both the orbital quantum number,  $L$  and spin quantum number,  $S$ :

$$C = \frac{Ng^2(\mu_B)^2 J(J+1)}{3k_B} \quad 1.8$$

The constant terms ( $N\mu_B^2/3k_B$ ) equate to 1/8. For transition metal oxides, the orbital angular momentum is typically quenched due to crystal field effects, and the equation simplifies by substituting  $S$  for  $J$ . An effective “spin-only” moment,  $\mu_{eff}$ , can be defined in terms of the Lande  $g$  factor mentioned previously:

$$\mu_{eff} = g\sqrt{S(S+1)}\mu_B \quad 1.9$$

and the Curie constant can now be expressed in terms of the effective moment:

$$C = \frac{(\mu_{eff})^2}{8} \quad 1.10$$

An important thing to remember when dealing with ‘real’ compounds is that the Curie constants are directly additive, whereas the effective moments are additive in quadrature:

$$\mu_{eff}(total) = \sqrt{\sum (\mu_{eff})^2} \quad 1.11$$

When interactions between magnetic moments are not negligible, an extra term must be added to the Curie Law:

$$\chi = \frac{C}{T - \theta} \quad 1.12$$

where  $\theta$  is the Weiss constant. This sets the energy scale for the magnetic interactions.

In addition, when the proper form of the magnetic exchange Hamiltonian is used (see equation 1.13), the sign of the Weiss constant in the now so-called Curie-Weiss Law, can denote the type of magnetic interactions. According to Mean Field Theory, a negative

Weiss constant indicates antiferromagnetic interactions, whereas a positive Weiss constant denotes ferromagnetic interactions.

### *Magnetic Exchange*

Magnetic interactions between electrons in two different atomic orbitals on two different atoms can be described using the Heisenberg-Dirac-VanVleck magnetic exchange Hamiltonian:

$$H = -2J \sum_{ij} \vec{S}_i \cdot \vec{S}_j \quad 1.13$$

where  $J$  is the spin exchange constant (not the total angular momentum), and  $\vec{S}_i$  and  $\vec{S}_j$  are the values for the spin on the two interacting electrons, respectively. For this definition of the spin exchange Hamiltonian, when  $J$  is positive, a ferromagnetic interaction is preferred. For a negative  $J$  value, an antiferromagnetic alignment dominates.

The basics of magnetic exchange can be described in terms of electron transfer and interaction between ions. For simple cases, application of Hund's rule and the Pauli principle can help explain the sign of the exchange interaction. Goodenough and Kanamori developed a set of "rules" to treat cation-cation, cation-anion-cation and cation-anion-anion-cation magnetic superexchange for 180° and 90° interactions.<sup>24,25</sup> Due to many competing exchange interactions for intermediate angles, reliable predictions are difficult to estimate.

For oxides compounds, understanding cation-anion-cation magnetic superexchange is important. In this case, the diamagnetic oxygen anion mediates the exchange between the two paramagnetic transition metal centres. Figure 1.4 details the

180° superexchange interaction between two Mn<sup>3+</sup> centres ( $S = 2$ ). From the overlap of the metal d orbitals and the oxygen 2p orbitals, and application of the Pauli principle, antiferromagnetic exchange would be preferred. Depending on the angle, the sign of the superexchange interaction might be different. For example, 90° superexchange in this case would be ferromagnetic.

Often, two different metal ions are involved in the 180° superexchange pathway. This case is illustrated in Figure 1.5. Here, a ferromagnetic interaction between a partially occupied  $e_g$  and empty  $e_g$  orbital on the two different metal centres is preferred.

A common method for determining the magnitude of the magnetic interactions within a solid is to measure the magnetic susceptibility ( $\chi$ ), which was discussed earlier with respect to the Curie Law.

#### *Characterization of Magnetic Systems*

A more quantitative treatment of magnetic interactions is to use the general Hamiltonian (H) for localized magnetic moments (S) under the influence of magnetic field,  $H$ :

$$H = -2 \sum_{ij} J_{ij} (aS_i^z S_j^z + b(S_i^x S_j^x + S_i^y S_j^y)) - g\mu_B H \sum_i S_i \quad 1.14$$

where  $J_{ij}$  is the exchange constant between two sites,  $i$  and  $j$ ; and the coefficients  $a$  and  $b$  are constants which depend on the dimensionality of the moments (D), or the anisotropy of the system. This is distinct from the dimensionality of the system (d), which is determined purely from crystallography. More details on spin and lattice dimensionality appear below. The final term in the above equation accounts for the effect of an external, applied magnetic field,  $H$ , on the localized moments on the lattice.

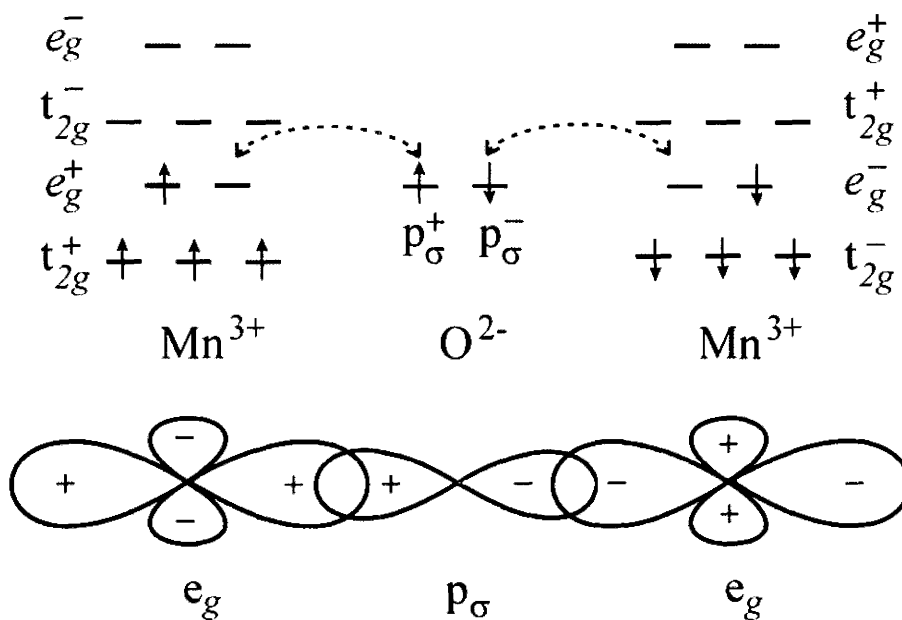


Figure 1.4. Magnetic superexchange illustrated for  $\text{Mn}^{3+} - \text{O} - \text{Mn}^{3+}$  with  $180^\circ$  bonding angle and octahedral crystal field. The  $t_{2g}$  and  $e_g$  orbitals have been separated into up (+) and down (-) spin components. The orbital overlap is shown at the bottom. This particular superexchange results in antiferromagnetic coupling between the metal centres.

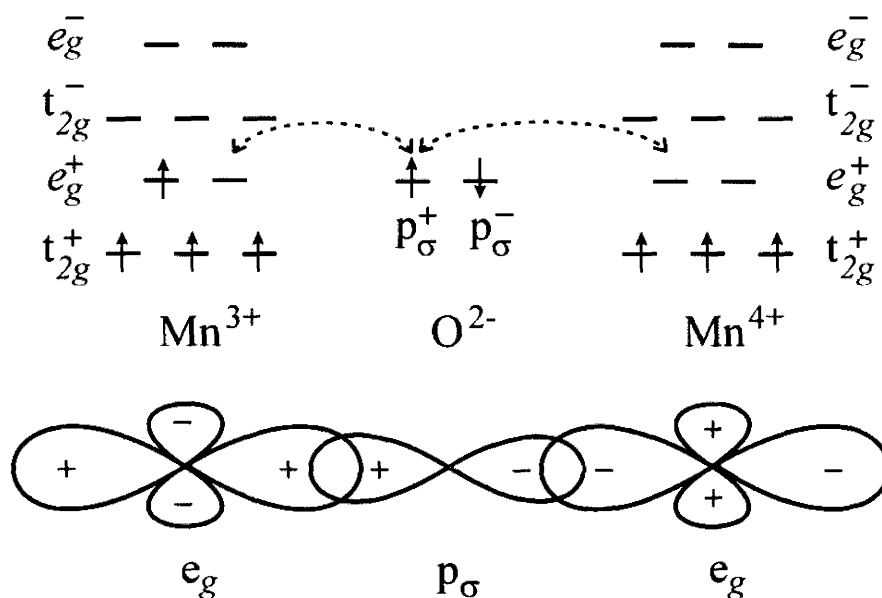


Figure 1.5. Magnetic superexchange illustrated for  $\text{Mn}^{3+} - \text{O} - \text{Mn}^{4+}$  with  $180^\circ$  bonding angle and octahedral crystal field. The  $t_{2g}$  and  $e_g$  orbitals have been separated into up (+) and down (-) spin components. The orbital overlap is shown at the bottom. This particular superexchange results in ferromagnetic coupling between the metal centres.

### *Dimensionality of Magnetic Lattices*

Magnetic systems can be classified according to two simple terms: the lattice dimensionality ( $d$ ) and the spin dimensionality ( $D$ ). The lattice dimensionality ( $d$ ) is related to the crystallographic structure of the system, and more precisely, the magnetic sublattice. Based on the location of the magnetic moments, a distinction between 1-dimensional (chain-like,  $d = 1$ ), 2-dimensional (planes or layers,  $d = 2$ ) and 3-dimensional (network,  $d = 3$ ) can be made.

On the other hand, the spin dimensionality ( $D$ ) describes the symmetry or geometric restrictions of the magnetic moments involved. It refers to the anisotropy of the magnetic spins. If the spins are constrained to lie, either up or down, along one preferred magnetization axis (e.g. the  $z$  axis), and do not deviate at all, they are called Ising spins ( $D = 1; a = 1, b = 0$ ). If the orientation of the spins lies in only one defined plane, with no component perpendicular to this plane, they are referred to as XY magnets ( $D = 2; a = 0, b = 1$ ). When the spins are allowed to point in any direction and are isotropic, they are referred to as Heisenberg spins ( $D = 3; a = b = 1$ ). The general spin Hamiltonian (equation 1.14) can account for all three models through the combinations of  $a$  and  $b$  coefficients shown. However, not all combinations of lattice and spin dimensionalities lead to uniquely defined long-range ordered ground states for the magnetic system. Table 1.1 lists the possible combinations of  $d$  and  $D$  for which magnetic long-range order is possible.

Table 1.1. Long-range Magnetic Order Possibilities for Lattice and Spin Dimensionality

Spin Dimensionality	Lattice Dimensionality		
	d = 1 (Chains)	d = 2 (Planes)	d = 3 (Network)
D = 1 (Ising)	×	✓	✓
D = 2 (XY)	×	×	✓
D = 3 (Heisenberg)	×	×	✓

Certain trends are clear from examination of the Table. In crystallographic 3-D networks ( $d = 3$ ), long-range magnetic order can exist for Ising, XY or Heisenberg spins. In contrast, no true  $d = 1$  system has been found to exhibit a transition to long-range magnetic order for any spin dimensionality,  $D$ . In the case of layered compounds ( $d = 2$ ), ordered systems with Ising spins ( $D = 1$ ) exist, but Heisenberg ( $D = 3$ ) do not, for example.

#### *Conventional Magnetic Ground States*

There are three classic motifs for arranging localized magnetic moments to achieve long-range magnetic order at low temperatures: ferromagnetism, antiferromagnetism and ferrimagnetism.

In a ferromagnet, all localized magnetic moments are aligned parallel to a preferred magnetization axis (Figure 1.6). This is manifested as an observation of a spontaneous magnetic moment at low temperatures. Large net magnetization results, which is proportional to the total or saturation magnetic moment:

$$\mu_{sat} = 2S\mu_B = g_J\mu_B \quad 1.15$$

Bulk magnetization measurements show hysteresis behaviour and large saturation at low temperatures. In magnetic susceptibility measurements, ferromagnetism is observed as a

large rise in susceptibility at low temperature, with the critical temperature ( $T_c$ ) taken as the inflection point of this curve.

Antiferromagnets can be thought of as two interpenetrating magnetic sublattices, with equal values for the magnetic moments, that are aligned antiparallel to each other along a preferred magnetization axis (Figure 1.7). As a result, the net magnetization along this axis in the ordered state is zero, apart from thermal excitations. In bulk susceptibility measurements, antiferromagnetism is identified as a peak in the data at low temperatures, with the apex typically taken as the critical temperature ( $T_c$ ) of the transition. Sharp peaks typically denote long-range order, whereas broader features are often indicative of shorter range interactions.

Ferrimagnets, similar to antiferromagnets, consist of two or more interpenetration magnetic sublattices, arranged antiparallel to each other, but where the values of the moments do not exactly cancel (Figure 1.8). This creates a net residual magnetic moment, similar to a ferromagnet. As a result, ferrimagnets often have characteristics that are similar to both antiferromagnets and ferromagnets. A canted antiferromagnetic is an interesting example of weak ferrimagnetism, as the slight tilting of the moments on one of the sublattices creates a small residual ferromagnetic component. Situations like ferrimagnetism and canted antiferromagnetism often arise on mixed valent materials.

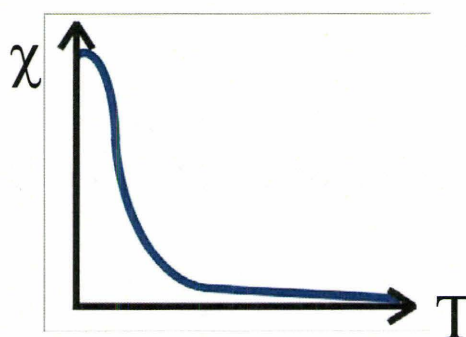
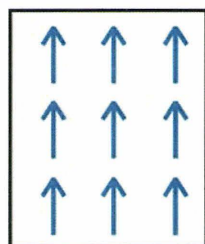


Figure 1.6. Ferromagnetism depicted for a 2-dimensional arrangement of spins [*left*], and manifested in a typical magnetic susceptibility measurement [*right*].

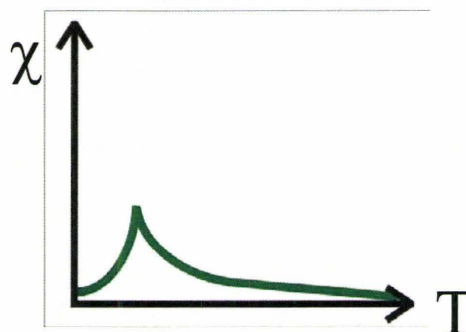
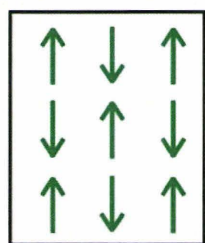


Figure 1.7. Antiferromagnetism depicted for a 2-dimensional arrangement of spins [*left*], and manifested in a typical magnetic susceptibility measurement [*right*].

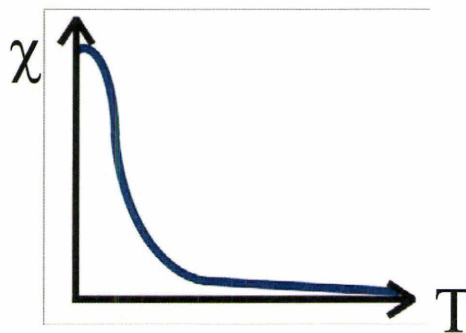
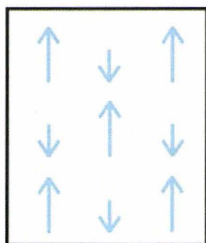


Figure 1.8. Ferrimagnetism depicted for a 2-dimensional arrangement of spins [*left*], and manifested in a typical magnetic susceptibility measurement [*right*].

#### 1.4 Metamagnetism and Spin Flop

The concepts of metamagnetism and spin flop are closely related. Both of these magnetic phenomena depend on the relative magnitudes of effective fields present within a sample below its critical temperature for magnetic long-range order. One such field is the exchange field ( $H_{ex}$ ), which controls the strength of the magnetic interactions between individual moments. If the exchange field is relatively weak, an external applied field is often able to destroy the magnetic order within a compound. The second effective field is the anisotropy field ( $H_{anis}$ ). The magnitude of this field dictates how strongly the moments are aligned along a particular preferred axis. The stronger the anisotropy field, the greater the external field applied antiparallel to the preferred axis of orientation required to change the orientation of the moments. As a result, a compound should possess relatively weak antiferromagnetic interactions as well as a preferred axis for the alignment of these moments, in order to manifest these behaviours.

In a spin flop transition, the exchange field is greater than the anisotropy field. However, both of these fields are much smaller than an applied laboratory field that would be necessary to cause a spin flop to occur ( $H_{SF}$ ). Since the exchange field is greater, an antiferromagnetic alignment is still favoured, albeit not necessarily along the magnetization axis. In this way, the spins “flop” to maintain an antiferromagnetic alignment perpendicular to the applied field (which is oriented along the preferred magnetization axis), as depicted in Figure 1.9. The field required for a spin flop transition, thus, depends on both the exchange and anisotropy fields:

$$H_{SF} = [2H_{ex}H_{anis} - (H_{anis})^2]^{1/2} \quad 1.16$$

As the field is increased further, the exchange field is eventually overcome and the moments align themselves with the applied field at some critical field. This critical field,  $H_C$ , can also be expressed in terms of the exchange and anisotropy fields:

$$H_C = 2H_{ex} - H_{anis} \quad 1.17$$

In a single crystal, a “spin flop” is manifested as a discontinuity in the magnetization along the critical direction. For powder samples, this effect is highly attenuated by powder averaging and is typically observed experimentally as a “bend” or gradual increase in a compound’s magnetization with increasing field, recorded at a constant temperature below  $T_c$  (Figure 1.9). The lower the temperature below  $T_c$ , the higher the applied field required to overcome the anisotropy field.

The phenomenon of metamagnetism is typically manifested in layered compounds. Strong intralayer ferro- or ferri-magnetic interactions, along with weaker antiferromagnetic interlayer coupling are necessary compound characteristics, as well as a preferred axis of orientation for the moments involved. In this case, the anisotropy field is greater than the weak interlayer antiferromagnetic exchange field. Within the layers, the moments do not move off of the preferred magnetization axis. Rather, when the field required for a metamagnetic transition ( $H_{MM}$ ) is larger than the weak interlayer exchange field, the layers of moments all align parallel along the preferred axis of magnetization, which is also where the applied field is oriented. This is illustrated in Figure 1.10.

Contrary to a spin flop transition, metamagnetism does not result in an intermediate state, but rather an applied field causes an antiferromagnetic arrangement of spins to align parallel along a preferred axis of magnetization directly. This is observed as a large,

sudden increase in magnetization with increasing field (for a single crystal), recorded at constant temperature below  $T_c$  (Figure 1.10), or a more gradual “S”-shaped curve to the magnetization (in the case of a powder). Again, the lower the temperature below  $T_c$ , the greater the applied field required to induce the metamagnetic transition. The inflection point of the “S”-shaped magnetization curve is the value of the metamagnetic field, and by measuring magnetization curves for many temperatures below  $T_c$  and graphing their  $H_{MM}$  values,  $H_{MM}$  at zero temperature can be extrapolated.

Both of these phenomena are observed better in single crystal samples, where oriented measurements can be made. However, in powder samples, there are enough crystallites that have their preferred magnetization axis aligned with the applied field to display these behaviours experimentally, although the features may not be as sharp.

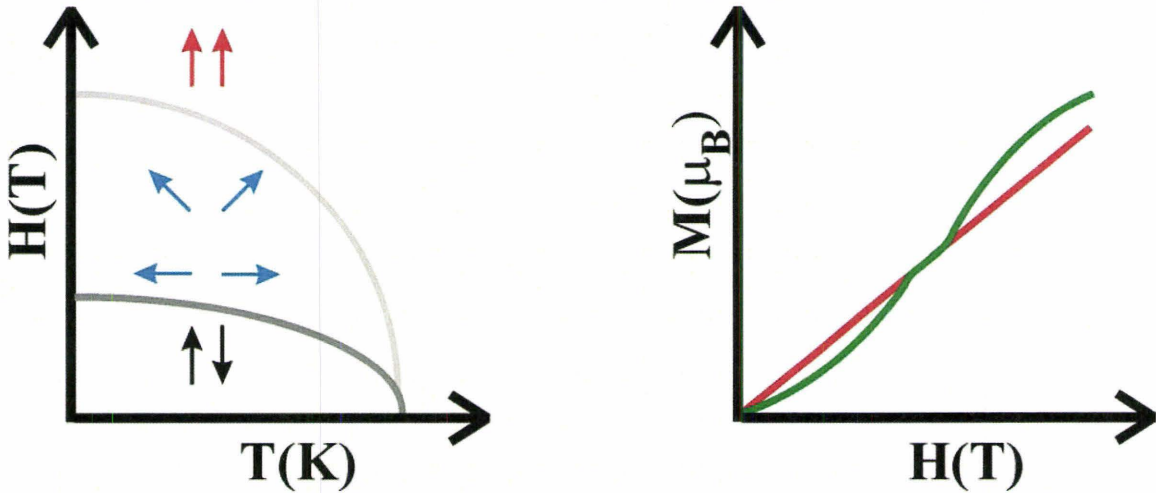


Figure 1.9. Spin flop depicted in terms of temperature (T) and field (H) [left]. The arrows indicate the magnetic coupling. The x-intercept of the curve is the critical ordering temperature ( $T_c$ ). A spin flop transition observed experimentally [right] as a slight curvature in magnetization (M) versus applied field (H) for a given temperature below  $T_c$  for a powder sample. A paramagnetic signal (red) is shown for comparison.

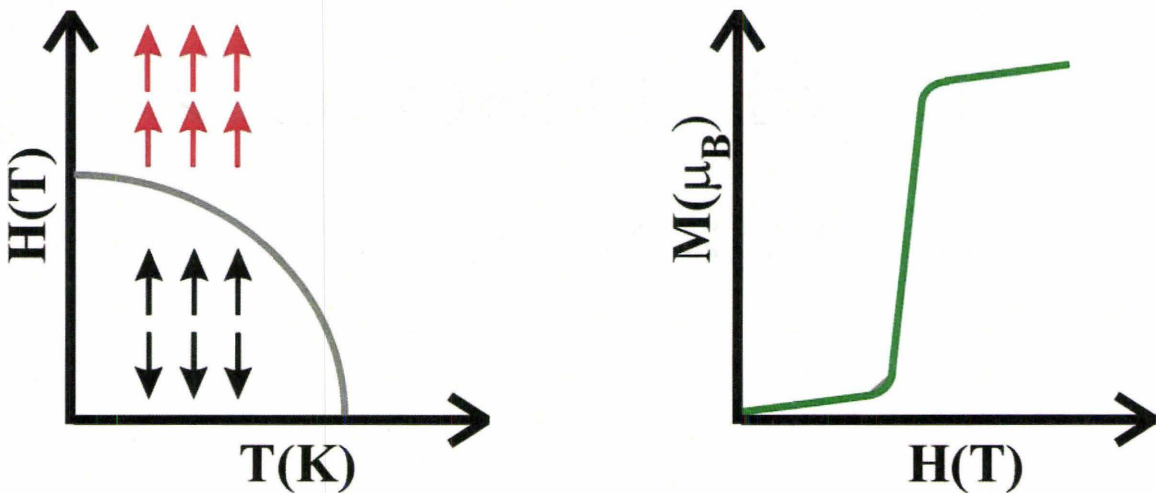


Figure 1.10. Metamagnetism displayed in terms of temperature (T) and field (H) [left]. The arrows depict the interlayer magnetic coupling. The y-intercept of the curve is the critical field ( $H_C$ ) for the metamagnetic transition, and the x-intercept is the critical ordering temperature ( $T_c$ ). A metamagnetic transition observed experimentally [right] as a large increase in magnetization (M) with applied field (H) for a given temperature below  $T_c$  for a powder sample. The inflection point of the “S”-shaped curve is taken as  $H_C$  for the transition.

## 1.5 References

1. *New Research on Superconductivity*; Martins, B. P., Ed.; Nova Science Publishers, Inc.: New York, 2007.
2. *Colossal Magnetoresistance, Charge Ordering and Related Properties of Manganese Oxides*; Rao, C. N. R.; Raveau, B., Eds.; World Scientific: Singapore, 1998.
3. Royal Academy of Sciences. *The 2007 Nobel Prize in Physics*, 2007; [http://nobelprize.org/nobel\\_prizes/physics/laureates/2007/press.html](http://nobelprize.org/nobel_prizes/physics/laureates/2007/press.html)
4. Cuthbert, H. L.; Greedan, J. E.; Cranswick, L. *J. Solid State Chem.* **2006**, *179*, 1938-1947.
5. Cuthbert, H. L.; Greedan, J. E.; Vargas-Baca, I.; Derakhshan, S.; Swainson, I. P. *Inorg. Chem.* **2007**, *46*, 8739-8745.
6. Xu, J.; Assoud, A.; Soheilnia, N.; Derakhshan, S.; Cuthbert, H. L.; Greedan, J. E.; Whangbo, M. H.; Kleinke, H. *Inorg. Chem.* **2005**, *44*, 5042-5046.
7. Derakhshan, S.; Cuthbert, H. L.; Greedan, J. E.; Rahaman, B.; Saha-Dasgupta, T. *Phys. Rev.* **2007**, *B76*, 104403(1-7).
8. Barth, T. *Norsk Geologisk Tidsskrift* **1925**, *8*, 201-216.
9. Glazer, A. M. *Acta Crystallogr.* **1972**, *B28*, 3384-3392.
10. Woodward, P. M. *Acta Crystallogr.* **1997**, *B53*, 32-43.
11. Woodward, P. M. *Acta Crystallogr.* **1997**, *B53*, 44-66.
12. Goldschmidt, V. M. *Matem. Naturvid. Klasse.* **1926**, *2*, 1-117.
13. Battle, P. D.; Gibb, T. C.; Jones, C. W.; Studer, F. *J. Solid State Chem.* **1989**, *78*, 281-293.
14. Anderson, M. T.; Greenwood, K. B.; Taylor, G. A.; Poepelmeier, K. R. *Prog. Solid St. Chem.* **1993**, *22*, 197-233.
15. Kim, S. H.; Battle, P. D. *J. Solid State Chem.* **1995**, *114*, 174-183.
16. Fang, M.; Kato, M.; Yoshimura, K.; Kosuge, K. *J. Alloys Comp.* **2001**, *317-8*, 136-140.
17. Ledesert, M.; Labbe, P.; McCarroll, W. H.; Leligny, H.; Raveau, B. *J. Solid State Chem.* **1993**, *105*, 143-150.
18. Ramanujachary, K. V.; Greenblatt, M.; McCarroll, W. H.; Goodenough, J. B. *Mat. Res. Bull.* **1993**, *28*, 1257-1267.
19. Ramanujachary, K. V.; Lofland, S. E.; McCarroll, W. H.; Emge, T. J.; Greenblatt, M. *J. Solid State Chem.* **2002**, *164*, 60-70.
20. Wiebe, C. R.; Gourrier, A.; Langet, T.; Britten, J. F.; Greedan, J. E. *J. Solid State Chem.* **2000**, *151*, 31-39.
21. Green, A.E.C.; Wiebe, C.R.; Greedan, J.E. *Solid State Sciences* **2002**, *4*, 305-310.
22. Chi, L.; Green, A. E. C.; Hammond, R.; Wiebe, C. R.; Greedan, J. E. *J. Solid State Chem.* **2003**, *170*, 165-175.
23. Chi, L.; Swainson, I. P.; Greedan, J. E. *J. Solid State Chem.* **2004**, *177*, 3086-3091.
24. Kanamori, J. *J. Phys. Chem. Solids* **1959**, *10*, 87-98.
25. Goodenough, J. B. *Magnetism and the Chemical Bond*; Wiley: New York, 1963.

## **Chapter 2**

### **Experimental Techniques**

This chapter details both the scientific theory and specific instrumentation behind each of the experimental techniques utilized by the candidate to characterize the materials studied. Topics include structural determination, diffraction theory, both x-ray and neutron powder diffraction methodology, including magnetic neutron diffraction, the Rietveld refinement method for powder diffraction data, DC SQUID magnetometry and heat capacity measurements. Each Chapter that discusses a unique research project also has its own experimental section, which describes the exact synthesis and specific instrumentation parameters in greater detail.

## 2.1 Structural Determination

One important aspect towards understanding magnetic interactions in solids is to know the crystal structure, which can be determined using diffraction methods.

X-ray powder and single crystal diffraction are two of the most common techniques used for crystal structural elucidation. Common laboratory X-ray sources (such as rotating anode or tube) operating at several thousand electron volts have wavelengths on the order of angstroms, associated with the elemental material used to construct the source (typically, Cu, Fe, Mo, or Co):

$$E_{x\text{-ray}} = \frac{hc}{\lambda} \quad 2.1$$

where  $h$  is Planck's constant and  $c$  is the speed of light. Synchrotron sources possess brighter beams and tunable wavelengths, for higher resolution, however, these experiments must be performed at large facilities, with less freely available access.

Electron diffraction is fairly accessible, however, the electrons interact so strongly that multiple diffraction occurs in most samples. This is very problematic for structural work, but electron diffraction is excellent for investigating symmetry and single microcrystals.

Neutron diffraction is also an extremely powerful tool for structural determination. However, neutrons beams are not as bright as either x-rays or electrons and interact rather weakly with matter, meaning that much larger sample sizes (i.e. gram quantities) must be used. On the other hand, neutron scattering lengths are not dependent on electron density. This means that lighter elements such as Li or O that are not well located in X-ray experiments are easily found using neutrons. As such, X-ray and

neutron diffraction are very good complimentary techniques, as X-ray diffraction maps the electron density, whereas neutrons locate the nuclear positions.<sup>1</sup>

## 2.2 Diffraction Theory

Diffraction of x-rays, electrons or neutrons from a periodic lattice of atoms is explained by Bragg's theory. The incident beam is scattered by crystallographic planes of atoms, separated by a distance,  $d_{(hkl)}$ . A sharp peak appears in the scattered radiation if the rays from successive layers interfere constructively. For constructive interference, the path difference between two rays scattered from two successive planes must be  $2d_{(hkl)}\sin\theta$ . This condition is expressed as Bragg's Law:

$$n\lambda = 2d_{(hkl)}\sin\theta \quad 2.2$$

where  $\lambda$  is the wavelength of the incident beam and  $\theta$  is the angle of diffraction. Bragg's Law applied to a set of lattice planes is illustrated in Figure 2.1.

However, a more useful construct for visualizing diffraction is the concept of reciprocal space. For example, there are 3 vectors ( $\vec{a}$ ,  $\vec{b}$ ,  $\vec{c}$ ) that define a unit cell of atoms in direct space. In reciprocal space, the unit cell would be defined by three new vectors ( $\vec{a}^*$ ,  $\vec{b}^*$ ,  $\vec{c}^*$ ) that are related to their real space counterparts in the following manner:

$$\vec{a}^* = \frac{\vec{b} \times \vec{c}}{|\vec{a} \cdot (\vec{b} \times \vec{c})|} \quad \vec{b}^* = \frac{\vec{a} \times \vec{c}}{|\vec{a} \cdot (\vec{b} \times \vec{c})|} \quad \vec{c}^* = \frac{\vec{a} \times \vec{b}}{|\vec{a} \cdot (\vec{b} \times \vec{c})|} \quad 2.3$$

$$\vec{a}^* \cdot \vec{a} = 1 \quad \vec{b}^* \cdot \vec{b} = 1 \quad \vec{c}^* \cdot \vec{c} = 1 \quad 2.4$$

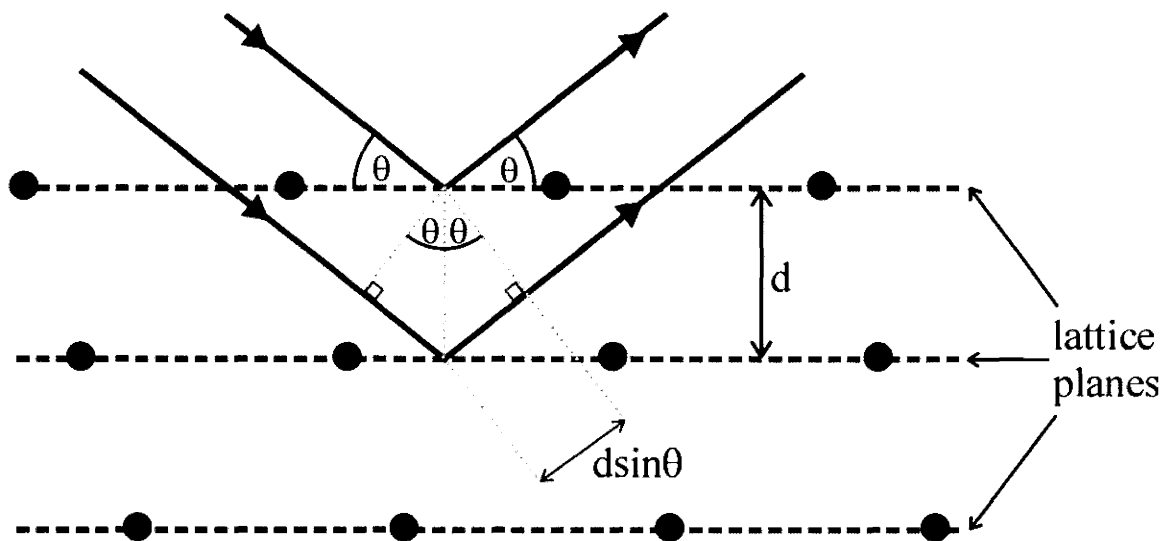


Figure 2.1. Bragg's Law illustrated for a set of reflections from lattice planes separated by a distance,  $d$ .

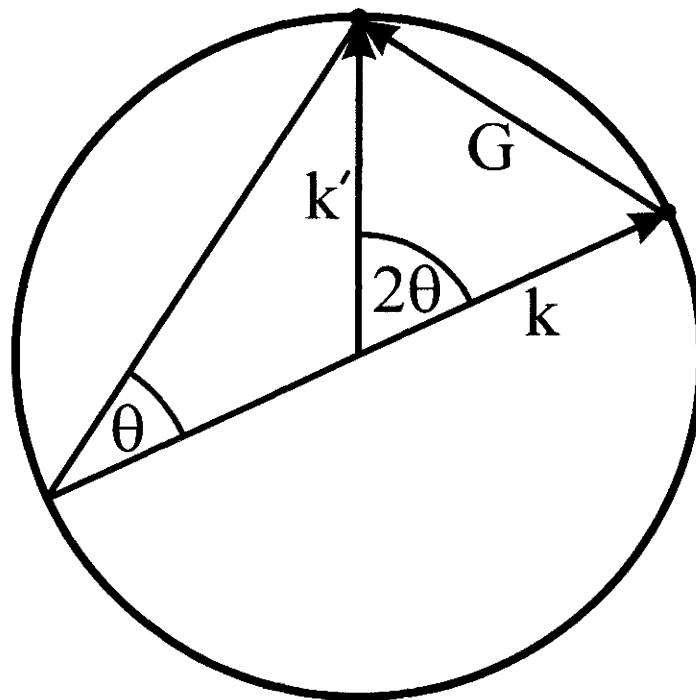


Figure 2.2. Ewald's Sphere for diffraction.

In elastic scattering, there is no energy transfer to the lattice, but there is a finite amount of momentum ( $\vec{Q}$ ) that is transferred:

$$\vec{Q} = \vec{k} - \vec{k}' \quad 2.5$$

where  $\vec{k}$  and  $\vec{k}'$  are defined as the incident and reflected wavevectors, respectively, that are equal in magnitude ( $2\pi/\lambda$ ). The difference between these two wavevectors, however, must satisfy a special condition for diffraction. Ewald expressed this condition geometrically in reciprocal space by constructing a sphere of radius,  $k$  (Figure 2.2).

Mathematically, Ewald's condition can be expressed as:

$$\vec{G} = \vec{k}' - \vec{k} \quad 2.6$$

For Bragg's Law to be satisfied, the difference in wavevectors,  $\vec{Q}$  must be equal to the reciprocal lattice vector  $\vec{G}$  which is defined geometrically as shown in the Figure and mathematically as:

$$\vec{G} = \frac{2\pi}{d_{(hkl)}} = h\vec{a}^* + k\vec{b}^* + l\vec{c}^* \quad 2.7$$

where  $h$ ,  $k$  and  $l$  are Miller indices which describe the vector space,  $\vec{G}$ .

This does simplify the observation of diffraction patterns in real space. A typical single-crystal X-ray diffraction consists of points in space that satisfy Ewald's condition. For a powder or polycrystalline sample, which consists of many randomly oriented crystals, the observed diffraction pattern is a series of Debye-Scherrer cones, each defining a reciprocal point,  $\vec{G}$  (Figure 2.3). Normally, only a portion of the Debye cone is detected, and therefore, the resulting pattern consists of many lines or peaks. These

peaks can then be indexed to a specific lattice plane with  $d_{(hkl)}$  (Figure 2.4). Often, due to symmetry, there is overlap between numerous Bragg reflections with the same  $d_{(hkl)}$ .

To determine the structure of a compound from its powder diffraction pattern, the observed peaks are indexed to a unit cell (with known dimensions and symmetry) and the contents of that unit cell are defined using the intensity of the reflections. The intensity ( $I_{(hkl)}$ ) of a Bragg reflection with Miller indices ( $h k l$ ) is roughly the square of the form factor,  $F_{(hkl)}$ :

$$F_{(hkl)} = \sum_{n=1}^N f_n(2\theta) \exp[i2\pi(hx_n + ky_n + lz_n)] \quad 2.8$$

where  $f_n(2\theta)$  is the atomic structure factor (discussed below), and  $x_n$ ,  $y_n$  and  $z_n$  are the atomic positions of each ion ( $n$ ) with respect to the unit cell. The summation is carried out over all  $N$  atoms of the unit cell.

For x-rays, the atomic structure factor defines the number and distribution of electrons for each atom  $n$  in the unit cell, and falls off rapidly as a function of scattering angle ( $2\theta$ ). The integral of  $f_n$  over one atomic site yields  $Z$ , the total number of electrons for the given atom. As a result, the intensity of scattered reflections for x-rays is approximately  $\sim Z^2$  and thus, x-rays are rather insensitive for determining the atomic positions of lighter atoms versus heavier ones.

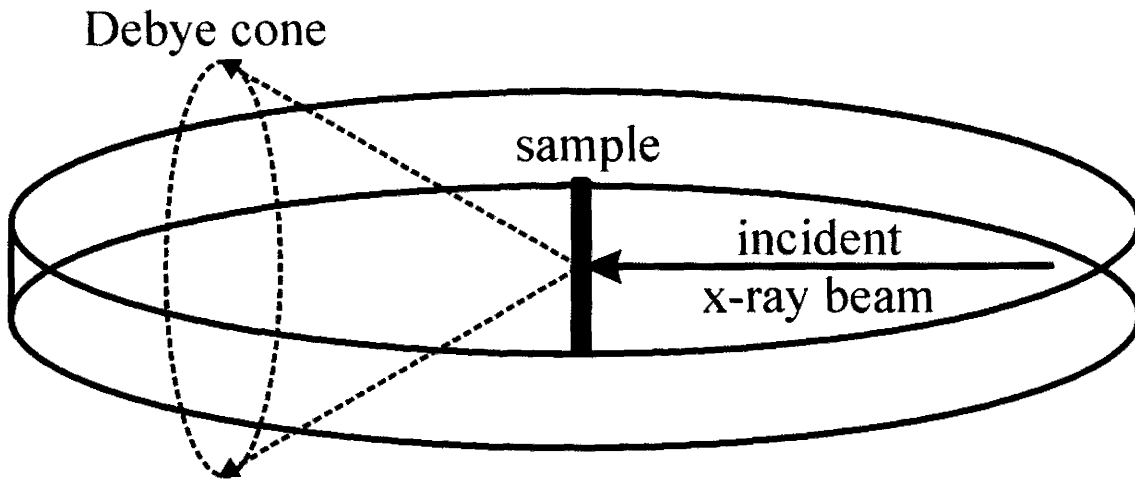


Figure 2.3. Transmission geometry powder diffraction illustrating a Debye cone of scattering.

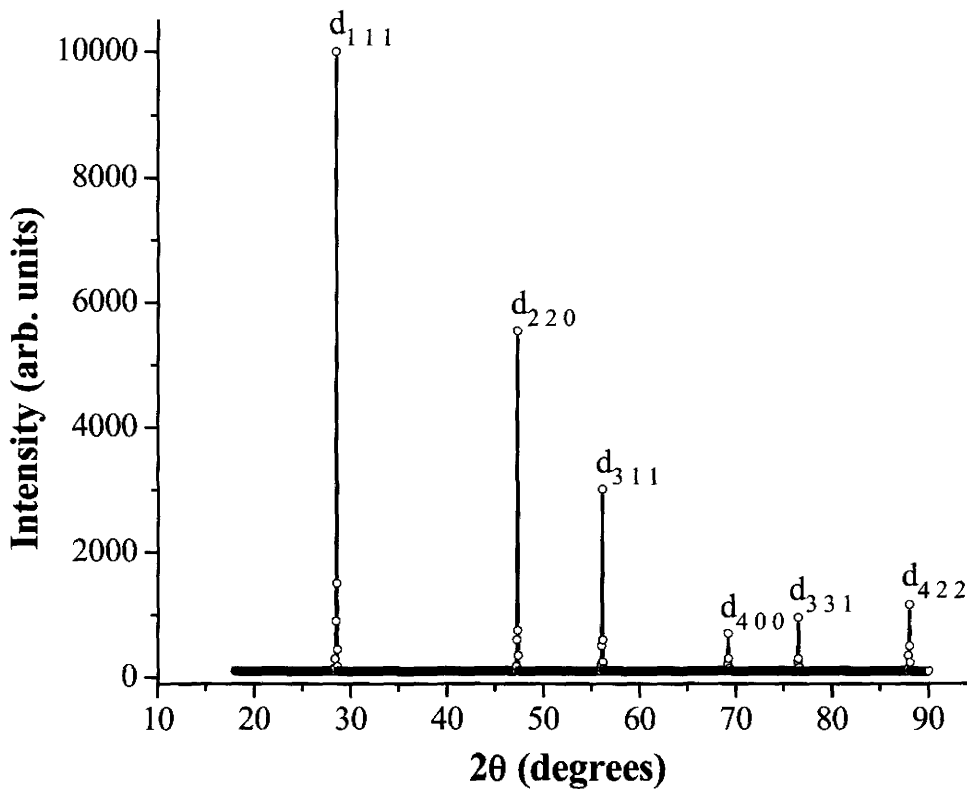


Figure 2.4. Powder x-ray diffraction pattern of silicon. Due to the cubic symmetry, there is significant overlap of the Bragg reflections. For example, the  $d_{220}$  peak is comprised of reflections from  $d_{\pm 2 \pm 2 0}$ ,  $d_{\pm 2 0 \pm 2}$  and  $d_{0 \pm 2 \pm 2}$ .

In contrast, neutrons scatter mainly from the nucleus of a given atom, rather than the electron density. The form factor for neutrons (called the neutron scattering length,  $b$ ) is determined from nuclear interactions, and is much more complex. Figure 2.5 displays the neutron and x-ray scattering lengths as a function of atomic number. There are no real systematics governing the dependence of the neutron scattering length and the atomic number. In fact, the neutron cross-sections are more uniform across the Periodic Table, and as a result, neutrons are incredibly useful for determining the atomic positions of lower  $Z$  atoms such as oxygen. In addition, since nuclei can be considered as point scatterers, there is no scattering angle dependence of  $b$ . However, other effects such as the strong absorption of neutrons by certain isotopes, must be taken into account. Absorption is usually a much stronger effect for x-rays in comparison to neutrons, however, and all of these factors should be considered when opting for one probe over the other.<sup>1</sup>

### 2.3 X-ray Diffraction

Conventional laboratory x-rays are produced using the inverse photoelectric effect. Electrons, usually produced by thermionic emission from a heated cathode, are accelerated in an evacuated tube towards a metal target (i.e. Cu, Mo, Fe, Co). Upon striking the surface of the metal, these electrons are immediately decelerated by “bremsstrahlung”, and most of their kinetic energy is lost as a continuous spectrum of background radiation. However, some of these electrons collide with atoms within the metal lattice and cause inner shell electron transitions. X-rays, characteristic of the metal

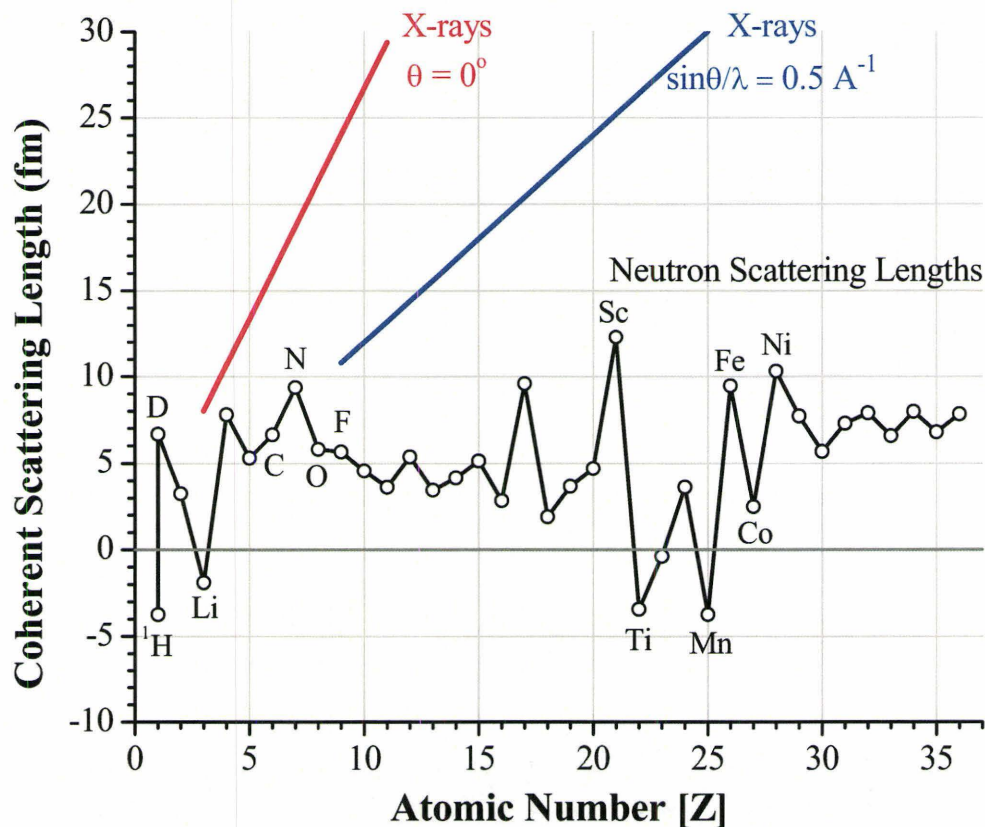


Figure 2.5. Neutron and X-ray coherent scattering lengths according to atomic number. Note the angular dependence of the X-ray scattering lengths.

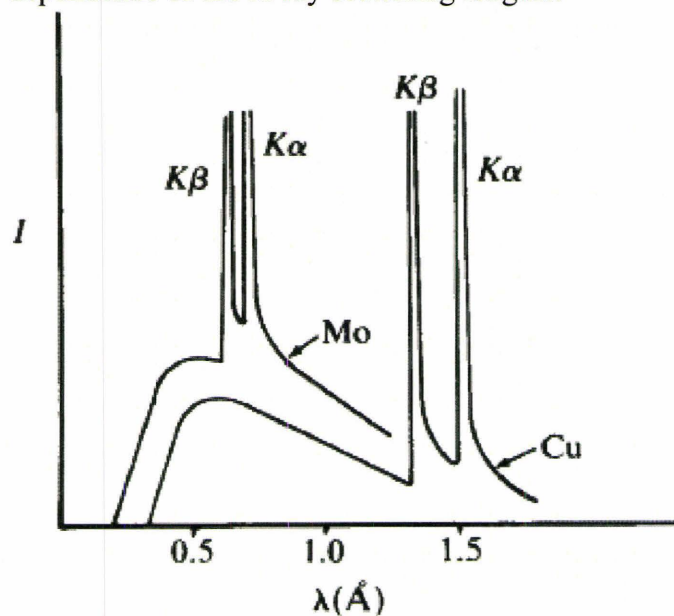


Figure 2.6. Characteristic X-ray spectra for Mo and Cu radiation. Note the doublets in the strong  $K\alpha$  and  $K\beta$  peaks.

used, are produced when these atoms settle back to their ground states by rearranging their electron configurations. These sharp features ( $K_{\alpha}$ ,  $K_{\beta}$ ) appear over a low intensity background (due to “bremsstrahlung”) in a typical x-ray spectrum as depicted in Figure 2.6 for Cu and Mo sources. Upon closer examination, the sharp lines are actually doublets, caused by the two electrons that occupy each shell. Due to the Pauli Principle, these electrons must have opposite spins, and hence, have slightly different energies associated with them. The two peaks of the doublet, therefore, are designated as  $K_{\alpha 1}$  and  $K_{\alpha 2}$ , for example. Monochromators, such as single crystal graphite or germanium, can be used to obtain a single wavelength beam ( $K_{\alpha 1}$ , for example), by using Bragg reflections to separate the emission lines.

As mentioned previously, x-rays are strongly absorbed by most materials, so the geometry of the experiment is very important. Typically, reflection geometry is used for powders to minimize absorption. In Bragg-Brentano mode, x-rays are reflected from a sample to a scintillation counter, where the intensity of the diffracted beam is measured as a function of angle. A Guinier-Hagg camera is well suited to collect high resolution powder diffraction patterns, using photographic film to record the positions of the Bragg peaks (Figure 2.7). After exposing the film to the scattered x-rays for about an hour, it can be developed and, using a line scanner, converted to digital form for further structural determination (such as very accurate unit cell parameters). Alternative x-ray detectors include charge-coupled devices (CCDs) paired with phosphor screens.

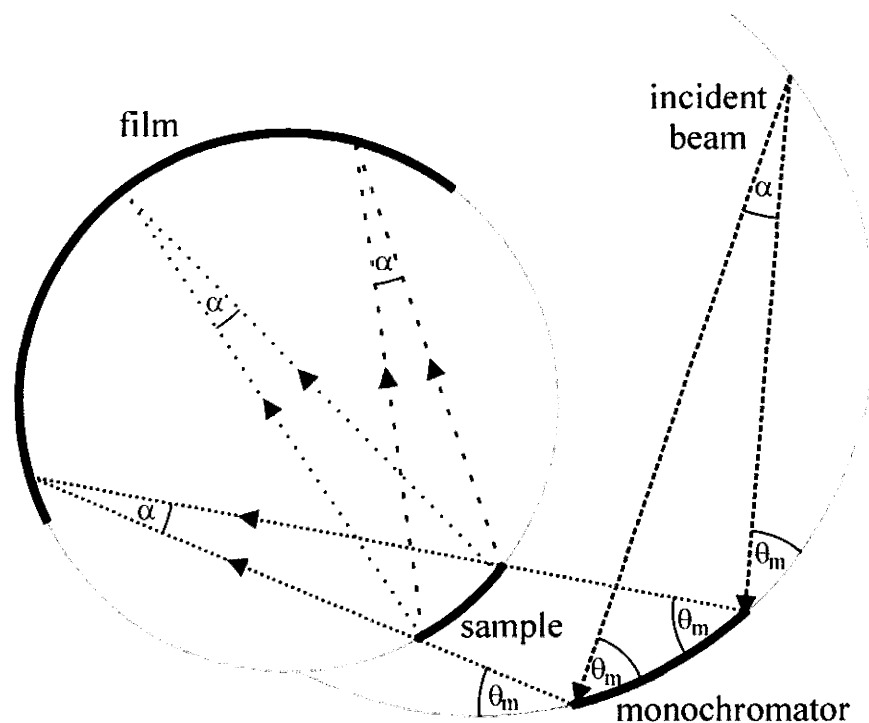


Figure 2.7. Geometry of the Guinier-Hagg camera. A divergent incident X-ray beam is focussed by the curved monochromator onto the sample, where it diffracts and exposes the photographic film that is placed on a circle of common focal points. The large light grey circles are the extension of the monochromator and camera.

## 2.4 Neutron Diffraction

A neutron is a neutral particle, with a mass of about  $1.675 \times 10^{-27}$  kg and an associated magnetic moment of  $1.891 \mu_N$ , where  $\mu_N$  is the nuclear magneton. As a result, it has an associated wavelength ( $\lambda$ ), according to the de Broglie equation:

$$\lambda = \frac{h}{mv} \quad 2.9$$

where  $h$  equals Planck's constant,  $m$  is the mass of the neutron, and  $v$  is the neutron's velocity. Within a nuclear reactor, there is a cavity that brings the neutrons to thermal equilibrium, called the moderator. This results in a Maxwellian distribution of velocities for the neutrons, that is peaked at a value that corresponds to the temperature of the moderator (Figure 2.8). Consequently, the maximum of the distribution can be shifted by altering the temperature of the moderator (i.e. by passing the neutrons through a medium of a particular temperature). Thermal neutrons ( $T \sim 300$  K) show a maximum in the distribution at about 2000 m/s, corresponding to a wavelength of about 1.978 Å, using heavy water (D<sub>2</sub>O) as the moderator. Slower neutrons are produced using liquid deuterium or hydrogen as a moderator ( $T \sim 10$  K, hence a "cold source") whereas faster neutrons are obtained from a "hot source" such as heated graphite ( $T \sim 2000$  K). Since the velocity of the neutrons is inversely related to the wavelength, slower, "cold source" neutrons have a longer wavelength than conventional thermal sources. This can be advantageous for certain experiments, for example, as a longer wavelength can provide higher resolution to better separate closely spaced Bragg reflections.<sup>2</sup>

Neutrons can be produced in two different ways. Reactor source neutrons are generated by the fission of <sup>235</sup>U in a chain reaction with thermal neutrons. Filters and

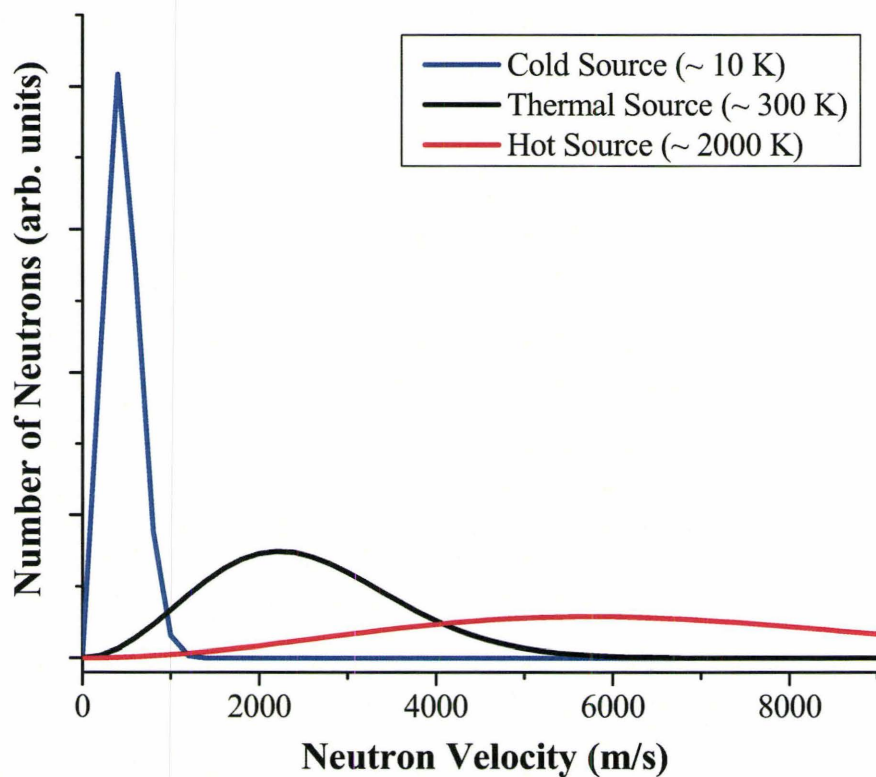


Figure 2.8. Maxwell distribution of the speed of neutrons produced from different reactor sources, using different moderators.

collimators (fabricated from neutron absorbing elements such as cadmium or gadolinium) are generally used to absorb the smaller amounts of higher order wavelengths and Bragg reflection from a single crystal monochromator (such as Si) is used to select a single wavelength to conduct experiments.

The second method involves bombarding a heavy metal target (such as Hg or W) with high energy particles, like protons from a particle accelerator. The nuclei in the target are activated and neutrons are released upon its nuclear decay. This so-called “spallation” process produces a white beam of neutrons with a time structure imposed by the pulse repetition rate of the particle accelerator (typically,  $\sim 50 - 60$  Hz). “Time of flight” is used to separate out the various neutron wavelengths produced in spallation sources. Due to the different characteristics of these two neutron sources, the powder diffraction patterns obtained differ markedly in terms of background and peak shape.<sup>1,2</sup>

In a similar manner to X-rays, neutrons diffract from planes of atoms, but interact with the nuclei instead of the electron density. As discussed previously, the scattering process can be described by the vector difference ( $\vec{Q}$ ) between the incident and scattered wavevectors ( $\vec{k}$  and  $\vec{k}'$ , respectively):

$$\vec{Q} = \vec{k} - \vec{k}' = \frac{4\pi \sin \theta}{\lambda} \quad 2.10$$

When a sample is placed in an incident beam of monochromatic neutrons (of intensity,  $I_0$ ), the neutrons are scattered with probability,  $\sigma$ , which is called the cross-section.

Scattered neutrons are detected for a solid angle,  $d\Omega$ . The differential cross-section,  $(\frac{d\sigma}{d\Omega} d\Omega)$ , therefore, is the probability of scattering a neutron into this region of solid

angle,  $d\Omega$ . Figure 2.9 illustrates the scattering geometry for neutron diffraction experiments. The total cross-section ( $\sigma_{tot}$ ) is the sum of various contributions: the absorption cross-section ( $\sigma_{abs}$ ), the coherent cross-section ( $\sigma_{coh}$ ) and the incoherent cross-section ( $\sigma_{incoh}$ ), which are all different for each element.

Previously, all of the discussion of neutron scattering has focussed on coherent scattering, which results in the well-defined Bragg peaks or spots in a diffraction pattern. However, when there is a large nuclear spin component for a given isotope or a wide distribution of isotopes for a given element, incoherent neutron scattering occurs. This phenomenon has no angular dependence and is reflected as a large diffuse background. For example, hydrogen ( $^1\text{H}$ ) has a large incoherent cross-section due to its nuclear spin. Deuterium ( $^2\text{H}$ ) has a much smaller incoherent cross-section, so powder samples are typically deuterated to avoid the background problem brought about by incoherent scattering.<sup>1-3</sup>

The neutron scattering length of an isotope ( $b$ ), then, is related to the total cross-section:

$$\sigma = 4\pi b^2 \quad 2.11$$

The structure factor for neutron diffraction then becomes:

$$F_{(hkl)} = \sum_{n=1}^N b \exp[i2\pi (hx_n + ky_n + lz_n)] \quad 2.12$$

The typical neutron powder diffractometer is depicted in Figure 2.10, illustrating the monochromator, sample stage, collimator and detector. Equipment designers exploit the fact that neutrons interact only weakly with matter and have variable scattering

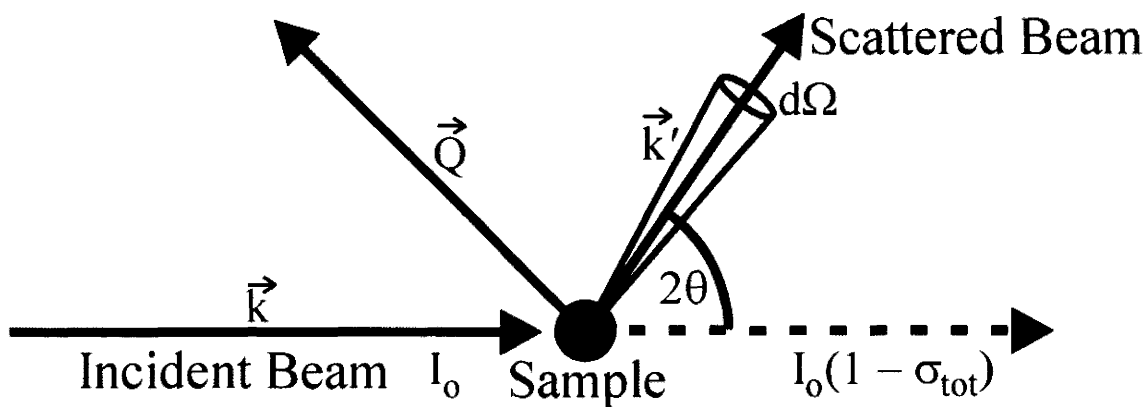


Figure 2.9. Geometry of a typical neutron experiment that involves elastic scattering.

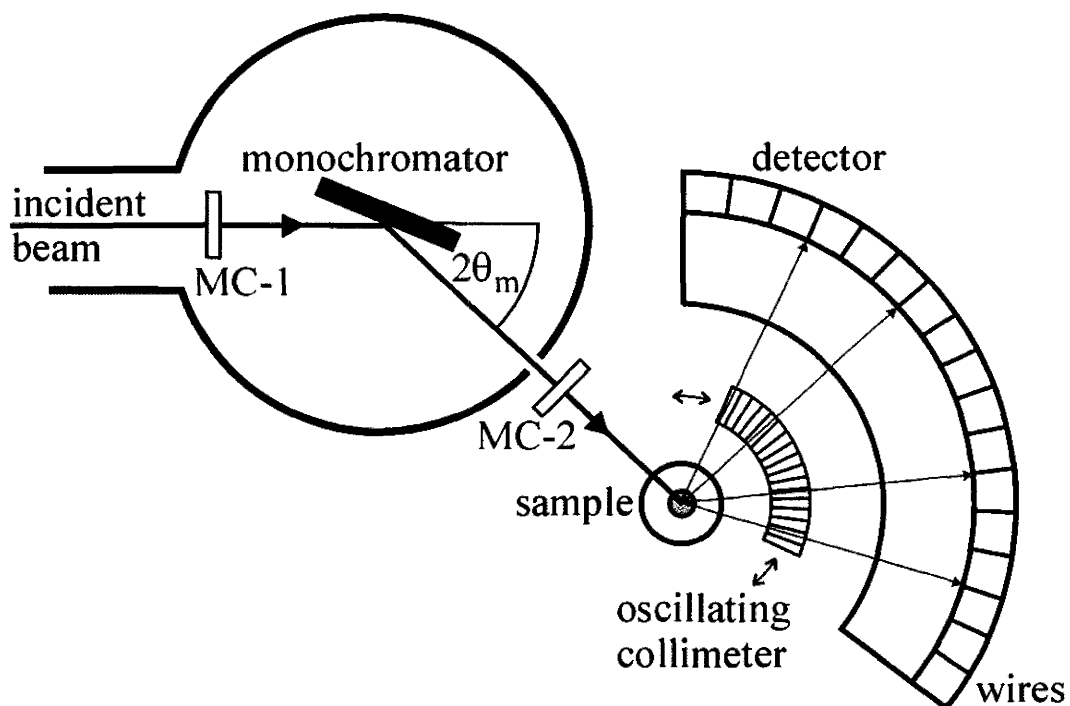


Figure 2.10. Neutron scattering geometry for a reactor source. MC-1 and MC-2 are two monitor counters that are used to normalize the data sets.

lengths, depending on the element. Extreme sample environments, such as low temperature refrigerators, high temperature furnaces and high pressure devices, can easily be used in a typical experiment, as neutrons usually have a long penetration length through the materials used to make them. Since vanadium has a scattering length of almost zero, it is used to construct the sample “cans”, making them virtually invisible to the neutron beam. Materials that absorb neutrons very well, such as  $^3\text{He}$  or B, are used in detectors, where the number of neutrons they absorb can be converted into an electrical signal.

## 2.5 Magnetic Neutron Diffraction

Since neutrons possess spin and therefore, a magnetic moment, they can also interact with magnetic moments due to unpaired electron density within a structure. This property is particularly useful for determining magnetic long-range order. However, the interaction between neutrons and ions in the paramagnetic state should be considered first.

Recall that in the paramagnetic state, the magnetic moments on the ions are not correlated with each other at all, and thus, there is no periodicity of the moments. The differential neutron scattering cross-section ( $d\sigma_{pm}$ ) therefore, depends on the magnetic moment density of the ions, as expressed by Halpern and Johnson:

$$d\sigma_{pm} = \frac{2}{3} S(S+1) \left( \frac{e^2 \gamma}{mc^2} \right)^2 f^2 \quad 2.13$$

where  $S$  is the spin quantum number,  $m$  equals the mass of the electron and  $e$  equals its charge,  $c$  equals the speed of light,  $\gamma$  is the magnetic moment of the neutron expressed in nuclear magnetons and  $f$  represents the magnetic form factor. Magnetic form factors for neutrons are similar to x-ray form factors, and have been tabulated.<sup>3</sup> Since the unpaired electrons contributing to the paramagnetism lie in the outer shells of the ions, the magnetic form factor diminishes much more rapidly as a function of scattering angle than even x-rays. As stated previously, since there is no periodicity associated with the paramagnetic state, no Bragg reflections would be observed. However, a broad background that decreases rapidly with increasing  $\sin\theta/\lambda$  would be seen at low angles in the powder diffraction pattern.

When the magnetic moments do interact and long-range order is achieved, Bragg's condition for diffraction is satisfied and the periodicity of the moments (in other words, the magnetic structure) can be elucidated. The differential magnetic scattering cross-section now becomes:

$$d\sigma_m = q^2 S^2 \left( \frac{e^2 \gamma}{mc^2} \right)^2 f^2 = q^2 p^2 \quad 2.14$$

where  $p$  is the magnetic equivalent to the neutron scattering length,  $b$  and is defined as:

$$p = Sf \left( \frac{e^2 \gamma}{mc^2} \right) \quad 2.15$$

and  $q$  is the magnetic interaction vector:

$$\vec{q} = \vec{\varepsilon}(\vec{\varepsilon} \cdot \vec{K}) - \vec{K} \quad 2.16$$

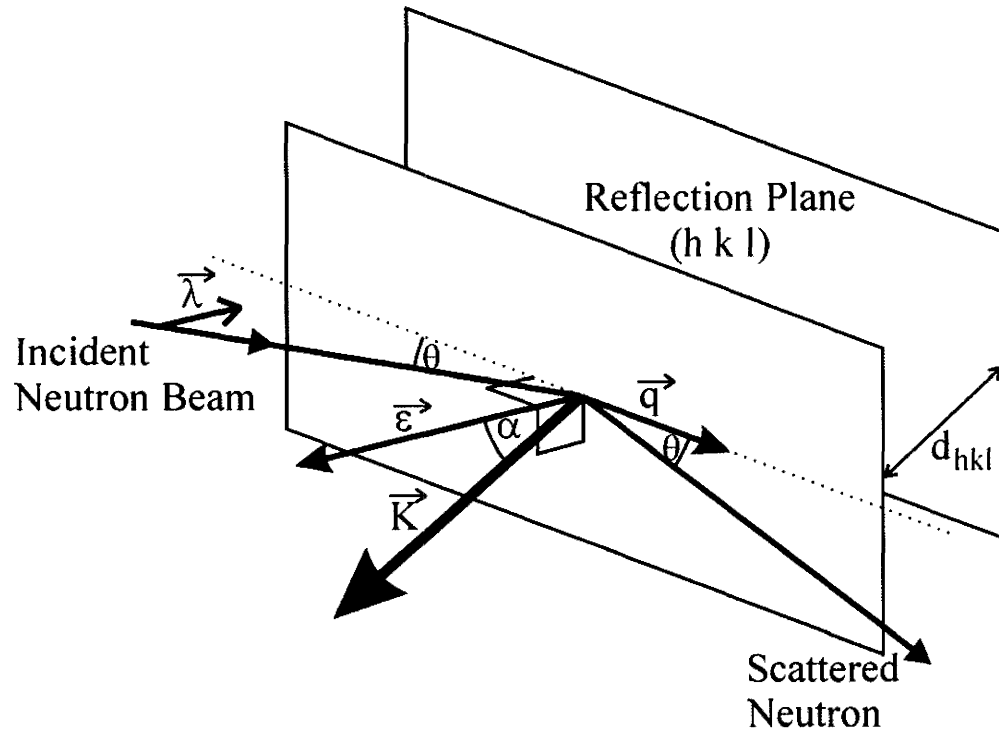


Figure 2.11. Geometry of a magnetic neutron experiment. The labelled vectors are defined in the text.

where  $\vec{\varepsilon}$  is the scattering vector (which is perpendicular to the reflection plane) and  $\vec{K}$  is the magnetic moment vector, illustrated in Figure 2.11. Note that the differential magnetic scattering cross-section for an ordered state is proportional to  $S^2$ , as compared to the paramagnetic state where it is dependent on  $S(S + 1)$ .

Due to the rapid drop off of the magnetic form factor, magnetic Bragg reflections are found at small diffraction angles. Unless the neutron beam is polarized (which is typically not the case in a standard experiment), there is no coherence between structural and magnetic neutron scattering, and hence, the intensities are additive:

$$|F_{hkl}|^2 = |F_{nuclear}|^2 + |F_{magnetic}|^2 \quad 2.17$$

where the magnetic structure factor is the sum over all atoms in the “magnetic unit cell”:

$$\vec{F}_{mag} = \sum_{n=1}^N \vec{q}_n p_n \exp[i2\pi(hx_n + ky_n + lz_n)] \quad 2.18$$

Note that the magnetic structure factor is a vector quantity with each magnetic sublattice contributing to the overall value and thus, there is an orientational dependence of the function. Only magnetic moment components within the reflection plane contribute to the magnetic structure factor. As a result, the orientation of the magnetic moments as well as their magnitude can be found by performing a neutron diffraction experiment below the ordering temperature,  $T_c$ .

Since the magnetic moment is a vector, the symmetry of the crystallographic lattice alone may not always be sufficient to accurately describe the ordered magnetic lattice. Ferromagnetism, where the magnetic moment vectors are all aligned in the same direction, is compatible with the symmetry imposed by the crystallographic unit cell. As

a result, magnetic Bragg reflections will occur in the same positions as structural features, and hence, only the intensities of the peaks in the powder pattern will change as a function of temperature, as ferromagnetic order is achieved.

In contrast, an antiferromagnet has magnetic moment vectors that align in opposing directions. Two or more interpenetrated sublattices, each describing the orientation of one set of magnetic moments aligned in the same direction, must be constructed. Consequently, the magnetic unit cell that comprises all of these sublattices may be larger than the crystallographic unit cell and additional Bragg reflections (with respect to the structural peaks) could appear in the powder diffraction pattern. These new magnetic reflections typically have non-integer Miller indices when indexed on the crystallographic unit cell. Another possibility is that the magnetic unit cell would have the same unit cell as the crystallographic unit cell, albeit with lower symmetry. This would result in Miller indices that were integers, however, they would not appear in the structural powder pattern due to symmetry restrictions. However, if the crystallographic unit cell is fairly large and of low symmetry, it is possible that the antiferromagnetic magnetic unit cell may have identical cell parameters to the crystallographic unit cell. Hence, the lack of additional reflections does not necessarily mean that long-range antiferromagnetic ordering is not present.

Magnetic structures can usually be expressed in terms of the magnetic reciprocal lattice translation vector ( $\bar{k}$ ), with respect to the crystallographic phase. This is a translation vector that locates the magnetic reflections in reciprocal space, defined using a vector sum:

$$\bar{\varepsilon} = \bar{G} + \bar{k} \quad 2.19$$

where  $\bar{G}$  is the crystallographic lattice translation vector and  $\bar{\varepsilon}$  is the scattering vector (as defined previously). If the magnetic Bragg peaks occur in the same positions as the crystallographic reflections, then  $\bar{k} = 0$ . In contrast, an antiferromagnetic magnetic structure that has Bragg reflections with non-integer Miller indices (for example, (0 0 1/2)) has  $\bar{k} = (0 \ 0 \ 1/2)$ .

## 2.6 Rietveld Refinement

Powder diffraction data can be refined using the Rietveld method to produce a crystallographic structure of the compound analyzed. Solving the structure is often complicated due to severe peak overlap between individual Bragg reflections in the powder pattern. However, the Rietveld refinement method involves fitting profile points of the entire diffraction data to a model for the structure, rather than individual Bragg peaks. The intensity of each profile point ( $y(2\theta)$ ) is therefore the sum of all the Bragg reflections that contribute at that scattering angle. A least squares refinement procedure is utilized to minimize the following function:

$$F = \sum_i^N w_i [y_i(\text{obs}) - \frac{1}{c} y_i(\text{calc})]^2 \quad 2.20$$

where  $w_i$  is a weighting factor, based on counting statistics ( $w_i = 1/y_i(\text{obs})$ ),  $c$  is a scale factor and  $y_i(\text{obs})$  and  $y_i(\text{calc})$  are the observed and calculated intensities of the  $i^{\text{th}}$  step, respectively. A starting model of the structure is required to determine the initial calculated profile points. This structural model is then modified during refinement until the best agreement between the observed and calculated patterns is reached.

In order to describe the whole diffraction pattern properly, instrumental parameters need to be incorporated into the model. Variables that can be refined include the zero point, background, peak asymmetry, preferred orientation, instrument resolution and peak shape. The instrument resolution function describes the variation of the width of the diffraction peaks as a function of angle:<sup>4,5</sup>

$$H_{(hkl)}^2 = U \tan^2 \theta + V \tan \theta + W \quad 2.21$$

where  $U$  is defined by the wavelength resolution ( $\Delta\lambda/\lambda$ ),  $V$  is related to beam divergence and mosaic spread of the sample, and  $W$  is associated with the incident beam cross-section and sample diameter.

Individual Bragg peaks are usually fairly well described by a Gaussian line shape and the total profile is simply a superposition of Gaussians. The intensity is calculated for a given position,  $2\theta_i$ :

$$y_i = t F_{(hkl)}^2 j_{(hkl)} L_{(hkl)} \frac{2\sqrt{2\ln 2}}{H_{(hkl)}\sqrt{\pi}} \exp\left[-\frac{4\ln 2(2\theta_i - 2\theta_{(hkl)})^2}{H_{(hkl)}^2}\right] \quad 2.22$$

where  $t$  is the step width of the counter,  $F_{(hkl)}$  is the structure factor of the reflection,  $j_{(hkl)}$  is the multiplicity of the reflection,  $L_{(hkl)}$  is the Lorentz factor and  $2\theta_{(hkl)}$  is the calculated position of the Bragg peak. The Lorentz factor is a geometric factor that accounts for how a reciprocal lattice point passes through Ewald's sphere, especially the direction of approach. Other line shapes, such as the Lorentzian or Pseudo-Voigt (a convolution of Gaussian and Lorentzian shapes), can also be employed. The inherent assumption is that contributions from each Bragg reflection will add algebraically to contribute to the

overall diffraction pattern. This holds for samples with more than one phase, as well as for structural and magnetic peaks.

The quality of the fit of the calculated model to the observed powder diffraction pattern can be gauged by examining the following agreement factors:

$$R_p = \frac{\sum_i |y_i(\text{obs}) - y_i(\text{calc})|}{\sum_i |y_i(\text{obs})|} \quad 2.23$$

$$R_{wp} = \sqrt{\frac{\sum_i w_i [y_i(\text{obs}) - y_i(\text{calc})]^2}{\sum_i w_i [y_i(\text{calc})]^2}} \quad 2.24$$

$$R_{exp} = \sqrt{\frac{(N - P + C)}{\sum_i w_i [y_i(\text{obs})]^2}} \quad 2.25$$

$$\chi^2 = \frac{R_{wp}^2}{R_{exp}^2} \quad 2.26$$

$$R_{Bragg} = \frac{\sum_k |I_k(\text{obs}) - I_k(\text{calc})|}{\sum_k |I_k(\text{obs})|} \quad 2.27$$

where  $R_p$  is the profile  $R$ -value,  $R_{wp}$  is the weighted  $R$ -value,  $R_{exp}$  is the expected  $R$ -value,  $\chi^2$  is the goodness of the fit and  $R_{Bragg}$  is the Bragg  $R$ -value. In addition to these variables,  $N$  is the number of data points,  $P$  is the number of parameters in the refinement,  $C$  is the number of constraints and  $I_k$  refers to the intensity of the reflection, whereas  $y_i$  refers to the intensity of the profile point.<sup>6,7</sup>

## 2.7 DC SQUID Magnetometry

As discussed previously, the magnetic susceptibility of a sample can provide important information about the short-range and long-range magnetic interactions within the solid, as well as the nature of any magnetic transitions. It is defined as:

$$\chi = \frac{\partial M}{\partial H} \quad 2.28$$

where  $M$  is the magnetization and  $H$  is the applied field. A DC-SQUID magnetometer is a very sensitive instrument that measures the magnetic moment of a sample ( $\mu$ , in emu), which can be easily converted into magnetic susceptibility:

$$\chi = \frac{\mu}{\text{mols}} \div H \quad 2.29$$

A plot of magnetic susceptibility versus temperature is very diagnostic of the type of magnetic interactions. The temperature can be varied from 2 to 330 K ( $\pm 0.5\%$ ) in incremental steps for a standard experiment. Higher temperature measurements from 310 to 600 K ( $\pm 0.5\%$ ) can be made using an additional furnace insert. Sample masses range from about 20 to 100 mg, depending on moment size, sample volume and sample availability. For low temperature operations, powders are weighed out accurately into gelatin capsules, and held in place by plastic straws. For furnace operation, the sample is weighed accurately into 1 mm diameter quartz tubes for subsequent measurement.

Typical susceptibility graphs are shown in Figure 2.12 for a paramagnet, antiferromagnet and ferromagnet. In a paramagnet, with a random arrangement of spins, the susceptibility and temperature are inversely related, and the graph appears like a hyperbola. When the spins are coupled anti-parallel along a preferred magnetization axis,

as in an antiferromagnet, a prominent cusp appears with a maximum at the ordering temperature,  $T_c$ . If the order is short-range, the cusp typically broadens, creating a larger feature or a shoulder. For a ferromagnetic arrangement of spins (all coupled parallel along a preferred axis), the susceptibility rises sharply at lower temperatures before levelling off at a fairly high value, and the inflection point of the curve is usually the critical ordering temperature,  $T_c$ .

A conventional magnetic susceptibility experiment consists of two measurements – Zero Field Cooled (ZFC) and Field Cooled (FC). In a ZFC experiment, the sample is cooled without applying a magnetic field. A small field is applied at the lowest temperature of the experiment, and measurements made with the field on as the temperature is incrementally increased. In contrast, a FC measurement is made after the sample has been cooled in the presence of an applied field (typically, the same magnitude as the field applied for measurement). The divergence, if any, between these two measurements can indicate a rearrangement of domains in the long-range ordered state.

Plotting the inverse susceptibility against temperature provides an ideal data treatment method for determining the parameters of the Curie-Weiss Law in the paramagnetic regime. At high temperatures, the inverse magnetic susceptibility appears as a straight line, with a slope that represents the Curie constant (diagnostic of the number of unpaired electrons) and an intercept that indicates the Weiss constant (diagnostic of the dominant type of magnetic interactions). Figure 2.13 displays the different inverse susceptibility curves obtained for a paramagnet, antiferromagnet, ferromagnet and ferrimagnet, respectively.

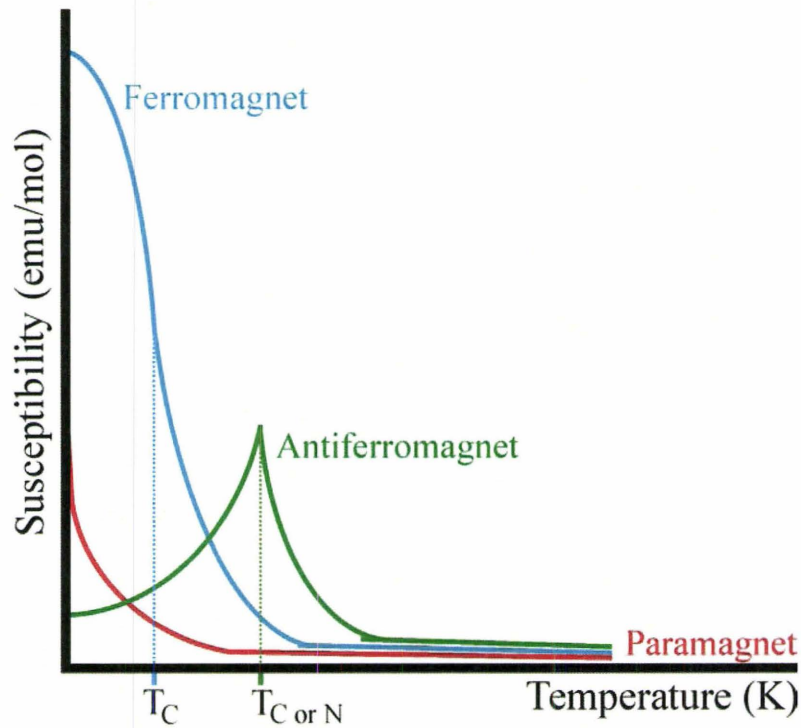


Figure 2.12. Susceptibility ( $\chi$ ) versus temperature plot for typical magnetic systems.

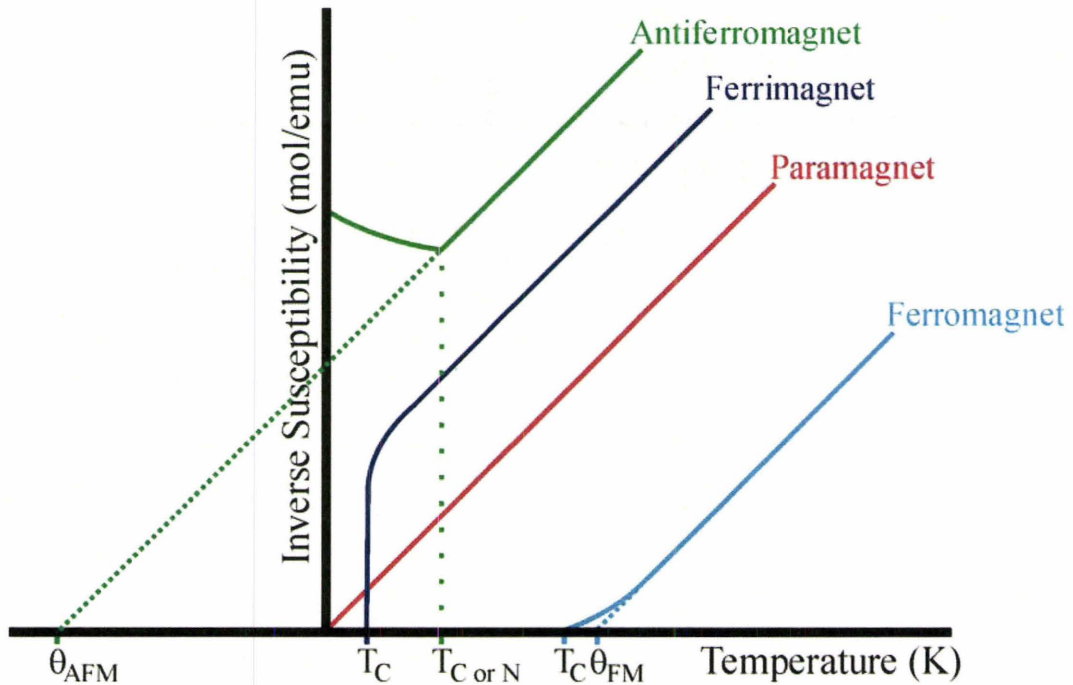


Figure 2.13. Inverse susceptibility versus temperature plots for typical magnetic systems.

Another data treatment method involves multiplying the magnetic susceptibility value with the temperature and plotting it against the temperature (Figure 2.14). Features, such as an antiferromagnetic transition, are typically sharper in this plot. In addition, at higher temperatures, the data should approach the expected value of the Curie constant for the magnetic system as the paramagnetic state is achieved. The position of the low temperature data is important as well. If the data lie above the horizontal line indicating the calculated Curie constant for the sample, ferromagnetic interactions are dominant, whereas if the data lie below this line, antiferromagnetic behaviour is favoured.

The derivative of  $\chi T$  versus temperature, or the so-called “Fisher heat capacity”, is also a good method for determining the critical temperature for long-range order (Figure 2.15). Fisher proved mathematically that the profile of this derivative approximates the experimental heat capacity for the magnetic system.<sup>8</sup> If the shape of the anomaly obtained in this plot is lambda-like, long-range magnetic order is expected, with a critical temperature at the apex of the anomaly. If the anomaly in the plot is broad or symmetric, short-range correlations are typically present. This can be useful for determining the nature and temperature of magnetic transitions.

The SQUID magnetometer can also be used to measure a sample’s net magnetization as a function of field for a given temperature (Figure 2.16). The superconducting magnet can apply an adjustable magnetic field from  $-5.5$  T to  $+5.5$  T. Again, the SQUID measures the magnetic moment of the sample, which can be converted to magnetization (in Bohr magnetons):

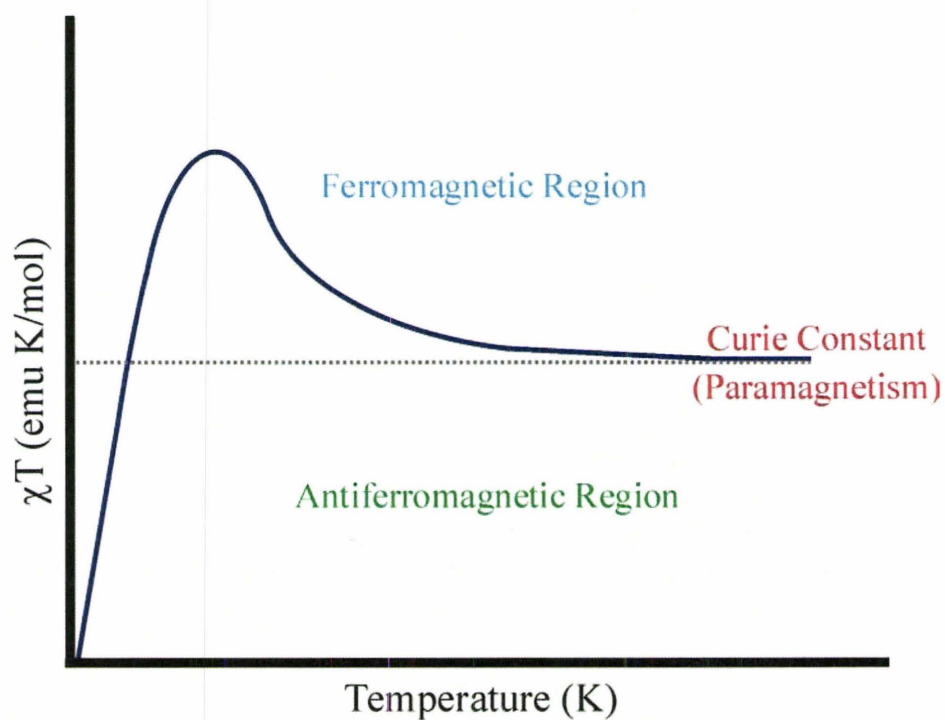


Figure 2.14. Susceptibility ( $\chi$ ) multiplied by temperature (T) versus temperature plot.

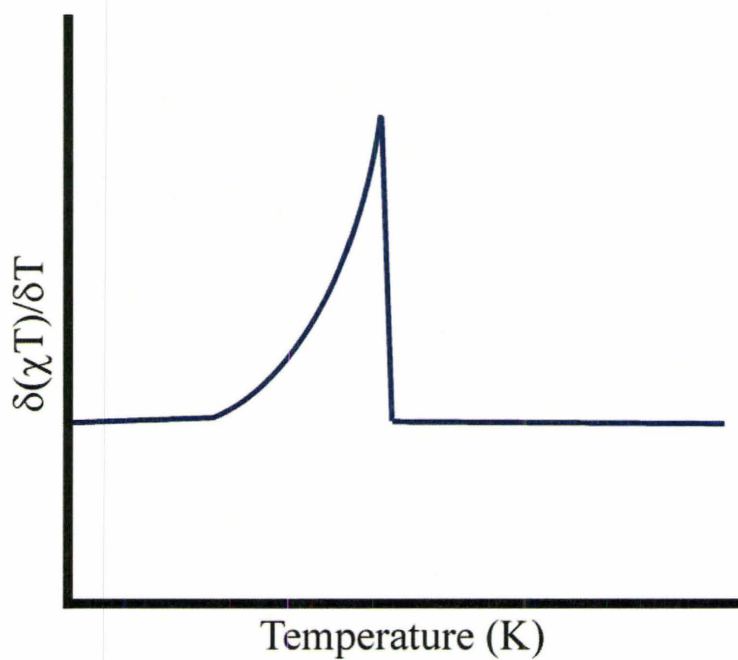


Figure 2.15. Fisher heat capacity (derivative of  $\chi T$  with respect to T) for an antiferromagnet. The lambda-like shape of the anomaly indicates long-range order.

$$M = \frac{\mu}{\text{mols}} \div 5585 \mu_B \quad 2.30$$

Typically, a full magnetization curve for a given temperature is measured starting from zero field and increasing it incrementally until the highest available field (i.e. +5.0 T). The field is then incrementally decreased to the lowest possible field (i.e. -5.0 T) before returning to zero field (see Figure 2.16).

There are some specific points on the magnetization curve that correspond to some important properties of the magnetic system. The highest measured magnetization for the highest value of the field is known as the saturation magnetization ( $\mu_{sat}$ ), which is related to the spin quantum number ( $S$ ):

$$\mu_{sat} = 2S \mu_B \quad 2.31$$

If the field is large enough to overcome any magnetic interactions and force all of the individual magnetic moments to align with it, then this is the expected magnetization value at that field. When the field is gradually decreased from its highest set value, the measured magnetization at 0.0 T is known as the remanence magnetization. This is the magnetization that persists in the system after the field that has forced alignment in a certain direction has been removed. Another important feature is the coercivity of the magnet, or the field required to reduce the magnetization back to zero after full saturation has been reached. The higher the coercivity, the greater the field required to demagnetize the magnet. The “hardness” of a magnet, or its ability to retain its magnetization after the removal of an aligning field, is a factor of both remanence and coercivity.

Depending on the type of magnetic interaction, interesting features may arise in the magnetization curve. Ferromagnets typically saturate in a laboratory field, often with

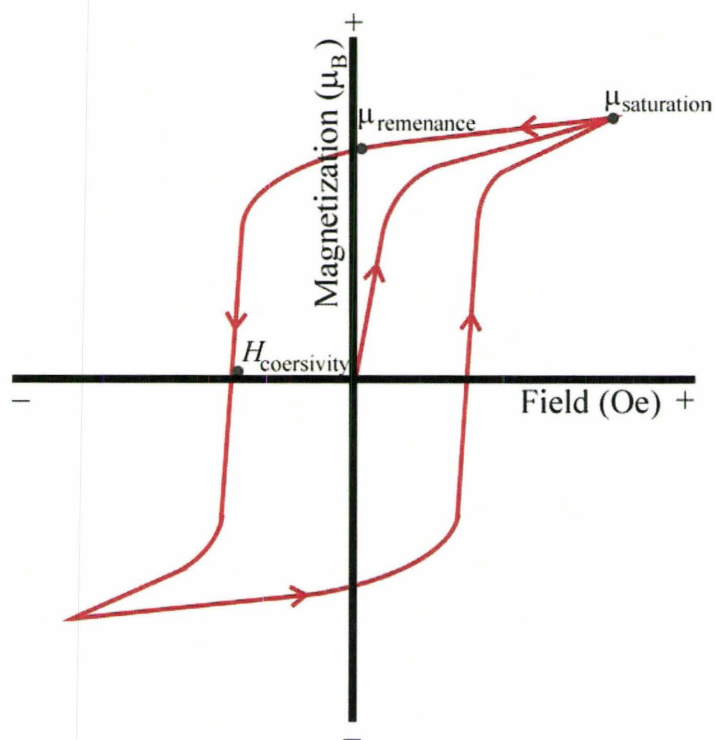


Figure 2.16. A typical magnetization curve for a ferromagnet.

large remanence values, depending on the strength of the magnetic coupling. Hysteresis between the data measured as the field is increased as compared with when the field is decreased is often very large. In contrast, a strongly coupled antiferromagnet rarely saturates in a laboratory field, and no hysteresis is typically observed. The interesting phenomena of metamagnetism and spin flop transitions have been discussed previously.

### *Instrumentation*

The DC-SQUID magnetometer is an extremely sensitive device for measuring the magnetic properties of a substance. It uses an inductance method, whereby the magnetic magnetization is determined by the current induced in a small wire loop that the sample passes through. From this small current, an output voltage is actually measured, and the magnetic moment of the sample can be calculated.

The sample translation system in the Quantum Design SQUID magnetometer consists of three inductance coils. Before measuring, the sample is centred in the coils within the specified scan length (typically 4 cm). The main pick up coil is in the centre, with two smaller coils above and below with half as many windings in the opposing direction to the main coil (Figure 2.17). The recorded voltage signal appears as an inverted parabola (Figure 2.17). Each magnetic measurement at a given temperature consists of 3 independent scans over the sample length, with each scan consisting of about 25 data points. These points are fitted to a function that describes the expected voltage signal from the coil geometry.

There are two different modes for collecting magnetic data: (1) the DC or Direct Current and (2) the RSO or Reciprocating Sample Option. In the DC mode, the sample is

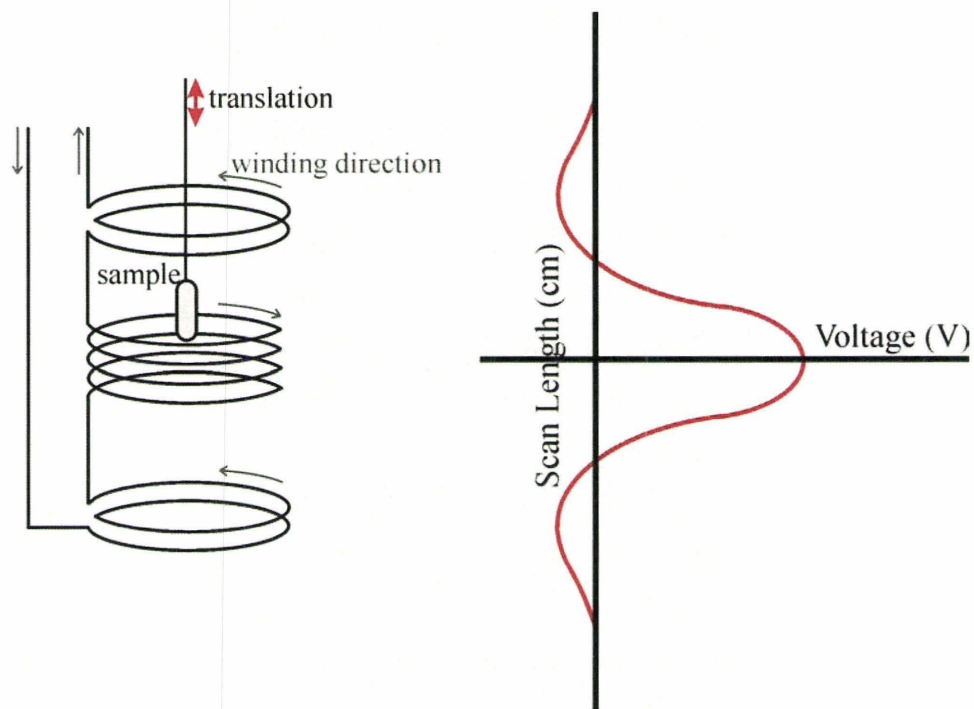


Figure 2.17. Sample translation inside the pick-up coils of a SQUID magnetometer (*left*) and the voltage signal that is produced (*right*). The two diagrams are on a common length scale for direct comparison.

slowly passed through the three coils multiple times, resulting in an average signal with relatively small error bars. This is the traditional sample translation methodology. For the RSO mode, the sample is quickly oscillated through the detection coils. In theory, this results in faster data acquisition times (which reduces the overall experiment time and any non-linear drift in the applied field) and greater sensitivity (usually by one or two orders of magnitude), with a substantial reduction in noise. Due to these many advantages, RSO mode is typically utilized in most SQUID measurements.

How exactly the SQUID converts the incredibly small current induced by the sample magnetic moments in the pick-up coils into a measurable voltage is a complex matter of physics. In the early 1960's, Josephson discovered that large electric currents could be produced from relatively small changes in the magnetic field, by sandwiching a small insulating layer between two superconductors. The quantum mechanical wavefunctions that describe the Cooper pair responsible for the superconductivity "bleed" into the forbidden insulating layer from either side. For a thin enough insulating layer, the two wavefunctions can overlap and the Cooper pairs can effectively "tunnel" between the two superconductors without breaking apart. If a DC current is applied across the junction, the AC Josephson effect causes oscillations in the current in the radio frequency range.

The Quantum Design SQUID magnetometer is equipped with an RF SQUID device, which consists of a single Josephson junction within a superconducting loop. This RF SQUID is then coupled to a parallel resonant LC circuit (i.e. an inductor connected across a capacitor), as in Figure 2.18. Application of a DC current through the

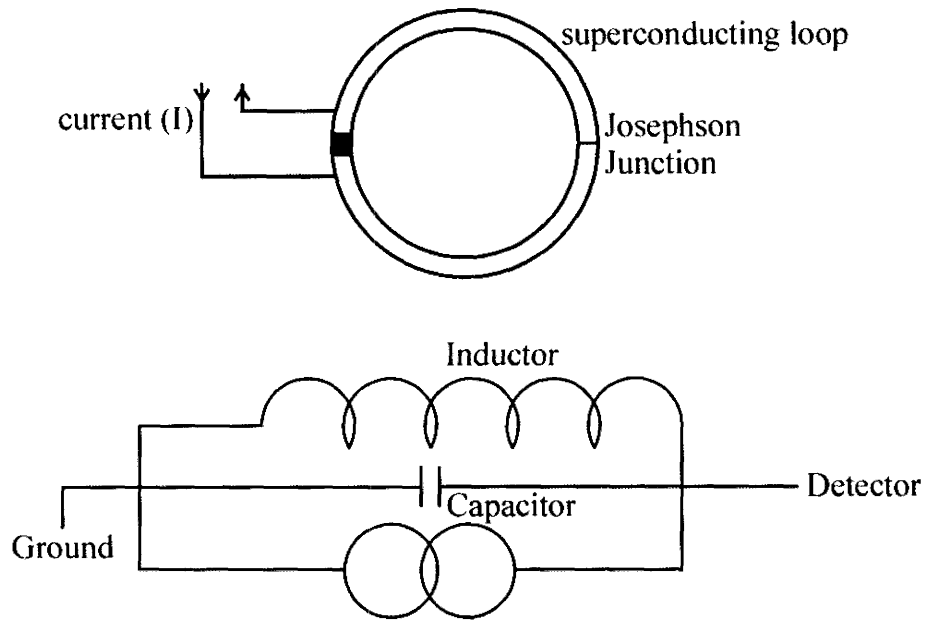


Figure 2.18. Diagram of a RF SQUID, detailing the Josephson Junction (*top*) and the LC circuit (*bottom*).

SQUID results in Cooper pairs tunnelling across the junction in an oscillating manner, according to the AC Josephson effect. However, if there is a magnetic field present within the superconducting loop, the Meissner effect will produce currents that oppose changes in the magnetic flux by quantized amounts of  $hc/2e = 2 \times 10^{-7}$  Oe/cm<sup>2</sup>, and the flow of Cooper pairs will be changed accordingly. The net result of these two competing currents is that the phase of the wavefunction of the Cooper pairs is modified, which, in turn, changes the AC voltage induced in the loop. The resonant LC circuit parallel to this loop picks up these AC voltage changes and sends this signal to a lock-in amplifier, which further enhances it. It is this measured AC voltage change that is fitted to a function and converted into a measured magnetic moment.<sup>9-12</sup>

## 2.8 Heat Capacity Measurements

The heat capacity ( $C$ ) of a system at constant volume (typical for a solid) is:

$$C = \lim_{\Delta T \rightarrow 0} \frac{Q}{\Delta T} \quad 2.32$$

where  $Q$  represents the heat and  $\Delta T$  is the difference in temperature. At low

temperatures, ideally all substances should obey the empirical heat capacity law:

$$C = \gamma T + \beta T^3 \quad 2.33$$

where  $\gamma$  represents the electronic contribution to the specific heat and  $\beta$  is the phonon component. The electronic part is related to the density of states of the conduction electrons in the material, which should be relatively small in the case of a magnetic insulator. The crystal lattice also contributes to the overall heat capacity of a compound,

typically in the  $T^3$  term. At low temperatures, the specific heat of a solid should have a linear dependence, which becomes quickly dominated by the cubic component as the temperature increases. However, this simple law is only valid in the low temperature regime, where a detailed knowledge of the phonon modes is not required.

The heat capacity of a magnetic system can provide some important information, particularly about the nature of a magnetic phase transition. A transition to long-range magnetic order appears as a lambda-like anomaly, which is a sharp, asymmetric feature. In contrast, a broad feature is typically indicative of short-range interactions. However, the area under the feature is related to the entropy removed from the system due to the magnetic transition:

$$\Delta S = \int \frac{C}{T} dT \quad 2.34$$

where  $\Delta S$  is the change in magnetic entropy of the system. According to Boltzmann, the entropy is related to the number of states:  $\Delta S = R \ln W$  where  $W$  is the state degeneracy.

For a magnetic system of spins ( $S$ ), this is:

$$\Delta S = R \ln(2S + 1) \quad 2.35$$

If there is substantial short-range order present, the calculated entropy loss associated with the lambda anomaly could be much lower than expected, as much of the magnetic entropy would already have been removed. An ideal lattice match compound is essential to account for the lattice contribution, so that only the magnetic entropy can be isolated.<sup>13,14</sup>

*Instrumentation*

The Oxford MagLab EXA measures the heat capacity of a sample using the relaxation method. The sample, typically a powder pressed into a pellet and sintered at high temperature to ensure good thermal contact between grains, is placed on an isolated sample platform that is connected to a thermal bath by only very weak thermal links. A heat pulse can be defined as:

$$Q = U \times I \times t = P \times t \quad 2.36$$

where  $Q$  is the heat,  $U$  is the applied voltage,  $I$  is the current,  $t$  is the heating time and  $P$  is the power. This pulse is applied to the sample with a magnitude dependent on the final temperature of the system. The final temperature ( $T_o$ ) is related to the initial temperature of the sample ( $T_i$ ) by an exponential:

$$T = T_i + \Delta T_o (1 - \exp^{-t/\tau}) \quad 2.37$$

where  $\tau$  is the relaxation time constant, determined by the heat capacity ( $C$ ) and the thermal resistance ( $R_{TH}$ ) between the sample and the surroundings:

$$\tau = R_{TH} C \quad 2.38$$

with  $R_{TH}$  defined as:

$$R_{TH} = \frac{\Delta T_o}{\Delta P} \quad 2.39$$

By knowing the temperature of the chip accurately before and after the pulse, as well as the applied power, and measuring the relaxation time, accurate determination of the sample's heat capacity can be made.

The Oxford Instruments Heat Capacity Probe insulates the sample from the surroundings quite well, and is evacuated to very low pressure ( $\sim 10^{-5}$  torr) to ensure adequate thermally isolated conditions. Measurements can be made reliably from about 2 to 100 K. The probe itself is pictured in Figure 2.19. A small, thin sample (approximately 2 mm  $\times$  2 mm  $\times$  < 1 mm thick) is affixed to a sapphire chip using a small amount of Apiezon grease. The chip is connected to the probe by 8 very thin (20  $\mu$ m) gold plated tungsten wires. A Cernox temperature sensor is also connected to the chip by 50  $\mu$ m gold leads to carefully monitor the chip temperature. Very small heat pulses applied through the smaller wires results in large temperature changes due to the weakness of the thermal link. The contribution of the sapphire chip, gold leads and Apiezon grease to the measured heat capacity are calibrated and accounted for by the instrument software.<sup>15</sup>

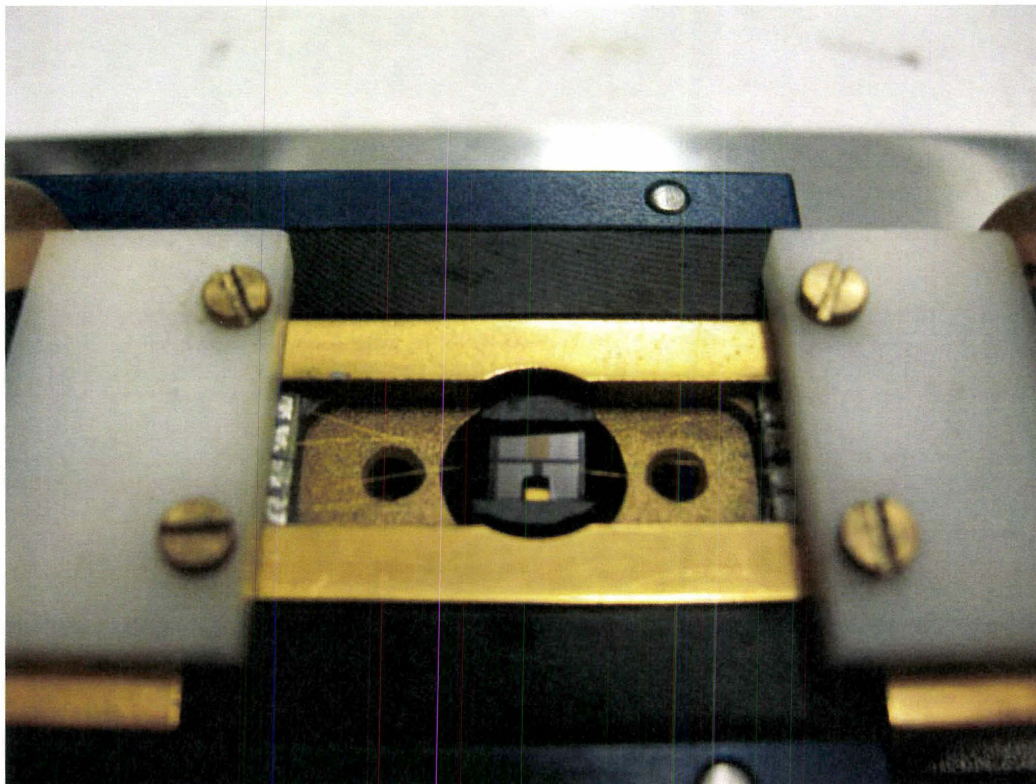


Figure 2.19. Sample mount for the Oxford Instruments Heat Capacity probe.

## 2.9 References

1. Stout, G.H.; Jensen, L.H. *X-ray Structure Determination: A Practical Guide*; 2nd ed.; Wiley & Sons, Inc.: New York, 1989.
2. Canadian Neutron Beam Centre. *Neutron Diffraction Summer School Lecture Notes*. CNBC, 2004.
3. *Neutron Data Booklet*; 2nd ed.; Dianoux, A.-J.; Lander, G., Eds.; Institut Laue-Langevin: Grenoble, 2003.
4. Caglioti, G.; Paoletti, A.; Ricci, F. P. *Nucl. Instrum.* **1958**, *3*, 223-228.
5. Guinebretiere, R.; Boule, A.; Masson, O.; Dauger, A. *Powder Diffraction* **2005**, *20*, 294-305.
6. McCusker, L. B.; VonDreele, R. B.; Cox, D. E.; Louer, D.; Scardi, P. *J. Appl. Cryst.* **1999**, *32*, 36-50.
7. *The Rietveld Method*; Young, R. A., Ed.; Oxford University Press: Oxford, 1993.
8. Fisher, M. E. *Philos. Mag.* **1962**, *7*, 1731-43.
9. Tinkham, M. *Introduction to Superconductivity*; 2nd ed.; McGraw-Hill Inc.: New York, 1996.
10. VanDuzer, T.; Turner, C. W. *Principles of Superconductive Devices and Circuits*; 2nd ed.; Prentice Hall: New Jersey, 1999.
11. *New Research on Superconductivity*; Martins, B. P., Ed.; Nova Science Publishers, Inc.: New York, 2007.
12. *Magnetic Property Measurement System Software Manual*; Quantum Design: San Diego, 1987.
13. Cezairliyan, A. *Specific Heat of Solids*; Hemisphere Publishing Corp.: New York, 1988; Vol. I-2.
14. Hann, B. F. *The Physics of Heat Capacity*; Macmillan Education Ltd.: London, 1971.
15. *Heat Capacity Relaxation Probe Manual*; Oxford Instruments Superconductivity Ltd.: England, 2000.

### Chapter 3

#### **Investigations of the Magnetic Properties and Structures of the Pillared Perovskites, $\text{La}_5\text{Re}_3\text{MO}_{16}$ ( $M = \text{Co}, \text{Ni}$ )**

This chapter encompasses the manuscript “Investigations of the Magnetic Properties and Structures of the Pillared Perovskites,  $\text{La}_5\text{Re}_3\text{MO}_{16}$  ( $M = \text{Co}, \text{Ni}$ )”, published in the Journal of Solid State Chemistry (*J. Solid State Chem.* **2006**, *179*, 1938-1947). The candidate completed all of the experimental synthesis and measurements, as well as data processing and interpretation. In addition, the candidate prepared the manuscript and submitted it to the journal as corresponding author.

Reproduced with permission from Cuthbert, H.L.; Greedan, J.E.; Cranswick, L. *J. Solid State Chem.* **2006**, *179*, 1938-1947. Copyright 2006 Elsevier.

**Investigations of the Magnetic Properties and Structures of the Pillared  
Perovskites,  $\text{La}_5\text{Re}_3\text{MO}_{16}$  ( $M = \text{Co}, \text{Ni}$ )**

Heather L. Cuthbert<sup>a</sup>, John E. Greedan<sup>a,b</sup> and Lachlan Cranswick<sup>c</sup>

*a* Department of Chemistry, McMaster University, Hamilton, ON, Canada

*b* Brockhouse Institute for Materials Research, McMaster University, Hamilton, ON, Canada

*c* The Canadian Neutron Beam Centre, National Research Council of Canada, Chalk River Laboratories, Chalk River, ON, Canada

### 3.1 Abstract

$\text{La}_5\text{Re}_3\text{CoO}_{16}$  and  $\text{La}_5\text{Re}_3\text{NiO}_{16}$  were synthesized by solid state reaction and studied by SQUID magnetometry, heat capacity and powder neutron diffraction measurements. These two compounds belong to a series of isostructural Re-based pillared perovskites (*J. Solid State Chem.* **2003**, *170*, 165-175.). Magnetic susceptibility measurements indicate apparent short range ferri or ferromagnetic correlations and possible long-range antiferromagnetic order for  $\text{La}_5\text{Re}_3\text{CoO}_{16}$  at 35 K and at 38 K and 14 K for  $\text{La}_5\text{Re}_3\text{NiO}_{16}$ . Heat capacity measurements of the Co compound show a lambda anomaly, typical of long-range magnetic order, at 32 K. In contrast, the Ni compound displays a broader, more symmetric feature at 12 K in the heat capacity data, indicative of short-range magnetic order. Low temperature powder neutron diffraction revealed contrasting magnetic structures. While both show an ordering wave vector,  $k = (0\ 0\ 1/2)$ , in  $\text{La}_5\text{Re}_3\text{CoO}_{16}$ , the  $\text{Co}^{2+}$  and  $\text{Re}^{5+}$  moments are ordered ferrimagnetically within the corner-shared octahedral layers, while the layers themselves are coupled

antiferromagnetically along the  $c$ -axis, as also found in  $\text{La}_5\text{Re}_3\text{MnO}_{16}$  and  $\text{La}_5\text{Re}_3\text{FeO}_{16}$ . In the case of the Ni material, the  $\text{Re}^{5+}$  and  $\text{Ni}^{2+}$  moments in the perovskite layers couple ferromagnetically and are canted  $30^\circ$  away from the  $c$ -axis, angled  $45^\circ$  in the  $ab$ -plane. The layers then couple antiferromagnetically at low temperature, a unique magnetic structure for this series. The properties of the  $\text{La}_5\text{Re}_3\text{MO}_{16}$  series, with  $M = \text{Mn, Fe, Co, Ni}$  and  $\text{Mg}$  are also reviewed.

### 3.2 Introduction

In recent years, a new family of “pillared perovskite” compounds has been discovered and investigated. This structure type has been found for oxides of molybdenum,  $\text{La}_5\text{Mo}_{4-x}\text{M}_x\text{O}_{16}$  ( $x = 0$  and  $x \sim 0.7$  for  $M = \text{Mn, Fe, Co, Mg}$ )<sup>1-3</sup>, rhenium,  $\text{La}_5\text{Re}_3\text{MO}_{16}$  ( $M = \text{Mn, Fe, Co, Ni, Mg}$ )<sup>4-6</sup> and osmium,  $\text{La}_5\text{Os}_3\text{MnO}_{16}$ <sup>7</sup>. The unit cell is pictured in Figure 3.1. It consists of perovskite-like layers of corner-shared  $MM'\text{O}_6$  octahedra, in which the  $M$  and  $M'$  ions are site ordered, avoiding like ion nearest neighbours. These layers are “pillared” by dimeric units of two edge-shared  $\text{MO}_6$  octahedra. The  $\text{La}^{3+}$  ions occupy interstitial sites.

Magnetically, the pillared perovskites have displayed some interesting properties, as a result of their structure. The dimeric ‘pillars’ involve metal-metal bonding between the  $4d$  or  $5d$  transition metals and the units are diamagnetic. Within the layers, due to site ordering of the  $M$  and  $M'$  ions, both transition metals exhibit local moment behaviour with nearly spin only values. Although the layers are separated by  $\sim 10 \text{ \AA}$ , long range magnetic order exists in these compounds. For the  $\text{La}_5\text{Re}_3\text{MO}_{16}$  series, the critical

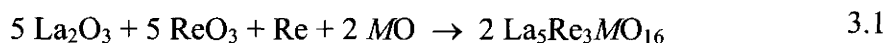
temperature ( $T_c$ ) varies from 161 K in the Mn compound to 33 K in the Co compound.<sup>5,6</sup>

Detailed magnetic property studies on two members of the Re series ( $M = \text{Mn}$  and  $\text{Fe}$ ) indicate that the magnetic structure consists of ferrimagnetically coupled layers that are coupled antiferromagnetically in three dimensions.<sup>5,6</sup> This current work examines the magnetic properties of two remaining Re family members,  $\text{La}_5\text{Re}_3\text{CoO}_{16}$  and  $\text{La}_5\text{Re}_3\text{NiO}_{16}$ , in greater detail.

### 3.3 Experimental

#### *Synthesis*

The title compounds,  $\text{La}_5\text{Re}_3\text{MO}_{16}$  ( $M = \text{Co}, \text{Ni}$ ), were synthesized by solid state reaction, as outlined previously.<sup>6</sup>



Stoichiometric amounts of the starting reagents,  $\text{La}_2\text{O}_3$  (99.9%, Aldrich, calcined at  $900^\circ\text{C}$  overnight before use),  $\text{ReO}_3$  (Rhenium Alloys),  $\text{Re}$  (Rhenium Alloys) and  $\text{MO}$  ( $M = \text{CoO}$ , 99.99%, Aldrich;  $M = \text{NiO}$ , 99.995%, CERAC) were accurately weighed, ground together, pressed into a pellet and placed into a platinum crucible, which was sealed in a quartz tube under vacuum ( $\sim 10^{-5}$  torr). The reaction was heated to  $1050^\circ\text{C}$  in a tube furnace and held for 48 hours. The products obtained were black powders. The non-magnetic lattice match compound for heat capacity,  $\text{La}_5\text{Re}_2\text{TaMgO}_{16}$ , was made in a similar manner, using stoichiometric amounts of  $\text{Ta}_2\text{O}_5$  (99.99%, CERAC) and  $\text{MgO}$  (99.95%, Alfa Aesar) as well.

### *X-ray and Neutron Diffraction*

X-ray diffraction data were collected using a Guinier-Hagg camera with  $\text{CuK}\alpha_1$  radiation ( $\lambda = 1.5406 \text{ \AA}$ ) and high-purity silicon powder as an internal reference. In addition, x-ray diffraction data suitable for Rietveld refinement was obtained from a Bruker D8 diffractometer using  $\text{CuK}\alpha$  radiation from  $10^\circ$  to  $80^\circ$  in the  $2\theta$  range. A step size of  $0.025^\circ$  and a step time of 12 s were employed.

Variable temperature powder neutron diffraction measurements were performed on the C2 diffractometer operated by the Canadian Neutron Beam Centre at NRC Chalk River Laboratories. The crystal structure data (285 K) were collected at a wavelength of  $1.32917 \text{ \AA}$  in the angular range of  $12^\circ \leq 2\theta \leq 113^\circ$  with  $0.1^\circ$  steps. Similarly, the magnetic structure data (variable temperatures from 4 K) were measured at a longer wavelength of  $2.36957 \text{ \AA}$  in the range  $5^\circ \leq 2\theta \leq 85^\circ$  with  $0.1^\circ$  intervals.

### *Magnetic Data*

Magnetic measurements were collected using a Quantum Design MPMS SQUID magnetometer. Zero field cooled and field cooled (ZFC/FC) magnetic susceptibility data from 2-300 K and isothermal magnetization measurements from 0-5 T were recorded on samples incased in gelatin capsules.

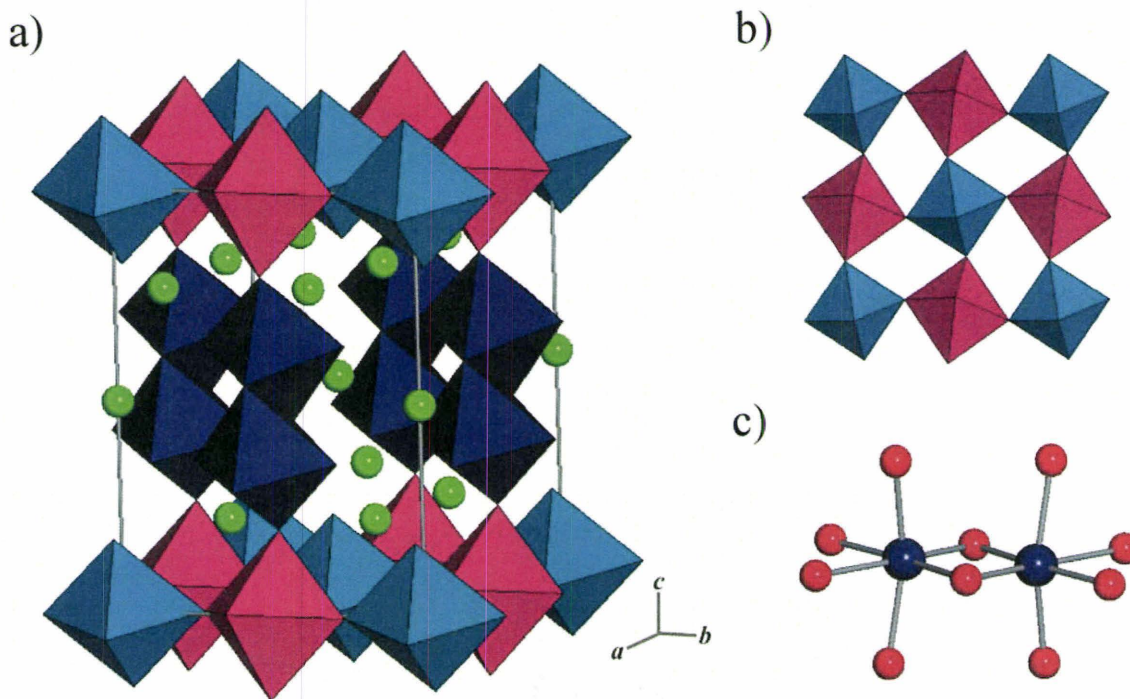


Figure 3.1. Crystal structure of  $\text{La}_5\text{Re}_3\text{MO}_{16}$ . a) A view of the unit cell:  $\text{ReO}_6$  octahedra in blue,  $\text{MO}_6$  octahedra in pink,  $\text{Re}_2\text{O}_{10}$  dimer units in dark blue and La ions in green. b) A perovskite-like layer of corner sharing  $\text{ReO}_6$  (blue) and  $\text{MO}_6$  (pink) octahedra. Notice the large octahedral tilt angles away from the ideal  $180^\circ$ . c) A  $\text{Re}_2\text{O}_{10}$  "pillar" of two edge shared  $\text{ReO}_6$  octahedra: Re atoms in dark blue and O atoms in red.

### *Heat Capacity*

Heat capacity data were measured using the heat capacity probe in an Oxford MagLab at McMaster University. Thin sample blocks of approximately 10 mg were prepared by repressing and resintering a portion of the previously synthesized product. Sample structure integrity was verified by powder X-ray diffraction (Guinier). The sample block was mounted onto a sapphire measurement chip with Apiezon grease. Contributions to the measured heat capacity by the grease and sample chip were accounted for.

## **3.4 Results and Discussion**

### *Structural Characterization*

The structures of both title compounds were verified by their Guinier powder patterns, which matched well with the patterns obtained for the same compositions synthesized previously.<sup>6</sup> Further structure characterization was accomplished through Rietveld refinement of room temperature powder X-ray ( $\text{La}_5\text{Re}_3\text{NiO}_{16}$ ) and neutron ( $\text{La}_5\text{Re}_3\text{CoO}_{16}$ ) diffraction data using WINPLOTR in the FULLPROF program.<sup>8</sup> The unit cell constants and agreement indices are displayed in Table 3.1, with the previously published values in square parentheses. From these results, it is clear that the synthesized compounds are  $\text{La}_5\text{Re}_3\text{CoO}_{16}$  and  $\text{La}_5\text{Re}_3\text{NiO}_{16}$ . This structure type is illustrated in Figure 3.1 and has been discussed previously. The short Re-Re distance found in the dimer (2.380(8) Å for Co and 2.419(6) Å for Ni) is indicative of a Re – Re double bond, which would pair the  $\text{Re}^{5+}$  electrons and quench the magnetic moment within the pillars.

The only magnetic ions in these compounds are  $\text{Re}^{5+}$  ( $S = 1$ ) and  $M^{2+}$  (Co,  $S = 3/2$ ; Ni,  $S = 1$ ) within the perovskite layers.

Table 3.1. Unit Cell Parameters and Agreement Factors for the Structural Refinement of Diffraction Data for  $\text{La}_5\text{Re}_3\text{CoO}_{16}$  and  $\text{La}_5\text{Re}_3\text{NiO}_{16}$ . Literature values are shown in square parentheses.

Compound	$\text{La}_5\text{Re}_3\text{CoO}_{16}$	$\text{La}_5\text{Re}_3\text{NiO}_{16}$
Data source	Neutron	X-ray
Space group	$C-1$	$C-1$
Cell parameters	$a = 7.9621(8) \text{ \AA} [7.9694(7) \text{ \AA}]$	$a = 7.9280(4) \text{ \AA} [7.9383(4) \text{ \AA}]$
	$b = 7.9957(8) \text{ \AA} [8.0071(8) \text{ \AA}]$	$b = 7.9888(4) \text{ \AA} [7.9983(5) \text{ \AA}]$
	$c = 10.172(1) \text{ \AA} [10.182(1) \text{ \AA}]$	$c = 10.1585(5) \text{ \AA} [10.1732(6) \text{ \AA}]$
	$\alpha = 90.248(5)^\circ [90.248(4)^\circ]$	$\alpha = 90.274(2)^\circ [90.287(3)^\circ]$
	$\beta = 94.975(4)^\circ [94.980(4)^\circ]$	$\beta = 94.876(2)^\circ [94.864(3)^\circ]$
	$\gamma = 89.977(8)^\circ [89.983(6)^\circ]$	$\gamma = 89.967(3)^\circ [89.968(4)^\circ]$
Agreement factors	$R_p = 0.0282$	$R_p = 0.128$
	$R_{wp} = 0.0380$	$R_{wp} = 0.168$
	$\chi^2 = 2.02$	$\chi^2 = 1.22$
	$R_B = 0.0543$	$R_B = 0.0708$

### *Magnetic Measurements*

#### *a. $\text{La}_5\text{Re}_3\text{CoO}_{16}$*

Zero field cooled and field cooled (ZFC/FC) magnetic susceptibility measurements from 5-300 K at a field of 0.05 T and from 2-200 K at fields of 2.0 T and 5.0 T respectively are shown in Figure 3.2. Data acquired at the lowest applied field (0.05 T) show a large cusp at 35 K and two smaller, broader shoulders centred at 75 and 100 K respectively. The sharp feature is attributed to long-range antiferromagnetic order (with an ordering temperature,  $T_c$  of 35 K), while the features at higher temperatures are indicative of short-range magnetic correlations. The ZFC and FC data begin to diverge at approximately 140 K. This result is comparable to the ZFC-FC susceptibility ( $\chi$ ) data

measured previously.<sup>6</sup> However, the small feature at 100 K did not appear in the earlier measurements. A plot of  $\chi T$  versus temperature, shown in Figure 3.3, shows this feature more prominently. The horizontal line in the plot represents the calculated spin only Curie constant for the combination of  $\text{Re}^{5+}$  ( $S = 1$ ;  $C_{\text{SO}} = 1.00 \text{ emu}\cdot\text{K/mol}$ ) and  $\text{Co}^{2+}$  ( $S = 3/2$ ;  $C_{\text{SO}} = 1.87 \text{ emu}\cdot\text{K/mol}$ ) ions. At higher temperatures ( $\sim 300 \text{ K}$ ),  $\chi T$  approaches this value, which is as expected if the compound obeys the Curie-Weiss law in that temperature regime. The new, broad peak at 100 K may represent very short range intraplanar magnetic order, perhaps in the form of one dimensional chains. The sharper cusp at 35 K is even more pronounced, which is indicative of short range ferro- or ferrimagnetic correlations.

When the field is increased to 2.0 T, the ZFC-FC divergence moves to a lower temperature (20 K), the sharp cusp at 35 K broadens significantly in the ZFC data, and the weaker features are lost. Finally, at 5.0 T, the ZFC-FC divergence is negligible and all the features are gone. The 5.0 T curve suggests ferrimagnetic behaviour, with a saturation moment of about  $1.3(1) \mu_{\text{B}}$ . This is slightly larger than the expected spin-only saturation moment ( $1.0 \mu_{\text{B}}$ ) for ferrimagnetically coupled  $\text{Co}^{2+}$  ( $S = 3/2$ ) and  $\text{Re}^{5+}$  ( $S = 1$ ) moments. The magnetic moment of  $\text{Co}^{2+}$  ions often exceed the spin only value and the  $\text{Re}^{5+}$  moment is expected to be smaller, due to orbital contributions. However, this experimental moment is well below that calculated for ferromagnetically coupled  $\text{Co}^{2+}$  ( $S = 3/2$ ) and  $\text{Re}^{5+}$  ( $S = 1$ ) moments within the layers ( $5.0 \mu_{\text{B}}$ ).

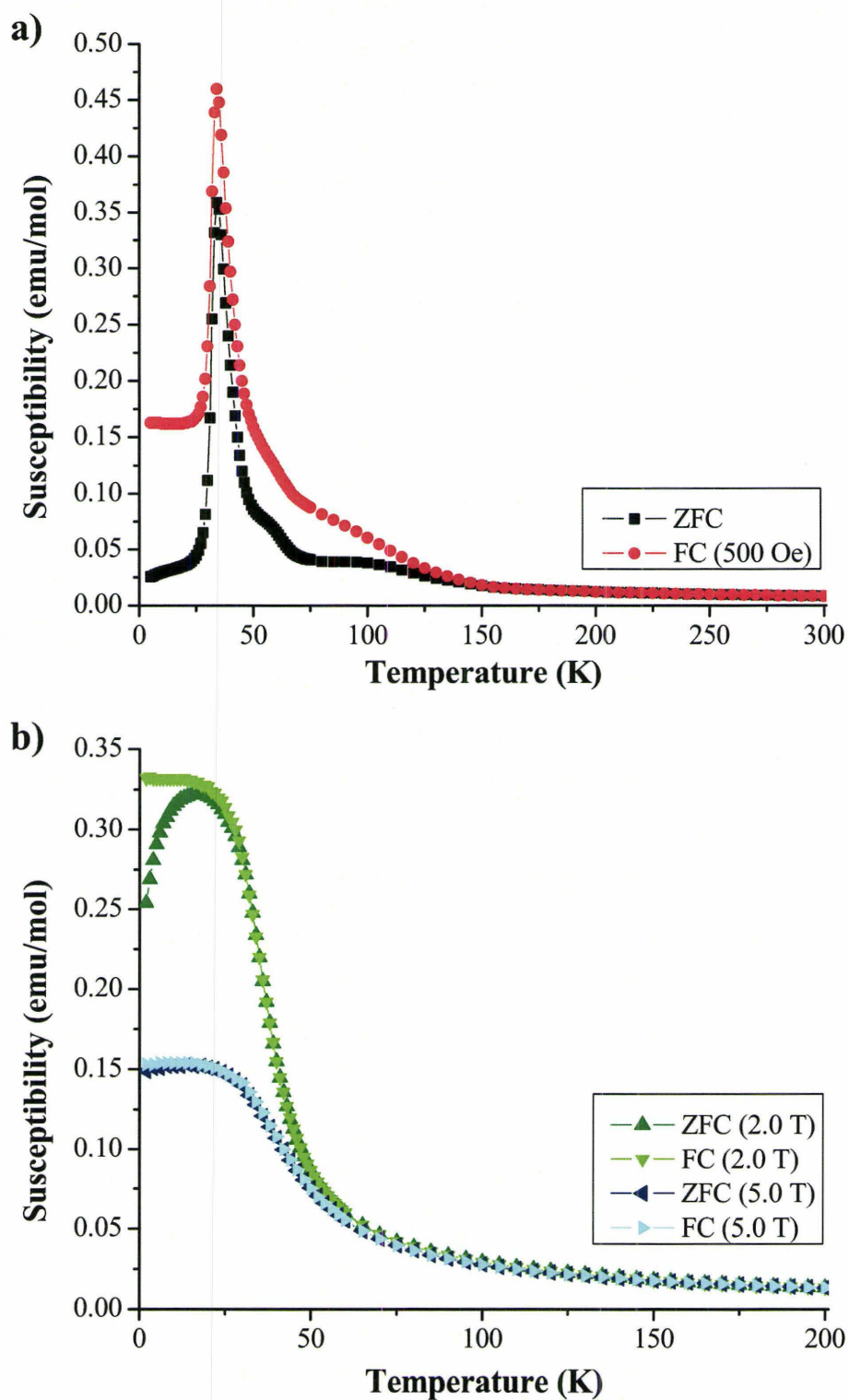


Figure 3.2. ZFC (darker shade) and FC (lighter shade) magnetic susceptibility measurements of  $\text{La}_5\text{Re}_3\text{CoO}_{16}$  with applied fields of a) 0.05 T (red) and b) 2.0 T (green) and 5.0 T (blue).

From the crystal structure of  $\text{La}_5\text{Re}_3\text{CoO}_{16}$ , there are two different types of magnetic interaction – intraplanar and interplanar. Intraplanar magnetic coupling would involve Re-O-Co superexchange pathways within the perovskite layer, and would be relatively strong because of geometry (comparatively short distances and angles of approximately  $155^\circ$ ). However, interplanar coupling would require magnetic superexchange through the diamagnetic  $\text{Re}_2\text{O}_{10}$  dimer and over much greater a distance (approximately  $10 \text{ \AA}$ ). This type of interaction would be expected to be much weaker, and could be overcome with the modest magnetic field applied here, such as 5.0 T.

Isothermal magnetization data at temperatures of 2, 32, 40, 55, 80 and 200 K were collected on  $\text{La}_5\text{Re}_3\text{CoO}_{16}$  for fields between 0 and 5.0 T and are shown in Figure 3.4. At 2 K, the magnetization increases sharply at an applied field of 6500 Oe, and curves gradually to approach a saturation moment of  $1.3 \mu_B$  at 5.0 T. Again, this value matches the saturation moment obtained from the 5.0 T ZFC/FC susceptibility data and is indicative of ferrimagnetically coupled moments through out the structure. There is very strong hysteresis present at 2 K, and a rather large remanent magnetization of  $0.63 \mu_B$ . The sharp increase at low field is interpreted as the onset of a transition analogous to metamagnetism, in which the weak antiferromagnetic interlayer coupling is reversed by the applied field. A slight hysteresis persists in this compound up to 40 K. The 32 K data show a more gradual upturn at 3000 Oe, and then begin to level off. The 40 K data also curve gradually upwards, however at 55, 80 and 200 K, the signal is linear. At these higher temperatures, the data are consistent with paramagnetism. All of these responses corroborate the hypothesis that  $T_c$  for this compound is 35 K.

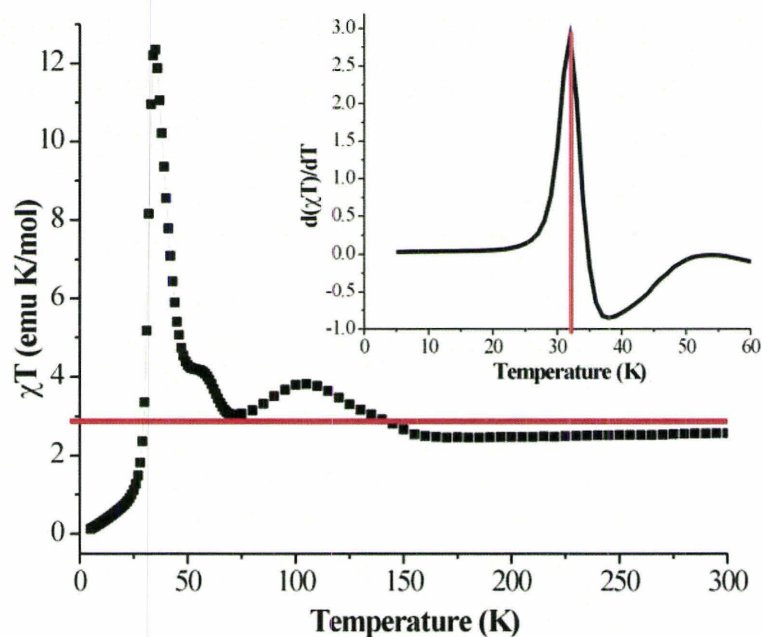


Figure 3.3.  $\chi T$  versus  $T$  plot of  $\text{La}_5\text{Re}_3\text{CoO}_{16}$  using the ZFC data only. The horizontal line is the sum of the calculated spin only Curie constants for  $\text{Re}^{5+}$  ( $S = 1$ ;  $C_{\text{SO}} = 1.00$  emu·K/mol) and  $\text{Co}^{2+}$  ( $S = 3/2$ ;  $C_{\text{SO}} = 1.87$  emu·K/mol). Inset - Fisher heat capacity of  $\text{La}_5\text{Re}_3\text{CoO}_{16}$  calculated using the ZFC magnetic susceptibility data. The vertical line denotes the peak centre. Note the peak asymmetry.

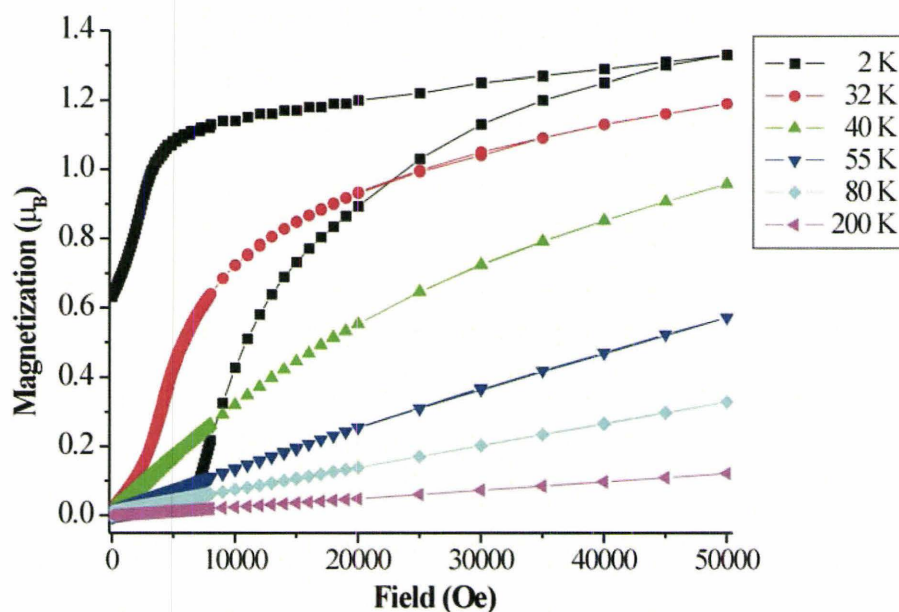


Figure 3.4. Isothermal magnetization versus applied field data for  $\text{La}_5\text{Re}_3\text{CoO}_{16}$ . Note the large residual magnetization at 2 K and the sharp jumps at low applied field in the 2 K and 32 K curves.

Heat capacity data collected from 10 to 50 K on  $\text{La}_5\text{Re}_3\text{CoO}_{16}$  in the absence of a magnetic field and with a 7 T field applied, as well as the heat capacity measured for the non-magnetic lattice match compound,  $\text{La}_5\text{Re}_2\text{TaMgO}_{16}$  are pictured in Figure 3.5. From Figure 3.6, subtraction of the lattice component discloses a lambda-like anomaly, albeit somewhat broad, with a peak at 32 K. This signals the onset of relatively long-range magnetic order. The inset graph in Figure 3.3 shows the so-called Fisher heat capacity for  $\text{La}_5\text{Re}_3\text{CoO}_{16}$ . There is one clear peak, whose maximum is at about 32 K and whose shape is quite asymmetric and lambda-like. Both of these features indicate good agreement between the heat capacity and SQUID magnetometry measurements. Application of a 7 T field significantly decreases the height of the heat capacity anomaly of  $\text{La}_5\text{Re}_3\text{CoO}_{16}$  and broadens it, indicating that the transition to long-range magnetic order is field dependent. As noted previously from the SQUID magnetometry data, the interplanar magnetic coupling is relatively weak, and can be overcome by modest magnetic fields.

Integration of the area under the curve for the zero applied field measurements results in an estimation of the change in entropy associated with this magnetic transition,

$$\Delta S = \int (C_{mol}/T) dT \quad 3.2$$

yielding  $\Delta S = 3.56 \text{ J/K}\cdot\text{mol}$ . This value is only 17 % of the  $20.66 \text{ J/K}\cdot\text{mol}$  expected for  $\text{Re}^{5+}$  ( $S = 1$ ) and  $\text{Co}^{2+}$  ( $S = 3/2$ ) moments and indicates that most of the magnetic entropy is lost in the intraplanar short range order.

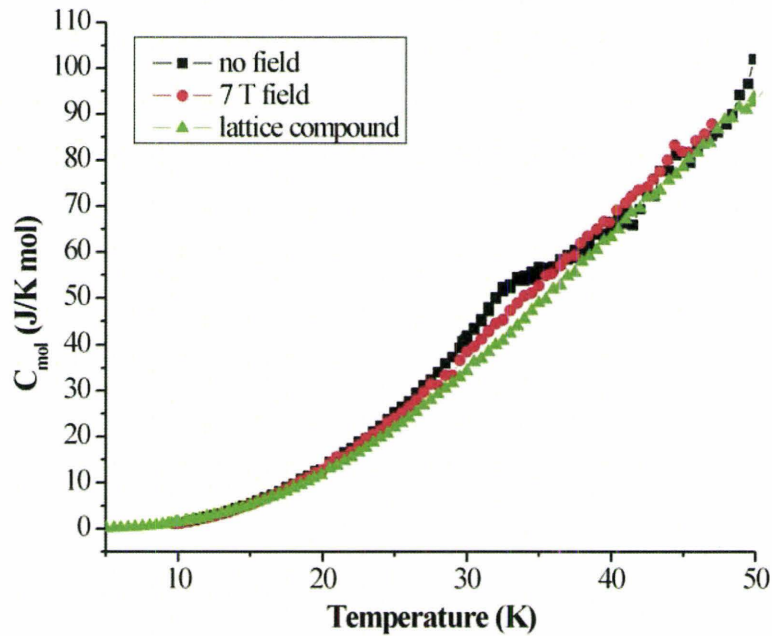


Figure 3.5. Heat capacity measurements of  $\text{La}_5\text{Re}_3\text{CoO}_{16}$  with no field applied (black squares) and in a 7.0 T field (red circles). The heat capacity measured for the non-magnetic lattice match compound is denoted by green triangles.

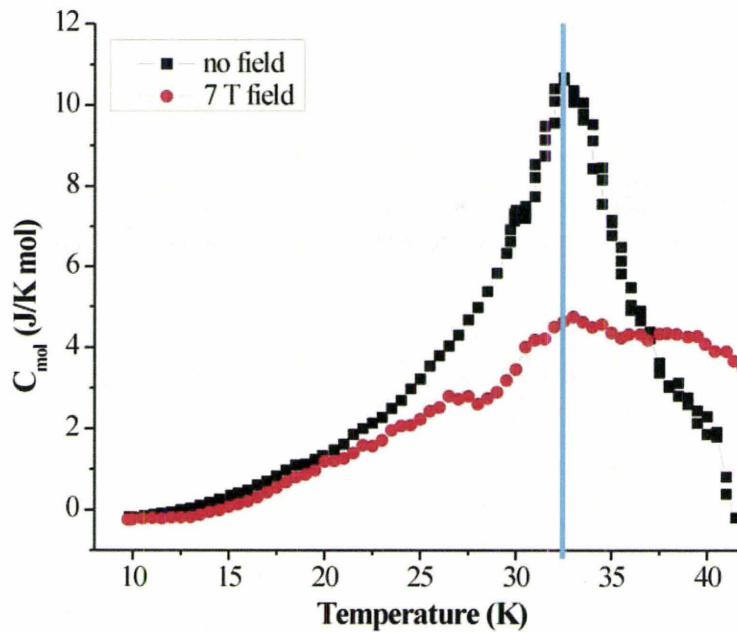


Figure 3.6. Magnetic component of the heat capacity of  $\text{La}_5\text{Re}_3\text{CoO}_{16}$ , in zero applied field (black squares) and in a 7 T field (red circles). The blue line denotes the peak centre. Note the lambda-like shape.

Variable temperature powder neutron diffraction measurements were also performed on  $\text{La}_5\text{Re}_3\text{CoO}_{16}$  to elucidate its magnetic structure. Figure 3.7 shows low angle neutron diffraction data of this compound at selected temperatures, to highlight the development of the new magnetic Bragg reflections. At 5 K, the two high intensity peaks (at  $2\theta = 24.7^\circ$  and  $25.5^\circ$ ) can be indexed to a magnetic unit cell with ordering vector,  $\mathbf{k} = (0\ 0\ 1/2)$  (i.e.  $a_{\text{mag}} = a$ ,  $b_{\text{mag}} = b$ ,  $c_{\text{mag}} = 2c$ , where  $a, b, c$  are the axes of the structural unit cell). This magnetic unit cell is the same as  $\text{La}_5\text{Re}_3\text{MnO}_{16}$ <sup>5</sup> and  $\text{La}_5\text{Re}_3\text{FeO}_{16}$ <sup>6</sup>. For these materials, the magnetic structure consists of ferrimagnetically coupled perovskite layers, coupled antiferromagnetically along the  $c$ -axis, which is depicted in Figure 3.8.

Using the same model, attempts were made to refine the magnetic structure of  $\text{La}_5\text{Re}_3\text{CoO}_{16}$ . However, due to a high degree of correlation between the  $\text{Re}^{5+}$  ( $S = 1$ ) and  $\text{Co}^{2+}$  ( $S = 3/2$ ) moments, their values could not be refined independently. The best fit, as seen in the difference plot and  $R_{\text{mag}}$  values, was obtained when the moments were fixed parallel to the  $c$ -axis at  $1.5\ \mu_{\text{B}}$  and  $2.5\ \mu_{\text{B}}$  for the Re and Co, respectively as shown in Figure 3.9. The magnitudes of these moments are not unreasonable, and are close to the spin only values for these ions. A plot of the relative intensity of the  $(1\ -1\ 1/2)/(1\ 1\ 1/2)$  magnetic peak as a function of temperature is displayed in Figure 3.10. The critical temperature of 35 K suggested by neutron diffraction is consistent with both the SQUID magnetometry and heat capacity results. Note also that the magnetic reflections appear to be resolution limited (they are not obviously broader than the chemical structure reflections) indicating that the correlation length for magnetic order is at least 100 Å or more.

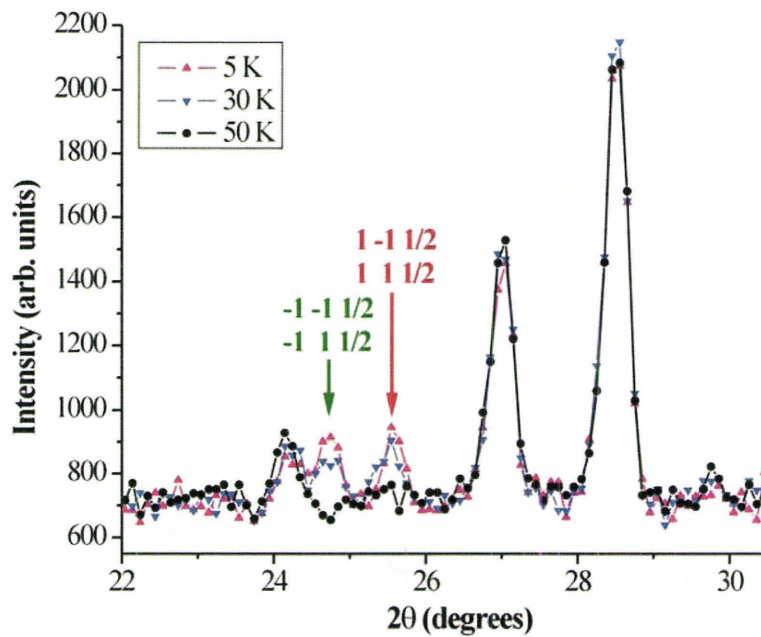


Figure 3.7. Powder neutron diffraction patterns of  $\text{La}_5\text{Re}_3\text{CoO}_{16}$  at 5 K (pink triangles), 30 K (blue inverted triangles) and 50 K (black circles). The peaks marked with arrows are the two new magnetic Bragg reflections, indexed as indicated.

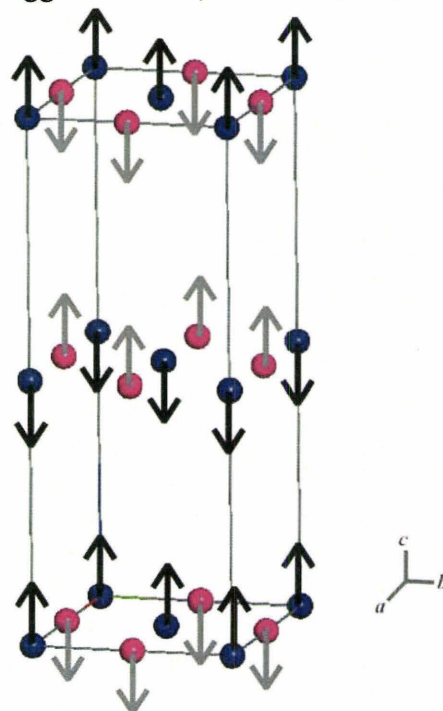


Figure 3.8. Magnetic structure of  $\text{La}_5\text{Re}_3\text{CoO}_{16}$ , showing the moments on the Re atoms (blue spheres, black arrows) and Co atoms (pink spheres, grey arrows).

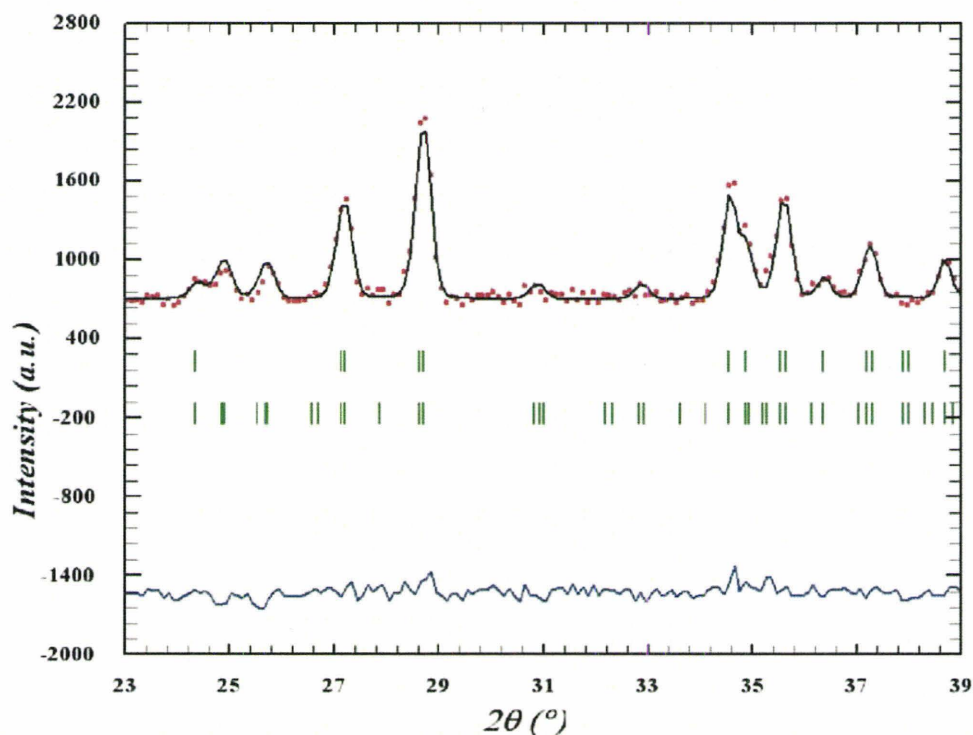


Figure 3.9. Rietveld refinement of the low angle powder neutron diffraction data for  $\text{La}_5\text{Re}_3\text{CoO}_{16}$  at 5 K. The red circles are the experimental data; the black line is the calculated pattern; the top green tick marks denote the structural Bragg reflections; the bottom green tick marks are the magnetic Bragg reflections and the blue line is the difference plot. Only the crystal structure was refined, the magnetic structure was simulated as described in the text.

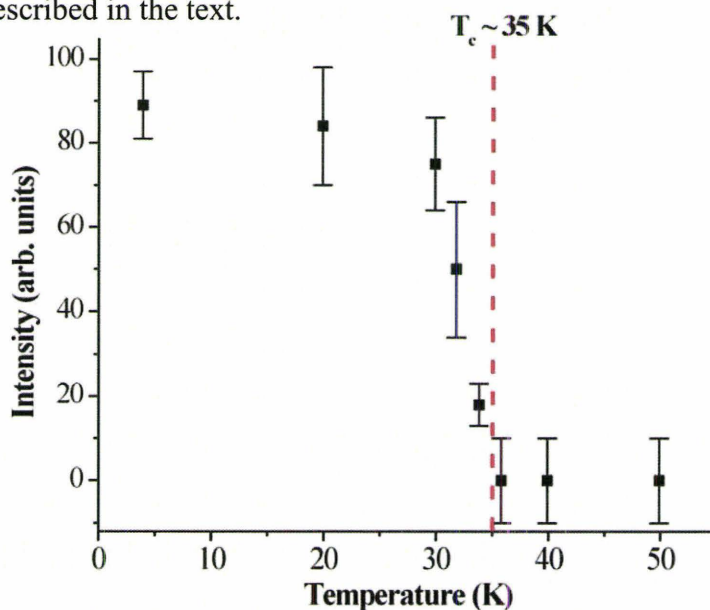


Figure 3.10. Temperature dependence of the magnetic peak indexed as  $(1-1\ 1/2) / (1\ 1\ 1/2)$  in  $\text{La}_5\text{Re}_3\text{CoO}_{16}$  indicating the critical temperature of  $\sim 35$  K.

*b. La<sub>5</sub>Re<sub>3</sub>NiO<sub>16</sub>*

Zero field cooled (ZFC) and field cooled (FC) magnetic susceptibility measurements at fields of 0.05 T, 2.0 T and 5.0 T are plotted in Figure 3.11. The data collected at the lowest field ranges from 5-300 K, whereas the 2.0 T and 5.0 T data sets were collected from 2-200 K. At 0.05 T, the ZFC and FC curves begin to diverge at approximately 40 K. There are two prominent cusps below this temperature, centred at 38 K and 14 K, respectively, which are indicative of magnetic ordering. As the peak at 38 K is suppressed in the field cooled data, the cusp at 14 K is attributed to the onset of relatively long-range antiferromagnetic order. This is in contrast to the previously reported  $T_c$  of 36 K for La<sub>5</sub>Re<sub>3</sub>NiO<sub>16</sub>.<sup>6</sup> A plot of  $\chi T$  versus T is shown in Figure 3.12 with the Fisher heat capacity included in the inset. Similar to the case with the Co phase, a sharp upturn is seen below 50 K with a maximum at 36 K and a clear inflection point at 14 K. However, the broad maxima above 50 K seen in the Co data are absent. These observations are consistent with short range ferro- or ferromagnetic order. Here again the horizontal line on the graph is the sum of the calculated spin only Curie constants for Re<sup>5+</sup> ( $S = 1$ ;  $C_{SO} = 1.00$  emu·K/mol) and Ni<sup>2+</sup> ( $S = 1$ ;  $C_{SO} = 1.00$  emu·K/mol). For La<sub>5</sub>Re<sub>3</sub>NiO<sub>16</sub>, even at 300 K, the value of  $\chi T$  does not reach this line.

When the field is increased to 2.0 T, the divergence between the two curves moves to lower temperature (7 K), and the peak associated with long-range order broadens and moves to lower temperature (6 K) as well. By 5.0 T, there is no longer a divergence between the ZFC and FC curves and the signal suggests ferro- or ferrimagnetic ordering of the moments in the perovskite layers. Again, as with the Co

analogue, it appears that the interplanar coupling is relatively weak and can be overcome with laboratory magnetic fields. However, the supposed “saturation moment” obtained from the 5.0 T data is about  $0.9(1) \mu_B$ , which is much lower than the value calculated for ferromagnetically coupled  $\text{Re}^{5+}$  ( $S = 1$ ) and  $\text{Ni}^{2+}$  ( $S = 1$ ) layers ( $4.0 \mu_B$ ), but of course, much larger than the  $\sim 0 \mu_B$  expected for ferrimagnetic coupling. This suggests that  $\text{La}_5\text{Re}_3\text{NiO}_{16}$  has not reached saturation at this field. This compound may have unique magnetic properties, such as a much higher anisotropy field than seen in the other isostructural pillared perovskites.

Magnetization curves were collected from 0-5.0 T at temperatures of 2 K, 12 K, 30 K, 42 K and 100 K and are pictured in Figure 3.13. The 2 K data show a large hysteresis (which persists up to 30 K) but virtually no remnant magnetization. Unlike the Co compound, there are no sharp increases in the magnetization, but rather a smooth *S*-shaped curve, with an inflection point at about 1.5 T. This may be indicative of a metamagnetic transition as in the Co phase, albeit with a much higher critical field. Also, the curve does not reach saturation at 5.0 T. The 12 K magnetization curve maintains the *S*-shape, however by 30 K, the data are linear, indicating paramagnetism, and corroborating the assignment of  $T_c$  as 14 K.

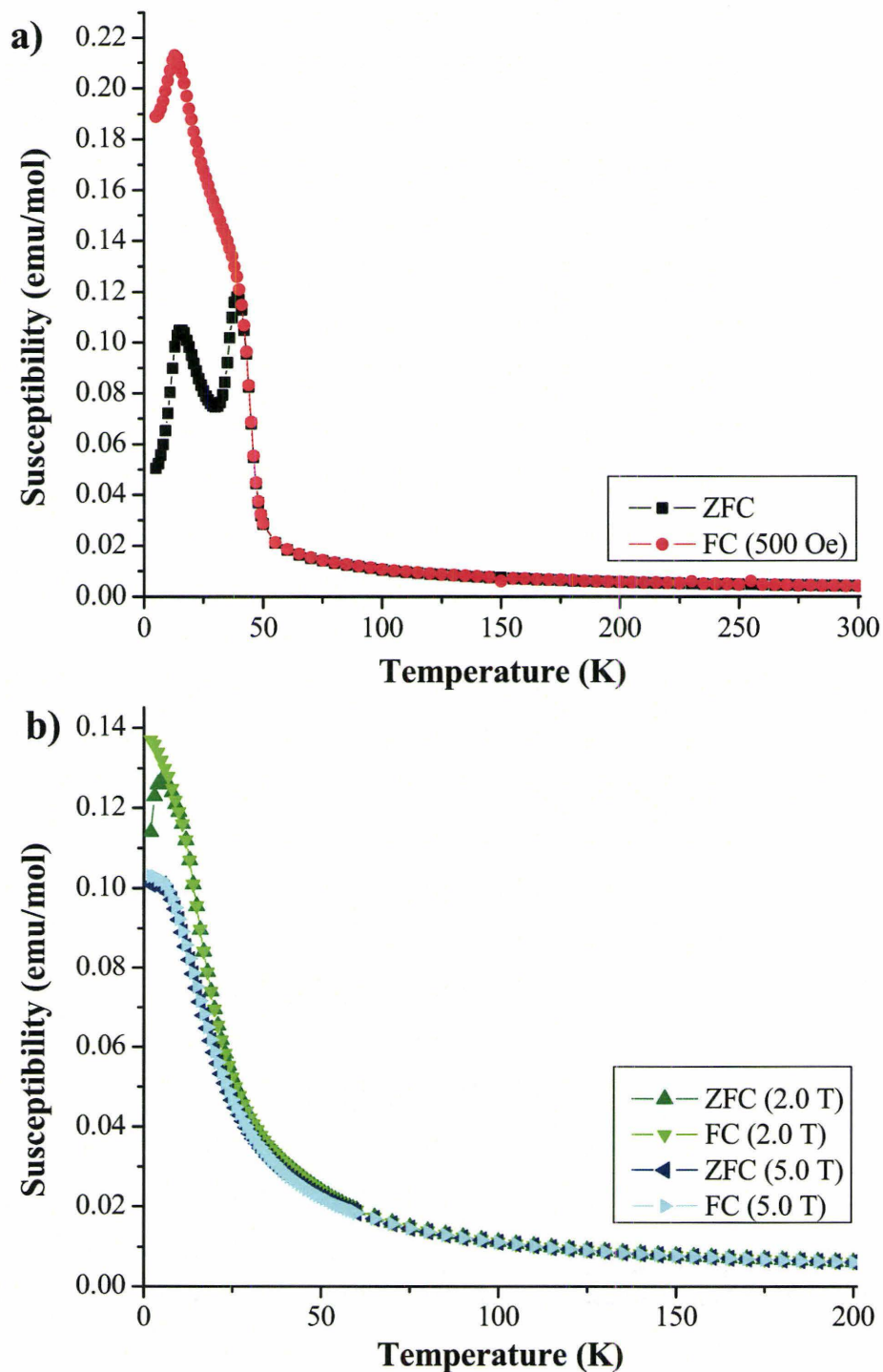


Figure 3.11. ZFC (darker shade) and FC (lighter shade) magnetic susceptibility measurements of  $\text{La}_5\text{Re}_3\text{NiO}_{16}$  with applied fields of a) 0.05 T (red) and b) 2.0 T (green) and 5.0 T (blue).

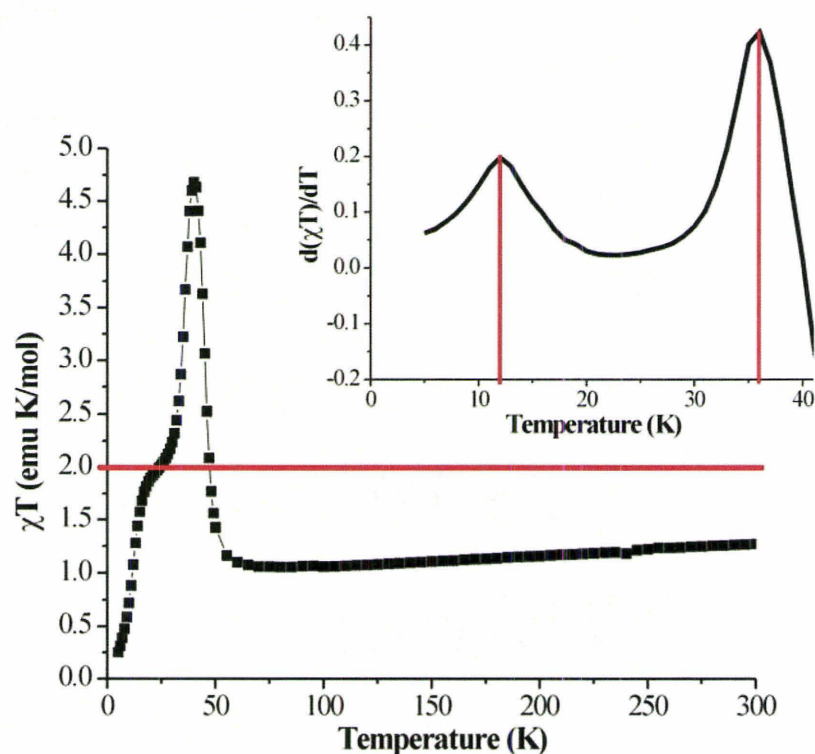


Figure 3.12.  $\chi T$  versus  $T$  plot of  $\text{La}_5\text{Re}_3\text{NiO}_{16}$  using the ZFC data only. The horizontal line is the sum of the calculated spin only Curie constants for  $\text{Re}^{5+}$  ( $S = 1$ ;  $C_{\text{SO}} = 1.00$  emu·K/mol) and  $\text{Ni}^{2+}$  ( $S = 1$ ;  $C_{\text{SO}} = 1.00$  emu·K/mol). Inset - Fisher heat capacity of  $\text{La}_5\text{Re}_3\text{NiO}_{16}$  calculated using the ZFC magnetic susceptibility data. The vertical line denotes the peak centres.

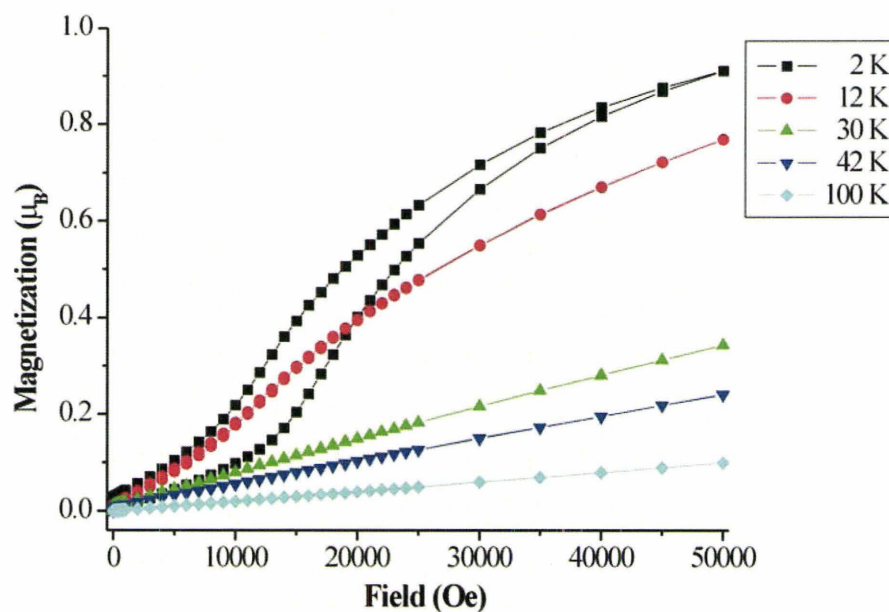


Figure 3.13. Isothermal magnetization versus applied field data for  $\text{La}_5\text{Re}_3\text{NiO}_{16}$ .

Heat capacity measurements on  $\text{La}_5\text{Re}_3\text{NiO}_{16}$  were also collected from about 5-50 K, with no field applied and in a 7.0 T field. The two data sets, along with the heat capacity of the lattice match compound,  $\text{La}_5\text{Re}_2\text{TaMgO}_{16}$  are shown in Figure 3.14. After subtraction of the lattice component, the heat capacity of  $\text{La}_5\text{Re}_3\text{NiO}_{16}$  pictured in Figure 3.15 shows one small anomaly present with a maximum near 12 K. The shape of the 12K feature is not lambda-like, but relatively symmetric, suggesting that the magnetic ordering present in this compound has a finite correlation length. Due to instrument restrictions, it was not possible to collect heat capacity data below 5 K, which may have clarified the peak shape. The unusual peak shape notwithstanding, smooth transient data collected on this compound demonstrates that it has good overall thermal contact, despite not being a single crystal or a dense pellet. Heat capacity data were also collected on a mixture of  $\text{La}_5\text{Re}_3\text{NiO}_{16}$  and metallic silver powder (25 % by weight) in an effort to improve the thermal contact. The shape and position of the anomaly remained unchanged. However, the temperature of the peak centre agrees well with the estimate of  $T_c$  for this compound from the magnetic susceptibility and magnetization data. The Fisher heat capacity of  $\text{La}_5\text{Re}_3\text{NiO}_{16}$  is displayed in Figure 3.12 (inset) showing two peaks at about 12 and 36 K. Interestingly, the peak at 12 K is again relatively symmetric in shape, although data were not collected below 5 K. There are no other features in the thermally derived heat capacity of  $\text{La}_5\text{Re}_3\text{NiO}_{16}$  at higher temperatures (for example, at 38 K), indicating the assignment of  $T_c$  as 14 K is correct. This contrasts with the assignment of  $T_c$  as 36 K for this compound reported previously.<sup>6</sup>

Application of a 7.0 T field appears to decrease the height of the anomaly, broaden it significantly and shift the peak maximum. The strong field dependence of this feature suggests that the transition to long-range magnetic order involves a relatively weak coupling (i.e. interlayer). Integration of  $C_{mol}/T$  with respect to temperature leads to a change of entropy of 3.68 J/K·mol for  $\text{La}_5\text{Re}_3\text{NiO}_{16}$ . This is comparable to the value obtained for  $\text{La}_5\text{Re}_3\text{CoO}_{16}$ . The calculated entropy for this compound, with  $\text{Re}^{5+}$  moments ( $S = 1$ ) and  $\text{Ni}^{2+}$  moments ( $S = 1$ ) is 18.27 J/K·mol, which is considerably higher than the experimental value. Again, as with the Co compound, most of the entropy is removed due to short range intraplanar correlations prior to the onset of relatively long-range three dimensional magnetic order.

Low temperature powder neutron diffraction measurements were taken to determine the magnetic structure of  $\text{La}_5\text{Re}_3\text{NiO}_{16}$ , and the diffraction data at 4 K and 50 K are plotted in Figure 3.16. Unlike the Co compound, there is only one very weak, new magnetic Bragg peak at very low angle ( $6.5^\circ 2\theta$ ). This reflection can also be indexed to a magnetic unit cell with ordering vector,  $\mathbf{k} = (0\ 0\ 1/2)$ . However, the peak index is  $(0\ 0\ 1/2)$ , which indicates that the moments within the layer are not oriented parallel to the  $c$ -axis, unlike most of the other members of the pillared perovskite family studied to date. An exception is  $\text{La}_5\text{Re}_3\text{MnO}_{16}$ , where the Mn moments are canted  $\sim 18^\circ$  with respect to the  $c$ -axis.<sup>5</sup> In addition, no magnetic reflections of indices  $(k\ h\ 1/2)$  and  $(h\ k\ 3/2)$ , ubiquitous at higher angles in the magnetic neutron diffraction patterns of the other phases, are present in the Ni data. These reflections are diagnostic of intraplanar ferrimagnetic correlations.

Attempts to refine the magnetic neutron diffraction data were hampered due to background problems, the paucity of data and the same high level of correlation between the Re and Ni moments as encountered for the Co compound. However, a plausible magnetic structure model, guided by simulations, was found and is pictured in Figure 3.17. In all models tested, the intralayer coupling was ferromagnetic and the interlayer coupling was antiferromagnetic along the  $c$  direction and with the moments inclined away from the  $c$ -axis, as dictated by the details of the diffraction pattern. Due to the aforementioned correlation problem, the moments of the two magnetic ions,  $\text{Re}^{5+}$  ( $S = 1$ ) and  $\text{Ni}^{2+}$  ( $S = 1$ ), were fixed at  $1.5 \mu_{\text{B}}$  and  $1.8 \mu_{\text{B}}$ , respectively, which are close to the spin only moments for each ion. Then, the projection angles of the net moment with respect to the crystallographic axes were varied. The best fit, determined by monitoring  $R_{\text{mag}}$ , was obtained when the net moment was canted  $30(3)^\circ$  away from the  $c$ -axis with a projection of  $45(5)^\circ$  in the  $ab$  plane. Not surprisingly, results were less sensitive to the  $ab$  plane angle. Of course, given the constraints, this is not a unique solution. Information from single crystal magnetization studies would be needed to fix the canting angles and the net moment values.

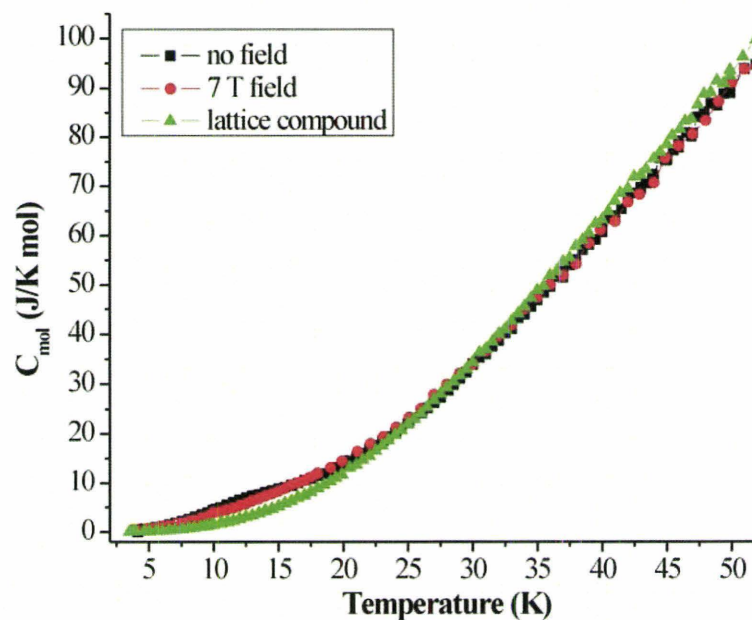


Figure 3.14. Heat capacity measurements of  $\text{La}_5\text{Re}_3\text{NiO}_{16}$  in zero applied field (black squares) and in a 7.0 T field (red circles). The heat capacity measured for the non-magnetic lattice match compound is denoted by green triangles.

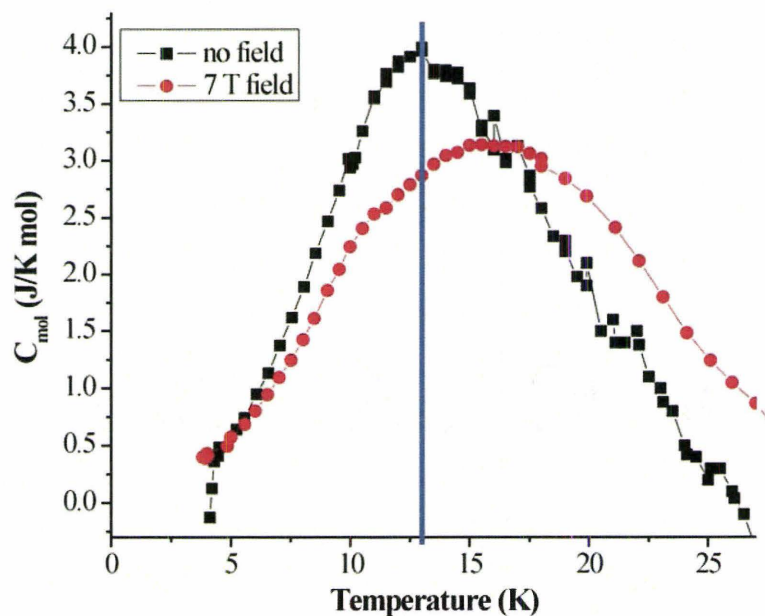


Figure 3.15. Magnetic component of the heat capacity of  $\text{La}_5\text{Re}_3\text{NiO}_{16}$ , in zero field (black squares) and in a 7 T field (red circles). The blue line denotes the peak centre.

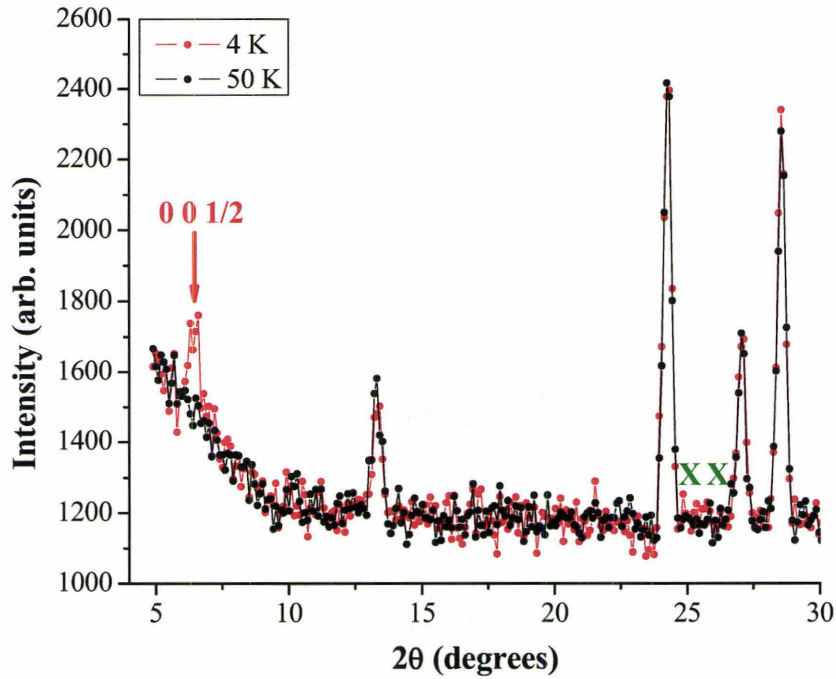


Figure 3.16. Powder neutron diffraction patterns of  $\text{La}_5\text{Re}_3\text{NiO}_{16}$  at 4 K (red circles) and 50 K (black circles). The peak marked with an arrow is the new magnetic Bragg reflection, indexed accordingly. Note the absence of reflections of the type  $(+/-1 +/-1 1/2)$  and  $(+/-1 +/-1 3/2)$  – (green 'X's).

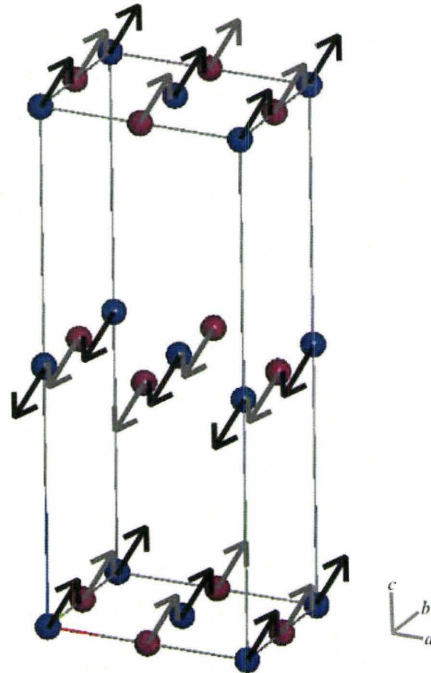


Fig. 3.17. Possible magnetic structure of  $\text{La}_5\text{Re}_3\text{NiO}_{16}$ , showing the moments on the Re atoms (blue spheres, black arrows) and Ni atoms (purple spheres, grey arrows).

### 3.5 Summary and Conclusions

Detailed magnetic property studies on two isostructural pillared perovskites,  $\text{La}_5\text{Re}_3\text{CoO}_{16}$  and  $\text{La}_5\text{Re}_3\text{NiO}_{16}$ , has revealed some unique and unexpected results. As with the other members of this family, both compounds show evidence of three dimensional magnetic order from SQUID magnetometry, powder neutron diffraction and heat capacity measurements, despite an interplanar separation of over 10 Å. From these studies it is now possible to assign a  $T_c$  of 14 K for the  $\text{La}_5\text{Re}_3\text{NiO}_{16}$  compound and  $T_c \sim 35$  K for the Co phase. In addition, the appearance of the heat capacity peaks differs between the two compounds.  $\text{La}_5\text{Re}_3\text{CoO}_{16}$  shows a more typical, asymmetric lambda shape (albeit somewhat broadened), while the peak shape for the Ni material is very broad and more symmetric. This suggests that the length scale for interplanar three dimensional order in the Ni phase is shorter than for the Co compound.

Both the magnetic susceptibility and the heat capacity are strongly affected by the application of relatively modest magnetic fields. Isothermal magnetization data indicate the presence of metamagnetic-like transitions at  $\sim 0.65$  T for  $\text{La}_5\text{Re}_3\text{CoO}_{16}$  and  $\sim 1.5$  T for  $\text{La}_5\text{Re}_3\text{NiO}_{16}$ . As well, the magnetic anisotropy appears to be much stronger in the Ni phase as evidenced by a lack of saturation even in fields up to 5.0 T. The onset of metamagnetism at such low applied fields is taken as evidence for relatively weak interplanar exchange coupling.

Powder neutron diffraction measurements showed that the Co series member has a magnetic structure similar to  $\text{La}_5\text{Re}_3\text{MnO}_{16}$  and  $\text{La}_5\text{Re}_3\text{FeO}_{16}$ .<sup>5</sup> The  $\text{Re}^{5+}$  and  $M^{2+}$

moments within the layers are coupled ferrimagnetically, and the layers are coupled antiferromagnetically.

In contrast, the magnetic structure of  $\text{La}_5\text{Re}_3\text{NiO}_{16}$  is unique among the pillared perovskites. Within the layers, the two moments are ordered ferromagnetically, angled  $45^\circ$  in the  $ab$  plane and canted  $30^\circ$  away from the  $c$ -axis. The layers are then coupled antiferromagnetically.

At this stage it is useful to review the known magnetic properties of the  $\text{La}_5\text{Re}_3\text{MO}_{16}$  series. In Table 3.2, a slightly revised version of a table of collected magnetic data (Table 7 from Chi *et. al.*<sup>6</sup>) is presented.

Table 3.2. Magnetic Data for the  $\text{La}_5\text{Re}_3\text{MO}_{16}$  Series. The values in square parentheses are from Chi *et. al.*<sup>6</sup>.

$M$	$\theta$ (K)	$T_c$ (K)	$T_c/S^2$ (K)	$C_{\text{expt}}$ (emu·K/mol)	$C_{\text{so}}^a$ (emu·K/mol)
Mn	[-48(5)]	[161]	[26]	[4.43(4)]	5.38
Fe	[-84(4)]	[155]	[39]	[3.60(2)]	4.00
Co	[-71.2(5)]	35 [33]	16 [15]	[3.578(3)]	2.87
Ni	-74(4) [-217(3)]	14 [36, 14]	14 [36]	1.49(2) [2.29(1)]	2.00
Mg	-424(28) [-575(12)]	-	-	0.81(5) [1.00(1)]	1.00

<sup>a</sup>The Curie constant based on the spin-only model.

In particular, the value for  $T_c$  of the  $M = \text{Ni}$  compound is modified in light of these new results and new Curie-Weiss fits were made for the  $M = \text{Ni}$  and  $\text{Mg}$  phases. The revision of the  $T_c$  value for the  $\text{Ni}$  phase results in the existence of two categories of materials in terms of the  $T_c/S^2$  value (column 3, Table 3.2). Both  $\text{Mn}$  and  $\text{Fe}$  show relatively large values, around 30, while this ratio is halved for  $\text{Co}$  and  $\text{Ni}$ . The  $T_c/S^2$  ratio

is, within the mean field approximation, proportional to the product of  $J_{\text{inter}}$  (the intraplanar exchange coupling) and  $(\zeta_{\text{intra}})^2$ , the square of the intraplanar correlation length.<sup>9</sup> However, the two contributions cannot be separated without an independent measurement.

In addition, after re-examining the data for the  $M = \text{Mg}$  and  $\text{Ni}$  phases, it was noted that the  $\chi^{-1}$  vs  $T$  plots were not linear throughout the temperature range 300K – 600K. In such cases, an ambiguity arises concerning the fitting procedure. For example, in the previous study<sup>6</sup>, only high temperature data which appeared to be linear over a limited range were fit to the Curie-Weiss law. Alternatively, a fit can be made using a wider temperature range by including a TIP term (arising, presumably, from van Vleck type contributions) to account for the curvature. The results from the latter approach are listed in Table 3.2 along with the previous values in square brackets.

As expected, the values for the Curie constant ( $C$ ) and the Weiss temperature ( $\theta$ ) are somewhat reduced from those reported previously, but are not unreasonable. The  $M = \text{Mg}$  compound is key here as only  $\text{Re} - \text{Re}$  exchange is involved. Note that  $\theta$ , which is the weighted, algebraic sum of all of the magnetic exchange pathways, is very large and negative ( $\sim -400$  to  $-600$  K) for this phase, regardless of the fitting method used. For  $M^{2+} = \text{Mn}, \text{Fe}, \text{Co}$  and  $\text{Ni}$ , the  $\theta$  values are much less negative. This implies that at least some of the  $\text{Re}-M$  magnetic interactions are ferromagnetic, which is consistent with the Goodenough-Kanamori rules for magnetic superexchange.<sup>10, 11</sup>  $\text{Re}^{5+}$  has only  $t_{2g}$  electrons while all of the  $M^{2+}$  cations have half-occupied  $e_g$  levels. Magnetic exchange from half-filled  $e_g$  (on  $M^{2+}$ ) to empty  $e_g$  (on  $\text{Re}^{5+}$ ) should always be ferromagnetic. Thus, one might

normally expect to find the magnetic structure seen for the  $\text{La}_5\text{Re}_3\text{NiO}_{16}$  material with ferromagnetic intralayer correlations. However, somehow, the magnetic ground state that results in the majority of cases shows overall ferrimagnetic order within the planes. It is fair to say that the origin of the magnetic structures observed for these Re-based pillared perovskites is not well understood and a deeper analysis is called for.

#### *Acknowledgements*

The authors wish to thank the Natural Sciences and Engineering Research Council (NSERC) of Canada for a Doctoral Postgraduate Scholarship (HLC) and for a research grant (JEG). We also thank Dr. Paul Dube and Dr. Graeme Luke for their assistance and use of instruments in the magnetic and heat capacity measurements.

#### **3.6 References**

1. Ledesert, M.; Labbe, P.; McCarroll, W. H.; Leligny, H.; Raveau, B., *J. Solid State Chem.* **1993**, *105*, 143-150.
2. Ramanujachary, K. V.; Greenblatt, M.; McCarroll, W. H.; Goodenough, J. B., *Mat. Res. Bull.* **1993**, *28*, 1257-1267.
3. Ramanujachary, K. V.; Lofland, S. E.; McCarroll, W. H.; Emge, T. J.; Greenblatt, M., *J. Solid State Chem.* **2002**, *164*, 60-70.
4. Wiebe, C. R.; Gourrier, A.; Langet, T.; Britten, J. F.; Greedan, J. E., *J. Solid State Chem.* **2000**, *151*, 31-39.
5. Green, A. E. C.; Wiebe, C. R.; Greedan, J. E., *Solid State Sciences* **2002**, *4*, 305-310.
6. Chi, L.; Green, A. E. C.; Hammond, R.; Wiebe, C. R.; Greedan, J. E., *J. Solid State Chem.* **2003**, *170*, 165-175.
7. Chi, L.; Swainson, I. P.; Greedan, J. E., *J. Solid State Chem.* **2004**, *177*, 3086-3091.
8. Roisnel, T.; Rodriguez-Carvajal, J. *FULLPROF*, April 2005.
9. de Jongh, L. J., In *Magnetic Properties of Layered Transition Metal Compounds*, de Jongh, L. J., Ed. Kluwer Academic Publishers: Dordrecht, 1990; p 19.
10. Goodenough, J. B., *Magnetism and the Chemical Bond*. Wiley: New York, 1963.
11. Kanamori, J., *J. Phys. Chem. Solids* **1959**, *10*, 87-98.

## Chapter 4

### **Synthesis, Structure and Magnetic Properties of the Pillared Perovskites, $\text{La}_5\text{Re}_{3-x}\text{Ta}_x\text{BO}_{16}$ ( $B = \text{Mn, Fe, Co, Ni}$ )**

This chapter describes the synthesis, structural characterization and magnetic properties of the series of compounds,  $\text{La}_5\text{Re}_{3-x}\text{Ta}_x\text{BO}_{16}$  ( $B = \text{Mn, Fe, Co, Ni}$ ) that was performed by the candidate. Steve Kuprich and Fred Pearson of the Canadian Centre for Electron Microscopy (CCEM) at McMaster University performed the SEM-EDS and TEM-EDS measurements, respectively, to investigate the question of  $\text{Ta}^{5+}$  substitution in greater detail. High field magnetization measurements (up to 14.0 T) on two compounds were performed by Van Griffin and Jan Jaroszynski at the National High Magnetic Field Laboratory in Gainesville, Florida using a Vibrating Sample Magnetometer. Dr. Paul Dube assisted with the heat capacity measurements, and Lachlan Cranswick and Ian Swainson aided with powder neutron diffraction data collection.

#### 4.1 Abstract

The synthesis of a new family of pillared perovskites was accomplished and the resulting materials magnetically characterized by SQUID magnetometry, heat capacity and variable temperature powder neutron diffraction. The general formula has been determined to be  $\text{La}_5\text{Re}_2\text{Re}_{1-x}\text{Ta}_x\text{BO}_{16}$ , ( $B = \text{Mn, Fe, Co, Ni}$ ;  $x \sim 0.5$ ), and because of metal-metal bonding, the cations within the layers ( $\sim 50\% \text{Re}^{5+}/50\% \text{Ta}^{5+}$  and  $100\% B^{2+}$ ) are the only magnetic species present in the compound. Despite extensive optimization of the synthesis parameters, pure phase materials were not obtained. Hence, further experimental characterization was accomplished on samples with secondary phases (many of which were non-magnetic). SEM-EDS and TEM-EDS were used to determine the approximate amount of Ta substitution. Subsequent synthesis and characterization of the analogous compound,  $\text{La}_5\text{Re}_{3-x}\text{Nb}_x\text{MnO}_{16}$ , also confirmed the degree of substitution of a non-magnetic  $5+$  ion to be about 50%. Long-range magnetic ordering occurs in all synthesized compounds, with critical temperatures of 160 K (Mn), 135 K (Fe), 32 K (Co) and 12 K (Ni), respectively, which are all very similar to the ordering temperatures of the  $\text{La}_5\text{Re}_3\text{BO}_{16}$  ( $B = \text{Mn, Fe, Co, Ni}$ ) series.<sup>1-4</sup> Heat capacity measurements of the Co and Ni members confirm the ordering temperatures. From neutron diffraction, the magnetic structure of compounds involving Mn, Fe and Co appears to consist of ferrimagnetically coupled moments aligned along the  $c$ -axis within the perovskite layers, which are then coupled antiferromagnetically. The Ni series member has a similar structure, however, the moments in the layers are oriented perpendicular to the  $c$ -axis. These magnetic structures are also consistent with their  $\text{La}_5\text{Re}_3\text{BO}_{16}$  ( $B = \text{Mn, Fe, Co, Ni}$ ) counterparts,

and suggest that the relatively weaker interplanar magnetic coupling through the diamagnetic ‘pillar’ is vital to the overall magnetism of these compounds.

## 4.2 Introduction

The “pillared perovskites” are a relatively new and magnetically interesting family of compounds due to their unique layered structure. The general formula is  $\text{Ln}_5\text{D}_2\text{ABO}_{16}$ , where Ln is a lanthanide ion; *A* and *D* are transition metals, typically from the *4d* or *5d* series and *B* is a *3d* (or *4d*) transition element. The unit cell is pictured in Figure 4.1. Perovskite-like layers of site ordered, corner-shared  $\text{AO}_6$  and  $\text{BO}_6$  octahedra are separated by  $\text{D}_2\text{O}_{10}$  dimer “pillars” that consist of two edge-shared octahedra. The layers are about 10 Å apart, and the dimers share corners with only the *B*-site octahedra. The lanthanide ions are also found between the layers. The pillared perovskite is a relatively robust structure type, as oxides of molybdenum,  $\text{La}_5\text{Mo}_{4-x}\text{B}_x\text{O}_{16}$  ( $x = 0$  and  $x \sim 0.7$  for  $B = \text{Mn, Fe, Co, Ni, Mg}$ )<sup>5-7</sup>, rhenium,  $\text{La}_5\text{Re}_3\text{BO}_{16}$  ( $B = \text{Mn, Fe, Co, Ni, Mg}$ )<sup>14</sup>, and osmium,  $\text{La}_5\text{Os}_3\text{MnO}_{16}$ <sup>8</sup> are all known.

These compounds exhibit some unusual and unexpected magnetic properties. Multiple metal-metal bonding between the *4d* or *5d* transition metals within the dimeric “pillars” pairs all the electrons and, thus, these units are diamagnetic. Consequently, the magnetic ions are constrained to the perovskite layers. Due to site ordering of the *A* and *B* ions within these layers, local moment behaviour is observed with nearly spin-only values. Despite the 10 Å separation between layers, long-range magnetic order is often present in the pillared perovskites, with critical temperatures ( $T_c$ ) as high as 180 K.<sup>6</sup>

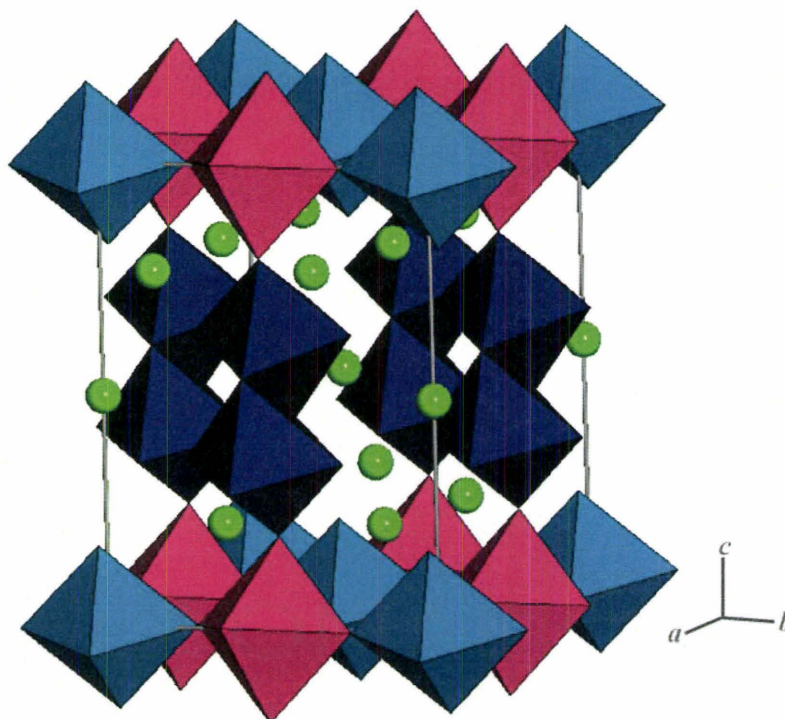


Figure 4.1. Crystal structure of a “pillared perovskite”,  $\text{La}_5\text{Re}_{3-x}\text{Ta}_x\text{BO}_{16}$ . The  $\text{La}^{3+}$  ions are green spheres; the  $\text{Re}_2\text{O}_{10}$  dimer “pillar” is in dark blue; the ordered Ta and B cations are the light blue and pink octahedra, respectively, with oxygens located at the corners.

Examination of the rhenium-based family,  $\text{La}_5\text{Re}_3\text{BO}_{16}$  ( $B = \text{Mn, Fe, Co, Ni, Mg}$ ), in greater detail reveals some interesting trends. Some key magnetic data for these compounds appear in Table 4.1, which would be useful to review. Within the perovskite layers, there are two magnetic ions,  $\text{Re}^{5+}$  ( $S = 1$ ) and  $B^{2+}$  ( $S = 5/2 - 0$ , depending on  $B$ ). The critical temperature ( $T_c$ ) for long-range magnetic order decreases as the spin quantum number ( $S$ ) of the  $B^{2+}$  ion decreases, until  $S = 0$  (Mg) where no long-range order is evident.<sup>3</sup> According to mean field theory for layered compounds,  $T_c$  is related to the intraplanar correlation length ( $\xi_{\text{intra}}$ ), the interplanar exchange coupling ( $J_{\text{inter}}$ ) and the spin quantum number ( $S$ ):<sup>9</sup>

$$T_c \sim \xi_{\text{intra}} J_{\text{inter}} S^2/k \quad 4.1$$

When the  $S^2$  dependence is divided out for these compounds, there is no obvious trend, but rather two categories of materials emerge. Both the Mn and Fe members have  $T_c/S^2$  values of about 30, while for the Co and Ni compounds,  $T_c/S^2$  is roughly half of that amount.

Table 4.1. Magnetic Data for the  $\text{La}_5\text{Re}_3\text{BO}_{16}$  Series.<sup>3,4</sup>

$B$	$\theta$ (K)	$T_c$ (K)	$T_c/S^2$ (K)	$C_{\text{expt}}$ (emu·K/mol)	$C_{\text{so}}^a$ (emu·K/mol)
Mn	-48(5)	161	26	4.43(4)	5.38
Fe	-84(4)	155	39	3.60(2)	4.00
Co	-71.2(5)	35	16	3.578(3)	2.87
Ni	-74(4)	14	14	1.49(2)	2.00
Mg	-424(28)	-	-	0.81(5)	1.00

<sup>a</sup>The Curie constant based on the spin-only model.

Another interesting feature of the rhenium-based pillared perovskites is their long-range ordered magnetic structures, as elucidated by powder neutron diffraction. For Mn, Fe and Co, the magnetic structure consists of ferrimagnetically coupled layers, which are then coupled antiferromagnetically.<sup>2,4</sup> In contrast, in the Ni compound, moments within the layers are coupled ferromagnetically, and the layers themselves are coupled antiferromagnetically.<sup>4</sup> Application of the Goodenough-Kanamori rules for magnetic superexchange predict predominantly ferromagnetic  $\text{Re}^{5+} - B^{2+}$  couplings.<sup>10,11</sup> Magnetic exchange involving transfer from a half-filled  $e_g$  level (as is the case for  $\text{Mn}^{2+}$ ,  $\text{Fe}^{2+}$ ,  $\text{Co}^{2+}$  and  $\text{Ni}^{2+}$ ) to an empty  $e_g$  level (as in  $\text{Re}^{5+}$ ) should always be ferromagnetic. As a result, it is surprising that ferrimagnetic intralayer coupling dominates for most of this series of compounds.

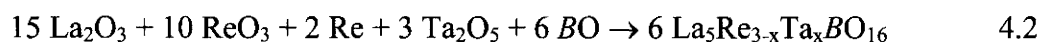
The current investigation expands on the family of known pillared perovskites through substitution on the *A* site of  $\text{La}_5\text{Re}_3\text{BO}_{16}$ . The initial goal was to completely replace  $\text{Re}^{5+}$  ( $S = 1$ ) within the perovskite layers with non-magnetic  $\text{Ta}^{5+}$  ions. Since  $\text{Ta}^{5+}$  has no electrons for metal-metal bonding, the  $\text{Re}^{5+}$  preferentially occupies the dimer sites. This exchange would further dilute the low-dimensional magnetic system, leaving the  $B^{2+}$  ion as the only magnetic site in the compound,  $\text{La}_5\text{Re}_{3-x}\text{Ta}_x\text{BO}_{16}$  ( $x = 1$ ). By varying the  $B^{2+}$  element from Mn ( $S = 5/2$ ) to Ni ( $S = 1$ ), the effect of the spin quantum number on the resulting magnetism could be studied by SQUID magnetometry, heat capacity and variable temperature powder neutron diffraction measurements. Further studies, including SEM-EDS and TEM-EDS as well as the synthesis and characterization of a

niobium analogue -  $\text{La}_5\text{Re}_{3-x}\text{Nb}_x\text{MnO}_{16}$ , were also undertaken in an attempt to discern to what extent the  $\text{Ta}^{5+}$  substituted within the structure.

### 4.3 Experimental

#### *Syntheses*

The compounds  $\text{La}_5\text{Re}_{3-x}\text{Ta}_x\text{BO}_{16}$  ( $x = 1$ ) were synthesized by solid state reaction, according to the following equation:



Stoichiometric amounts of the starting reagents,  $\text{La}_2\text{O}_3$  (99.9%, Aldrich),  $\text{ReO}_3$  (Rhenium Alloys), Re (Rhenium Alloys),  $\text{Ta}_2\text{O}_5$  (99.99%, CERAC) and either MnO (99.5%, Alfa), “FeO”, CoO (99.99%, Aldrich), NiO (99.995%, CERAC) or MgO were accurately weighed, ground together, and pressed into a pellet. The  $\text{La}_2\text{O}_3$  was fired at  $900^\circ\text{C}$  overnight before use. The “FeO” was prepared by heating a mixture of  $\text{Fe}_2\text{O}_3$  and Fe at  $900^\circ\text{C}$  for 12 hours. An excess of Fe was used in the final product synthesis due to the well-known nonstoichiometry of FeO.<sup>12</sup> Each sample pellet was placed into a platinum crucible, which was sealed in a quartz tube under vacuum ( $\sim 10^{-5}$  torr) and heated according to a specific temperature program in a tube furnace. The products obtained were all dark grey-black powders.

#### *Powder X-ray and Neutron Diffraction Data*

X-ray diffraction data were collected using a Guinier-Hagg camera with  $\text{CuK}\alpha_1$  radiation ( $\lambda = 1.5406 \text{ \AA}$ ) and high-purity silicon powder as an internal reference. The

reflections were recorded on photographic film and converted to digital form using the KEJ LS20 line scanner.

Variable temperature powder neutron diffraction measurements were performed on the C2 diffractometer at the Canadian Neutron Beam Centre at Chalk River. The crystal structure data (285 K) were collected at a wavelength of 1.32917 Å in the angular range of  $12^\circ \leq 2\theta \leq 113^\circ$  with 0.1° steps. Similarly, the magnetic structure data (4 K and above) were measured at a longer wavelength of 2.36957 Å in the range  $5^\circ \leq 2\theta \leq 85^\circ$  with 0.1° intervals.

#### *SEM-EDS*

Images were acquired using the Philips SEM 515 at the Canadian Centre for Electron Microscopy at McMaster University, equipped with a LaB<sub>6</sub> electron gun. The system was calibrated such that the measurement bars that appear with the images are accurate. Energy dispersive X-ray spectroscopy (EDS) was collected using the Link Systems Pentafet X-ray microanalyser with a resolution of 143 eV at 5.9 keV. No standards (other than those used to calibrate the system) were used to quantify the spectra obtained. The pure phase sample La<sub>5</sub>Re<sub>3</sub>NiO<sub>16</sub> was used as an external standard.

#### *TEM-EDS*

Rectangular images in real and reciprocal space were collected using the JEOL-2010F-FEG TEM/STEM system at the Canadian Centre for Electron Microscopy at McMaster University, equipped with a Roper Scientific DualView camera. A variety of camera lengths were used, all calibrated with respect to the measurement bar that appears with the image. High resolution data were collected using the Gatan GIF 2K CCD

camera. Energy dispersive X-ray spectroscopy (EDS) analysis was accomplished using the Oxford INCA Semi-Quantitative Analysis Suite. No standards (other than those used to calibrate the system) were used to quantify the spectra obtained. The pure phase sample  $\text{La}_5\text{Re}_3\text{NiO}_{16}$  was used as an external standard.

#### *Magnetic Data*

Magnetic measurements were collected using the Quantum Design SQUID magnetometer. Zero field cooled and field cooled (ZFC/FC) magnetic susceptibility data from 5 – 300 K and isothermal magnetization measurements from 0 – 5.0 T were recorded on powder samples encased in gelatin capsules. High temperature measurements (300 – 500 K) were collected using an oven insert and quartz sample holders. Diamagnetic corrections were applied to the data, using Pascal's constants<sup>13</sup> for the individual ions involved. For  $\text{Re}^{5+}$ ,  $22 \times 10^{-6}$  emu/mol was used, which is an intermediate value between  $\text{Re}^{4+}$  and  $\text{Re}^{6+}$ .

#### *Heat Capacity Data*

Heat capacity data were measured from 2 K (for  $\text{La}_5\text{Re}_{3-x}\text{Ta}_x\text{NiO}_{16}$ ) or 10 K (for  $\text{La}_5\text{Re}_{3-x}\text{Ta}_x\text{CoO}_{16}$ ) to 50 K with no applied field and in a 9.0 T field using the heat capacity probe in the Oxford MagLab EXA at McMaster University. A suitable block for analysis was prepared by repressing and resintering a portion of the previously synthesized product. Sample integrity was verified by powder X-ray diffraction (Guinier). The sample was mounted onto a sapphire measurement chip with Apiezon grease. Contributions to the measured heat capacity by the grease and sample chip were accounted for by the software.

## 4.4 Results and Discussion

### *Structural Characterization*

The structure of the title compounds was first verified by X-ray diffraction (Guinier camera). As this series of pillared perovskites should be isostructural with the previous rhenium compounds, direct comparison of the two patterns confirmed the presence of the desired phase for an initial firing program of 1100°C for 48 hours. A few relatively weak extra lines were detected, indicating the presence of one or more additional phases. More rigorous structural analysis was carried out using powder neutron diffraction data, collected at the Canadian Neutron Beam Centre (CNBC) in Chalk River. One secondary phase that appeared to be present in the  $\text{La}_5\text{Re}_{3-x}\text{Ta}_x\text{BO}_{16}$  series of compounds was tentatively identified as  $\text{La}_3\text{TaO}_7$ , which remained even after regrinding and refiring. As  $\text{La}_3\text{TaO}_7$  is non-magnetic, it would not interfere with bulk magnetic measurements, or magnetic structure determination.

However, the diffraction data for the series did contain additional peaks that could not be indexed to any known phase involving various combinations of the oxides involved. Increasing the reaction temperature to 1150°C resulted in the elimination of some secondary phase peaks, however, some reflections persisted (Figure 4.2). Further increasing the reaction temperature to 1200°C also eliminated some of the secondary phase peaks at lower angle. Similarly, as observed for the 1150°C sample, some reflections remained. In addition, refiring the compound at this temperature caused a significant increase in some of these extra reflections, indicating that the major pillared perovskite phase may not be very stable at high temperature.

Additional studies regarding the stability of the pillared perovskite phase showed that a longer firing time (96 hours versus 48 hours) did not improve sample purity. In fact, some secondary phase peaks were enhanced upon longer initial firing, as well as any subsequent refiring.

One additional attempt to obtain a pure phase sample was undertaken, assuming only 50% incorporation of tantalum in the starting reaction stoichiometry. The sample was prepared in an analogous way, fired to a maximum temperature of 1150°C for 48 hours. X-ray powder diffraction data of the final product did indicate the presence of a pillared perovskite phase (Figure 4.3), however, there were many other phases present in the sample. In fact, there were more phases with higher intensity reflections than in any of the previously synthesized samples. Some of these additional phases were not observed in the previous patterns, and none of them could be positively identified. Since this synthesis resulted in a pillared perovskite sample with even more and higher intensity secondary phase reflections in the X-ray diffraction pattern than previously observed, it was not pursued further.

Although a suitable model could not be found to account for these additional reflections in the powder neutron data, Rietveld refinement did result in reasonable values for the unit cell parameters and atomic positions for all members of the  $\text{La}_5\text{Re}_3\text{Ta}_x\text{BO}_{16}$  series, synthesized assuming full Ta incorporation stoichiometry, with a firing time of 48 hours at a maximum temperature of 1150°C, with no refiring. The observed and calculated diffraction patterns, as well as the difference plot for all four compounds

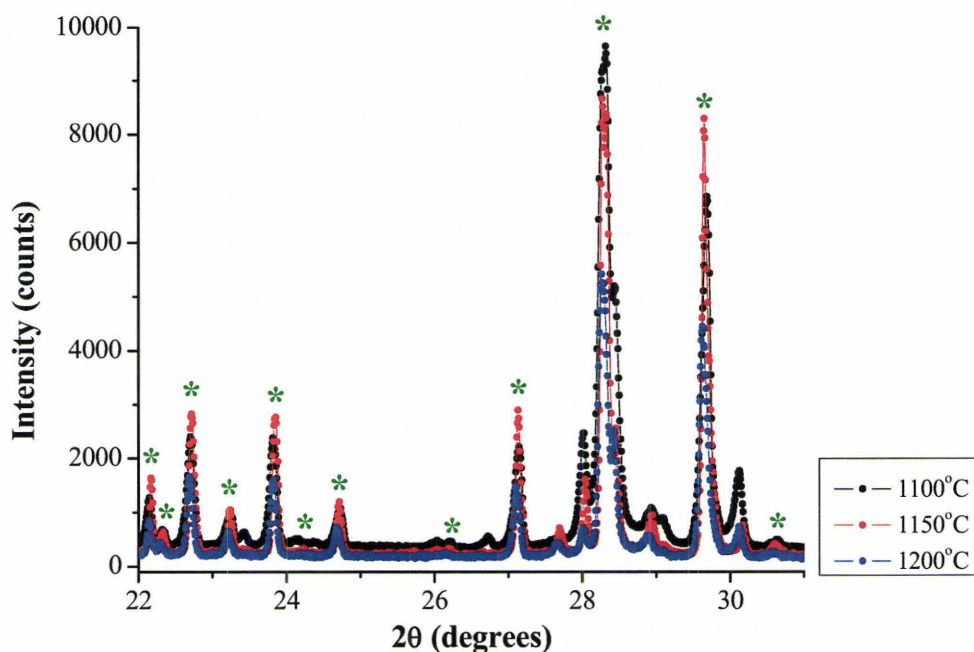


Figure 4.2. Comparison plot of the X-ray diffraction patterns of  $\text{La}_5\text{Re}_{3-x}\text{Ta}_x\text{MnO}_{16}$  from  $22\text{-}32^\circ$   $2\theta$ , fired at three different temperatures. The green asterisks denote structural reflections for  $\text{La}_5\text{Re}_{3-x}\text{Ta}_x\text{MnO}_{16}$ .

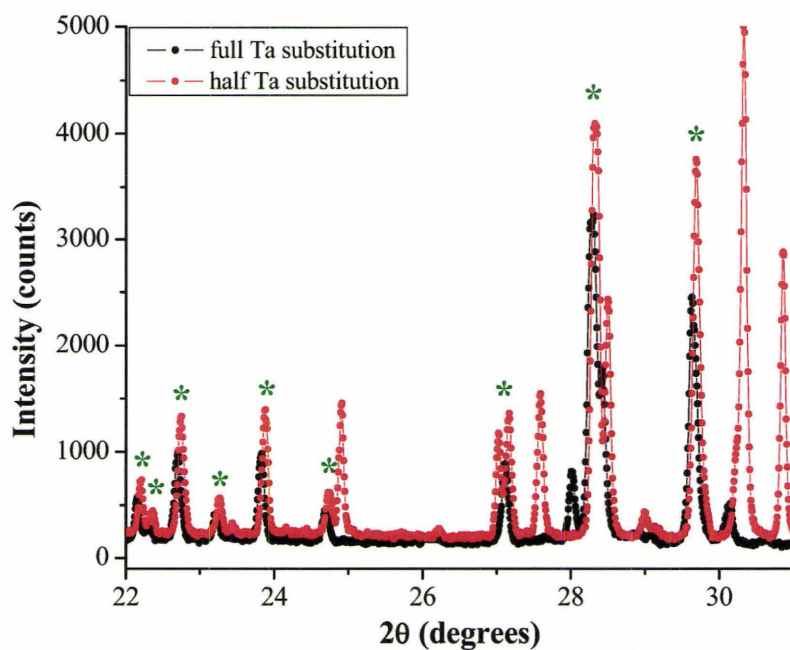


Figure 4.3. Comparison plot of the X-ray diffraction patterns of  $\text{La}_5\text{Re}_{3-x}\text{Ta}_x\text{MnO}_{16}$  from  $22\text{-}32^\circ$   $2\theta$ , assuming full or half Ta substitution in the starting stoichiometry. The green asterisks denote structural reflections for  $\text{La}_5\text{Re}_{3-x}\text{Ta}_x\text{MnO}_{16}$ .

are pictured in Figure 4.4 a-d. Table 4.2 lists the unit-cell constants and refinement agreement indices.

Table 4.2. Unit Cell Constants and Agreement Indices for the Rietveld Pattern Refinement of Powder Neutron Diffraction Data for  $\text{La}_5\text{Re}_{3-x}\text{Ta}_x\text{BO}_{16}$  ( $B = \text{Mn, Fe, Co, Ni}$ )

<b><i>B</i></b>	<b>Mn</b>	<b>Fe</b>	<b>Co</b>	<b>Ni</b>
$a$ (Å)	7.996(1)	7.974(3)	7.974(1)	7.947(2)
$b$ (Å)	8.021(1)	8.006(3)	7.996(1)	7.992(2)
$c$ (Å)	10.243(2)	10.195(5)	10.186(2)	10.185(2)
$\alpha$ (°)	90.12(1)	90.66(3)	90.20(1)	90.26(1)
$\beta$ (°)	95.16(1)	95.36(4)	94.99(1)	94.89(1)
$\gamma$ (°)	89.97(2)	89.99(4)	90.02(2)	90.00(2)
$V$ (Å <sup>3</sup> )	654.28(2)	647.96(4)	646.99(2)	644.51(2)
$R_p$	0.0453	0.0850	0.0412	0.0452
$R_{wp}$	0.0597	0.111	0.0578	0.0631
$\chi^2$	10.8	37.5	9.64	11.7
$R_B$	0.0908	0.162	0.0731	0.0884

Atomic co-ordinates are provided in the Chapter Appendix. It is clear that  $\text{La}_5\text{Re}_{3-x}\text{Ta}_x\text{BO}_{16}$  ( $B = \text{Mn, Fe, Co, Ni}$ ) are isostructural to the previously reported rhenium compounds. However, the degree of Ta incorporation could not be unambiguously determined from the diffraction data alone. Tantalum has a similar atomic radius (0.78 Å versus 0.72 Å for  $\text{Re}^{5+}$ )<sup>14</sup> and differs from rhenium by only two electrons. As a result, X-ray diffraction would not be suitable for this type of analysis. Neutron diffraction would provide slightly better contrast between Re ( $b = 9.2$  fm) and Ta ( $b = 6.91$  fm). However, given the multiphasic nature of the samples and the fact that the impurity phases could not be identified (and accounted for in the refinement), refining site occupancies would be very difficult, and the results would be highly dubious.

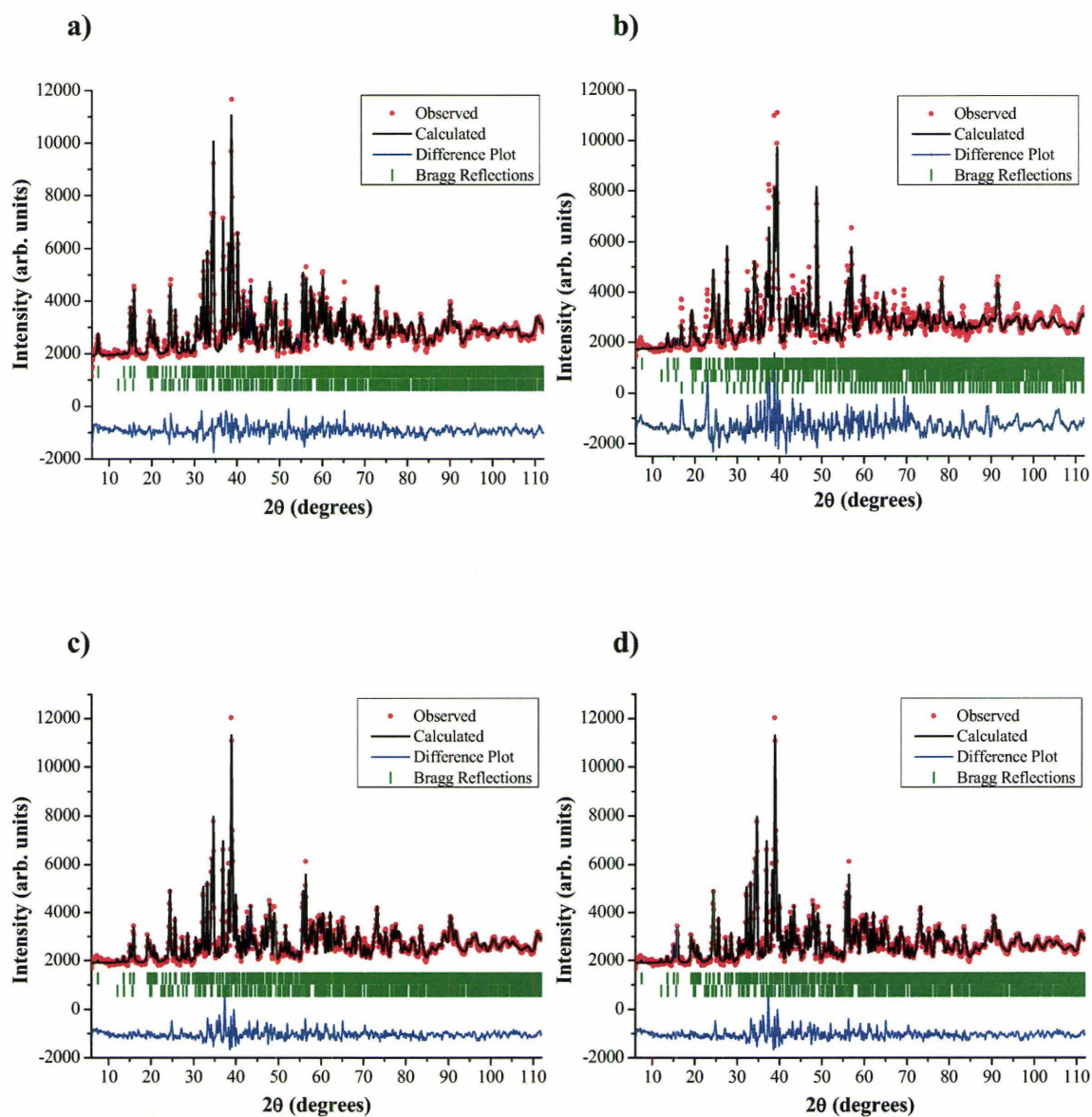


Figure 4.4. Rietveld refinements of powder neutron diffraction data for  $\text{La}_5\text{Re}_{3-x}\text{Ta}_x\text{BO}_{16}$ : a) Mn, b) Fe, c) Co, d) Ni. The top Bragg reflections are for the major phase, and the lower Bragg reflections are for  $\text{La}_3\text{TaO}_7$ . For the Fe sample, a second impurity,  $\text{LaFeO}_3$  was also positively identified and included in the refinement (bottom Bragg reflections).

*SEM-EDS and TEM-EDS Analysis*

The extent of tantalum substitution within the series was investigated microscopically for a single sample of  $\text{La}_5\text{Re}_{3-x}\text{Ta}_x\text{MnO}_{16}$ . Scanning Electron Microscopy (SEM) images (Figure 4.5) show the compound is comprised of bulky, irregular pieces that appear to be relatively homogeneous. However, Energy Dispersive X-ray Spectroscopy (EDS) of selected points of the sample revealed that certain areas were more lanthanum and tantalum rich than others. This indicates the presence of lanthanum-tantalum based oxide impurities, which corroborates the X-ray and neutron structural analyses. Nevertheless, EDS analysis of other points in the sample clearly suggests the incorporation of tantalum within some grains, in addition to lanthanum, rhenium, manganese and, of course, oxygen. Figure 4.6 depicts a typical EDS spectrum from this sample, and Table 4.3 outlines the experimentally derived values of the elements from the EDS analysis, as well as the calculated atomic percentages for 50% and 100% tantalum incorporation. Unfortunately, due to the similarities between rhenium and tantalum, it may have been difficult for the software to deconvolute their individual contributions. However, the spectrum obtained clearly shows peaks due solely to tantalum and solely to rhenium.

Table 4.3. SEM-EDS Analysis of  $\text{La}_5\text{Re}_{3-x}\text{Ta}_x\text{MnO}_{16}$  and Calculated Atomic Percentages.

Element	Experimental EDS Atomic %	Calculated 50% Ta Atomic %	Calculated 100% Ta Atomic %
La	21.77	20.00	20.00
Re	5.92	10.00	8.00
Ta	5.16	2.00	4.00
Mn	3.84	4.00	4.00
O	63.75	64.00	64.00

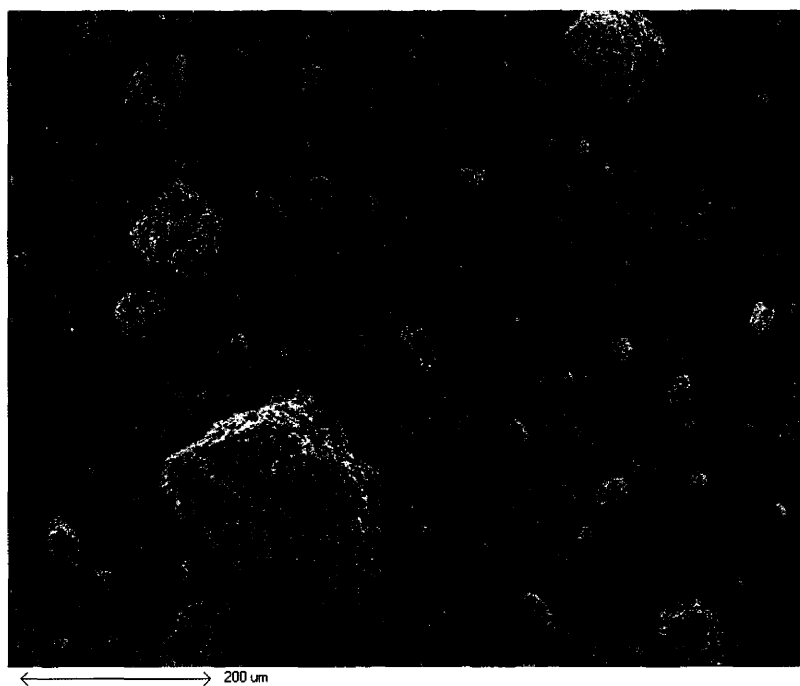


Figure 4.5. SEM image of  $\text{La}_5\text{Re}_{3-x}\text{Ta}_x\text{MnO}_{16}$ , showing the granular, homogeneous nature of the sample.

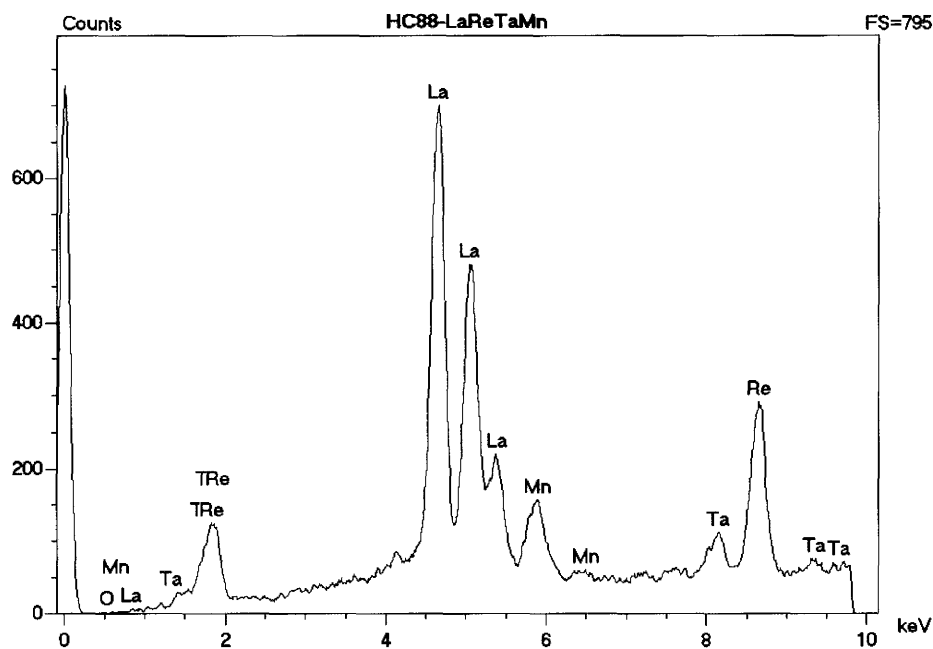


Figure 4.6. SEM-EDS spectrum of the elemental composition of  $\text{La}_5\text{Re}_{3-x}\text{Ta}_x\text{MnO}_{16}$ . Note the distinct Re and Ta peaks at higher energy.

One drawback of SEM is the inability to determine if the area being examined by EDS contains only one phase or a mixture. Transmission Electron Microscopy (TEM) has the capability of switching from imaging mode to diffraction mode. By examining the diffraction pattern and measuring  $d$  spacings (the distance between spots), it is possible to correlate these values with the crystal structure ( $d$  spacings indexed from neutron diffraction data) and with the EDS spectrum. The TEM images (Figure 4.7) show that the sample grains prefer stacking on top of each other. High resolution images (inset Figure 4.7) highlight the nice, crystalline habit of the sample as well as the fact that each grain appears to be single phase, albeit with the occasional stacking fault. The stacking behaviour of multiple sample grains does present some difficulties in the analysis of the diffraction patterns, as some spots could be due to different sample pieces, oriented at different angles. Analysis of a typical diffraction pattern (Figure 4.8) shows  $d$  spacings that correspond to the pillared perovskite phase,  $\text{La}_5\text{Re}_{3-x}\text{Ta}_x\text{MnO}_{16}$ . Table 4.4 reports some of these  $d$  spacing values from TEM, in addition to the experimental  $d$  spacings and indices for  $\text{La}_5\text{Re}_{3-x}\text{Ta}_x\text{MnO}_{16}$ , determined from powder neutron diffraction. The estimated error in the  $d$  spacings measured from the TEM images is approximately 0.01 Å, which is a function of camera length, pixel intensity and resolution, software restrictions and operator error.



Figure 4.7. TEM image of crystallites of  $\text{La}_5\text{Re}_{3-x}\text{Ta}_x\text{MnO}_{16}$ , and their tendency to overlay. *Inset* – High resolution image of the sample, highlighting the packing habit.

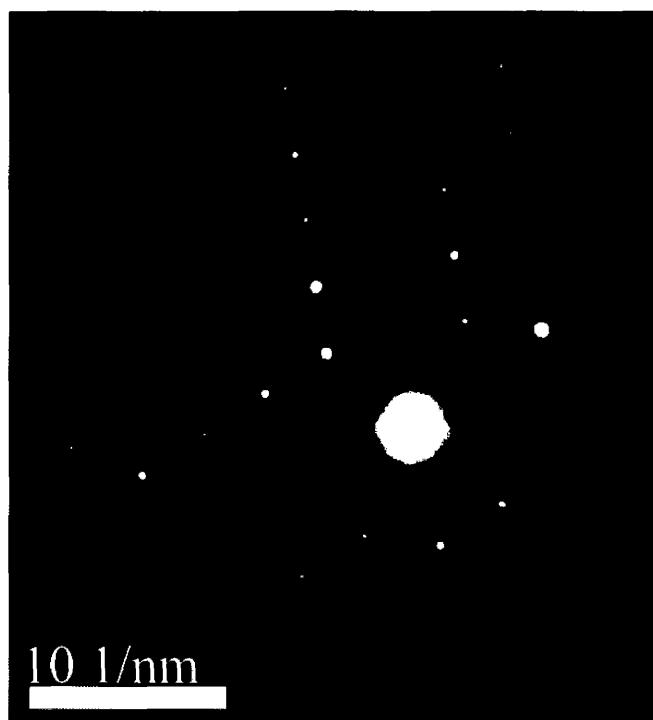


Figure 4.8. TEM diffraction pattern of a single crystal of  $\text{La}_5\text{Re}_{3-x}\text{Ta}_x\text{MnO}_{16}$ .

Table 4.4. Diffraction Image Analysis of  $\text{La}_5\text{Re}_{3-x}\text{Ta}_x\text{MnO}_{16}$  and Comparison with Pillared Perovskite Phase.

<b>TEM <i>d</i> spacing (Å)</b>	<b>Diffraction <i>d</i> spacing (Å)</b>	<b><i>hkl</i> Indices</b>
5.61	5.636	1 1 0
	5.633	1 -1 0
5.08	5.071	-1 -1 1
5.06	5.066	-1 1 1
4.00	3.997	0 2 0
3.97	3.972	2 0 0
2.83	2.828	1 -1 3
	2.827	1 1 3
2.69	2.702	-2 0 3
2.68	2.672	2 -2 1
	2.672	2 2 1
2.59	2.588	0 -2 3
	2.585	0 2 3
1.93	1.917	4 0 1

EDS analysis (Figure 4.9) was able to deconvolute the rhenium and tantalum contributions better, and Table 4.5 outlines the experimental atomic percentages, as well as those calculated for half and full tantalum substitution.

Table 4.5. TEM-EDS Analysis of  $\text{La}_5\text{Re}_{3-x}\text{Ta}_x\text{MnO}_{16}$  and Calculated Atomic Percentages.

<b>Element</b>	<b>Experimental EDS – Spot 1 Atomic %</b>	<b>Experimental EDS – Spot 2 Atomic %</b>	<b>Calculated 50% Ta Atomic %</b>	<b>Calculated 100% Ta Atomic %</b>
La	25.71	27.49	20.00	20.00
Re	9.16	9.10	10.00	8.00
Ta	1.95	1.45	2.00	4.00
Mn	4.66	4.88	4.00	4.00
O	58.52	57.18	64.00	64.00

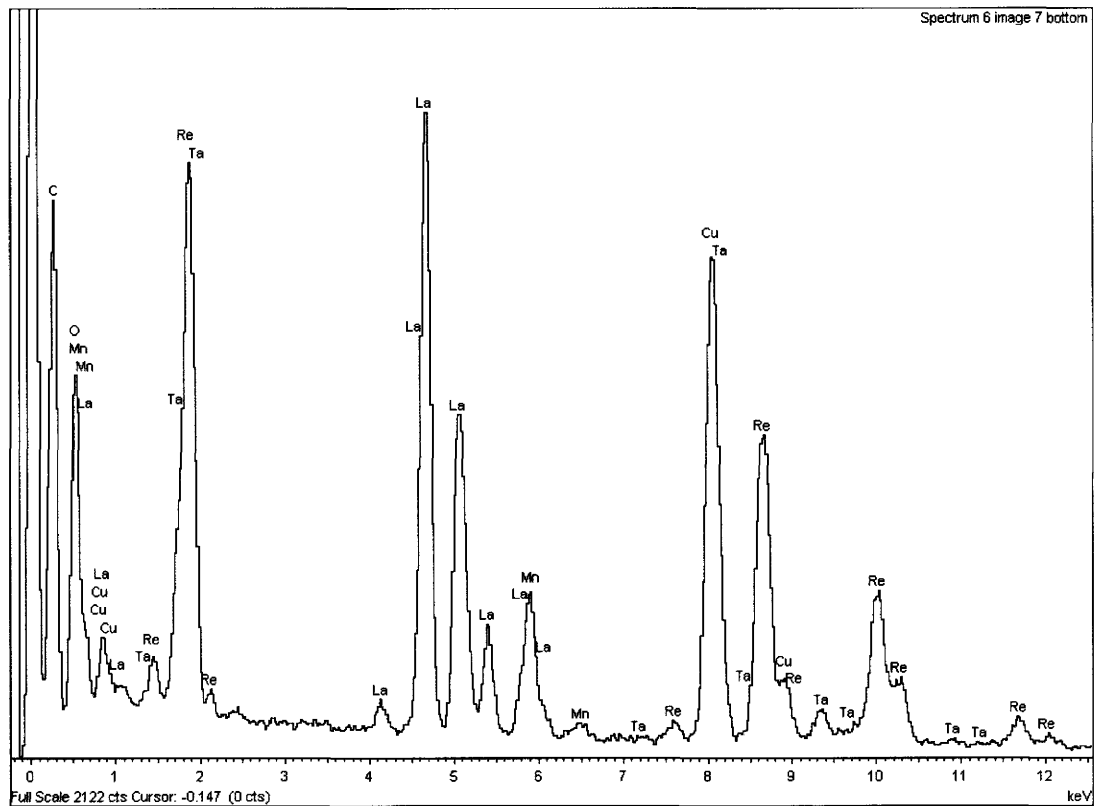


Figure 4.9. TEM-EDS spectrum of the elemental composition of  $\text{La}_5\text{Re}_{3-x}\text{Ta}_x\text{MnO}_{16}$ . Note the distinct Re and Ta peaks at higher energy.

It is apparent from the Table that the experimental EDS values match well with those calculated for half substitution of tantalum in the sample. The atomic percentages obtained from the experimental TEM results, however, are calculated by the software based on the area of the peaks in the spectra in comparison to a series of standard compounds. These standards are typically metals, with very different EDS spectral intensity as compared to oxides. This could cause significant problems with the absolute accuracy of the measurements.

In an effort to understand how the atomic percentages could be affected, the pure phase compound,  $\text{La}_5\text{Re}_3\text{NiO}_{16}$  was also examined. Diffraction images were used to verify the sample identity, and subsequent EDS analysis revealed some interesting deviations from the expected values. The experimentally determined atomic percentages for two sample spots, their average, as well as the expected values are shown in Table 4.6.

Table 4.6. TEM-EDS Analysis of  $\text{La}_5\text{Re}_3\text{NiO}_{16}$  and Calculated Atomic Percentages.

<b>Element</b>	<b>Experimental EDS - 1 Atomic %</b>	<b>Experimental EDS - 2 Atomic %</b>	<b>Average Experimental Atomic %</b>	<b>Calculated Atomic %</b>
La	33.60	39.02	36(3)	20.00
Re	12.82	13.18	13.0(2)	12.00
Ni	5.10	5.07	5.08(2)	4.00
O	48.49	42.74	46(3)	64.00

It is clear that the percentage of lanthanum is significantly overestimated, whereas the amount of oxygen is underestimated. The rhenium and nickel amounts are close to the expected values. The ratio of rhenium to nickel is slightly below the expected

amount, but the ratio of lanthanum to nickel is much higher than calculated using the chemical formula. However, this analysis does serve as a benchmark to use when comparing the EDS spectra and atomic percentages estimated for other compounds.

The overall conclusion from both the SEM-EDS and TEM-EDS data and their subsequent analysis was that some tantalum was incorporated within the pillared perovskite structure. Although the exact amount of tantalum substitution is not known, it appears to be about 50%. Given that the charge and size of rhenium and tantalum are so close, and there were no apparent superstructure reflections in the TEM diffraction patterns, the substitution appears to be random throughout the perovskite layers.

*Structural Analogue -  $\text{La}_5\text{Re}_{3-x}\text{Nb}_x\text{MnO}_{16}$*

In an effort to gain a better understanding as to the extent of non-magnetic 5+ ion substitution within the pillared perovskite structure, a trial sample synthesized using  $\text{Nb}_2\text{O}_5$  (99.9985%, Alfa Aesar) in place of  $\text{Ta}_2\text{O}_5$  for the Mn member of the series was attempted. Niobium has approximately the same radius as rhenium (0.78 Å versus 0.72 Å)<sup>14</sup>, however, it has 34 fewer electrons, making subsequent analysis by X-ray diffraction possible. The reaction was carried out in an analogous way, and fired at a maximum temperature of 1150°C for 48 hours. The resulting grey-black powder product was analyzed by X-ray diffraction. Along with the expected pillared perovskite main phase, two secondary phases,  $\text{La}_3\text{NbO}_7$  and  $\text{LaNbO}_4$ , were identified and included in the subsequent Rietveld refinement (Figure 4.10). No other peaks were unaccounted for in the pattern. The unit cell parameters and agreement indices are reported in Table 4.7.

Table 4.7. Unit Cell Constants and Agreement Indices for the Rietveld Pattern Refinement of Powder X-ray Diffraction Data for  $\text{La}_5\text{Re}_{3-x}\text{Nb}_x\text{MnO}_{16}$ 

$\text{La}_5\text{Re}_{3-x}\text{Nb}_x\text{MnO}_{16}$			
$a$ (Å)	7.9963(1)	$\alpha$ (°)	90.127(2)
$b$ (Å)	8.01538(9)	$\beta$ (°)	95.159(1)
$c$ (Å)	10.2414(1)	$\gamma$ (°)	89.970(3)
$V$ (Å <sup>3</sup> )	653.747(1)		
$R_p$	0.0733		
$R_{wp}$	0.0972		
$\chi^2$	1.908		

Using the method of Hill and Howard<sup>15</sup>, the weight percentage of the impurities were calculated as 5.35%  $\text{LaNbO}_4$  and 12.91%  $\text{La}_3\text{NbO}_7$ , respectively. Based on the amount of niobium added into the synthesis, 0.291 mmol of niobium is unaccounted for by the impurity phases. This is lower than the 0.556 mmol of niobium expected for fully substituted  $\text{La}_5\text{Re}_2\text{NbMnO}_{16}$ . Consequently, the occupancy of the niobium position was allowed to refine within this phase, and rhenium was included in this position. This value was refined to about 42% niobium and therefore, 58% rhenium, which is very close to the estimated occupancy from the impurity investigation (about 52% Nb substitution). Although full substitution was not achieved, these results indicate that it is possible to substitute some of the  $\text{Re}^{5+}$  ions within the perovskite layers.

Since it is evident that approximately 50% Nb was incorporated into the  $\text{La}_5\text{Re}_{3-x}\text{Nb}_x\text{MnO}_{16}$  structure, the starting stoichiometry was altered accordingly to obtain a phase pure product, and fired to a maximum temperature of 1150°C for 48 hours. X-ray powder diffraction of the resulting product (Figure 4.11) revealed that no pillared perovskite phase formed. In fact, the major constituents were tentatively identified as

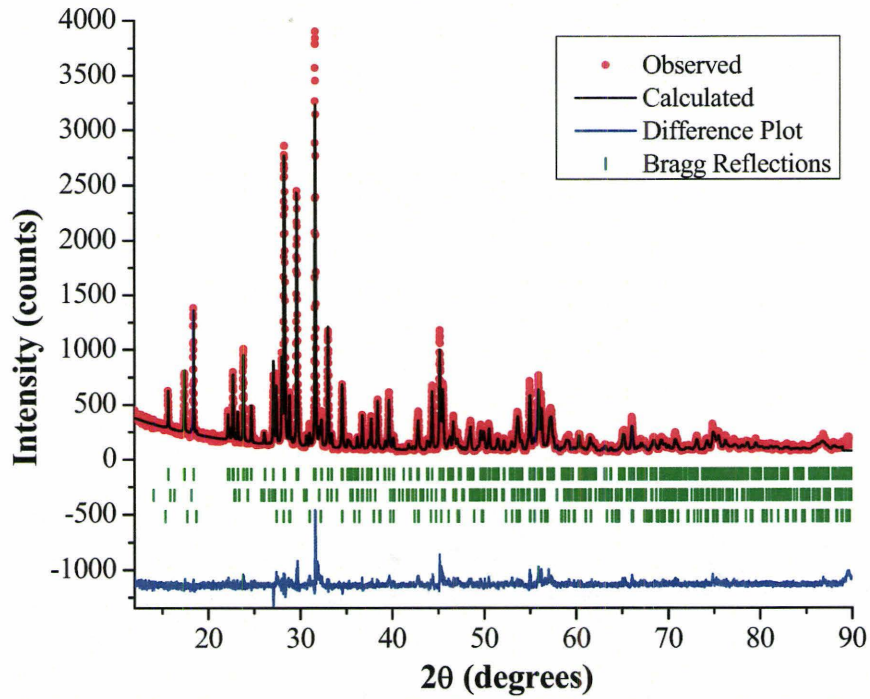


Figure 4.10. Rietveld refinement of powder X-ray diffraction data for  $\text{La}_5\text{Re}_{3-x}\text{Nb}_x\text{MnO}_{16}$ . The top Bragg reflections are for the major phase, and the lower Bragg reflections are for  $\text{La}_3\text{NbO}_7$  and  $\text{LaNbO}_4$ , respectively.

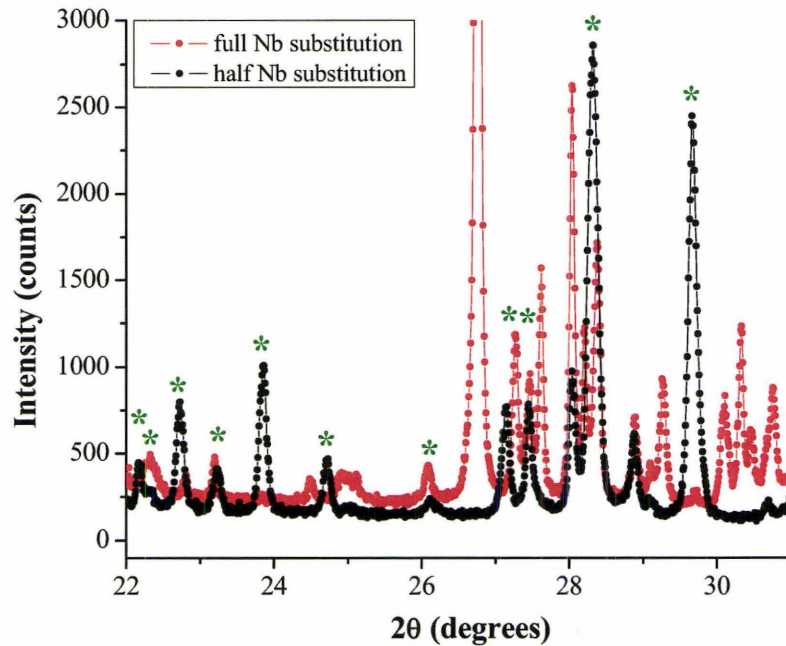


Figure 4.11. Comparison plot of the X-ray diffraction patterns of  $\text{La}_5\text{Re}_{3-x}\text{Nb}_x\text{MnO}_{16}$  from  $22\text{-}32^\circ$   $2\theta$ , assuming full or half Nb substitution in the starting stoichiometry. The green asterisks denote structural reflections for  $\text{La}_5\text{Re}_{3-x}\text{Nb}_x\text{MnO}_{16}$ .

$\text{La}_4\text{Re}_2\text{O}_{10}$ ,  $\text{LaMnO}_3$ ,  $\text{La}_3\text{NbO}_7$  and  $\text{LaNbO}_4$ . One possible hypothesis for the lack of formation of  $\text{La}_5\text{Re}_{3-x}\text{Nb}_x\text{MnO}_{16}$  could be that excess Nb might be necessary for any incorporation of Nb in the pillared perovskite structure at all, as more thermodynamically stable products (such as  $\text{La}_4\text{Re}_2\text{O}_{10}$ ,  $\text{LaMnO}_3$ ,  $\text{La}_3\text{NbO}_7$  and  $\text{LaNbO}_4$ ) could be favoured in the overall synthesis.

To further probe the degree of Nb substitution within the pillared perovskite phase, SEM-EDS and TEM-EDS analyses were also performed on the  $\text{La}_5\text{Re}_{3-x}\text{Nb}_x\text{MnO}_{16}$  sample. SEM images (Figure 4.12) illustrate the bulky and relatively homogeneous nature of the sample. The estimates of each element's relative atomic percentage by EDS analysis (Figure 4.13) of selected sample grains agrees well with the calculated value for 50% Nb incorporation (Table 4.8).

Table 4.8. SEM-EDS Analysis of  $\text{La}_5\text{Re}_{3-x}\text{Nb}_x\text{MnO}_{16}$  and Calculated Atomic Percentages.

Element	Experimental EDS Atomic %	Calculated 50% Nb Atomic %	Calculated 100% Nb Atomic %
La	24.13	20.00	20.00
Re	7.51	10.00	8.00
Nb	1.51	2.00	4.00
Mn	4.05	4.00	4.00
O	62.80	64.00	64.00
<i>Total</i>	<i>100</i>	<i>100</i>	<i>100</i>

Further, TEM-EDS analysis (Figure 4.14) corroborates the SEM findings (Table 4.9). Again, as previously noted for the Ta-based sample, the values for lanthanum are overestimated, and the atomic percent of oxygen is underestimated. A TEM image of the

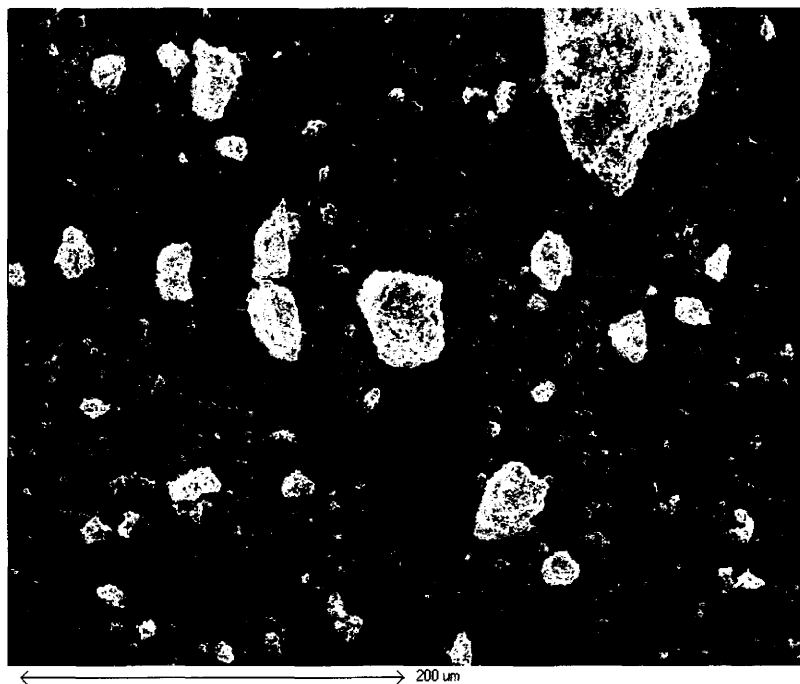


Figure 4.12. SEM image of  $\text{La}_5\text{Re}_{3-x}\text{Nb}_x\text{MnO}_{16}$ , showing the granular, homogeneous nature of the sample.

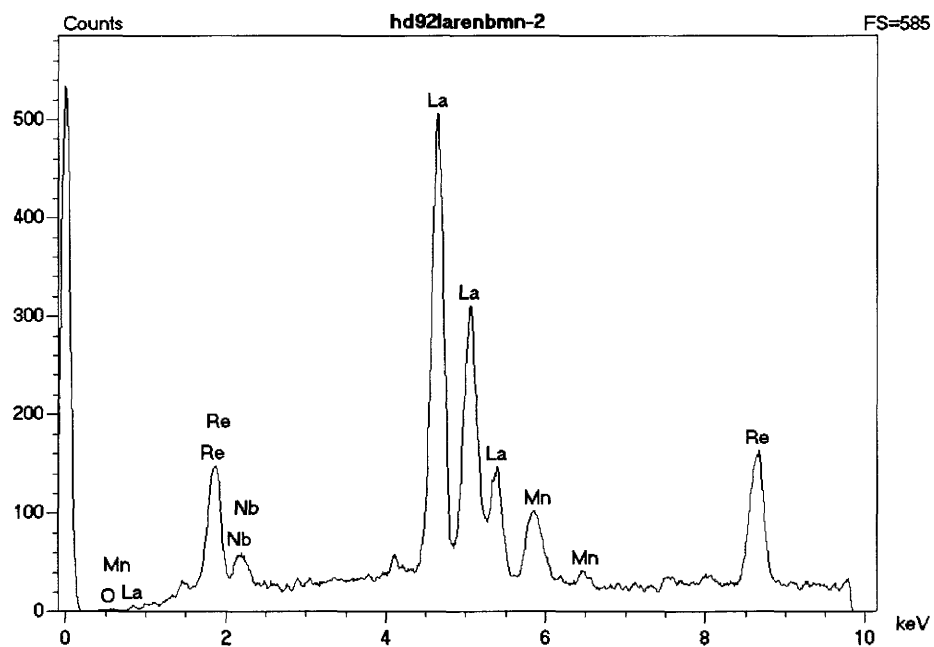


Figure 4.13. SEM-EDS spectrum of the elemental composition of  $\text{La}_5\text{Re}_{3-x}\text{Nb}_x\text{MnO}_{16}$ . Note the distinct Re and Nb peaks.

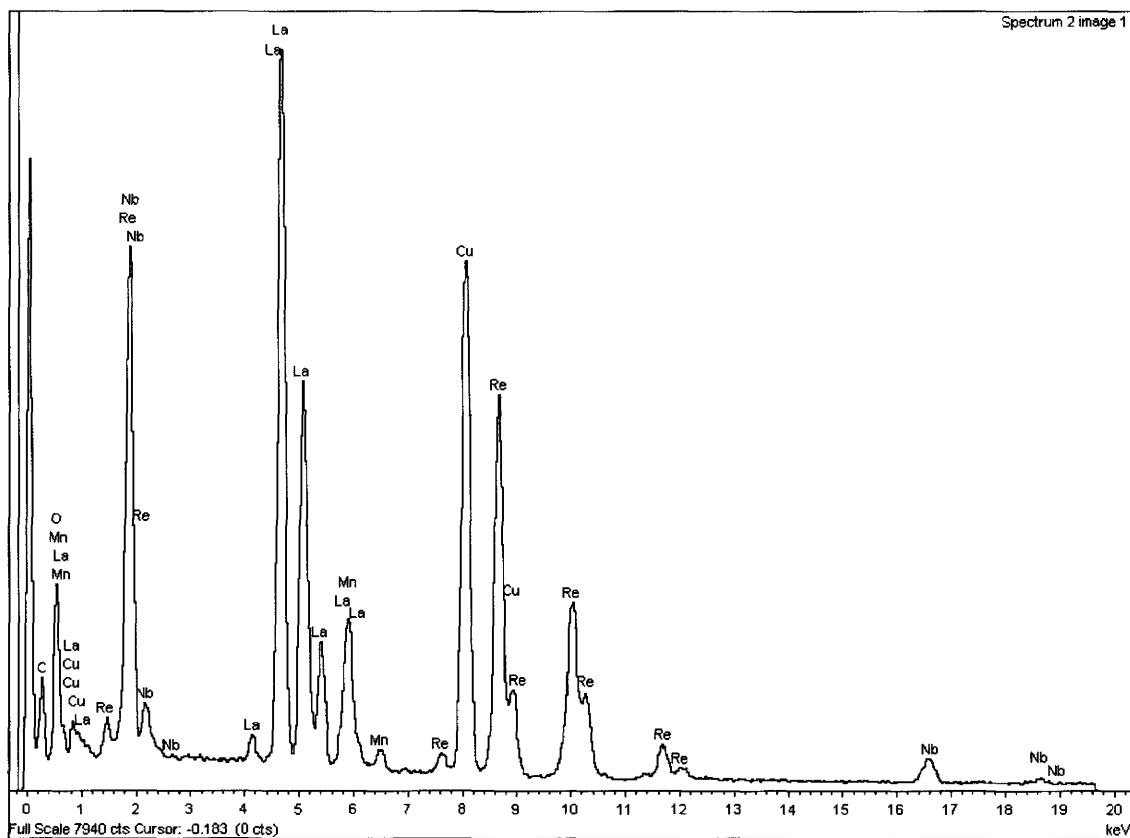


Figure 4.14. TEM-EDS spectrum of the elemental composition of  $\text{La}_5\text{Re}_{3-x}\text{Nb}_x\text{MnO}_{16}$ . Note the distinct Re and Nb peaks at higher energy.

sample (Figure 4.15) shows a clear crystalline facet, and high resolution images (Figure 4.15, inset) illustrate the regular stacking pattern of the atoms within the structure.

Table 4.9. TEM-EDS Analysis of  $\text{La}_5\text{Re}_{3-x}\text{Nb}_x\text{MnO}_{16}$  and Calculated Atomic Percentages.

Element	Experimental EDS – Spot 1 Atomic %	Experimental EDS – Spot 2 Atomic %	Calculated 50% Nb Atomic %	Calculated 100% Nb Atomic %
La	19.16	43.23	20.00	20.00
Re	7.51	11.21	10.00	8.00
Nb	1.94	2.40	2.00	4.00
Mn	3.41	7.08	4.00	4.00
O	67.98	36.08	64.00	64.00

Diffraction images (Figure 4.16) were also collected,  $d$  spacings measured and compared to the phases present in the sample ( $\text{La}_5\text{Re}_{3-x}\text{Nb}_x\text{MnO}_{16}$ ,  $\text{La}_3\text{NbO}_7$  and  $\text{LaNbO}_4$ ). Table 4.10 reports some of the  $d$  spacings measured from the TEM images, as well as the corresponding  $d$  spacings in the pillared perovskite phase (from X-ray powder diffraction) and their  $hkl$  indices. There are no  $d$  spacings in either of the other impurity phases that are close to these experimentally determined values. Again, as previously noted, the estimated error in the  $d$  spacings measured from the TEM images is approximately 0.01 Å, which is a function of camera length, pixel intensity and resolution, software restrictions and operator error.



Figure 4.15. TEM image of crystallites of  $\text{La}_5\text{Re}_{3-x}\text{Nb}_x\text{MnO}_{16}$ , and their tendency to overlay. *Inset* – High resolution image of the sample, highlighting the packing of the grains.

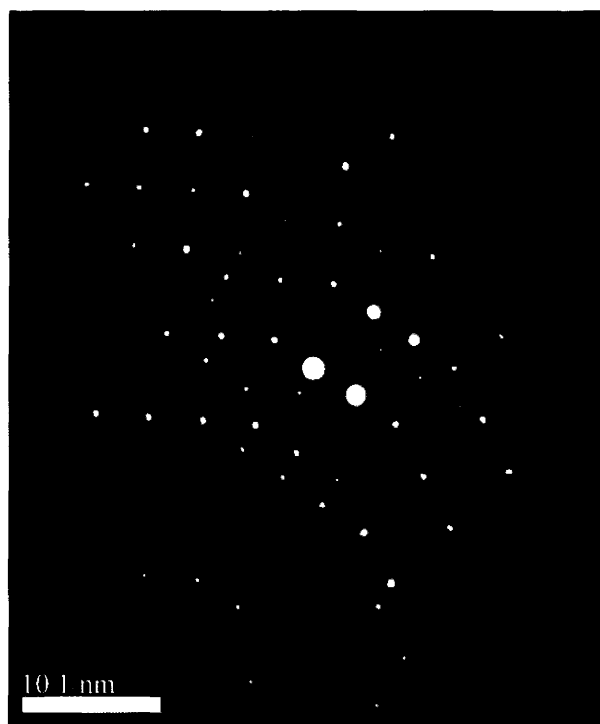


Figure 4.16. TEM diffraction pattern of a single crystal of  $\text{La}_5\text{Re}_{3-x}\text{Nb}_x\text{MnO}_{16}$ .

Table 4.10. Diffraction Image Analysis of  $\text{La}_5\text{Re}_{3-x}\text{Nb}_x\text{MnO}_{16}$  and Comparison with Pillared Perovskite Phase.

TEM <i>d</i> spacing (Å)	Diffraction <i>d</i> spacing (Å)	<i>hkl</i> Indices
4.00	4.009	0 2 0
3.16	3.156	0 -2 2
	3.150	0 2 2
2.51	2.521	3 -1 0
	2.522	3 1 0
2.49	2.497	-3 1 1
	2.498	-3 -1 1
2.27	2.273	1 -1 4
	2.270	1 1 4

All in all, it is obvious from the combination of SEM-EDS and TEM-EDS data and X-ray powder diffraction that approximately 50% niobium is substituted within the perovskite layers of  $\text{La}_5\text{Re}_{3-x}\text{Nb}_x\text{MnO}_{16}$ . This is also consistent with the SEM-EDS and TEM-EDS findings for  $\text{La}_5\text{Re}_{3-x}\text{Ta}_x\text{MnO}_{16}$ . Although not microscopically investigated directly, by analogy the other  $\text{La}_5\text{Re}_{3-x}\text{Ta}_x\text{BO}_{16}$  compounds ( $B = \text{Fe}, \text{Co}, \text{Ni}$ ) should have approximately 50% tantalum substitution as well.

#### *Magnetic Properties*

##### *$\text{La}_5\text{Re}_{3-x}\text{Ta}_x\text{MnO}_{16}$*

Zero field-cooled (ZFC) and field cooled (FC) magnetic susceptibility data, measured from 2 to 300 K are displayed in Figure 4.17. There is a small but distinct peak centred at 160 K, which could be an indication of long-range magnetic order. At a temperature slightly below the apex of this feature, the two curves begin to diverge greatly. The ZFC data show a second broad, asymmetric feature, more indicative of short-range order, with a maximum at 32 K and a sharp decrease at lower temperature.

The sudden rise at very low temperatures is most likely a paramagnetic impurity. The FC data increases significantly at lower temperatures – a sign of ferromagnetism – with a possible shoulder at 32 K. At very high temperatures, both the ZFC and FC data decrease rapidly at 290 K, which is where the two curves actually begin to diverge. This unusual behaviour could be due to an unidentified magnetic secondary phase. This magnetic behaviour is remarkably similar to  $\text{La}_5\text{Re}_3\text{MnO}_{16}$  (inset, Figure 4.17).<sup>1,2</sup> However, there are some distinct differences.

The ZFC/FC data for  $\text{La}_5\text{Re}_3\text{MnO}_{16}$  has a much sharper and larger peak at 161 K, as well as a significantly smaller short-range order feature at much higher temperature (~90 K). In  $\text{La}_5\text{Re}_{3-x}\text{Ta}_x\text{MnO}_{16}$ , the random replacement of some of the magnetic  $\text{Re}^{5+}$  within the layers with non-magnetic  $\text{Ta}^{5+}$  would disrupt the regular magnetic coupling between ions within the layers. This would lead to more short-range order at a lower temperature, as ‘decoupled’ moments would attempt to arrive at some sort of order. If the interlayer coupling of  $B^{2+}$  through the diamagnetic pillar dictates the transition to long-range magnetic order, the same critical temperature would be expected, as this coupling pathway does not involve the in-layer  $A^{5+}$  cation at all.

Due to the presence of an unknown amount of impurity phases, quantitative evaluation of the high temperature data is not possible. However, further qualitative analysis of the magnetic data does provide some insights into the fascinating magnetism of these compounds.

A plot of the product of susceptibility and temperature ( $\chi T$ ) versus temperature (Figure 4.18) shows the sharp peak at 160 K more prominently. The second feature

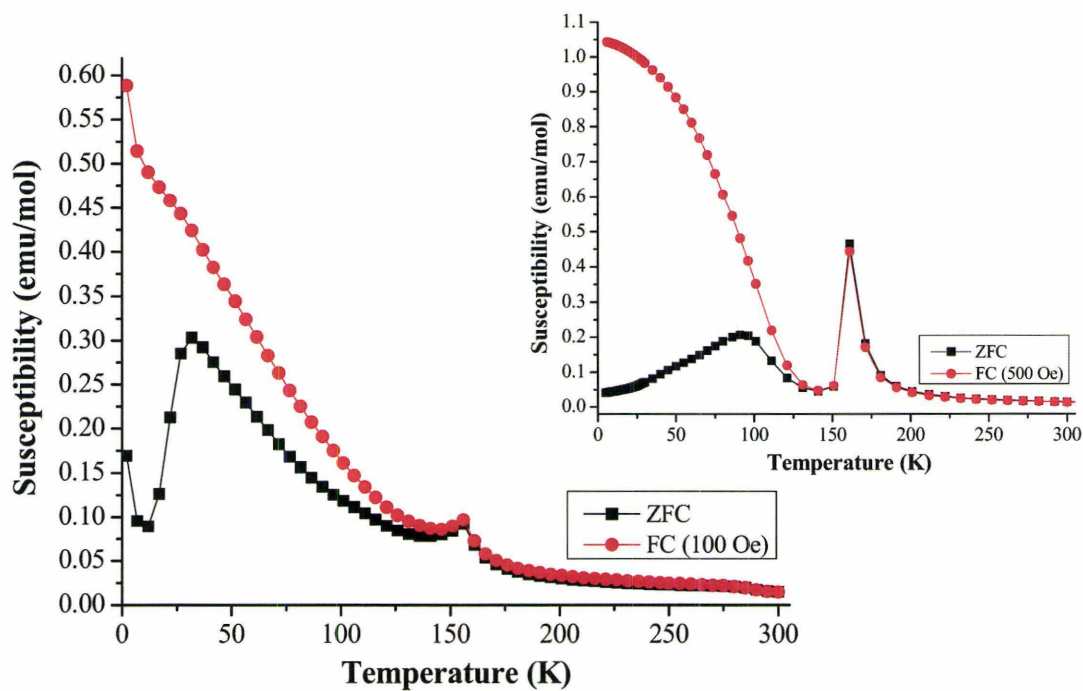


Figure 4.17. ZFC/FC magnetic susceptibility of  $\text{La}_5\text{Re}_{3-x}\text{Ta}_x\text{MnO}_{16}$ . *Inset* – ZFC/FC susceptibility data for  $\text{La}_5\text{Re}_3\text{MnO}_{16}$ .<sup>2</sup>

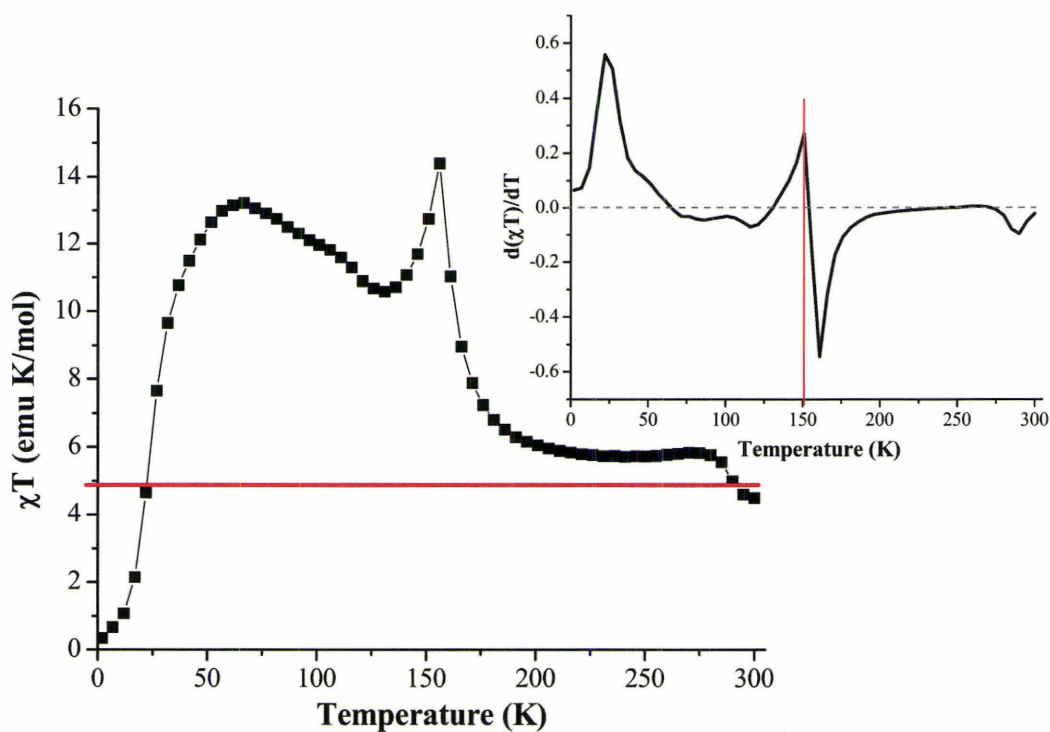


Figure 4.18.  $\chi T$  versus temperature plot for  $\text{La}_5\text{Re}_{3-x}\text{Ta}_x\text{MnO}_{16}$ . The horizontal line is the estimated spin-only Curie constant. *Inset* – Fisher heat capacity for  $\text{La}_5\text{Re}_{3-x}\text{Ta}_x\text{MnO}_{16}$ .

appears as more of a rise in the data, indicating dominant ferro- or ferri-magnetic interactions, before taking a sharp downturn at about 60 K. An approximate ‘spin-only’ Curie constant of 4.875 emu K/mol was calculated, assuming 50%  $\text{Re}^{5+}$  within the layers ( $S = 1$ , full  $C = 1.00$  emu K/mol) and 100%  $\text{Mn}^{2+}$  ( $S = 5/2$ ,  $C = 4.375$  emu K/mol). Both features appear above this line, consistent with ferro- or ferri-magnetism. However the steep downturn at lower temperatures signifies antiferromagnetic interactions, as the data fall below the Curie constant line.

The derivative of  $\chi T$  plotted against temperature (inset Figure 4.18), or the so-called Fisher heat capacity<sup>16</sup>, has two distinct features, centred at about 22 and 151 K, respectively. The first peak at 22 K appears to be more symmetric, whereas the feature at 151 K has a clear, lambda-like profile, which is more indicative of long-range magnetic order.

The magnetization of  $\text{La}_5\text{Re}_{3-x}\text{Ta}_x\text{MnO}_{16}$ , plotted as a function of applied field, at temperatures of 5, 80, 120, 155, 165 and 250 K is pictured in Figure 4.19. At all temperatures, the magnetization at highest field falls far short of the expected saturation moment of  $5 \mu_B$  or higher for this compound. Interestingly, the 80 K data has the highest magnetization value at the highest field measured (5.0 T). The magnetization curves from 5 to 155 K all show hysteresis at low fields, with a maximum remanence value at 80 K of  $0.3 \mu_B$ . All of these curves also have an “S”-shape at low fields. This is indicative of a metamagnetic transition, which causes the highly anisotropic, weakly antiferromagnetically coupled layers to uncouple and align with the applied magnetic field. At 165 K, a slight curve to the data is still apparent, indicating a paramagnetic state

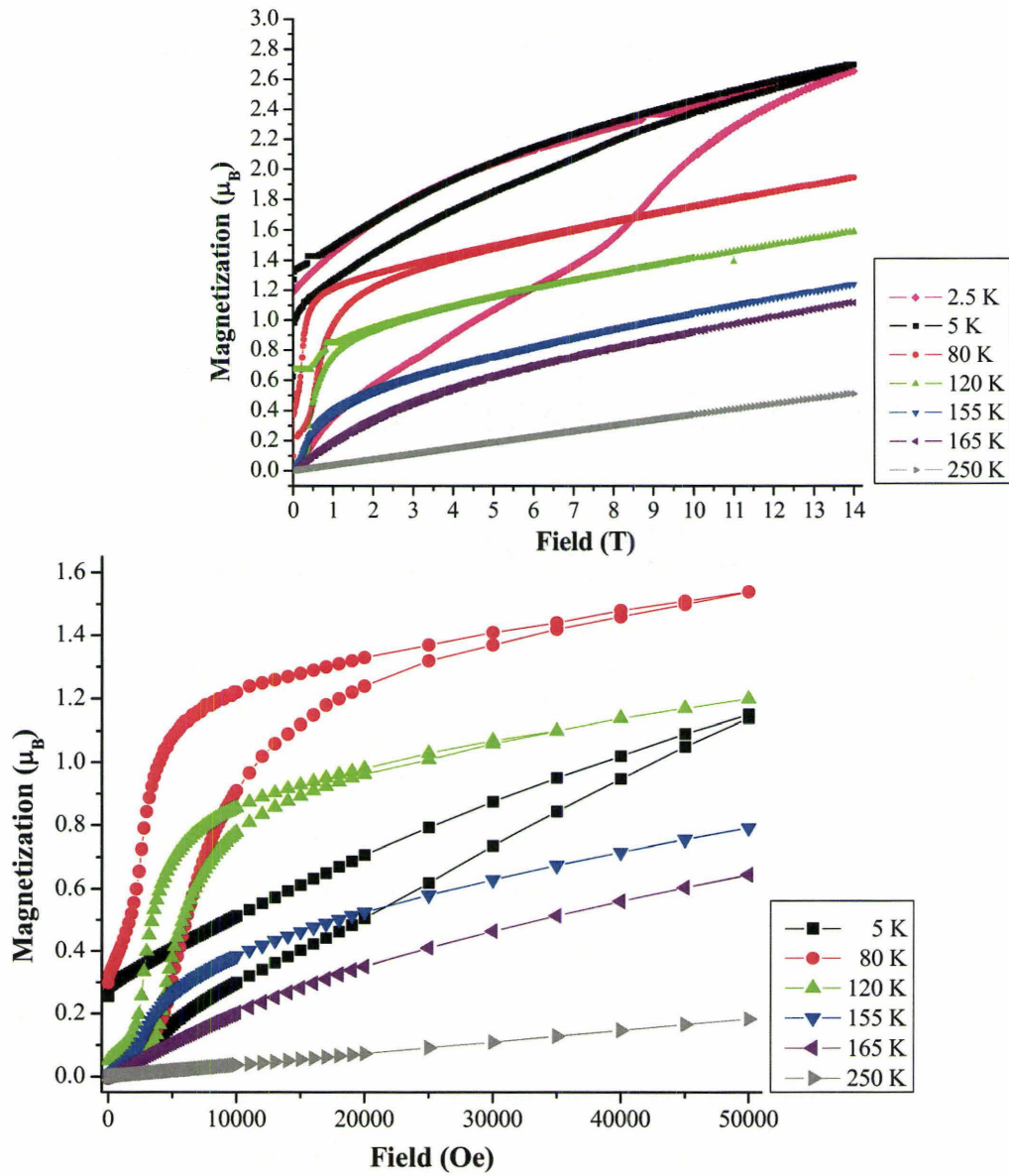


Figure 4.19. Magnetization curves recorded for  $\text{La}_5\text{Re}_{3-x}\text{Ta}_x\text{MnO}_{16}$  with a 5.0 T maximum field. *Inset* – High field magnetization data recorded using a VSM at the NHMFL with a 14.0 T maximum field.

has not been reached at this temperature. By 250 K, however, the magnetization does scale linearly with applied field – a clear signal of paramagnetism.

Since  $\text{La}_5\text{Re}_{3-x}\text{Ta}_x\text{MnO}_{16}$  did not saturate at 5.0 T, this sample was studied using a Vibrating Sample Magnetometer (VSM) at the National High Magnetic Field Laboratory (NHMFL) in Tallahassee, Florida. Magnetization curves up to 14.0 T were measured at 2.5, 5, 80, 120, 155, 165 and 250 K (inset Figure 4.19). At low fields (5.0 T and below), almost the same magnetization behaviour was observed, albeit with higher remanent magnetization values. However, in this series of measurements, the 2.5 and 5 K data clearly had the maximum magnetization values, even at lower fields. In addition, a second broader “S”-shaped transition at about 8 T in the 2.5 K curve was found. The cause of this second metamagnetic-like transition could be related to the canting of the  $\text{Mn}^{2+}$  spins, which was observed in the variable temperature powder neutron diffraction measurements.

#### *$\text{La}_5\text{Re}_{3-x}\text{Ta}_x\text{FeO}_{16}$*

ZFC/FC magnetic susceptibility data, measured from 2 to 300 K are pictured in Figure 4.20. The two curves begin to diverge just before a peak centred at about 135 K, which could be due to long-range magnetic ordering. Both data show a second broader feature at about 60 K. The ZFC curve has another shoulder at about 25 K. These smaller features could be due to shorter range magnetic interactions. The ZFC/FC data for  $\text{La}_5\text{Re}_{3-x}\text{Ta}_x\text{FeO}_{16}$  is very similar to that reported for  $\text{La}_5\text{Re}_3\text{FeO}_{16}$  (inset, Figure 4.20).<sup>3</sup> Both data have a ZFC/FC divergence just before a fairly broad peak. However, the critical temperature of this peak is slightly different (155 K for  $\text{La}_5\text{Re}_3\text{FeO}_{16}$  and 135 K

for  $\text{La}_5\text{Re}_{3-x}\text{Ta}_x\text{FeO}_{16}$ ), which could be due to some magnetic impurity phases in the case of  $\text{La}_5\text{Re}_{3-x}\text{Ta}_x\text{FeO}_{16}$ . Also, the ZFC data of  $\text{La}_5\text{Re}_{3-x}\text{Ta}_x\text{FeO}_{16}$  show two broad but significant features at lower temperatures due to short-range order, which is not obvious in the  $\text{La}_5\text{Re}_3\text{FeO}_{16}$  sample at all. As discussed previously for the  $\text{La}_5\text{Re}_{3-x}\text{Ta}_x\text{MnO}_{16}$  data, this could be due to the random  $\text{Ta}^{5+}$  substitution within the layer. Again, the presence of an unknown amount of secondary phases prevents a quantitative analysis of the high temperature data.

A plot of  $\chi T$  versus temperature (Figure 4.21) reveals that the peak at 135 K is actually quite broad, and the second feature at 60 K is now just a shoulder. Only the 135 K feature appears above the calculated 'spin-only' Curie constant line, signifying dominant ferro- or ferri-magnetism. As before, the approximate 'spin-only' Curie constant (3.50 emu K/mol) was calculated assuming 50%  $\text{Re}^{5+}$  within the layers ( $S = 1$ , full  $C = 1.00$  emu K/mol) and 100%  $\text{Fe}^{2+}$  ( $S = 2$ ,  $C = 3.00$  emu K/mol). At higher and lower temperatures, the curve is actually well below this line, indicating antiferromagnetism in these temperature ranges.

The Fisher heat capacity (inset Figure 4.21) is, again, quite inconclusive. The largest lambda-like anomaly is centred at 125 K, indicating possible magnetic long-range order. There are also two smaller, broader features at 20 and 50 K, which may be due to short-range magnetic interactions.

The magnetization of  $\text{La}_5\text{Re}_{3-x}\text{Ta}_x\text{FeO}_{16}$ , plotted as a function of applied field, at temperatures of 5, 20, 50, 80, 120 and 300 K is pictured in Figure 4.22. At all temperatures, the magnetization at highest field is much lower than the expected

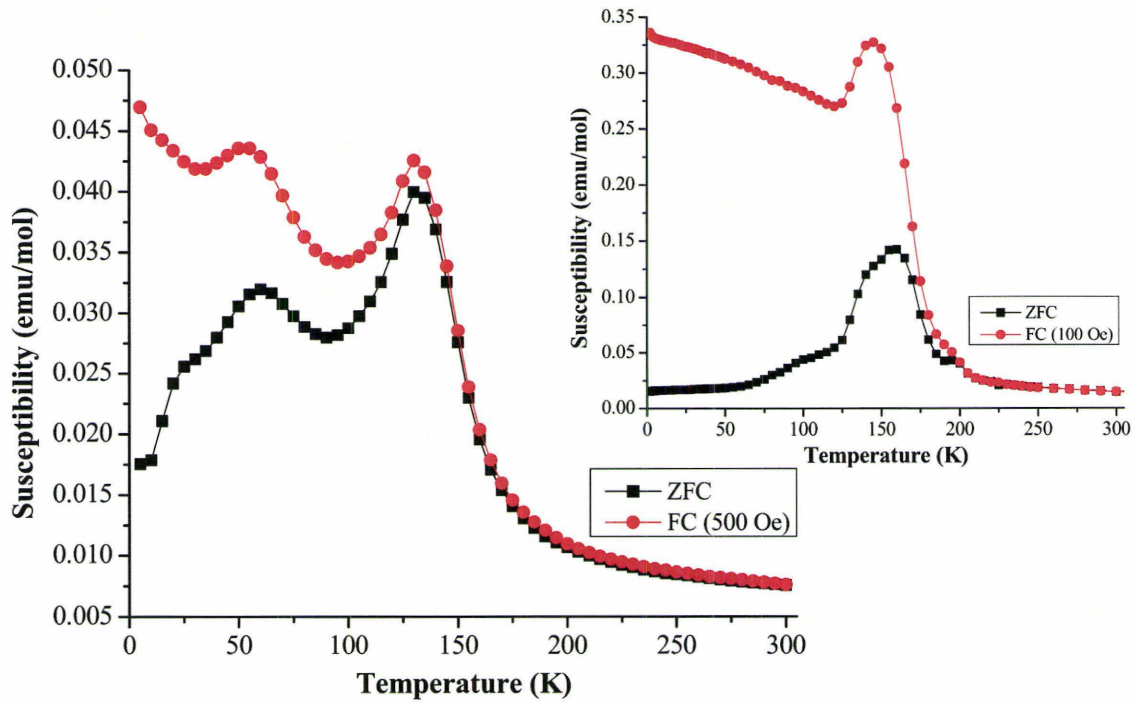


Figure 4.20. ZFC/FC magnetic susceptibility of  $\text{La}_5\text{Re}_{3-x}\text{Ta}_x\text{FeO}_{16}$ . *Inset* – ZFC/FC susceptibility data for  $\text{La}_5\text{Re}_3\text{FeO}_{16}$ .<sup>3</sup>

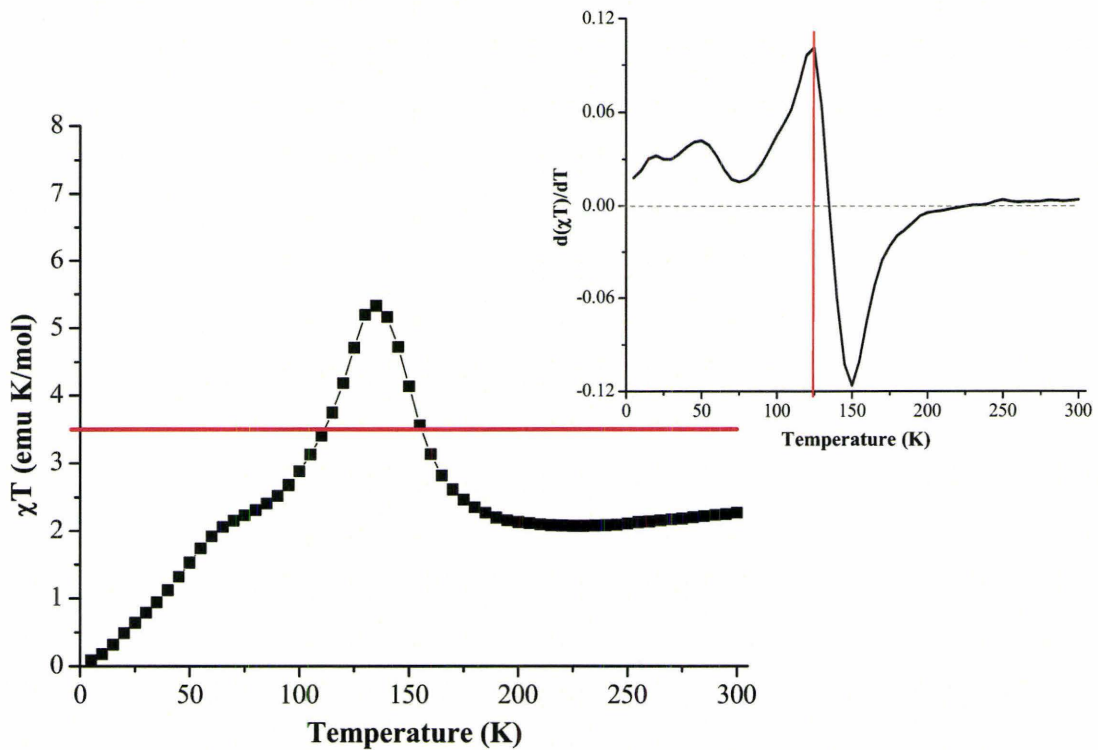


Figure 4.21.  $\chi T$  versus temperature plot for  $\text{La}_5\text{Re}_{3-x}\text{Ta}_x\text{FeO}_{16}$ . The horizontal line is the estimated spin-only Curie constant. *Inset* – Fisher heat capacity for  $\text{La}_5\text{Re}_{3-x}\text{Ta}_x\text{FeO}_{16}$ .

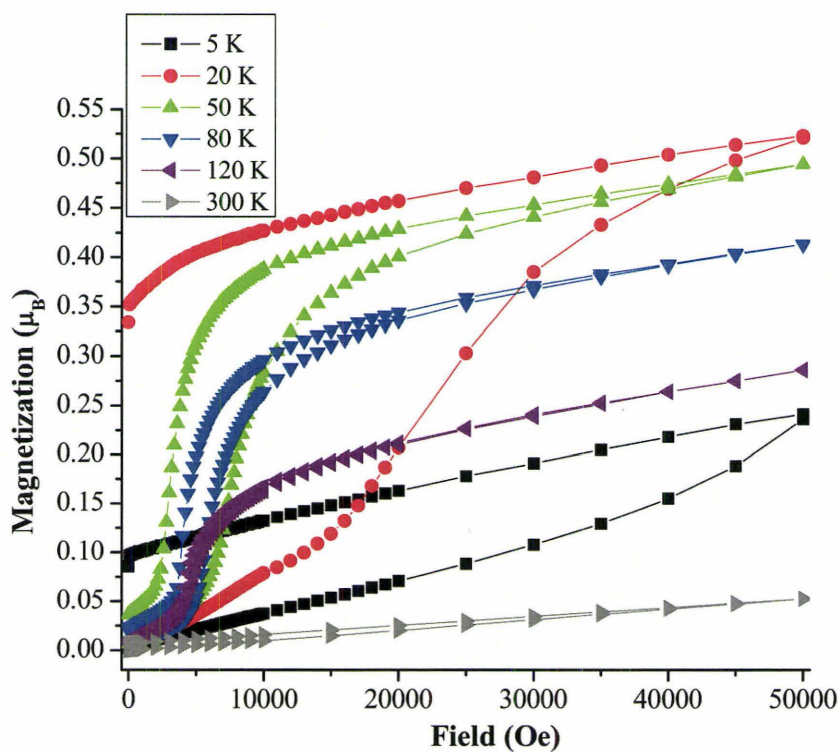


Figure 4.22. Magnetization curves for  $\text{La}_5\text{Re}_{3-x}\text{Ta}_x\text{FeO}_{16}$  with 5.0 T maximum field.

saturation moment of  $4 \mu_B$  or higher for this compound. Again, the 20 K data has the highest magnetization value at the highest field (5.0 T) and not the lowest temperature measured. The magnetization curves from 5 to 120 K all show hysteresis at low fields, with a maximum remanence value at 20 K of  $0.35 \mu_B$ . All of these data also show a metamagnetic transition. Similar to the Mn compound, the 5 K data has rather large hysteresis. In addition, a second, broader “S” at about 2.5 T is present in the 20 K curve. This secondary transition is very similar to the 8.0 T feature in the 2.5 K magnetization curve of the Mn compound, measured at the NHMFL. At 300 K, the data are linear (an indication of paramagnetism), however, some slight hysteresis is still present. This could indicate another impurity in the Fe sample – one that is ferromagnetic above room temperature (i.e.  $\text{LaFeO}_3$ , an identified impurity phase, is a canted G-type antiferromagnet with  $T_c \sim 740$  K, which has a weak ferromagnetic moment).

#### *La<sub>5</sub>Re<sub>3-x</sub>Ta<sub>x</sub>CoO<sub>16</sub>*

Figure 4.23 displays ZFC/FC magnetic susceptibility data for  $\text{La}_5\text{Re}_{3-x}\text{Ta}_x\text{CoO}_{16}$ , measured from 2 to 300 K. The two curves diverge at about 120 K. After the divergence, the ZFC data have a large, broad shoulder and a sharper peak, centred at 35 K, before falling sharply at lower temperatures. The FC data also shows the sharp peak, which is indicative of long-range magnetic order, but at a slightly lower temperature, indicating possible field dependence of the transition. There is a slight dip in the FC data at temperatures below this peak, however, at the lowest temperature measured, the susceptibility measured remains high ( $\sim 0.37$  emu/mol).

Comparing the ZFC/FC data measured for  $\text{La}_5\text{Re}_{3-x}\text{Ta}_x\text{CoO}_{16}$  to the ZFC/FC susceptibility curves collected for  $\text{La}_5\text{Re}_3\text{CoO}_{16}$ ,<sup>4</sup> (inset Figure 4.23) shows some clear similarities and stark differences. Both data diverge at fairly high temperature, followed by some broader features indicative of short-range order at slightly lower temperatures. However, the short-range order is much more pronounced in  $\text{La}_5\text{Re}_{3-x}\text{Ta}_x\text{CoO}_{16}$ , for reasons discussed previously. There also is a sharp peak at  $\sim 35$  K in both data sets, signifying the same critical temperature in both cases. Still, in  $\text{La}_5\text{Re}_{3-x}\text{Ta}_x\text{CoO}_{16}$ , this peak is a lot less pronounced than for  $\text{La}_5\text{Re}_3\text{CoO}_{16}$ . As previously noted, quantitative analysis of high temperature data would be dubious due to the presence of an unknown amount of impurity phases.

A plot of  $\chi T$  versus temperature (Figure 4.24) reveals the dominance of ferro- or ferri-magnetic interactions, as most of the data appears above the approximate ‘spin-only’ Curie constant line [2.375 emu K/mol, calculated assuming 50%  $\text{Re}^{5+}$  within the layers ( $S = 1$ , full  $C = 1.00$  emu K/mol) and 100%  $\text{Co}^{2+}$  ( $S = 3/2$ ,  $C = 1.875$  emu K/mol)]. The broad shoulder in the susceptibility data becomes a much more prominent feature, and the small peak at 35 K persists.

The Fisher heat capacity of  $\text{La}_5\text{Re}_{3-x}\text{Ta}_x\text{CoO}_{16}$  (inset Figure 4.24) has only one rather sharp peak at about 32 K. This feature appears to have a lambda-like profile, which is characteristic of long-range magnetic ordering.

The magnetization of  $\text{La}_5\text{Re}_{3-x}\text{Ta}_x\text{CoO}_{16}$ , measured as a function of applied field, at temperatures of 5, 17, 30, 48, 100 and 250 K is displayed in Figure 4.25. The expected saturation moment is  $3 \mu_B$  for this compound, and at all temperatures, the magnetization

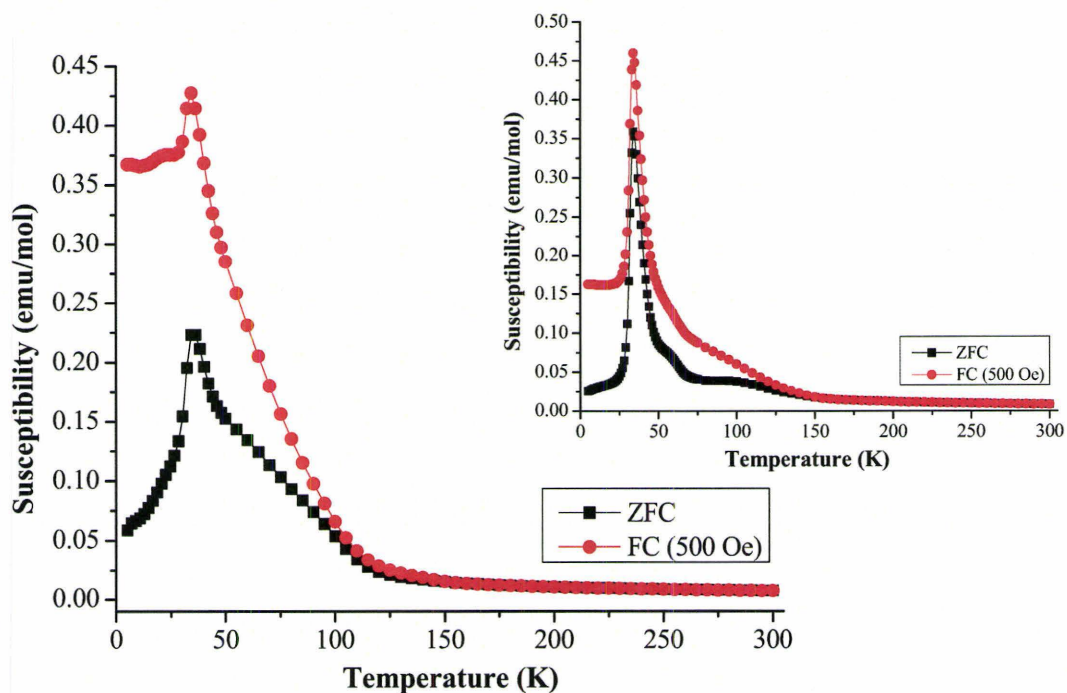


Figure 4.23. ZFC/FC magnetic susceptibility of  $\text{La}_5\text{Re}_{3-x}\text{Ta}_x\text{CoO}_{16}$ . *Inset* – ZFC/FC susceptibility data for  $\text{La}_5\text{Re}_3\text{CoO}_{16}$ .

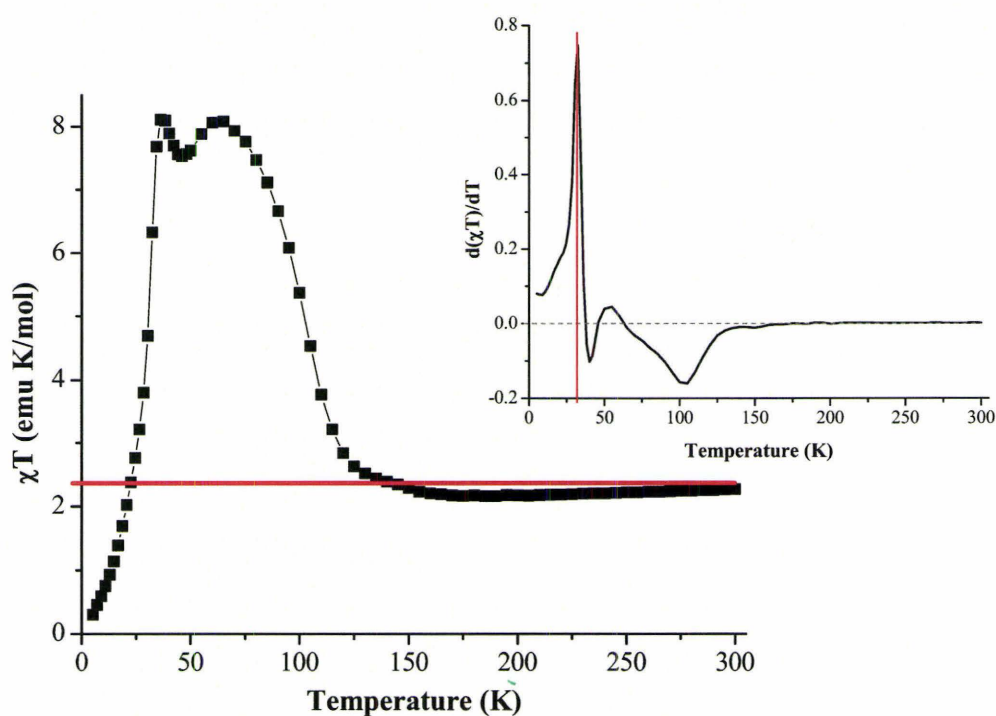


Figure 4.24.  $\chi T$  versus temperature plot for  $\text{La}_5\text{Re}_{3-x}\text{Ta}_x\text{CoO}_{16}$ . The horizontal line is the estimated spin-only Curie constant. *Inset* – Fisher heat capacity for  $\text{La}_5\text{Re}_{3-x}\text{Ta}_x\text{CoO}_{16}$ .

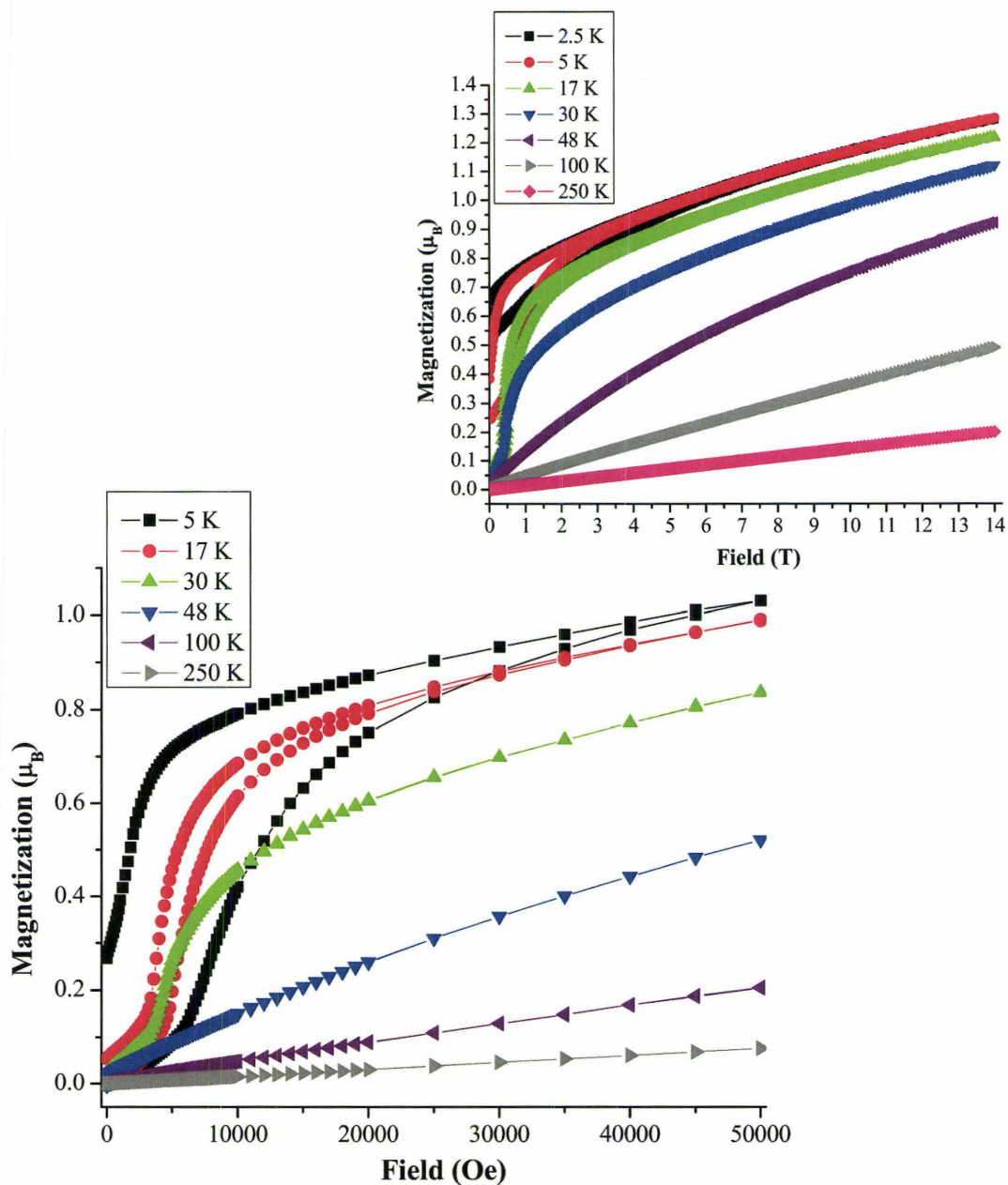


Figure 4.25. Magnetization curves recorded for  $\text{La}_5\text{Re}_{3-x}\text{Ta}_x\text{CoO}_{16}$  with a 5.0 T maximum field. *Inset* – High field magnetization data recorded using a VSM at the NHMFL with a 14.0 T maximum field.

value at highest field is much lower than this. The highest saturation magnetization measured is  $\sim 1 \mu_B$  at 5 K. The curves from 5 to 30 K all show hysteresis at low fields, with a maximum remanence value of about  $0.25 \mu_B$ . All of these data also have an “S”-shaped curve at low fields, indicating a metamagnetic transition. At 48 K, a slight curve to the data is still apparent, indicating a paramagnetic state has not quite been reached at this temperature. By 100 and 250 K, however, the magnetization does scale linearly with applied field, as expected for a paramagnet.

Since  $\text{La}_5\text{Re}_{3-x}\text{Ta}_x\text{CoO}_{16}$  also did not saturate at 5.0 T, high field magnetization measurements using the VSM at the NHMFL were conducted at 2.5, 5, 17, 30, 48, 100 and 250 K (inset Figure 4.25) up to 14.0 T. At low fields (5.0 T and below), almost the same magnetization behaviour was observed, albeit with higher remanent magnetization values. At higher fields, no other transitions were apparent, and the data simply increased in an almost linear fashion. Hence, it appears that only the Mn and Fe compounds exhibit a second transition at higher field.

#### *La<sub>5</sub>Re<sub>3-x</sub>Ta<sub>x</sub>NiO<sub>16</sub>*

ZFC/FC magnetic susceptibility data collected from 2 to 300 K are pictured in Figure 4.26. The two curves begin to diverge at about 250 K, which is at a much higher temperature than any of the other compounds. The ZFC data has two very broad features at about 50 and 125 K, respectively, indicating substantial short-range antiferromagnetic interactions. A small cusp at about 12 K, slightly more visible in the FC data, may be the transition to long-range magnetic order. This data differs significantly from that recorded for  $\text{La}_5\text{Re}_3\text{NiO}_{16}$ <sup>4</sup> (inset Figure 4.25). In  $\text{La}_5\text{Re}_{3-x}\text{Ta}_x\text{NiO}_{16}$ , the divergence is at much

higher temperature, there is substantially greater short-range order, and the transition to long-range order is barely visible. However, the critical temperature remains approximately the same. Given the large number of differences in the ZFC/FC susceptibility data for these two analogous compounds, it is somewhat surprising that the critical temperature would remain the same – unless the long-range order coupling pathway were not affected by the substitution.

As with the other Ta substituted samples, quantitative analysis of the high temperature data was not possible due to the inability to quantify the amount of impurity phases.

A  $\chi T$  versus temperature plot (Figure 4.27) reveals a few interesting features. An approximate ‘spin-only’ Curie constant line of 1.50 emu K/mol was added to the plot, calculated assuming 50%  $\text{Re}^{5+}$  within the layers ( $S = 1$ , full  $C = 1.00$  emu K/mol) and 100%  $\text{Ni}^{2+}$  ( $S = 1$ ,  $C = 1.00$  emu K/mol). Most of the curve lies above this value, indicating dominant ferro- or ferri-magnetism. Only at the 14 K transition (and at temperatures about 150 K) does the  $\chi T$  value dip below this line, signalling antiferromagnetic behaviour. The transition to long-range order, therefore, appears to be the antiferromagnetic coupling of the layers. There are three broader features at 75, 135 and 250 K, respectively, that may be due to shorter-range antiferromagnetic interactions. The Fisher heat capacity (inset Figure 4.27) is inconclusive, with no apparent transitions.

The magnetization of  $\text{La}_5\text{Re}_{3-x}\text{Ta}_x\text{NiO}_{16}$ , plotted as a function of applied field, at temperatures of 5, 16, 80, 130, 200 and 300 K is pictured in Figure 4.28. At all temperatures, the magnetization at highest field is much lower than the expected

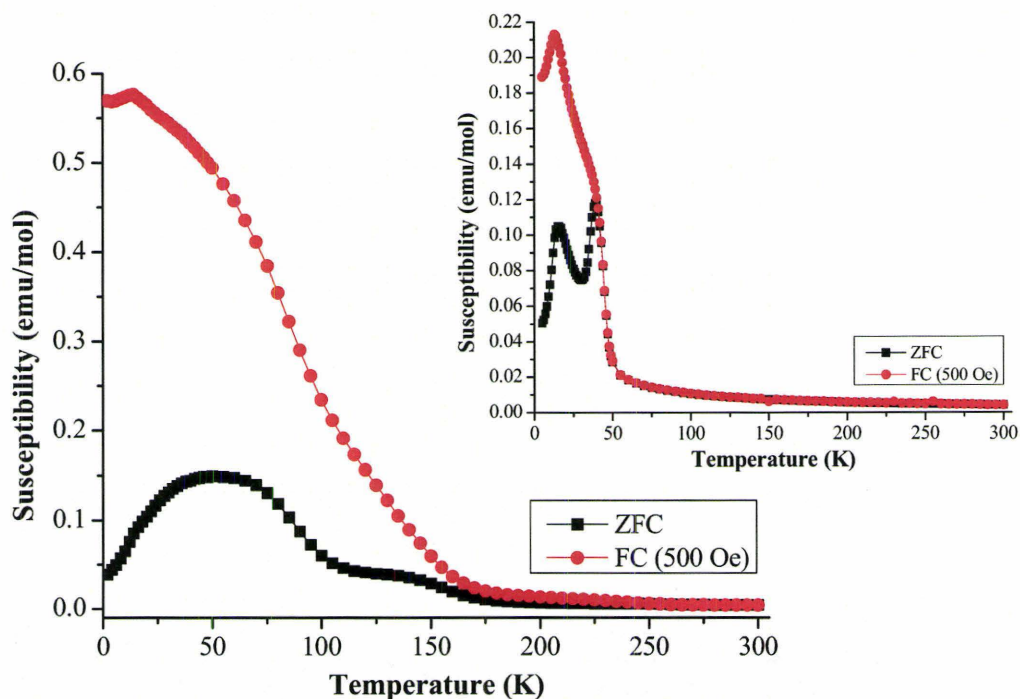


Figure 4.26. ZFC/FC magnetic susceptibility of  $\text{La}_5\text{Re}_{3-x}\text{Ta}_x\text{NiO}_{16}$ . *Inset* – ZFC/FC susceptibility data for  $\text{La}_5\text{Re}_3\text{NiO}_{16}$ .<sup>4</sup>

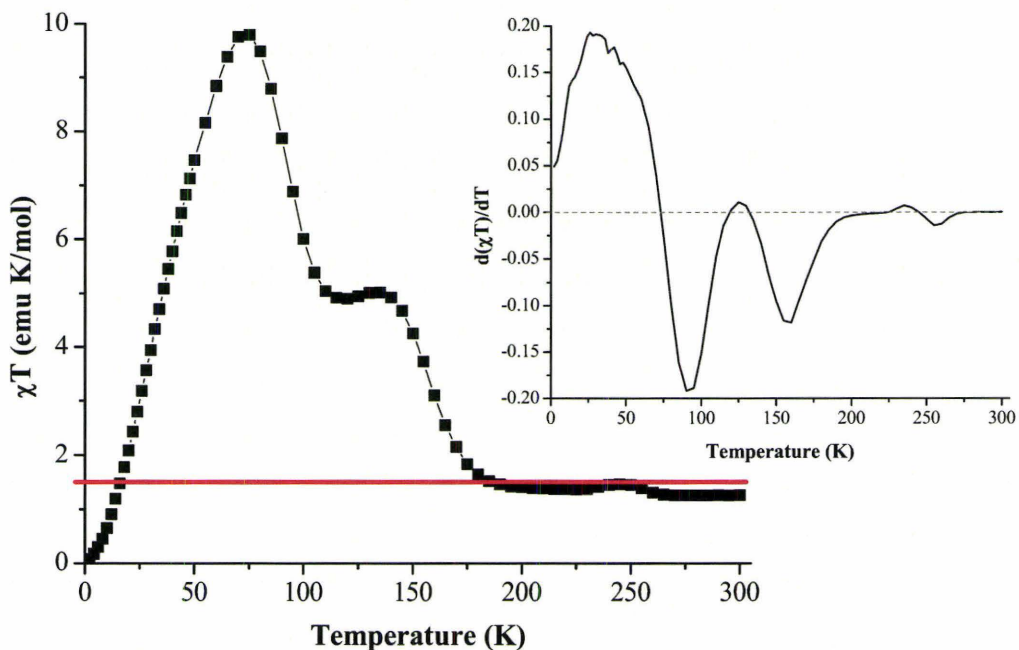


Figure 4.27.  $\chi T$  versus temperature plot for  $\text{La}_5\text{Re}_{3-x}\text{Ta}_x\text{NiO}_{16}$ . The horizontal line is the spin-only Curie constant. *Inset* – Fisher heat capacity for  $\text{La}_5\text{Re}_{3-x}\text{Ta}_x\text{NiO}_{16}$ .

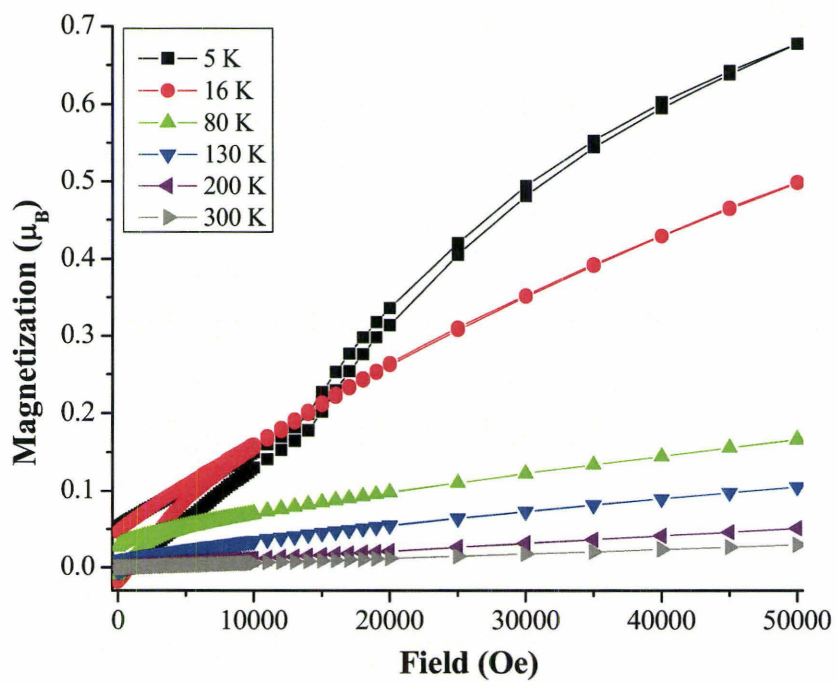


Figure 4.28. Magnetization curves for  $\text{La}_5\text{Re}_{3-x}\text{Ta}_x\text{NiO}_{16}$  with a 5.0 T maximum field.

saturation moment of  $2 \mu_B$  or higher for this compound. The magnetization curves at 5, 16 and 80 K show slight hysteresis at low fields, with a very small maximum remanence value of only  $0.05 \mu_B$ . Instead of the typical “S”-shaped feature, there is a sharp ‘kink’ visible in the 5 K curve at about 1.4 T, before a pronounced curvature of the data at higher fields. A slight curvature to the magnetization remains until 130 K, where it becomes linear and remains so until 300 K. This clearly indicates paramagnetic behaviour.

As all of the compounds studied displayed metamagnetic behaviour in their magnetization curves recorded below their transition temperatures, attempts were made at estimating the critical field ( $H_C$ ) required for this phenomena at each temperature measured (Table 4.11). The critical field is generally taken as the inflection point of the “S”-shaped magnetization curve. A good estimation of the inflection point of a curve is to take the first derivative, as the inflection point should appear as a sharp peak. This was performed on the magnetization curves of  $\text{La}_5\text{Re}_{3-x}\text{Ta}_x\text{BO}_{16}$  ( $B = \text{Mn, Fe, Co, Ni}$ ) below their corresponding critical temperatures.

Table 4.11. Critical Fields for Metamagnetic Transitions Observed for  $\text{La}_5\text{Re}_{3-x}\text{Ta}_x\text{BO}_{16}$  ( $B = \text{Mn, Fe, Co, Ni}$ )

<i>B</i>	<i>T</i> (K)	<i>H<sub>C</sub></i> (Oe)	<i>B</i>	<i>T</i> (K)	<i>H<sub>C</sub></i> (Oe)
Mn	5	27 500	Fe	5	50 000
	80	5200		20	18 000
	120	4300		50	7400
	155	2800		80	5800
		120		4800	
Co	5	7600	Ni	5	15 500
	17	5000			
	30	4200			

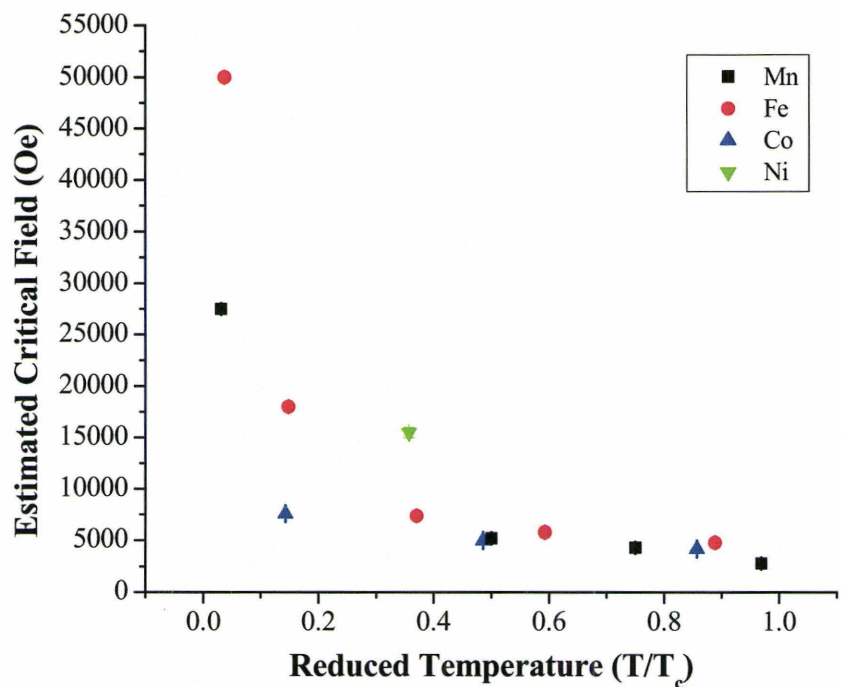


Figure 4.29. Critical field versus reduced temperature for the metamagnetic transitions of La<sub>5</sub>Re<sub>3-x</sub>Ta<sub>x</sub>MO<sub>16</sub> (M = Mn, Fe, Co, Ni)

Generally, there appears to be no real systematics in this series. A plot of critical fields versus reduced temperature ( $T/T_c$ ) shows that at temperatures close to their critical temperatures, the compounds behave similarly, with relatively low values of the critical fields (Figure 4.29). At lower temperatures, all materials experience an increase in the critical field required for the metamagnetic transition. However, both the Mn and Fe compounds seem to have relatively higher values than the Co. The Ni member is difficult to place, as only one measurement below its transition temperature was completed. Relative to the other compounds, though, the Ni appears to have a much higher value. This could be due to the different orientation of magnetic spins (perpendicular to the  $c$ -axis as opposed to parallel to it, as is the case with Mn, Fe and Co). Overall, given the relatively high values of the critical fields at low temperatures, it appears that the interlayer coupling is quite strong. However, this magnetic coupling is still weak enough that it can be overcome by laboratory fields, especially at temperatures slightly below the magnetic transition point.

#### *La<sub>5</sub>Re<sub>3-x</sub>Nb<sub>x</sub>MnO<sub>16</sub>*

Preliminary investigation of the magnetic properties of  $\text{La}_5\text{Re}_{3-x}\text{Nb}_x\text{MnO}_{16}$  reveals some interesting behaviour. Although similar in nature to both the  $\text{La}_5\text{Re}_3\text{MnO}_{16}$ <sup>2</sup> and  $\text{La}_5\text{Re}_{3-x}\text{Ta}_x\text{MnO}_{16}$  data, there are still some distinct differences. The zero field-cooled (ZFC) and field cooled (FC) magnetic susceptibility data from 2 to 300 K (Figure 4.30) show a very small cusp at 160 K, which could signal long-range magnetic order. However, this feature is much smaller in the Nb compound, as compared to either of the other two. The two curves diverge just below the cusp. The ZFC data continue with a

broad shoulder at about 125 K, and a large broad feature, centred at about 65 K. All of these features are peaked in the ZFC susceptibility data, suggesting antiferromagnetic interactions. In addition, the susceptibility continues to decrease down to the lowest temperature measured. However, the FC data rise quickly after 160 K and continue increasing at lower temperatures, indicating ferromagnetism. This is very similar to the behaviour observed for the other two analogous compounds, but to a much greater extent.

Since both secondary phases could be identified and quantified, the high temperature data (from 320-450 K) could be fit to the Curie-Weiss law (inset Figure 4.30). The Curie constant was found to be 4.94(2) emu K/mol, with a Weiss constant of + 83(1) K. The positive Weiss constant suggests dominant ferromagnetic interactions, in contrast to the negative Weiss constant found for  $\text{La}_5\text{Re}_3\text{MnO}_{16}$ .<sup>1</sup> In addition, the Curie constant derived from the fit agrees well with the expected spin-only value (4.875 emu K/mol), calculated based on 50% Nb substitution [50%  $\text{Re}^{5+}$  ( $S = 1$ , full  $C = 1.00$  emu K/mol) and 100%  $\text{Ni}^{2+}$  ( $S = 1$ ,  $C = 1.00$  emu K/mol)]. In fact, this experimental Curie constant is actually quite close to that determined for  $\text{La}_5\text{Re}_3\text{MnO}_{16}$  (4.43(4) emu/mol)<sup>1</sup> as well. Yet, the Curie constant for  $\text{La}_5\text{Re}_3\text{MnO}_{16}$  should actually be higher (5.375 emu K/mol), since it would include the full contribution of  $\text{Re}^{5+}$ .

A plot of the product of ZFC susceptibility and temperature versus temperature (Figure 4.31) does show the 160 K cusp more prominently. The shoulder at 125 K, and the broad 65 K feature appear at very high values above the red line, which denotes the expected spin-only Curie constant of 4.875 emu K/mol for  $\text{La}_5\text{Re}_{2.5}\text{Nb}_{0.5}\text{MnO}_{16}$ . This behaviour is a clear sign of ferro- or ferri-magnetism. Only at the lowest temperatures

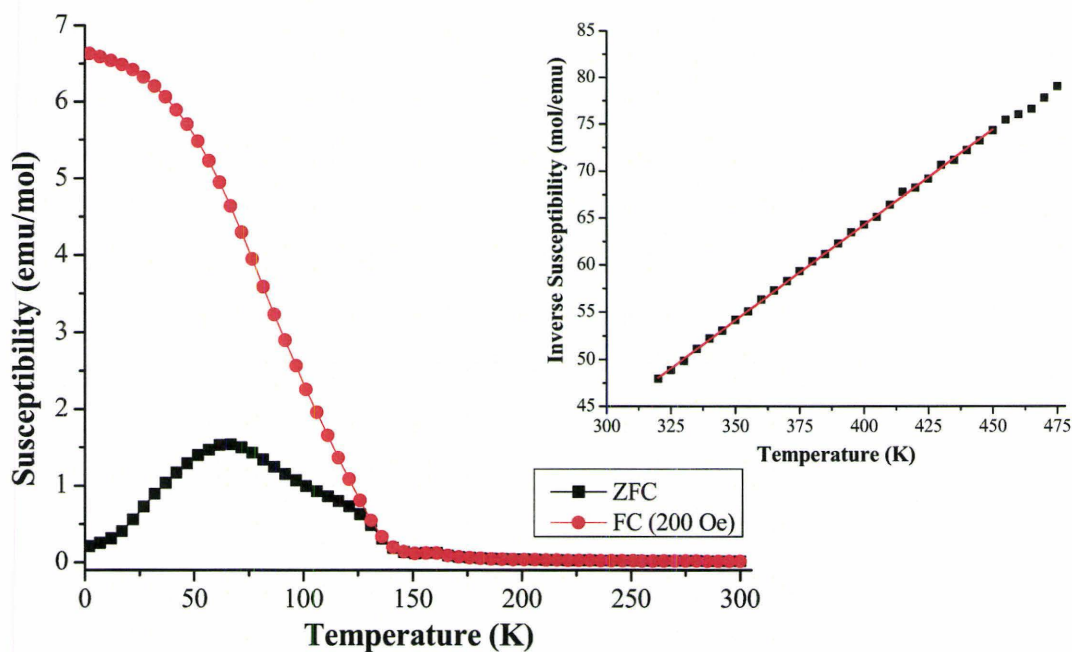


Figure 4.30 ZFC/FC magnetic susceptibility of  $\text{La}_5\text{Re}_{3-x}\text{Nb}_x\text{MnO}_{16}$ . *Inset* – Inverse susceptibility plot for  $\text{La}_5\text{Re}_{3-x}\text{Nb}_x\text{MnO}_{16}$ . The line is the fit to the Curie-Weiss Law.

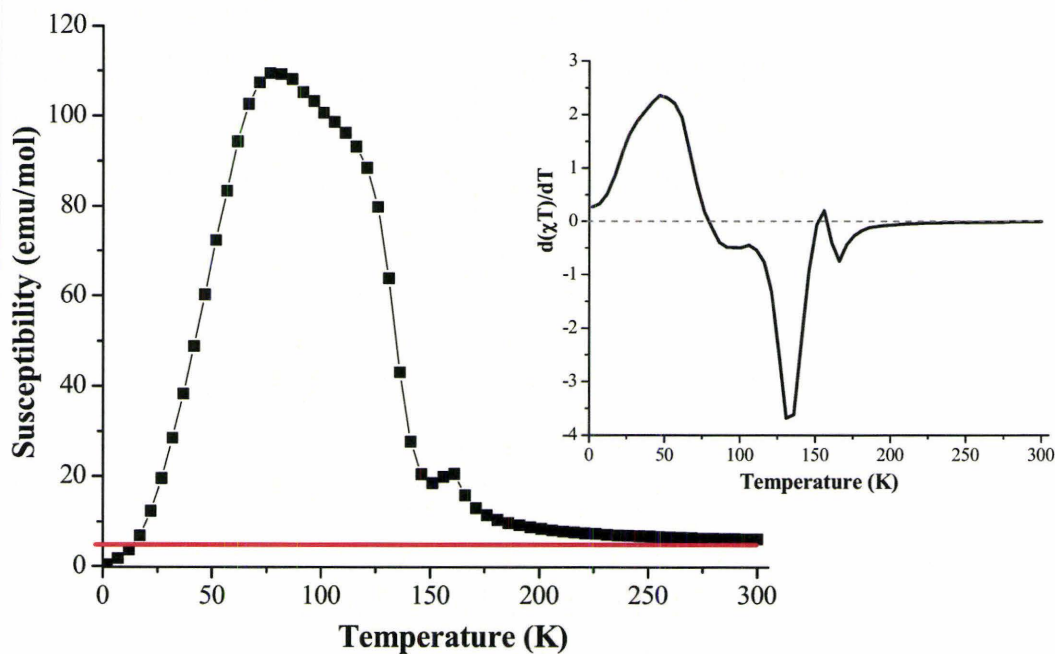


Figure 4.31.  $\chi T$  versus temperature plot for  $\text{La}_5\text{Re}_{3-x}\text{Nb}_x\text{MnO}_{16}$ . The horizontal line is the estimated spin-only Curie constant. *Inset* – Fisher heat capacity for  $\text{La}_5\text{Re}_{3-x}\text{Nb}_x\text{MnO}_{16}$ .

measured do the data cross this line. At higher temperatures,  $\chi T$  approaches the Curie constant line, indicating that the magnetism is nearing the paramagnetic regime.

Finally, the Fisher heat capacity<sup>16</sup> or derivative of  $\chi T$  with respect to temperature, plotted against the temperature is pictured in the inset of Figure 4.31. This graph approximates the expected heat capacity data for this compound, with respect to any magnetic transitions. The broad feature in the magnetic data remains large and very symmetric, a sign of short-range order. However, a very small portion of the lambda-like peak at 160 K remains above the zero line.

This niobium study supports the idea that some substitution of a 5+, spin zero ion for  $\text{Re}^{5+}$  within the layers of a pillared perovskite compound does indeed occur, and has some interesting effects on the resulting magnetic properties.

#### *Heat Capacity*

Due to the limitations of the equipment used, only compounds with suspected critical temperatures below 50 K could be measured with a high degree of accuracy. As such, heat capacity data was collected on the Co and Ni compounds. A non-magnetic analogue,  $\text{La}_5\text{Re}_{3-x}\text{Ta}_x\text{MgO}_{16}$ , was also synthesized in a similar manner and measured to account for the contribution of the lattice to the heat capacity. Unfortunately, due to the presence of unknown impurities in all of the samples measured, quantitative analysis of the heat capacity data would be dubious at best. However, qualitative information, such as the presence of lambda-like anomalies and the temperature of their peak maxima can still be extracted.

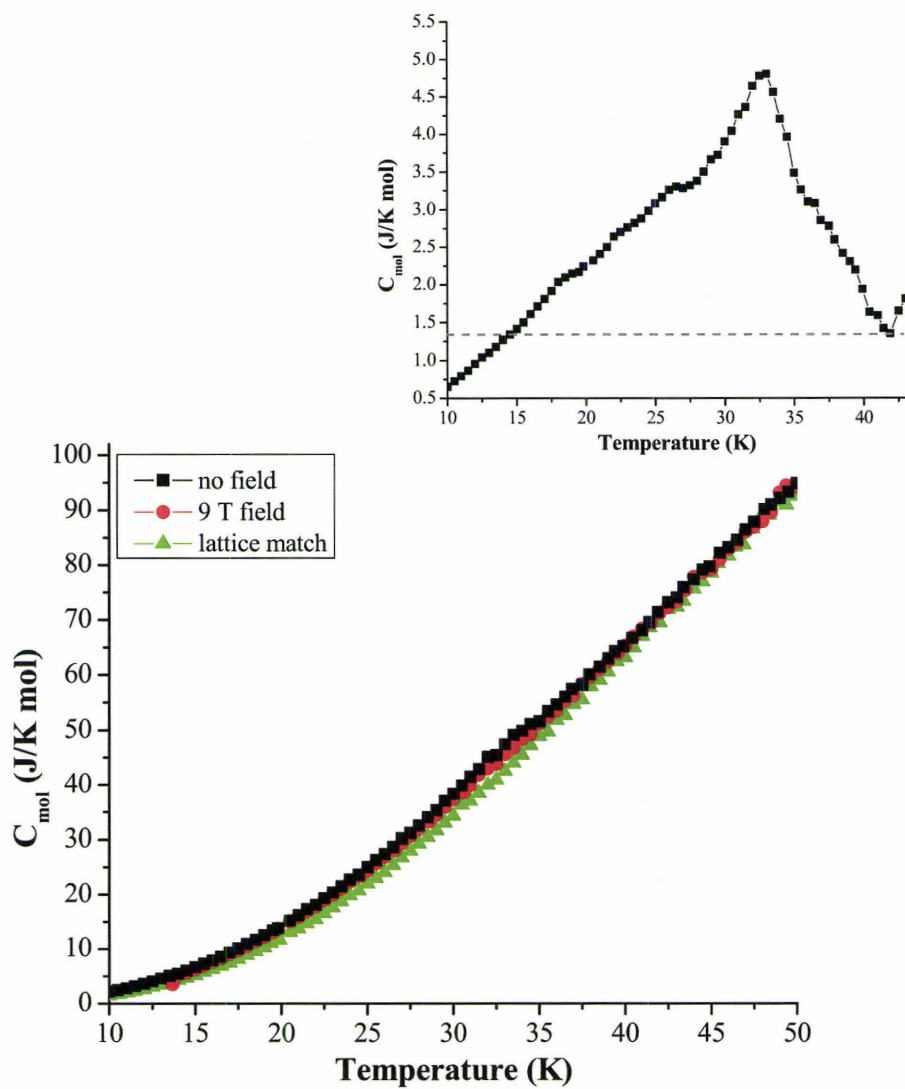


Figure 4.32. Heat capacity data for  $\text{La}_5\text{Re}_{3-x}\text{Ta}_x\text{CoO}_{16}$  with and without an applied field of 9.0 T. The lattice match compound,  $\text{La}_5\text{Re}_{3-x}\text{Ta}_x\text{MgO}_{16}$ , is also shown. *Inset* – Subtraction of the lattice match. Note the lambda-like shape of the anomaly.

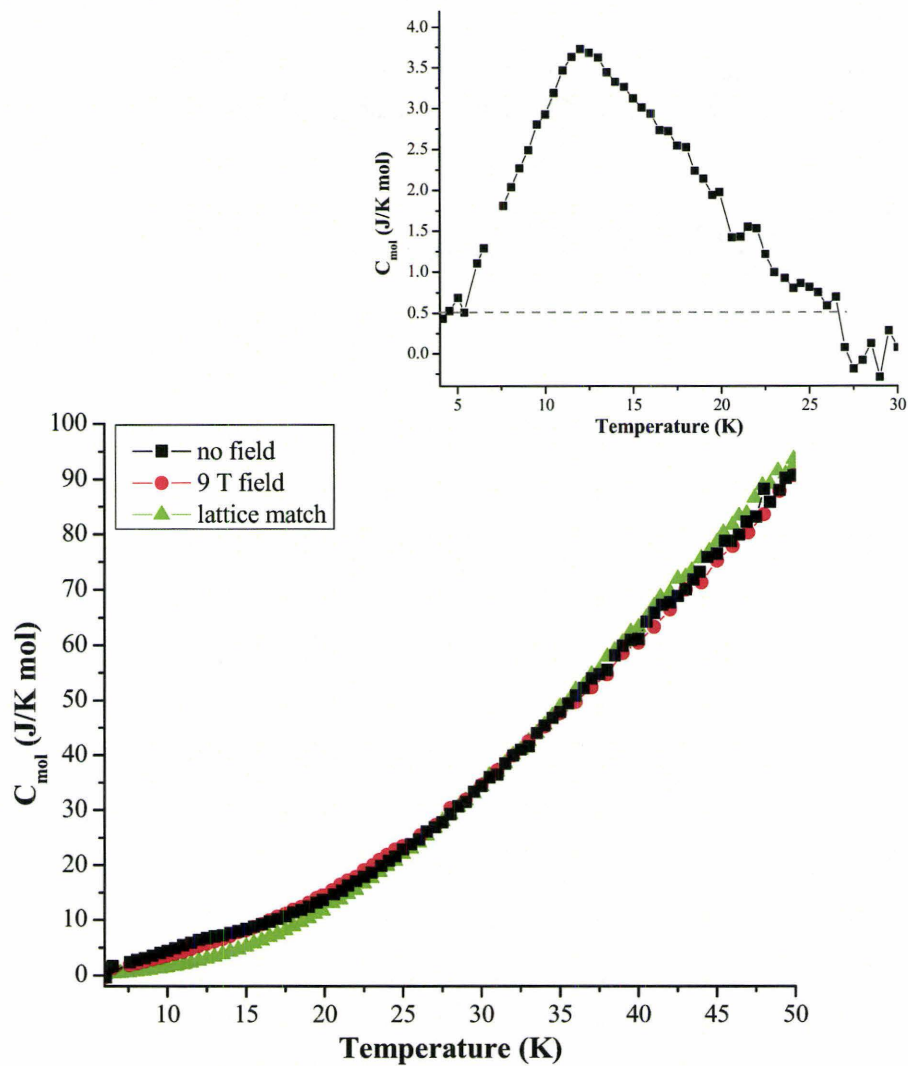


Figure 4.33. Heat capacity data for  $\text{La}_5\text{Re}_{3-x}\text{Ta}_x\text{NiO}_{16}$  with and without an applied field of 9.0 T. The lattice match compound,  $\text{La}_5\text{Re}_{3-x}\text{Ta}_x\text{MgO}_{16}$ , is also shown. *Inset* – Subtraction of the lattice match.

The heat capacity of  $\text{La}_5\text{Re}_{3-x}\text{Ta}_x\text{CoO}_{16}$  from 10 to 50 K, determined in the absence and presence of a 9.0 T magnetic field, as well as the heat capacity of the lattice match compound, is pictured in Figure 4.32. There is a very small, broad feature at about 32 K in the heat capacity of  $\text{La}_5\text{Re}_{3-x}\text{Ta}_x\text{CoO}_{16}$ , which is slightly suppressed upon application of the magnetic field. Subtraction of the lattice match (inset Figure 4.32) yields a lambda-shaped anomaly with peak maximum at about 33 K. The shape indicates long-range magnetic order and the temperature of this transition agrees well with the magnetic data.

Similarly, the heat capacity of  $\text{La}_5\text{Re}_{3-x}\text{Ta}_x\text{NiO}_{16}$ , collected from 2 to 50 K with and without a 9.0 T field applied, as well as the heat capacity due to the lattice is displayed in Figure 4.33. A small, broad anomaly in the  $\text{La}_5\text{Re}_{3-x}\text{Ta}_x\text{NiO}_{16}$  heat capacity is evident at about 12 K, and is somewhat suppressed when a 9.0 T field is applied. Upon subtraction of the lattice match (inset Figure 4.32), the broad, asymmetric shape of the feature is more apparent. Lower temperature data might be able to resolve the shape, however, it may also indicate that only short-range magnetic interactions are present in  $\text{La}_5\text{Re}_{3-x}\text{Ta}_x\text{NiO}_{16}$ . However, the peak maximum of 12 K agrees well with the assignment of  $T_C$  from the magnetic susceptibility data.

#### *Variable Temperature Neutron Diffraction*

The crystal structure of each compound in the  $\text{La}_5\text{Re}_{3-x}\text{Ta}_x\text{BO}_{16}$  series ( $B = \text{Mn}, \text{Fe}, \text{Co}, \text{Ni}, \text{Mg}$ ) was determined from powder neutron diffraction data collected at room temperature and has been discussed previously. However, when these samples were

subsequently cooled well below their suspected critical temperatures for magnetic order ( $\sim 4$  K), new peaks appeared in their powder neutron diffraction patterns.

For the Mn, Fe and Co members of the series, the new reflections could all be indexed to a magnetic unit cell with ordering vector  $\mathbf{k} = (0\ 0\ 1/2)$ . Figure 4.34 displays the patterns collected at various temperatures for the Mn member, highlighting the new reflections. This magnetic unit cell had been observed previously for the  $\text{La}_5\text{Re}_3\text{BO}_{16}$  ( $B = \text{Mn, Fe, Co}$ ) series of compounds.<sup>3,4</sup> The magnetic structure of  $\text{La}_5\text{Re}_3\text{BO}_{16}$  ( $B = \text{Mn, Fe, Co}$ ) can be described as ferrimagnetically coupled moments on the  $\text{Re}^{5+}$  ( $S = 1$ ) and  $B^{2+}$  ( $S = 5/2, 2, 3/2$ ) sites within the layers, and the layers themselves coupled antiferromagnetically. This interlayer antiferromagnetic coupling causes the doubling of the chemical  $c$ -axis in the magnetic unit cell. Since the same magnetic structural peaks were found for the Mn, Fe and Co members of the  $\text{La}_5\text{Re}_{3-x}\text{Ta}_x\text{BO}_{16}$  series, it follows that the magnetic structure is also the same or very similar. Random substitution of  $\text{Ta}^{5+}$  for approximately half of the  $\text{Re}^{5+}$  ions within the layers of the pillared perovskite could still result in ferrimagnetic intralayer coupling, however, with a much greater ferromagnetic component, as some of the  $B^{2+}$  moment would be uncompensated. Nonetheless, the overall magnetic contribution to certain reflections should be less, as some of the magnetic ions in the system have been removed. Assuming random replacement of  $\text{Ta}^{5+}$  for half of the  $\text{Re}^{5+}$  ions within the layers, the magnetic structure of  $\text{La}_5\text{Re}_{3-x}\text{Ta}_x\text{BO}_{16}$  compounds would consist of ferrimagnetically coupled  $B$  moments within the layers, which are then coupled antiferromagnetically, as shown (inset Figure 4.34).

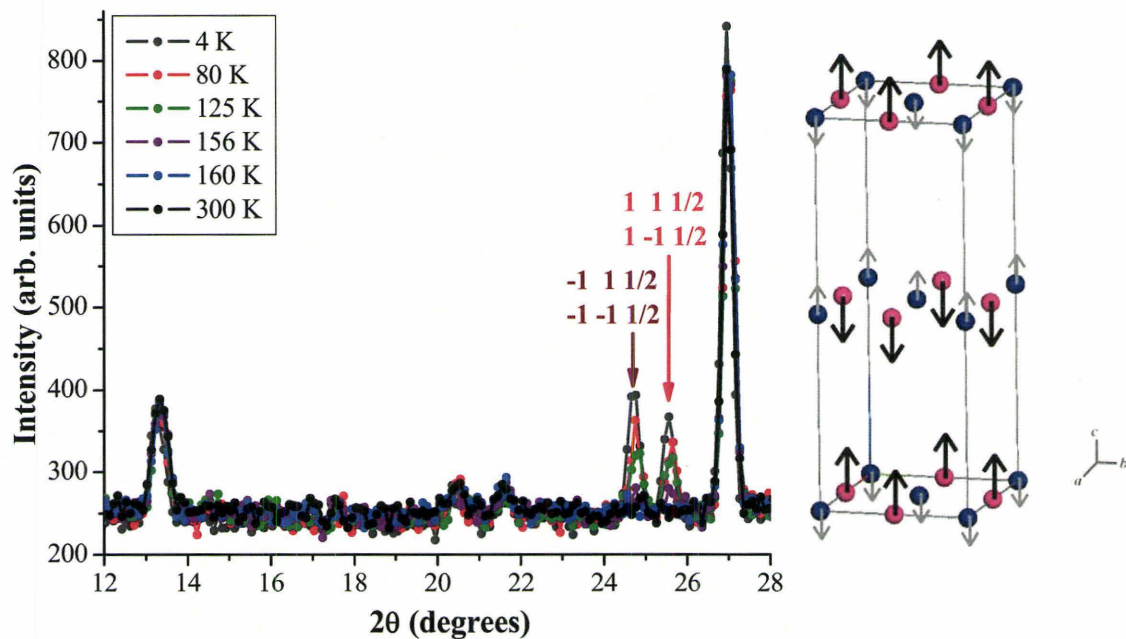


Figure 4.34. Powder neutron diffraction pattern of  $\text{La}_5\text{Re}_{3-x}\text{Ta}_x\text{MnO}_{16}$  taken at various temperatures. The new magnetic reflections are denoted with arrows, and their indices to the magnetic unit cell are also indicated. *Inset* – Magnetic unit cell of  $\text{La}_5\text{Re}_{3-x}\text{Ta}_x\text{BO}_{16}$  ( $B = \text{Mn, Fe, Co}$ ). The moments on the blue Re sites are much smaller, since they are partially substituted randomly by Ta. In the Mn compound, the moments on the pink Mn ions are canted slightly off-axis.

Unfortunately, due to significant sample contamination by unknown secondary phase peaks, the magnetic moments could not be refined directly. However, relatively good fits to the low temperature neutron data were found when approximate spin-only values for the *B* site moments were used (Figure 4.35 a-d). In the refinements of the Fe and Co members, the moments were oriented parallel to the *c*-axis. For the Mn sample, where off-axis canting of the moment is suspected, a small component was included in the *ab*-plane. Finally, for the Ni compound, the majority of the moment was oriented 45° in the *ab*-plane, with a small component due to spin canting, directed along the *c*-axis. In addition, a small moment (~ half the spin-only effective moment of a  $S=1$  magnetic ion) was placed on the in-layer Re position in an attempt to improve the refinements. However, this did not make a significant difference in the overall agreement of the fit, as evident by examination of the  $R_p$ ,  $R_{wp}$  and  $\chi^2$  values. It is not possible to refine the data further, as the quality of the samples is insufficient for such detailed analysis.

For Mn, Fe and Co, neutron powder patterns were collected as a function of temperature. The critical temperature determined from the neutron diffraction data matched well with the SQUID magnetometry data, confirming  $T_c$  for long-range magnetic order.

Some interesting features were also observed in the powder neutron diffraction data. In  $\text{La}_5\text{Re}_{3-x}\text{Ta}_x\text{MnO}_{16}$ , one low-angle reflection has a slightly different temperature dependence, disappearing by 80-100 K. In addition, the intensity of the other magnetic peaks appears to dip sharply between 40 and 80 K (Figure 4.36). This new reflection indexes to  $0\ 0\ 1/2$  in the magnetic unit cell. In order for this peak to have any intensity,

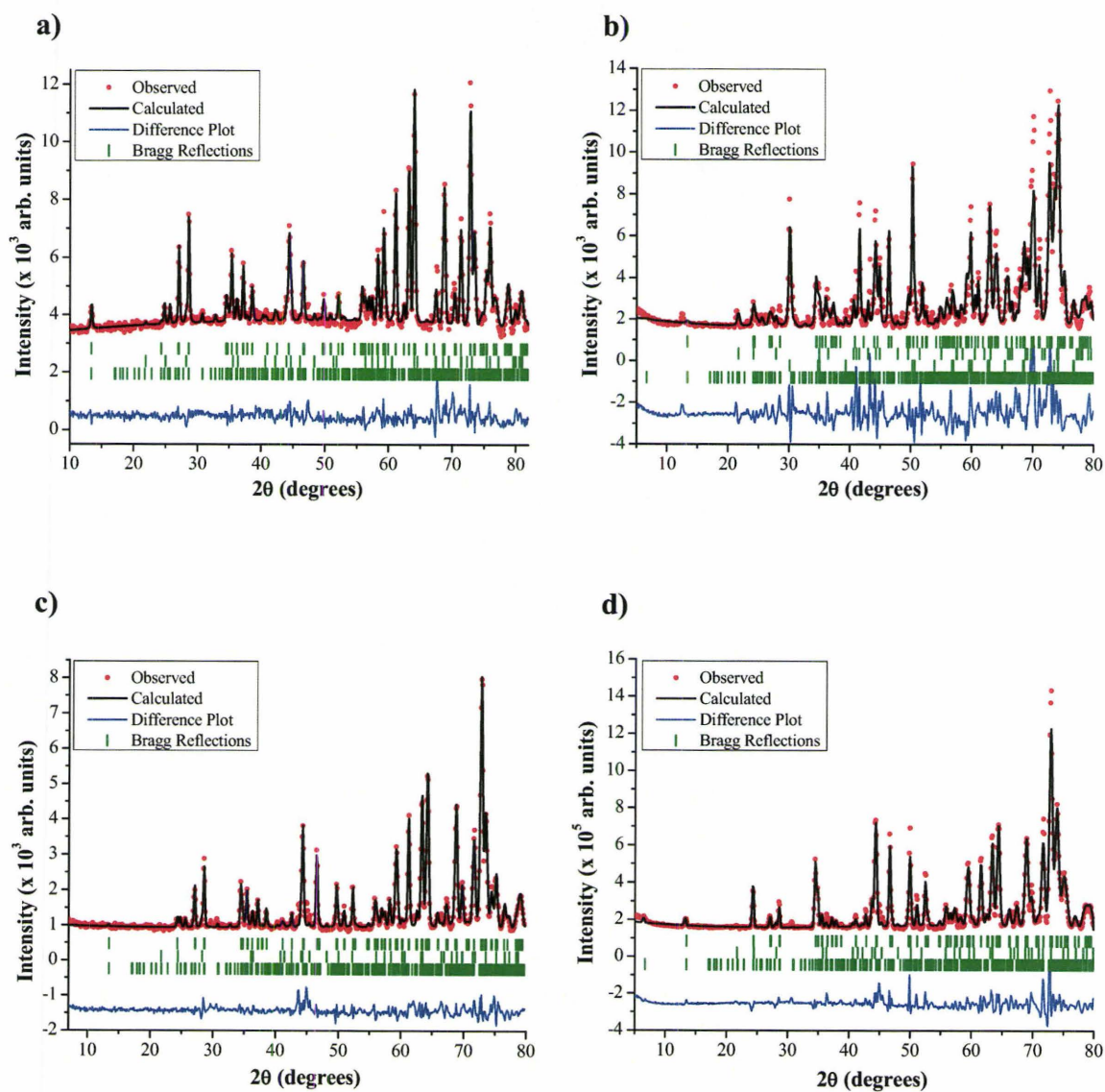


Figure 4.35. Rietveld refinements of low temperature powder neutron diffraction data for  $\text{La}_5\text{Re}_{3-x}\text{Ta}_x\text{BO}_{16}$ : a) Mn, b) Fe, c) Co, d) Ni. The top Bragg reflections are for the major phase, middle Bragg reflections are for  $\text{La}_3\text{TaO}_7$  and the bottom Bragg reflections are the magnetic phase.

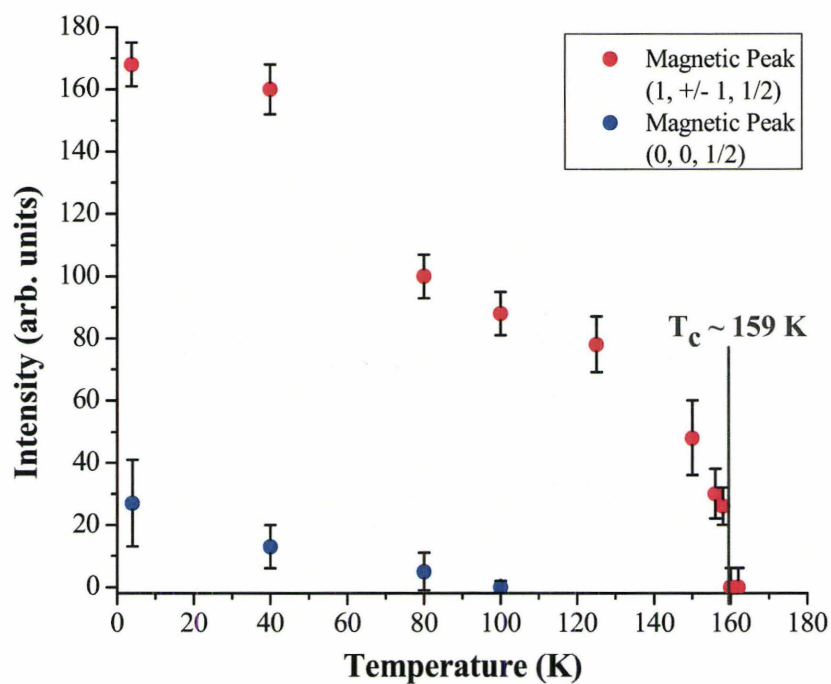


Figure 4.36. Intensity of the (0 0 1/2) and the (1 1 1/2)/(1 -1 1/2) reflection versus temperature for  $\text{La}_5\text{Re}_{3-x}\text{Ta}_x\text{MnO}_{16}$ . The vertical line denotes the critical temperature.

the moments must be directed off the  $c$ -axis, implying canting of the magnetic moments at lower temperatures. This was also observed previously in  $\text{La}_5\text{Re}_3\text{MnO}_{16}$ , but only the Mn moments were canted, about  $18^\circ$  off-axis.<sup>2</sup> The change in intensity for the other magnetic peaks may also imply slight off-axis canting of the Mn moments in  $\text{La}_5\text{Re}_{3-x}\text{Ta}_x\text{MnO}_{16}$ . The magnetic susceptibility curve showed a broad feature at about 100 K that could be caused by this spin reorientation. In addition, one of the “S”-shaped anomalies in the magnetization curve could be caused by realignment of the canted Mn moments. This secondary reflection was only observed for the Mn compound, however.

The Ni member had a very different powder diffraction pattern at 4 K (Figure 4.37). The only new reflection observed was a low angle peak that could be indexed as  $0\ 0\ 1/2$ . The higher angle reflections present in the patterns of the other  $\text{La}_5\text{Re}_{3-x}\text{Ta}_x\text{BO}_{16}$  compounds were not observed. This implies that in the Ni material, the moments are oriented perpendicular to the  $c$ -axis, rather than parallel to it. This behaviour was also noted previously, in the study of  $\text{La}_5\text{Re}_3\text{NiO}_{16}$ .<sup>4</sup> Similarly, the exact angle in the  $ab$  plane has a high degree of variability. However, for  $\text{La}_5\text{Re}_{3-x}\text{Ta}_x\text{NiO}_{16}$ , there appears to be a much smaller component to the moment along the  $c$ -axis. Due to the presence of the  $0\ 0\ 1/2$  reflection, the layers themselves are still coupled antiferromagnetically. The resulting magnetic structure of this compound is pictured in the inset of Figure 4.37. Since this reflection is so weak in  $\text{La}_5\text{Re}_{3-x}\text{Ta}_x\text{NiO}_{16}$ , measurements to follow the temperature dependence of the peak were not undertaken.

Another observation of note is that the relative intensity of the magnetic peaks with respect to the structural reflections is much lower in the  $\text{La}_5\text{Re}_{3-x}\text{Ta}_x\text{BO}_{16}$  series than

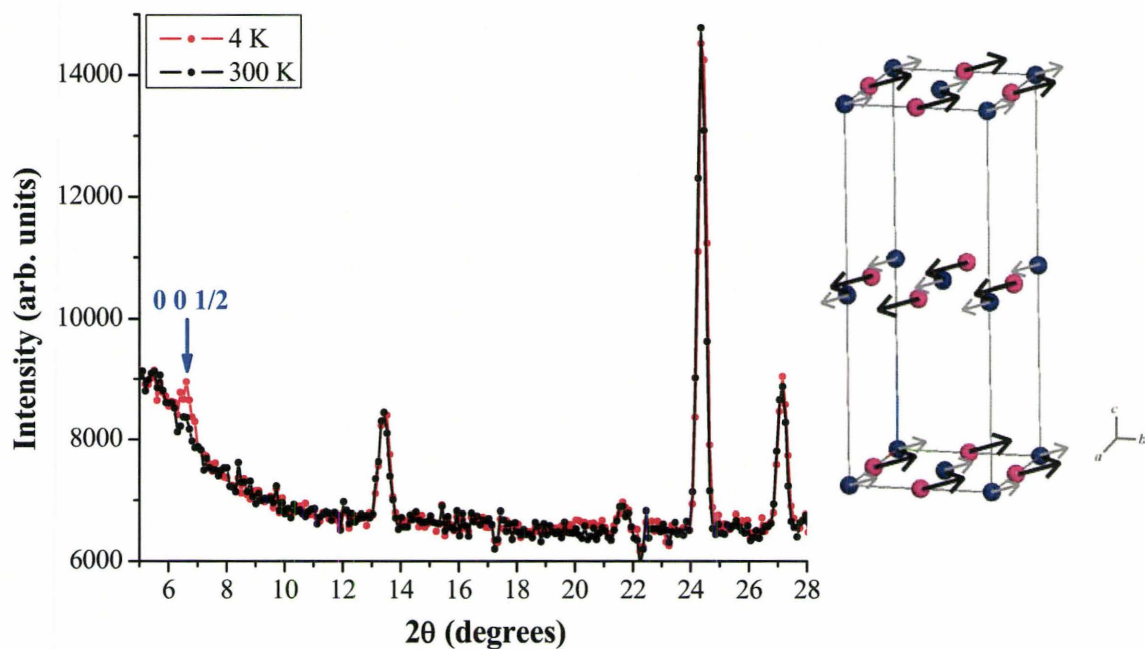


Figure 4.37. Powder neutron diffraction pattern of  $\text{La}_5\text{Re}_{3-x}\text{Ta}_x\text{NiO}_{16}$  at 4 K and room temperature. The new magnetic reflection is denoted with an arrow, and indexed as shown. *Inset* – Magnetic unit cell of  $\text{La}_5\text{Re}_{3-x}\text{Ta}_x\text{NiO}_{16}$ . The moments on the blue Re sites are much smaller, since they are partially substituted randomly by Ta.

for  $\text{La}_5\text{Re}_3\text{BO}_{16}$ . As discussed previously, this is expected if non-magnetic  $\text{Ta}^{5+}$  was partially substituted within the perovskite layers. The overall contribution to the magnetic reflections should be lower than in the parent compounds since the magnetic system is more dilute. This appears to be the case in all of the  $\text{La}_5\text{Re}_{3-x}\text{Ta}_x\text{BO}_{16}$  ( $B = \text{Mn, Fe, Co, Ni}$ ) compounds measured.

From the neutron diffraction data, apparent partial substitution of magnetic  $\text{Re}^{5+}$  for non-magnetic  $\text{Ta}^{5+}$  within the perovskite layers has little effect on the critical temperature for long-range order. This can be understood if the weaker interlayer coupling is the factor that determines the long-range magnetic ordering.

#### 4.5 Conclusions

The synthesized compounds,  $\text{La}_5\text{Re}_{3-x}\text{Ta}_x\text{BO}_{16}$  ( $B = \text{Mn, Fe, Co, Ni}$ ), would represent a more magnetically dilute subsystem of the previously investigated  $\text{La}_5\text{Re}_3\text{BO}_{16}$  compounds. There is evidence of approximately 50% Ta substitution. Both the SEM-EDS and TEM-EDS analyses of  $\text{La}_5\text{Re}_{3-x}\text{Ta}_x\text{MnO}_{16}$  and  $\text{La}_5\text{Re}_{3-x}\text{Nb}_x\text{MnO}_{16}$  showed the presence of tantalum and niobium, respectively, within the pillared perovskite phase. In addition, analysis of the X-ray diffraction pattern also confirmed approximately 50% Nb substitution within the  $\text{La}_5\text{Re}_{3-x}\text{Nb}_x\text{MnO}_{16}$  compound. The magnetic properties (i.e.  $T_c$ , magnetic structures) of both the  $\text{La}_5\text{Re}_{3-x}\text{Ta}_x\text{BO}_{16}$  ( $B = \text{Mn, Fe, Co, Ni}$ ) and  $\text{La}_5\text{Re}_{3-x}\text{Nb}_x\text{MnO}_{16}$  are very similar to those observed for the analogous  $\text{La}_5\text{Re}_3\text{BO}_{16}$  ( $B = \text{Mn, Fe, Co, Ni}$ ) compounds. However, it still is surprising that the removal of some of the magnetic ions per formula unit has little to no effect on the magnetic properties of the

pillared perovskites, most notably the magnetic ordering temperature, and magnetic structure. The similarities between the two series of rhenium-based pillared perovskites are summarized in Table 4.12 below.

Table 4.12. Magnetic Data Comparison of the  $\text{La}_5\text{Re}_{3-x}\text{Ta}_x\text{BO}_{16}$  and  $\text{La}_5\text{Re}_3\text{BO}_{16}$  Series and  $\text{La}_5\text{Re}_{3-x}\text{Nb}_x\text{MnO}_{16}$ .<sup>3,4</sup>

<i>B</i>	$\text{La}_5\text{Re}_{3-x}\text{Ta}_x\text{BO}_{16}$		$\text{La}_5\text{Re}_3\text{BO}_{16}$		$\text{La}_5\text{Re}_{3-x}\text{NbBO}_{16}$	
	$T_c$ (K)	$T_c/S^2$ (K)	$T_c$ (K)	$T_c/S^2$ (K)	$T_c$ (K)	$T_c/S^2$ (K)
Mn	160	26	161	26	160	26
Fe	135	34	155	39		
Co	35	16	35	16		
Ni	12	12	14	14		
Mg	-	-	-	-		

As previously mentioned in the Introduction, dividing the critical temperature by the square of the spin quantum number gives a relative estimation of the strength of the intraplanar correlation length and the interplanar exchange constant. For  $\text{La}_5\text{Re}_{3-x}\text{Ta}_x\text{BO}_{16}$  ( $B = \text{Mn, Fe, Co, Ni}$ ), two sets of compounds emerge: Mn and Fe have high values, whereas Co and Ni have low values, following the same trend as the  $\text{La}_5\text{Re}_3\text{BO}_{16}$  series. Both Mn and Fe show unusual and interesting magnetic behaviour, exhibiting shorter-range interactions below their critical temperatures, and a secondary transition at higher field in their magnetization curves.

One other striking similarity between the two series is the magnetic structures of the compounds. In both the  $\text{La}_5\text{Re}_{3-x}\text{Ta}_x\text{BO}_{16}$  and  $\text{La}_5\text{Re}_3\text{BO}_{16}$  series, the Mn, Fe and Co members have the moments of the  $B^{2+}$  ions aligned parallel to the  $c$ -axis, coupled

ferrimagnetically within the layers. There is slight off-axis canting of the Mn moments in both sets of compounds. In addition, the layers are coupled antiferromagnetically. The Ni species has the same basic magnetic structure in both series as well, which is completely different from the other materials. The Ni moments are also ferromagnetically correlated within the layers, however, they lie perpendicular or slightly canted with respect to the *c*-axis. The exact orientation of the moments within the *ab* plane is not well determined, as equally good fits are obtained for a range of angles. However, the layers remain antiferromagnetically coupled in this pillared perovskite as well.

With such similarities in the magnetic ordering temperatures and magnetic structures, it is fascinating that partial substitution of non-magnetic tantalum does not have a greater effect on these magnetic properties. However, closer analysis of the pillared perovskite structure reveals that only the  $B^{2+}$  cations are linked through the diamagnetic “pillars” connecting the layers. If the  $B^{2+}$  interlayer magnetic exchange pathway is important to the overriding magnetism, and dictates the transition to long range order, then it would not be surprising to see why Ta substitution would have little to no effect on those properties, since it is not involved in this interaction at all. Within the layers, ferrimagnetic coupling of the remaining  $Re^{5+}$  and  $B^{2+}$  ions persists, despite violating the Goodenough-Kanamori rules of magnetic superexchange. Again, if interlayer exchange were the dominant interaction, this would force the moments within the layer to align in this manner, despite their preference for ferromagnetic  $Re^{5+}-B^{2+}$

coupling. These facts suggest that the interplanar coupling pathway plays a key role in determining the magnetic ordering and magnetic structure of the pillared perovskites.

#### 4.6 References

1. Wiebe, C. R.; Gourrier, A.; Langet, T.; Britten, J. F.; Greedan, J. E. *J. Solid State Chem.* **2000**, *151*, 31-39.
2. Green, A. E. C.; Wiebe, C. R.; Greedan, J. E. *Solid State Sciences* **2002**, *4*, 305-310.
3. Chi, L.; Green, A. E. C.; Hammond, R.; Wiebe, C. R.; Greedan, J. E. *J. Solid State Chem.* **2003**, *170*, 165-175.
4. Cuthbert, H. L.; Greedan, J. E.; Cranswick, L. *J. Solid State Chem.* **2006**, *179*, 1938-1947.
5. Ledesert, M.; Labbe, P.; McCarroll, W. H.; Leligny, H.; Raveau, B. *J. Solid State Chem.* **1993**, *105*, 143-150.
6. Ramanujachary, K. V.; Greenblatt, M.; McCarroll, W. H.; Goodenough, J. B. *Mat. Res. Bull.* **1993**, *28*, 1257-1267.
7. Ramanujachary, K. V.; Lofland, S. E.; McCarroll, W. H.; Emge, T. J.; Greenblatt, M. *J. Solid State Chem.* **2002**, *164*, 60-70.
8. Chi, L.; Swainson, I. P.; Greedan, J. E. *J. Solid State Chem.* **2004**, *177*, 3086-3091.
9. de Jongh, L. J. In *Magnetic Properties of Layered Transition Metal Compounds*; de Jongh, L. J., Ed.; Kluwer Academic Publishers: Dordrecht, 1990, p 19.
10. Goodenough, J. B. *Magnetism and the Chemical Bond*; Wiley: New York, 1963.
11. Kanamori, J. *J. Phys. Chem. Solids* **1959**, *10*, 87-98.
12. Jette, E. R.; Foote, F. *J. Chem. Phys.* **1933**, *1*, 29-36.
13. Mulay, L. N. In *Theory and Applications of Molecular Paramagnetism*; Boudreaux, E. A., Mulay, L. N., Eds.; John Wiley & Sons: New York, 1976, p 494-495.
14. Shannon, R. D. *Acta Crystallogr.* **1976**, *A32*, 751-767.
15. Hill, R. J.; Howard, C. J. *J. Appl. Cryst.* **1987**, *20*, 467-474.
16. Fisher, M. E. *Philos. Mag.* **1962**, *7*, 1731-43.

**Appendix A – Atomic Position Data from Powder Neutron Diffraction Refinements for  $\text{La}_5\text{Re}_{3-x}\text{Ta}_x\text{BO}_{16}$  ( $B = \text{Mn, Fe, Co, Ni}$ )**

**$\text{La}_5\text{Re}_{3-x}\text{Ta}_x\text{MnO}_{16}$**

Atom	x	y	z
LA1	0.228(2)	0.748(2)	0.801(2)
LA2	0.228(2)	0.270(2)	0.781(2)
LA3	0.50000	0.50000	0.50000
RE1	0.055(2)	0.495(3)	0.396(1)
TA1	0.00000	0.00000	0.00000
MN1	0.00000	0.50000	0.00000
O1	0.190(2)	0.519(3)	0.568(2)
O2	0.280(2)	0.501(4)	0.323(2)
O3	-0.047(2)	0.489(4)	0.198(2)
O4	0.070(2)	0.012(4)	0.174(2)
O5	0.038(4)	0.723(3)	0.367(3)
O6	0.045(3)	0.258(3)	0.371(3)
O7	-0.062(2)	0.253(3)	-0.003(2)
O8	0.232(3)	0.061(2)	-0.040(2)

**$\text{La}_5\text{Re}_{3-x}\text{Ta}_x\text{FeO}_{16}$**

Atom	x	y	z
LA1	0.273(5)	0.773(3)	0.816(5)
LA2	0.212(6)	0.260(7)	0.796(5)
LA3	0.50000	0.50000	0.50000
RE1	0.062(5)	0.498(5)	0.442(4)
TA1	0.00000	0.00000	0.00000
FE1	0.00000	0.50000	0.00000
O1	0.230(8)	0.496(9)	0.602(7)
O2	0.292(8)	0.489(8)	0.305(7)
O3	-0.073(7)	0.511(9)	0.193(6)
O4	0.052(6)	-0.001(9)	0.182(6)
O5	0.071(8)	0.743(8)	0.414(6)
O6	0.018(8)	0.234(9)	0.358(6)
O7	-0.004(9)	0.246(8)	0.047(7)
O8	0.232(9)	0.066(7)	-0.045(6)

**La<sub>5</sub>Re<sub>3-x</sub>Ta<sub>x</sub>CoO<sub>16</sub>**

<b>Atom</b>	<b>x</b>	<b>y</b>	<b>z</b>
LA1	0.222(3)	0.755(2)	0.799(2)
LA2	0.229(3)	0.269(2)	0.800(2)
LA3	0.50000	0.50000	0.50000
RE1	0.057(2)	0.493(2)	0.393(1)
TA1	0.00000	0.00000	0.00000
CO1	0.00000	0.50000	0.00000
O1	0.186(3)	0.528(3)	0.567(2)
O2	0.292(2)	0.492(3)	0.323(2)
O3	-0.046(2)	0.504(4)	0.198(2)
O4	0.075(2)	0.004(4)	0.184(2)
O5	0.040(4)	0.726(3)	0.371(3)
O6	0.052(3)	0.256(3)	0.363(3)
O7	-0.059(2)	0.237(3)	-0.008(2)
O8	0.232(3)	0.051(2)	-0.039(2)

**La<sub>5</sub>Re<sub>3-x</sub>Ta<sub>x</sub>NiO<sub>16</sub>**

<b>Atom</b>	<b>x</b>	<b>y</b>	<b>z</b>
LA1	0.226(3)	0.755(2)	0.803(2)
LA2	0.222(3)	0.265(2)	0.798(2)
LA3	0.50000	0.50000	0.50000
RE1	0.053(2)	0.496(2)	0.389(1)
TA1	0.00000	0.00000	0.00000
NI1	0.00000	0.50000	0.00000
O1	0.192(3)	0.525(3)	0.569(2)
O2	0.285(2)	0.490(3)	0.321(2)
O3	-0.044(2)	0.515(3)	0.199(2)
O4	0.071(2)	0.001(4)	0.184(2)
O5	0.036(3)	0.729(3)	0.372(2)
O6	0.059(3)	0.259(3)	0.360(3)
O7	-0.053(2)	0.234(3)	-0.011(2)
O8	0.229(3)	0.052(2)	-0.034(2)

## Chapter 5

### **Synthesis, Structure and Unexpected Magnetic Properties of $\text{La}_3\text{Re}_2\text{O}_{10}$**

This chapter contains the manuscript “Synthesis, Structure and Unexpected Magnetic Properties of  $\text{La}_3\text{Re}_2\text{O}_{10}$ ”, published in the journal *Inorganic Chemistry* (*Inorg. Chem.* **2007**, *46*, 8739-8745). The candidate completed all of the experimental synthesis and measurements, as well as all data processing and interpretation. Collaborators Dr. Ignacio Vargas-Baca and Dr. Shahab Derakhshan performed all of the calculations (DFT and EHTB spin dimer analysis, respectively). The candidate also prepared the manuscript and submitted it to the journal as corresponding author.

Reproduced with permission from Cuthbert, H.L.; Greedan, J.E.; Derakhshan, S.; Vargas-Baca, I.; Swainson, I.P. *Inorg. Chem.* **2007**, *46*, 8739-8745. Copyright 2007 American Chemical Society.

## **Synthesis, Structure and Unexpected Magnetic Properties of $\text{La}_3\text{Re}_2\text{O}_{10}$**

Heather L. Cuthbert<sup>\*a,b</sup>, John E. Greedan<sup>a,b</sup>, Ignacio Vargas-Baca<sup>a</sup>, Shahab Derakhshan<sup>a,b</sup>  
and Ian P. Swainson<sup>c</sup>

*a* Department of Chemistry, McMaster University, Hamilton, Ontario, Canada, L8S 4M1

*b* Brockhouse Institute for Materials Research, McMaster University, Hamilton, Ontario  
Canada, L8S 4M1

*c* Canadian Neutron Beam Centre, National Research Council, Chalk River Laboratories,  
Chalk River, Ontario, Canada, K0J 1J0

### **5.1 Abstract**

The compound  $\text{La}_3\text{Re}_2\text{O}_{10}$  has been synthesized by solid state reaction, and characterized by powder neutron diffraction, SQUID magnetometry and heat capacity measurements. Its structure consists of isolated  $[\text{Re}_2\text{O}_{10}]^{9-}$  dimer units of two edge-shared  $\text{ReO}_6$  octahedra, separated by  $\text{La}^{3+}$  within the lattice. The Re-Re distance within the dimer units is 2.488 Å, which is indicative of metal-metal bonding with a bond order of 1.5. The average oxidation state of the Re atom is +5.5, leaving one unpaired electron per dimer unit ( $S = 1/2$ ). Although the closest inter-dimer distance is 5.561 Å, the magnetic susceptibility data and heat capacity measurements indicate this compound exhibits both short and long range magnetic order at surprisingly high temperatures. The zero field cooled (ZFC) magnetic susceptibility data show two broad features at 55 K and 105 K, indicating short range order, and a sharper cusp at 18 K, which signifies long range antiferromagnetic order. The heat capacity of  $\text{La}_3\text{Re}_2\text{O}_{10}$  shows a lambda-type anomaly at 18 K, which is characteristic of long range magnetic order. DFT calculations determined that the unpaired electron resides in a  $\pi$  bonding orbital and that the unpaired

electron density is widely delocalized over the atoms within the dimer, with high values at the bridging oxygens. Extended Hückel spin dimer calculations suggest possible interaction pathways between these dimer units within the crystal lattice. Results from the calculations and fits to the susceptibility data indicate that the short-range magnetic ordering may consist of 1-D antiferromagnetic linear chains of coupled  $S = 1/2$  dimers. The magnetic structure of the antiferromagnetic ground state could not be determined by unpolarized neutron powder diffraction.

## 5.2 Introduction

The magnetic properties of oxides involving the  $4d$  and  $5d$  transition metals have been much less explored, in comparison to the  $3d$  elements. The crystal chemistry and structures of the  $4d$  and  $5d$  oxides are often different, due to the more extended nature of the  $4d$  and  $5d$  orbitals, the occurrence of higher oxidation states and the tendency to form metal-metal bonds. These factors can have a detrimental effect on the resulting magnetism, however, novel magnetic properties are also possible.

There are a few known oxides involving lanthanum and rhenium and many of these contain multiple Re-Re bonds. Of course, in compounds such as  $\text{La}_3\text{ReO}_8$ , rhenium is in its maximum oxidation state and metal-metal bonding does not occur.<sup>1,2</sup> Instead, Re (VII) ions are found in isolated octahedral sites. In contrast,  $\text{La}_4\text{Re}_2\text{O}_{10}$  consists of isolated  $[\text{Re}_2\text{O}_8]^{8-}$  units, linked together by  $\text{La}^{3+}$  ions.<sup>3</sup> The very short Re-Re bond length of  $2.259(1) \text{ \AA}$  is attributed to a triple bond, pairing all electrons. A study of various

rhenium(IV) oxides demonstrated that they can be oxidized and reduced, however, the exact structures of the products were not determined.<sup>4</sup>

In addition, oxides exist with rhenium in a mixed oxidation state. In  $\text{La}_6\text{Re}_4\text{O}_{18}$ , the average oxidation state of rhenium is +4.5.<sup>5</sup> Two different, isolated Re-Re bonded clusters exist:  $[\text{Re}_2\text{O}_8]^{8-}$  and  $[\text{Re}_2\text{O}_{10}]^{10-}$ , with Re-Re bond lengths of 2.235(6) and 2.456(5) Å, respectively, consistent with triple and double bonds. In all of these cases, the metal-metal bonding pairs the electrons within the Re dimers and the result is diamagnetism. However, in  $\text{La}_4\text{Re}_6\text{O}_{19}$ , with Re in the +4.333 state, a three-dimensional framework of edge-shared octahedral dimers that share corners is formed.<sup>6,7</sup> Despite the existence of metal-metal double bonds (Re-Re distance of 2.42 Å), this compound is metallic, indicating the presence of unpaired, but delocalized electrons.

The title compound has been synthesized previously in single crystal form using a hydrothermal method.<sup>8</sup> An unidentified powder was also a product. Its structure is comprised of isolated  $[\text{Re}_2\text{O}_{10}]^{9-}$  dimeric units of two edge-shared  $\text{ReO}_6$  octahedra, separated by  $\text{La}^{3+}$  within the lattice. The Re-Re distance within the dimer units was reported as 2.484(1) Å, consistent with metal-metal bonding. The average oxidation state of the Re is +5.5, leaving one unpaired electron per dimer unit ( $S = 1/2$ ). Semiconducting behaviour was observed, indicating localization of the electrons, and the possibility of magnetism. However, the reported effective magnetic moment of about 6  $\mu_B$  at room temperature for  $\text{La}_3\text{Re}_2\text{O}_{10}$  ( $S = 1/2$ ) does not appear to make much physical sense, given the maximum spin-only effective moment for this system should be 1.73  $\mu_B$ .

The present report focuses on the synthesis of  $\text{La}_3\text{Re}_2\text{O}_{10}$  using conventional solid-state methodologies for the first time, as well as a comprehensive study of its structure by powder X-ray and neutron diffractometry and its magnetic properties, utilizing SQUID magnetometry and heat capacity measurements.

### 5.3 Experimental Methods

#### *Synthesis*

$\text{La}_3\text{Re}_2\text{O}_{10}$  was synthesized by solid state reaction, according to the following:



Stoichiometric amounts of the starting reagents,  $\text{La}_2\text{O}_3$  (99.9%, Aldrich, heated at  $900^\circ\text{C}$  overnight before use),  $\text{ReO}_3$  (Rhenium Alloys) and Re (Rhenium Alloys) were accurately weighed, ground together, pressed into a pellet and placed into a platinum crucible, which was sealed in a quartz tube under vacuum ( $\sim 10^{-5}$  torr). The reactants were heated to  $1050^\circ\text{C}$  in a tube furnace and held for 48 hours. The product obtained was a black powder.

#### *X-ray and Neutron Diffraction*

X-ray diffraction data were collected using a Guinier-Hagg camera with  $\text{CuK}\alpha_1$  radiation ( $\lambda = 1.5406 \text{ \AA}$ ) and high-purity silicon powder as an internal reference. The reflections were recorded on photographic film, and the line intensities were converted to digital format using the KEJ LS-20 line scanner.

Variable temperature powder neutron diffraction measurements were performed on the C2 diffractometer at the Canadian Neutron Beam Centre at Chalk River, Ontario.

Data for crystal structure refinement (285 K) were collected at a wavelength of 1.32917 Å in the angular range of  $12^\circ \leq 2\theta \leq 113^\circ$  with  $0.1^\circ$  steps. Similarly, data for investigation of the magnetic structure (4 and 285 K) were measured at a longer wavelength of 2.36957 Å in the range  $5^\circ \leq 2\theta \leq 85^\circ$  with  $0.1^\circ$  intervals.

#### *Magnetic Data*

Magnetic measurements were collected using a Quantum Design SQUID magnetometer. Zero field cooled and field cooled (ZFC/FC) magnetic susceptibility data from 5-300 K and isothermal magnetization measurements from 0-5 T were recorded on a powder sample encased in a gelatin capsule. Diamagnetic corrections of  $20 \times 10^{-6}$  emu/mol ( $\text{La}^{3+}$ ),  $16 \times 10^{-6}$  emu/mol ( $\text{Re}^{6+}$ ) and  $12 \times 10^{-6}$  emu/mol ( $\text{O}^{2-}$ ) were added to the susceptibility data. There was no diamagnetic correction for the sample holder.

#### *Heat Capacity*

Heat capacity data were measured from 5-115 K in zero applied field and from 5-30 K in a 9.0 T field using the heat capacity probe of the Oxford MagLab system. A suitable sample block was prepared by repressing and resintering a portion of the previously synthesized product. Sample structure integrity was verified by powder X-ray diffraction (Guinier). The thin block was mounted onto a sapphire measurement chip with Apiezon grease. Contributions to the measured heat capacity by the grease and sample chip were accounted for by the software.

#### *Calculations*

All DFT calculations described here were performed with the ADF 2004.01 density functional theory package.<sup>9-11</sup>

The calculation of model geometries was conducted using unrestricted calculations with the Adiabatic Local Density Approximation (ALDA) for the exchange-correlation kernel<sup>12,13</sup> and the differentiated static LDA expression was used with the Vosko-Wilk-Nusair parameterization.<sup>14</sup> Gradient corrections were performed with the exchange and correlation functionals of Perdew and Wang (PW91).<sup>15</sup> All basis functions had triple- $\zeta$  quality and were composed of uncontracted Slater-type orbitals (STOs), including frozen cores for O (1s), Re (4f) and La (4d) and two auxiliary basis set of STOs for polarization. Relativistic effects were modeled using ZORA.<sup>16-18</sup>

Extended Hückel spin dimer analysis using the CAESAR computational package was also performed to estimate the relative strength of the different inter-dimer exchange interactions.<sup>19</sup> Double zeta Slater-type orbitals were used for Re  $d$  as well as O  $s$  and  $p$  orbitals.

## 5.4 Results and Discussion

### *Structural Characterization*

The crystal structure of the compound was first verified from Guinier powder data. The obtained pattern and lattice constants matched well with the previous single crystal studies<sup>8</sup>, indicating the black powder produced was indeed  $\text{La}_3\text{Re}_2\text{O}_{10}$ . This work represents the first published preparation of  $\text{La}_3\text{Re}_2\text{O}_{10}$  as a phase pure polycrystalline powder using conventional solid state methodologies.

Larger batches of the compound were synthesized for powder neutron diffraction measurements. Unfortunately, these samples contained some  $\text{La}_6\text{Re}_4\text{O}_{18}$  impurity that was not present in the smaller batch preparation. Consequently, SQUID magnetometry

and heat capacity measurements were performed on the pure powder material, whereas neutron diffraction data was collected using a combination of slightly impure powders.

Rietveld refinement of the powder neutron diffraction data was accomplished using FULLPROF<sup>20</sup>, with the crystal structure values as the model for  $\text{La}_3\text{Re}_2\text{O}_{10}$  and the  $\text{La}_6\text{Re}_4\text{O}_{18}$  impurity phase included. A plot of the refinement is shown in Figure 5.1.

The overall agreement indices for the refinement were  $R_p = 0.0308$ ,  $R_{wp} = 0.0405$  and  $\chi^2 = 1.34$ . Agreement factors for the individual phases were  $R_f = 0.0378$  and  $R_B = 0.0200$  for  $\text{La}_3\text{Re}_2\text{O}_{10}$  and  $R_f = 0.0816$  and  $R_B = 0.0320$  for  $\text{La}_6\text{Re}_4\text{O}_{18}$ . The relative weight percent of the impurity, calculated using the method of Hill and Howard<sup>21</sup>, was about 13%. Although this value is slightly high, the presence of  $\text{La}_6\text{Re}_4\text{O}_{18}$  did not have a severe negative impact on the neutron data collected. This compound would not be magnetic due to the pairing of the Re electrons in metal-metal bonding.<sup>5</sup>

The crystal structure of  $\text{La}_3\text{Re}_2\text{O}_{10}$  is shown in Figure 5.2. The basic structural unit is a  $[\text{Re}_2\text{O}_{10}]^{9-}$  dimer of two edge-shared  $\text{ReO}_6$  octahedra. These dimers are isolated from each other within the lattice by  $\text{La}^{3+}$  ions. The closest dimer-dimer distance is 5.561 Å. The lattice constants and selected interdimer bond lengths are displayed in Table 5.1.

The Re-Re bond length within the dimer is 2.488 Å, which is indicative of metal-metal bonding. Comparing this distance with other halo-metal cluster systems, a bond order of 1.5 can be tentatively assigned.<sup>22</sup> The average oxidation state of Re in this complex is + 5.5, implying that there are three electrons in each Re dimer, and the dimers are magnetic ( $S = 1/2$  per dimer).

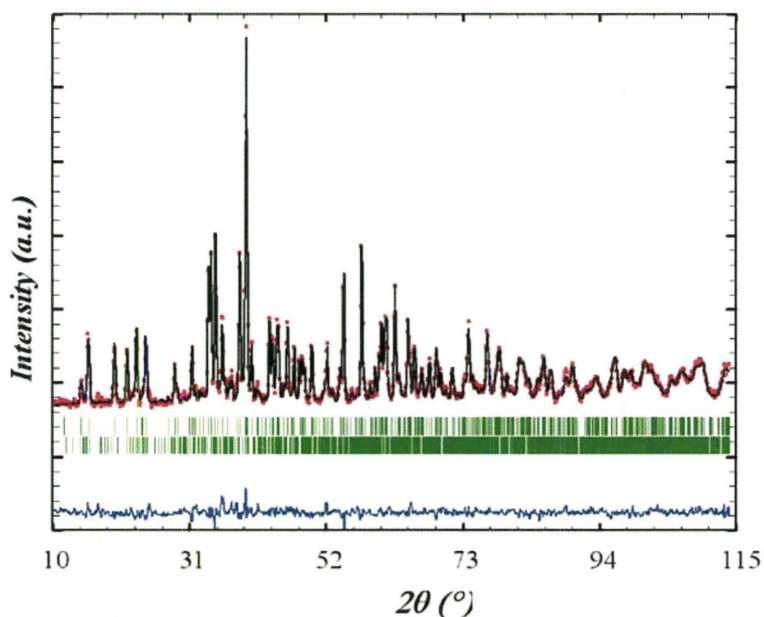


Figure 5.1. Rietveld refinement of the powder neutron diffraction data for  $\text{La}_3\text{Re}_2\text{O}_{10}$ . The circles are the experimental data and the line is the calculated fit. The top set of tick marks denote the Bragg reflections of the  $\text{La}_3\text{Re}_2\text{O}_{10}$  phase, whereas the bottom Bragg reflections are from the  $\text{La}_6\text{Re}_4\text{O}_{18}$  impurity. The line at the bottom of the Figure is the difference plot between the observed and calculated patterns.

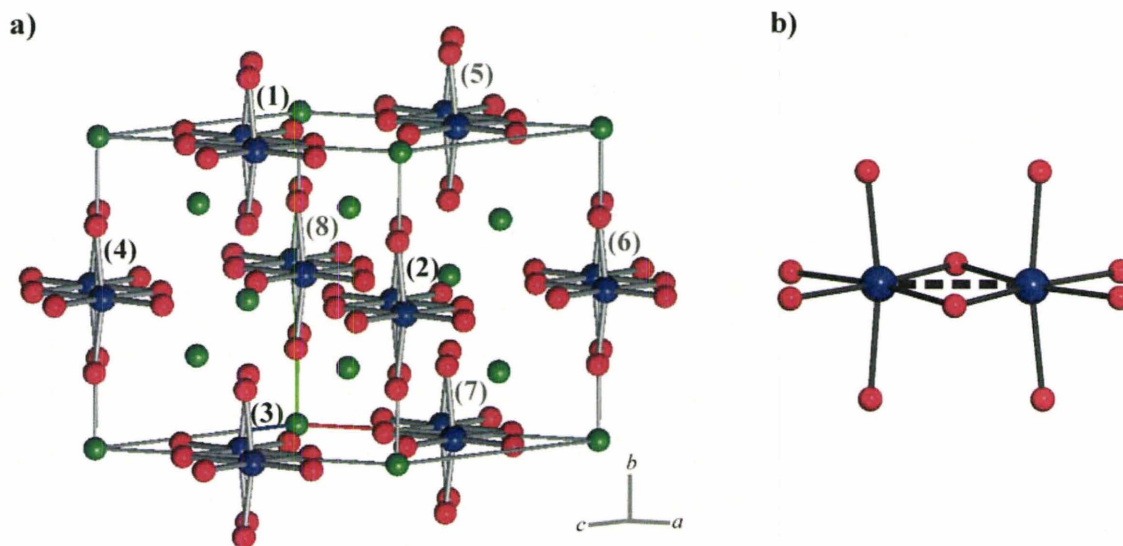


Figure 5.2. a) Unit cell of  $\text{La}_3\text{Re}_2\text{O}_{10}$ . The atoms are designated by shade: La (green), Re (blue), O (red). The numbers correspond to the selected interdimer distances reported in Table 1, as well as the magnetic coupling pathways considered in the calculations. b) Detail of an individual  $[\text{Re}_2\text{O}_{10}]^{9-}$  dimer unit, illustrating the metal-metal bond (dashed line).

Table 5.1. Lattice Constants and Selected Interdimer Distances for  $\text{La}_3\text{Re}_2\text{O}_{10}$ .

Space group	$C2/m$	
$a$ (Å)	7.8952(8)	[7.901(1)]
$b$ (Å)	7.8340(8)	[7.866(1)]
$c$ (Å)	7.1244(7)	[7.115(1)]
$\beta$ (°)	115.208(4)	[115.44(1)]
<b>Intralayer (<i>ab</i> plane) Distances</b>		
1-2	5.561 Å	
1-3	7.834 Å	
2-4	7.895 Å	
<b>Interlayer Distances*</b>		
1-5	7.124 Å	
1-8	7.598 Å	
2-8	8.073 Å	

Literature values are shown in square parentheses.<sup>8</sup>

\* The interlayer distances reported represent the distance between the same Re atoms of two different dimers.

### *Magnetic Properties*

The Zero Field Cooled /Field Cooled (ZFC/FC) magnetic susceptibility data collected from 2-300 K are plotted in Figure 5.3. The two curves diverge around 150 K. The ZFC data shows two broad maxima centred at 105 and 55 K respectively. These features are indicative of short range order. Attempts were made to fit the 55 K feature to various models of low dimensional magnetic correlations. Considering the compound's crystal structure, probable models of this order would be either 1-dimensional linear antiferromagnetic chains<sup>23</sup> or a 2-D antiferromagnetic square planar lattice<sup>24</sup>.

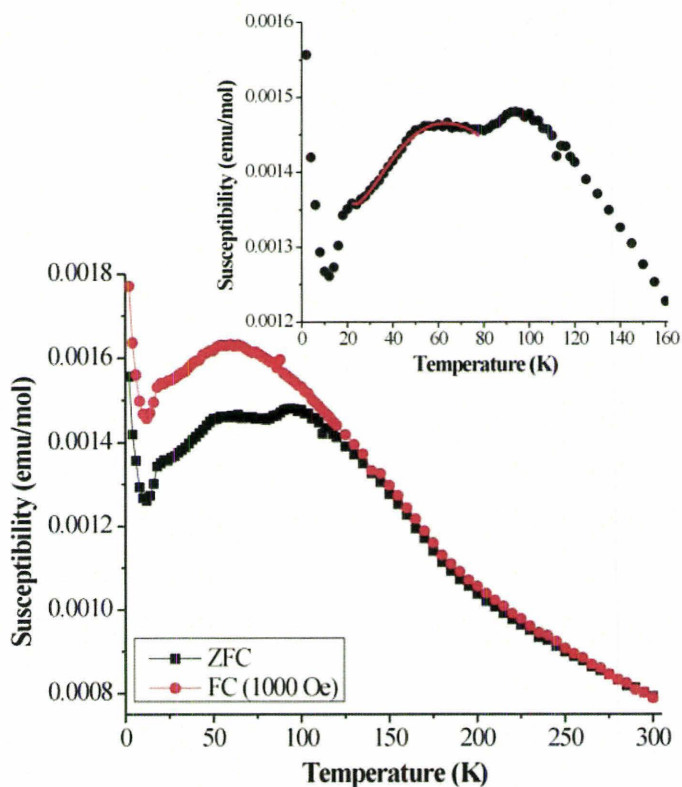


Figure 5.3. Zero Field Cooled /Field Cooled (ZFC/FC) magnetic susceptibility of  $\text{La}_3\text{Re}_2\text{O}_{10}$ . Inset. Fit of the low temperature feature in the ZFC magnetic susceptibility data to a 1D linear chain model. The circles are the experimental points, and the line is the fit.

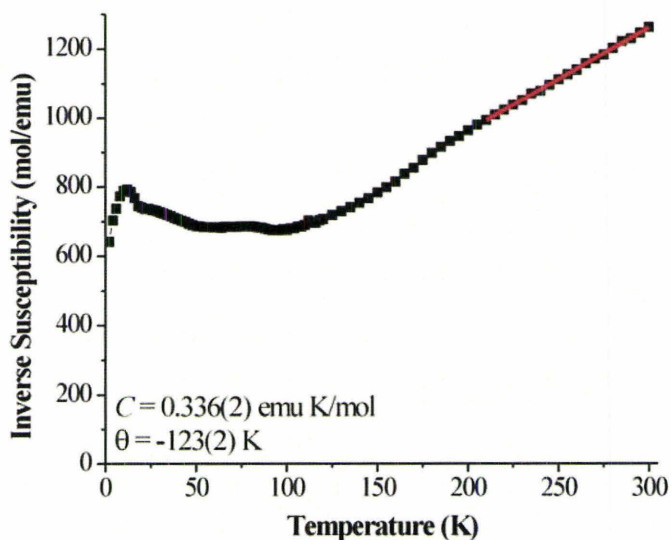


Figure 5.4. Fit of the ZFC magnetic susceptibility data from 200-300 K to the Curie-Weiss law.

The analytical expressions derived from these models are both based on the general form of the spin-spin Hamiltonian (5.2):

$$H = -2J \sum_{i < j} [S_x^i S_x^j + S_y^i S_y^j + S_z^i S_z^j] \quad 5.2$$

The 2-D fit failed to converge, and hence, was discarded. The 1-D Heisenberg  $S = 1/2$  antiferromagnetic linear chain model fit the data well, as seen in the inset of Figure 5.3. The  $g$ -factor found was 1.44(11), which is slightly low, and the magnitude of the exchange constant,  $|J/k_B|$  was 51(1) K. A Curie-Weiss term and a temperature independent paramagnetism term were included in the fit to model a low temperature paramagnetic impurity, yielding values of  $C = 1.2(1) \times 10^{-3}$  emu·K/mol,  $\theta = 11(5)$  K and  $3.1(2) \times 10^{-4}$  emu/mol, respectively.

Finally, a sharp cusp at 18 K can be found in the ZFC curve, followed by a large drop in the measured susceptibility, until very low temperatures when the susceptibility rises. This steep rise at low temperature can be attributed to a paramagnetic impurity. However, the 18 K feature could be indicative of the onset of long-range magnetic order.

A fit of the ZFC susceptibility data from 200-300 K to the Curie-Weiss law (5.3) was performed, and is pictured in Figure 5.4.

$$\chi = \frac{C}{T - \theta} \quad 5.3$$

The Curie constant found was 0.336(2) emu·K/mol, which is slightly below the calculated “spin only” value of 0.375 emu·K/mol. This could indicate delocalization of the lone unpaired electron within the dimer unit or contribution of an orbital moment due to intradimer spin-orbit coupling. The Weiss temperature was  $-123(2)$  K, suggestive of

dominant antiferromagnetic interactions. No temperature independent paramagnetic term was needed due to the clear linearity of the data in this temperature range.

The temperature derivative of  $\chi T$  plotted against the temperature (T), the so-called “Fisher heat capacity”<sup>25</sup>, is shown in Figure 5.5. There is an anomaly present at lower temperature, but due to the sloping background, it is difficult to assign an exact value for the peak. However, it appears to be centred at about 17 K, which corroborates the idea from the magnetic susceptibility data that long-range magnetic order sets in around 18 K.

Isothermal magnetization measurements at 10 and 30 K were collected using fields between 0 and 5.0 T (Figure 5.6). Neither curve approaches the expected saturation magnetization for a  $S = 1/2$  compound of  $1.0 \mu_B$ . In addition, no significant hysteresis or remanent magnetization were observed. The 30 K data are linear, indicating paramagnetism, however, the 10 K data are significantly curved. This is consistent with the presence of an antiferromagnetic state at low temperatures with the field-induced curvature due to a spin flop transition.

#### *Heat Capacity*

The heat capacity of  $\text{La}_3\text{Re}_2\text{O}_{10}$  measured from 5-24 K with no applied field is pictured in Figure 5.7. A distinct anomaly appears at approximately 18 K, indicative of long-range magnetic order, consistent with the susceptibility results. Application of a 9.0 T field had little effect, demonstrating the robustness of this magnetic feature. Unfortunately, a lattice match could not be synthesized.

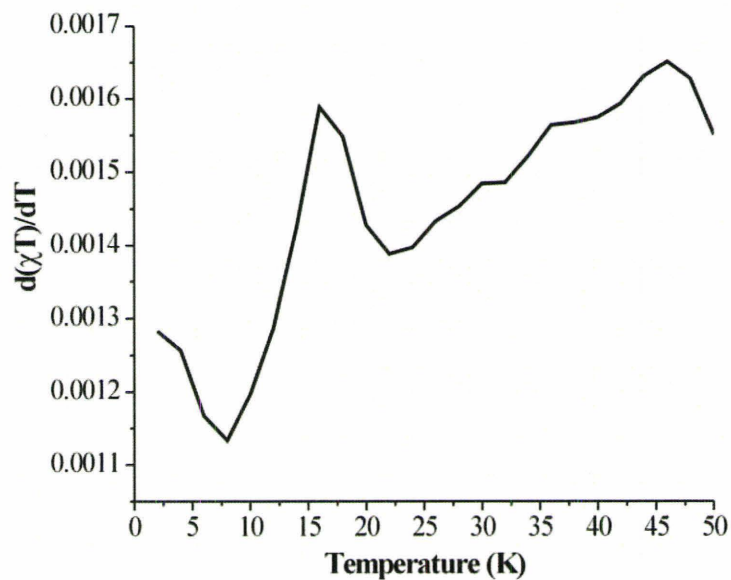


Figure 5.5. Fisher heat capacity of  $\text{La}_3\text{Re}_2\text{O}_{10}$ . The peak of the lambda-like anomaly is approximately 17 K.

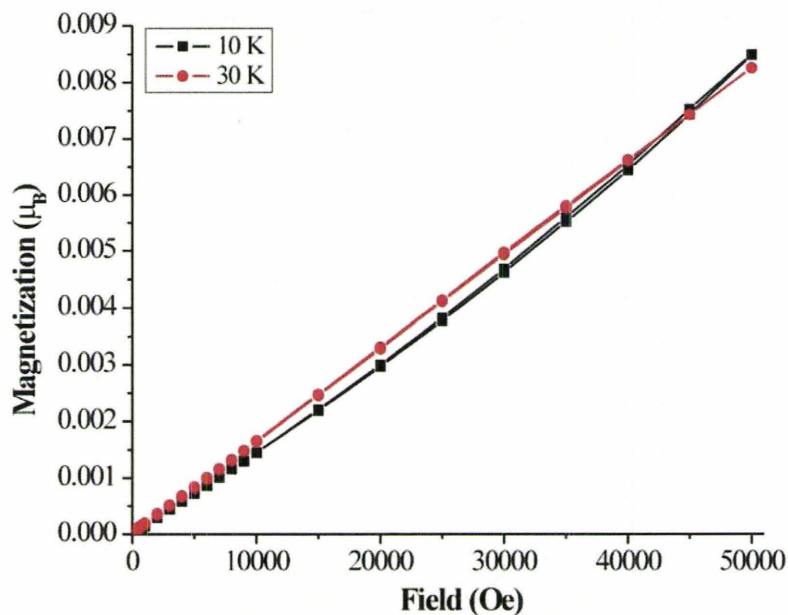


Figure 5.6. Isothermal magnetization curves for  $\text{La}_3\text{Re}_2\text{O}_{10}$  collected below (10 K, squares) and above (30 K, circles) the critical temperature,  $T_c$ .

However, fitting both the low temperature and higher temperature data (well below and above the anomaly) to the expression:

$$C = \gamma T + \beta T^3 \quad 5.4$$

leads to an estimation of the lattice contribution to the specific heat. Subtracting this function from the heat capacity data results in a more defined  $\lambda$ -like peak at 18 K (inset Figure 5.7).

The entropy associated with this magnetic transition can also be calculated from the heat capacity data. Integration of the area under the curve results in an estimation of the entropy loss according

to:

$$\Delta S = \int_0^T (C_{mol} / T) dT \quad 5.5$$

from which  $\Delta S = 0.12$  J/K mol. The entropy loss expected for a magnetic transition is equal to  $R \ln(2S+1)$ , and for  $\text{La}_3\text{Re}_2\text{O}_{10}$ , this would be 5.76 J/K mol. Although the measured magnetic entropy loss is only  $\sim 2\%$  of the total entropy, this is not unreasonable, given the importance of short-range correlations present at much higher temperatures which would eliminate much of this entropy before the transition to long-range order.

### *Neutron Diffraction*

The low angle part of the neutron powder patterns obtained at 4 K and 285 K, as well as a difference plot is shown in Figure 5.8. Despite over 60 hours of data collection at low temperature, no magnetic reflections were observed.  $\text{La}_3\text{Re}_2\text{O}_{10}$  is, of course, a

very dilute magnetic system (the one unpaired electron is extensively delocalized over 15 atoms) and it may be impossible to detect the ordered moment using unpolarized neutrons. An alternative explanation is that the compound does not exhibit long-range magnetic order. However, the Fisher heat capacity (Figure 5.5), the field dependence of the magnetization (Figure 5.6) and the thermal heat capacity (Figure 5.7) all indicate long range antiferromagnetic magnetic order below 18 K. It seems far more likely that the former explanation is correct.

#### *Computational Modeling*

DFT computational modeling was undertaken to investigate the electronic structure of the isolated, paramagnetic dimer, especially the distribution of the electron density. As well, an attempt was made to determine the relative strengths of selected interdimer interactions using DFT and EHTB. As a first approximation, the electronic structure of the isolated dimer cluster was mimicked using the model compound  $\text{Re}_2\text{O}_{10}\text{H}_8^-$  ( $C_{2h}$ ). Only the positions of the capping hydrogen atoms were optimized. The metal ions are formally in oxidation states +5 and +6. There are 3 electrons available for metal-metal bonding – two occupy a  $\sigma$  bonding orbital ( $a_g$ ) and the unpaired electron is located in a  $\pi$  bonding orbital ( $a_u$ ). Both orbitals are shown in Figure 5.9 a.

From the composition of the SOMO or the map of spin density (Figure 5.9 b), it is clear that there is significant delocalization of spin over the oxygen atoms, in particular those bridging the rhenium metal ions. This suggests that the lanthanum ions bonded to the bridging oxygens are likely to enable inter-dimer spin coupling.

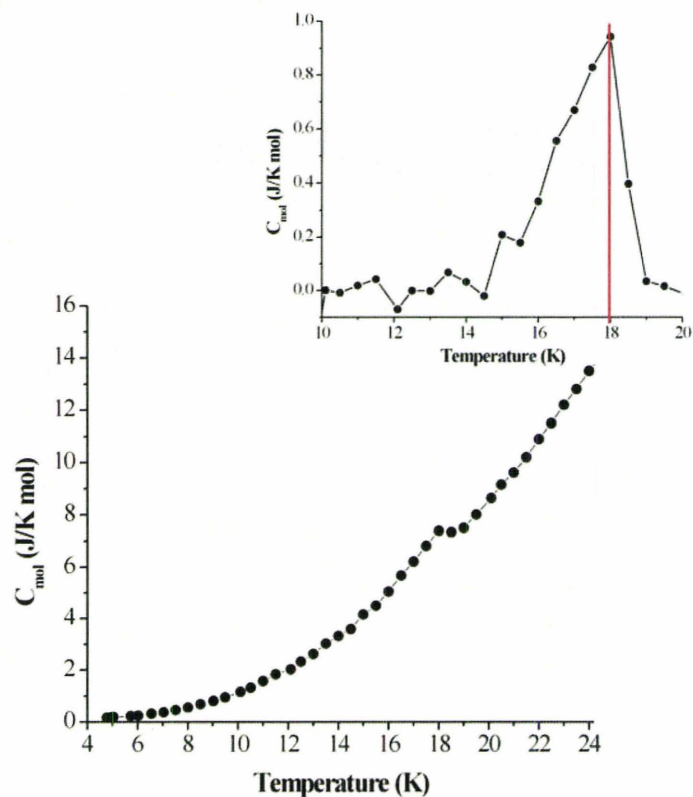


Figure 5.7. Heat capacity of  $\text{La}_3\text{Re}_2\text{O}_{10}$ , measured in the absence of a magnetic field. Inset. Heat capacity after subtraction of the lattice contribution. Note the lambda-like anomaly at 18 K.

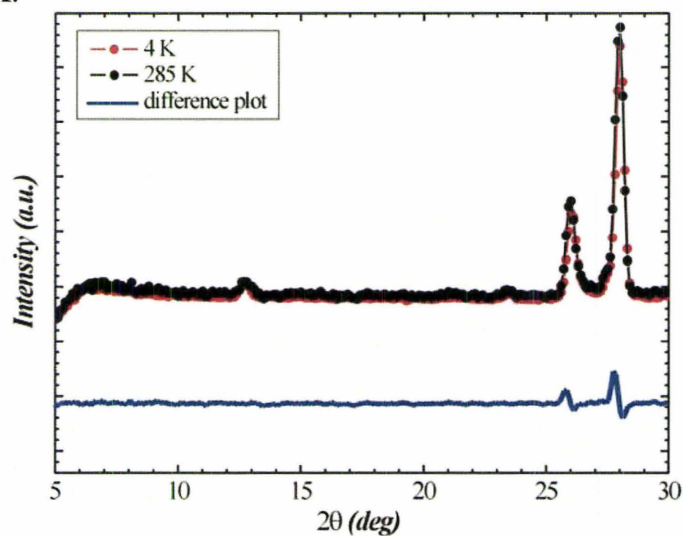


Figure 5.8. Comparison of the powder neutron diffraction patterns of  $\text{La}_3\text{Re}_2\text{O}_{10}$  taken below (4 K) and above (285 K) the critical temperature,  $T_c$ , as well as a difference plot (lower line).

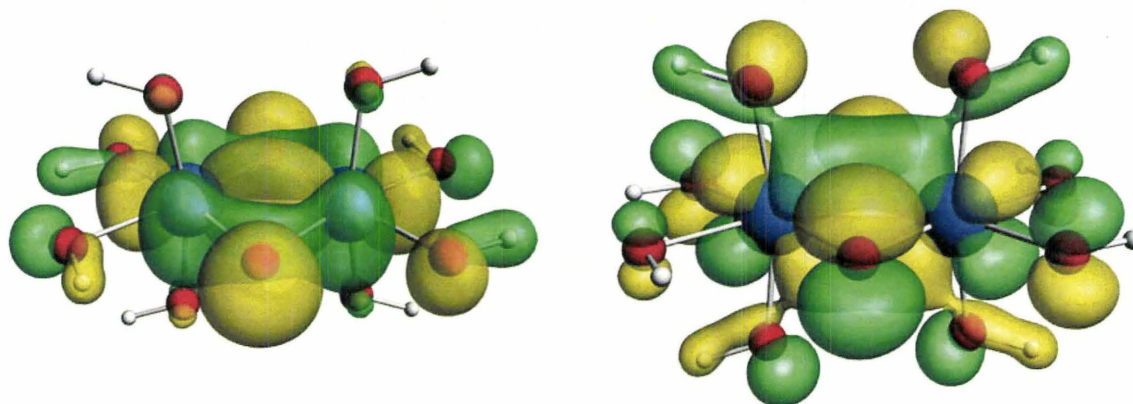


Figure 5.9. a) Re-Re bonding orbitals of  $\text{Re}_2\text{O}_{10}\text{H}_8^-$  as calculated using DFT. The picture on the left depicts the SOMO-1 or  $\sigma$ -bonding orbital, whereas the one on the right is the SOMO or  $\pi$ -bonding orbital (which is only half-filled). Legend of colours: Re (blue), O (red), H (white), orbital lobes (green, yellow).

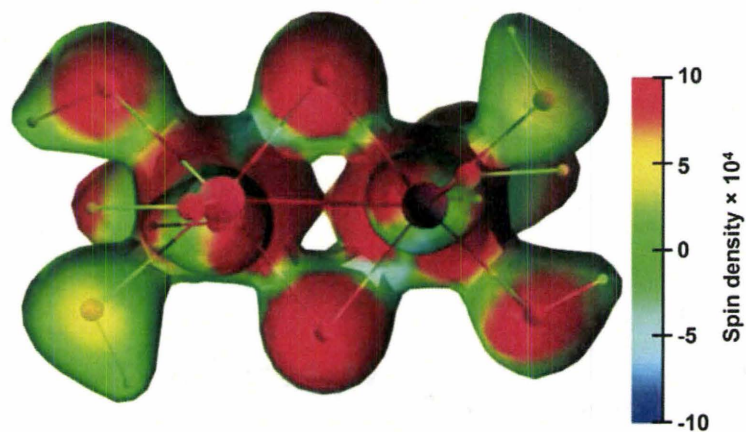


Figure 5.9. b) Spin density for  $\text{Re}_2\text{O}_{10}\text{H}_8^-$  mapped over the total density isosurface plotted at 0.05.

The bimetallic clusters are organized in layers within the *ab* plane, according to the crystal structure of  $\text{La}_3\text{Re}_2\text{O}_{10}$  (Figure 5.2). Within each layer, three different coupling pathways are possible: 1-2, 1-3, and 2-4, with respect to the labeling system depicted in Figure 5.2. These, as well as additional interlayer interaction pathways, were examined using DFT with small molecular models that included two dimers at a time. The relative strength of the interaction between unpaired electrons is quantified by the magnitude of the spin-spin coupling constants, but their accurate calculation is only possible with highly-correlated methods. Instead, the energy gap between the singlet and the triplet states can be used to estimate the coupling constants; the limitations of this approach and the accuracy of DFT methods have been examined before.<sup>26-30</sup>

In all of these calculations, the triplet states were consistently below the energy of the singlets. This would imply that the magnetic interaction between two dimers should be ferromagnetic. However, there is no experimental evidence for ferromagnetism. The observed magnetic behaviour must be a consequence of extended interactions throughout the lattice that cannot be accounted for with this approach. Instead, extended Hückel, spin dimer analysis<sup>31</sup> was employed to assess the relative magnitude of the spin interactions. In this method, the inter site hopping energy,  $\Delta e$ , is calculated by comparing the energy gap between the highest occupied state and the lowest unoccupied state. Assuming that  $J \sim -(\Delta e)^2/U$ , where  $U$  is the Coulomb integral (and can be considered as constant for a given magnetic ion), the relative magnitude of the various magnetic exchange coupling constants,  $J$ , can be determined. Each  $[\text{Re}_2\text{O}_{10}]^{9-}$  dimer is comprised of one half-filled electronic state. Accordingly, the exchange interactions between two of

these dimers, in various directions were investigated and the relative exchange energies are summarized in Table 5.2.

Table 5.2.  $(\Delta e)^2$  for Some Magnetic Exchange Pathways (Intralayer and Interlayer) Between Various Dimers Calculated using the Spin Dimer Model.

<b>Intralayer Pathways</b>			
	$(\Delta e)^2$ (meV) <sup>2</sup>	Relative	Relative (overall)
1-2	68.3	1	0.12
1-3	2.78	0.041	0.0050
2-4	0.125	0.002	0.00022
<b>Interlayer Pathways</b>			
	$(\Delta e)^2$ (meV) <sup>2</sup>	Relative	Relative (overall)
1-5	11.27	0.020	0.020
1-8	569.6	1	1
2-8	26.8	0.047	0.047

Within the *ab* plane, the 1-2 interaction is the strongest and the others are much weaker. This intralayer pathway is also the shortest. However, the strongest overall inter-dimer coupling, relative to all of the pathways examined, is the 1-8 dimer-dimer interaction. Surprisingly, this is an interlayer interaction, and is also not the shortest Re-Re inter-dimer contact (see Table 5.1). Dimer coupling between 1 and 8 would extend along the (1 1 2) direction, and lead to short-range magnetic order consisting of 1-D antiferromagnetically coupled dimer chains. This finding is consistent with the fits to the broad feature at 55 K in the SQUID magnetometry data. The 1-2 interaction is weaker (about 1/10 the strength of the 1-8 pathway), however, coupling of the chains in the (1 1

0) direction is still highly probable. This could lead to the long-range magnetic order evident from SQUID magnetometry and heat capacity data.

## 5.5 Conclusions

The synthesis of  $\text{La}_3\text{Re}_2\text{O}_{10}$  by solid state reaction was successfully carried out for the first time, yielding a pure phase black powder. Its magnetic properties were subsequently studied, revealing some interesting, unusual and unexpected results.

Despite a distance of over 5 Å between isolated  $S = 1/2$ ,  $[\text{Re}_2\text{O}_{10}]^{9-}$  dimer units, evidence for both short and long range magnetic order at relatively high temperatures is clear from both SQUID magnetometry and heat capacity measurements. The short-range order appears to consist of 1-D linear chains of antiferromagnetically coupled dimers. This conclusion was reached by experimental fits to the magnetic susceptibility data and extended Hückel spin dimer calculations. These chains would most likely extend diagonally across the unit cell in the (1 1 2) direction, as this is the configuration with the largest coupling predicted by the calculations.

Long-range magnetic ordering, however, is quite unexpected and unusual. Both the cusp in the magnetic susceptibility data and the lambda-like anomaly in the heat capacity measurements unambiguously confirm this long-range order and assign  $T_c = 18$  K. However, the magnetic structure of  $\text{La}_3\text{Re}_2\text{O}_{10}$  remains elusive. Unpolarized powder neutron diffraction data at 4 and 285 K showed no discernable difference, which is attributed to the very dilute and delocalized nature of the spin density in this material. Thus, the nature of the long-range order cannot be determined from the existing neutron data.

It is worth noting that the magnetic properties revealed in this investigation do not agree with the preliminary magnetic susceptibility measurements reported previously<sup>8</sup>, which found an unusually high effective magnetic moment of about  $6 \mu_B$  at room temperature. Using the Curie constant from the fit to the high temperature magnetic susceptibility data collected in this research, an effective moment of  $1.25(1) \mu_B$  can be calculated. This value is much closer to the calculated spin-only effective moment for a spin 1/2 system of  $1.73 \mu_B$ .

In conclusion,  $\text{La}_3\text{Re}_2\text{O}_{10}$  is an interesting magnetic oxide, given that the unpaired electron is extensively delocalized over the  $[\text{Re}_2\text{O}_{10}]^{9-}$  dimeric unit. In spite of long interdimer distances, short-range antiferromagnetic correlations are evident below 200 K and long range antiferromagnetic order sets in below 18 K.

HLC thanks Dr. Paul Dube for his assistance with the heat capacity measurements, Dr. Maggie Austen for useful discussions of the bonding in the  $\text{Re}_2\text{O}_{10}$  dimer and NSERC for a doctoral Post-Graduate Scholarship. JEG thanks NSERC for financial support. IVB acknowledges NSERC, OIT and CFI for funding.

## 5.6 References

1. Baud, G.; Besse, J.-P.; Chevalier, R.; Gasperin, M. *J. Solid State Chem.* **1979**, *29*, 267-272.
2. Rae-Smith, A. R.; Cheetham, A. K.; Fuess, H. Z. *Anorg. Allg. Chem.* **1984**, *510*, 46-50.
3. Waltersson, K. *Acta. Crystallogr.* **1976**, *B32*, 1485-1489.
4. Baud, G.; Capestan, M. *Bull. Soc. Chim. Fr.* **1968**, *10*, 3999-4004.
5. Besse, J.-P.; Baud, G.; Chevalier, R.; Gasperin, M. *Acta. Crystallogr.* **1978**, *B34*, 3532-3535.
6. Morrow, N. L.; Katz, L. *Acta. Crystallogr.* **1968**, *B24*, 1466-1471.
7. Sleight, T. P.; Hare, C. R.; Sleight, A. W. *Mat. Res. Bull.* **1968**, *3*, 437-444.

8. Torardi, C. C.; Sleight, A. W. *J. Less-Common Met.* **1986**, *116*, 292-299.
9. Velde, G. t.; Bickelhaupt, F. M.; Gisbergen, S. J. A. v.; Guerra, C. F.; Baerends, E. J.; Snijders, J. G.; Ziegler, T. *J. Comput. Chem.* **2001**, *22*, 931-967.
10. Guerra, C. F.; Snijders, J. G.; Velde, G. t.; Baerends, E. J. *Theor. Chem. Acc.* **1998**, *99*, 391-403.
11. *SCM, Theoretical Chemistry*, Vrije Universiteit: Amsterdam, The Netherlands, 2002.
12. Gisbergen, S. J. A. v.; Snijders, J. G.; Baerends, E. J. *Phys. Rev. Lett.* **1997**, *78*, 3097-3100.
13. Gisbergen, S. J. A. v.; Snijders, J. G.; Baerends, E. J. *J. Chem. Phys.* **1998**, *109*, 10644-10656.
14. Vosko, S. H.; Wilk, L.; Nusair, M. *Can. J. Phys.* **1980**, *58*, 1200-1211.
15. Perdew, J. P.; Chevary, J. A.; Vosko, S. H.; Jackson, K. A.; Pederson, M. R.; Singh, D. J.; Fiolhais, C. *Phys. Rev. B.* **1992**, *46*, 6671-6687.
16. Lenthe, E. v.; Baerends, E. J.; Snijders, J. G. *J. Chem. Phys.* **1993**, *99*, 4597-4610.
17. Lenthe, E. v.; Baerends, E. J.; Snijders, J. G. *J. Chem. Phys.* **1994**, *101*, 9783-9792.
18. Lenthe, E. v.; Ehlers, A.; Baerends, E. J. *J. Chem. Phys.* **1999**, *110*, 8943-8953.
19. Ren, J.; Liang, W.; Whangbo, M.-H. *Crystal and Electronic Structure Analysis using CAESAR*, 2005; <http://www.PrimeC.com/>
20. Roisnel, T.; Rodriguez-Carvajal, J. *Mater. Sci. Forum* **2000**, *378-381*, 118-123.
21. Hill, R. J.; Howard, C. J. *J. Appl. Crystallogr.* **1987**, *20*, 467-474.
22. Cotton, F. A. *Inorg. Chem.* **1965**, *4*, 334-336.
23. Estes, W.E.; Gavel, D.P.; Hatfield, W.E.; Hodgson, D.J. *Inorg. Chem.* **1978**, *17*, 1415-1421.
24. Navarro, R. In *Magnetic Properties of Layered Transition Metal Compounds*; Jongh, L. J. d., Ed.; Kluwer Academic Publishers: Dordrecht, 1990, pp 105-184.
25. Fisher, M. E. *Philos. Mag.* **1962**, *7*, 1731-1743.
26. Mitani, M.; Yamaki, D.; Takano, Y.; Kitagawa, Y.; Yoshioka, Y.; Yamaguchi, K. *J. Chem. Phys.* **2000**, *113*, 10486-10504.
27. Mitani, M.; Mori, H.; Takano, Y.; Yamaki, D.; Yoshioka, Y.; Yamaguchi, K. *J. Chem. Phys.* **2000**, *113*, 4035-4051.
28. Mitani, M.; Takano, Y.; Yoshioka, Y.; Yamaguchi, K. *J. Chem. Phys.* **1999**, *111*, 1309-1324.
29. Ruiz, E.; Alvarez, S.; Cano, J.; Polo, V. *J. Chem. Phys.* **2005**, *123*, 164110/164111-164110/164117.
30. Albores, P.; Slep, L. D.; Weyhermuller, T.; Rentschler, E.; Baraldo, L. M. *J. Chem. Soc. Dalton Trans.* **2006**, 948-954.
31. Whangbo, M.-H.; Koo, H.-J.; Dai, D. *J. Solid State Chem.* **2003**, *176*, 417-481.

## **Chapter 6**

### **Synthesis, Structure and Magnetic Properties of the Double Perovskite, SrLaRuNiO<sub>6</sub>**

This chapter describes the experimental synthesis, structural characterization and magnetic properties of the compound, SrLaRuNiO<sub>6</sub>, which was performed by the candidate.

## 6.1 Abstract

The magnetic properties of the title compound, SrLaRuNiO<sub>6</sub>, were studied. Verification of previous structural studies confirmed ordering between the two magnetic *B*-site cations, Ru<sup>5+</sup> and Ni<sup>2+</sup>. Bulk magnetic susceptibility measurements were hampered by the presence of small levels of ferromagnetic SrRuO<sub>3</sub>. However, variable temperature powder neutron diffraction measurements confirmed SrLaRuNiO<sub>6</sub> antiferromagnetically orders below 84 K, which can be described by a (1/2 0 1/2) magnetic ordering vector. However, because of orthorhombic pseudosymmetry and a high degree of correlation between the two different magnetic moments, the ordered magnetic structure could not be unambiguously determined.

## 6.2 Introduction

Perovskites are a very important structure type, as many fascinating physical phenomena such as superconductivity and colossal magnetoresistance can be found for various chemical compositions.<sup>1-4</sup> The general formula is *ABO*<sub>3</sub>. The *B* site cations (typically transition metals) form a three-dimensional network of corner-shared *BO*<sub>6</sub> octahedra that is extremely robust and amenable to substitution with many different elements. The larger *A* site ions (such as lanthanides, or alkaline earth metals) reside on 12 co-ordinate sites for cubic *Pm-3m* symmetry.

Double perovskites, *A<sub>2</sub>BB'O*<sub>6</sub>, involve substitution of two different metal ions on the *B* site. If the cations are sufficiently different in charge and size, they can order and each forms a face-centred cubic lattice.<sup>5</sup> This arrangement is known as 1:1 *B*-site

ordering. Each  $B$ -site octahedra shares all of its corners with  $B'$  ions and *vice versa*.

Ordering of the  $B$ -site cations plays a crucial role in the overall magnetic properties of the compounds.<sup>6-8</sup> Substitution of the  $A$  site is also possible to manipulate the oxidation states of the  $B$ -site transition metals.<sup>9</sup>

Ruthenium-based double perovskites are quite prevalent, involving many different elements such as main group metals, first row transition metals and lanthanides, for example.<sup>10,11</sup> Depending on the  $A$  site ions used (typically, either an alkaline earth metal such as  $\text{Ca}^{2+}$ ,  $\text{Sr}^{2+}$  or  $\text{Ba}^{2+}$ , or a non-magnetic trivalent ion such as  $\text{La}^{3+}$ ), the oxidation state of ruthenium is usually four (IV) or five (V). However, one clear trend has emerged. If the  $B$ -site cations are 1:1 ordered, long-range magnetic order is possible, whereas for a disordered arrangement, spin glassy behaviour is typically observed.<sup>6-8</sup>

Some ruthenium-nickel double perovskite systems have already been synthesized and their magnetic properties studied. Structurally,  $\text{La}_2\text{RuNiO}_6$  crystallizes with  $B$ -site ordering between the  $\text{Ru}^{4+}$  and  $\text{Ni}^{2+}$  cations. Magnetically, it orders antiferromagnetically between 20 to 30 K.<sup>12,13</sup> There is some controversy in the literature about the ordering of the  $B$ -site cations, which appears to depend on sample preparation.<sup>10</sup> Similarly,  $\text{BaLaRuNiO}_6$  may or may not contain  $B$ -site ordering. One group reported ordering between the  $\text{Ru}^{5+}$  and  $\text{Ni}^{2+}$  ions, and also reported antiferromagnetic long-range order in the range of 20–40 K. However,  $^{99}\text{Ru}$  Mössbauer spectroscopy did not indicate magnetic order down to 4.2 K.<sup>14</sup> Another group refined the crystal structure of  $\text{BaLaRuNiO}_6$  with a random  $B$ -site distribution from powder neutron diffraction data. A maximum in the susceptibility at  $\sim 20$  K was also observed, however there were no new Bragg reflections

in the low-temperature powder neutron diffraction pattern. Based on this observation, and the lack of magnetic order reported from the Mössbauer study, these researchers concluded that BaLaRuNiO<sub>6</sub> is a spin glass, with a glass transition temperature at about 20 K.<sup>6</sup>

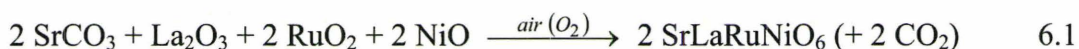
SrLaRuNiO<sub>6</sub> has been synthesized previously, however, its magnetic properties were not studied.<sup>15</sup> The synchrotron crystal structure study concluded that SrLaRuNiO<sub>6</sub> has an ordered *B*-site cation arrangement at room temperature, and this remains even in the high temperature (> 670 K) rhombohedral structure.

This work represents the first magnetic characterization of SrLaRuNiO<sub>6</sub> using SQUID magnetometry and variable temperature powder neutron diffraction.

### 6.3 Experimental

#### *Synthesis*

The compound SrLaRuNiO<sub>6</sub> has been synthesized previously<sup>15</sup> and was prepared in an analogous way by solid state reaction, according to the following equation:



Stoichiometric amounts of the starting reagents, SrCO<sub>3</sub>, La<sub>2</sub>O<sub>3</sub> (99.9%, Aldrich), RuO<sub>2</sub> (99.9%, CERAC) and NiO (99.995%, CERAC), were accurately weighed, ground together, and pressed into a pellet. La<sub>2</sub>O<sub>3</sub> was fired at 900°C overnight before use. The sample pellet was placed in a platinum foil-lined alumina boat, which was slowly heated to 1200°C, in an analogous way to the previous synthesis, in a tube furnace and held for

60 hours. The reaction product was reground and refired up to 1200 °C to ensure complete reaction.

#### *X-ray and Neutron Diffraction*

X-ray diffraction data to monitor sample purity were collected using a Guinier-Hagg camera with  $\text{CuK}\alpha_1$  radiation ( $\lambda = 1.5406 \text{ \AA}$ ) and high-purity silicon powder as an internal reference. The reflections were recorded on photographic film and converted to digital form using the KEJ LS20 line scanner.

Variable temperature powder neutron diffraction measurements were performed on the C2 diffractometer at the Canadian Neutron Beam Centre at Chalk River. The crystal structure data (285 K) were collected at a wavelength of 1.32917 Å in the angular range of  $12^\circ \leq 2\theta \leq 113^\circ$  with 0.1° steps. Similarly, the magnetic structure data (4 K and above) were measured at a longer wavelength of 2.36957 Å in the range  $5^\circ \leq 2\theta \leq 85^\circ$  with 0.1° intervals.

#### *Magnetic Data*

Magnetic measurements were collected using the Quantum Design SQUID magnetometer. Zero field cooled and field cooled (ZFC/FC) magnetic susceptibility data from 5 – 300 K and isothermal magnetization measurements from 0 – 5.0 T were recorded on powder samples encased in gelatin capsules. High temperature measurements (300 – 500 K) were collected using an oven insert and quartz sample holders. The inherent diamagnetism was corrected for using Pascal's constants for the appropriate ions (using a value of  $18 \times 10^{-6} \text{ emu/mol}$  for  $\text{Ru}^{5+}$ ).<sup>16</sup>

## 6.4 Results and Discussion

### *Structural Characterization*

The structure of the title compound was first verified by powder X-ray diffraction (Guinier camera). Along with the major phase, a few small reflections were found and identified as NiO, La<sub>2</sub>NiO<sub>4</sub> and possibly, SrRuO<sub>3</sub>. Repeated regrinding and refiring reduced the impurities slightly, but a pure-phase sample was not obtained.

Rietveld refinement of room temperature powder neutron diffraction data provided further structural verification. There was some debate in the literature about whether or not the Ru<sup>5+</sup> and Ni<sup>2+</sup> were site-ordered.<sup>15</sup> In the site-ordered structure, the alternating arrangement of *B* and *B'* ions would destroy one glide and one mirror plane, lowering the symmetry from *Pbnm* (random distribution) to *P2<sub>1</sub>/n* (ordered). In addition, since the differently sized ions would not be randomly distributed, the octahedral tilt angles could change from an average value and monoclinic symmetry would result. For SrLaRuNiO<sub>6</sub>, the significant charge and size difference between the two *B*-site ions (0.705 Å for Ru<sup>5+</sup> versus 0.83 Å for Ni<sup>2+</sup>)<sup>17</sup> leads to a better refinement in *P2<sub>1</sub>/n* (site-ordering) than in *Pbnm* (random distribution). The reported agreement indices for the two models were:  $R_p = 0.095$ ,  $R_{wp} = 0.106$ ,  $\chi^2 = 4.95$  for *P2<sub>1</sub>/n* and  $R_p = 0.104$ ,  $R_{wp} = 0.117$ ,  $\chi^2 = 5.99$  for *Pbnm*, respectively.<sup>15</sup> Subsequently, the neutron data were refined in *P2<sub>1</sub>/n*. The crystal structure and refinement results appear in Table 6.1 and atomic parameters in Table 6.2, with comparison to the literature values. It is worth noting that the  $\beta$  angle is 90° within the error of the measurement, implying pseudo-orthorhombic symmetry for this structure.

Table 6.1. Lattice Constants and Refinement Agreement Indices for SrLaRuNiO<sub>6</sub>.

Space group	$P2_1/n$		
$a$ (Å)	5.5846(4)	[5.5759(1)]	
$b$ (Å)	5.5538(2)	[5.5422(1)]	
$c$ (Å)	7.8699(1)	[7.8490(1)]	
$\beta$ (°)	90.06(6)	[90.00(1)]	
Refinement Agreement			
$R_p$	0.0542	$R_B$ (SrLaRuNiO <sub>6</sub> )	0.0641
$R_{wp}$	0.0781	$R_B$ (La <sub>2</sub> NiO <sub>4</sub> )	0.217
$\chi^2$	9.29	$R_B$ (NiO)	0.113
		$R_B$ (SrRuO <sub>3</sub> )	0.171

Literature values are shown in square parentheses.<sup>15</sup>

Table 6.2. Atomic Parameters for SrLaRuNiO<sub>6</sub>.

Atom	$x$		$y$		$z$	
Sr/La	0.005(3)	[0.0026(4)]	0.021(1)	[0.0206(1)]	0.251(4)	[0.2497(2)]
Ni/Ru (1)	0.50000	[0.50000]	0.00000	[0.00000]	0.50000	[0.50000]
Ru/Ni (2)	0.50000	[0.50000]	0.00000	[0.00000]	0.00000	[0.00000]
O1	0.276(6)	[0.289(2)]	0.267(5)	[0.276(2)]	0.027(3)	[0.037(3)]
O2	0.221(6)	[0.234(2)]	-0.212(5)	[-0.223(2)]	0.035(3)	[0.026(3)]
O3	-0.060(3)	[-0.063(2)]	0.496(2)	[0.495(1)]	0.254(8)	[0.255(2)]

Literature values are shown in square parentheses.<sup>15</sup>

The side products were also accounted for in the refinement, and were quantified using the method of Hill and Howard.<sup>18</sup> The weight percentages of NiO, La<sub>2</sub>NiO<sub>4</sub> and SrRuO<sub>3</sub> were determined as 2.8 %, 8.6 % and 4.5 %, respectively. Unfortunately, although the amount of impurities is relatively small, they could have a pronounced effect on the magnetic properties measured. Nickel(II) oxide is a f.c.c. Type II antiferromagnet that orders above room temperature ( $T_c = 523$  K).<sup>19</sup> Similarly, La<sub>2</sub>NiO<sub>4</sub> is also an antiferromagnet with a high ordering temperature ( $T_c = 325$  K).<sup>13</sup> Since both of these

antiferromagnetic phase transitions occur above room temperature, they would not interfere with the detection of magnetic transitions below 300 K. However, excess oxygen is often found in  $\text{La}_2\text{NiO}_4$ , which lowers the  $T_c$  and superconductivity has been observed for the oxygen-rich compound.<sup>12</sup> In addition, there are two structural phase transitions reported for  $\text{La}_2\text{NiO}_4$ . At 770 K, it transforms from tetragonal ( $I4/mmm$ ) to orthorhombic ( $Bmab$ ) and at 80 K, from orthorhombic to tetragonal ( $P4_2/ncm$ ). A weak ferromagnetic component also appears below this second phase transition, which could be an interference.<sup>12</sup> Finally,  $\text{SrRuO}_3$  is a metallic ferromagnet with a  $T_c$  of 165 K.<sup>20</sup> This could be the most problematic, as its contribution to bulk magnetic measurements could mask the signal due to  $\text{SrLaRuNiO}_6$ .

#### *Magnetic Properties*

The magnetic properties of  $\text{SrLaRuNiO}_6$  have not been previously reported, and hence, an extensive set of magnetic data was collected and analyzed. Zero field cooled/field cooled (ZFC/FC) magnetic susceptibility data were taken from 5 to 300 K, and are pictured in Figure 6.1. The two data sets diverge at 158 K, a slightly higher temperature than the relatively sharp feature at 152 K. The ZFC curve continues to rise due to a broad feature centred at about 35 K. Similarly, the FC data also rise, with a slight shoulder at about 35 K, before levelling off at low temperature. The peak at 152 K may indicate long-range antiferromagnetic order in  $\text{SrLaRuNiO}_6$ , however, this is also near the critical temperature reported for one of the suspected impurities, ferromagnetic  $\text{SrRuO}_3$ .

High temperature magnetic susceptibility data from 300-600 were collected, and fit to the Curie-Weiss law (equation 6.2) (inset Figure 6.1):

$$\chi = \frac{C}{T - \theta} \quad 6.2$$

The values found for the Curie constant and Weiss constant were 2.76(1) emu K/mol and -10(2) K, respectively. The Curie constant is slightly lower than the expected spin-only value for Ru<sup>5+</sup> ( $S = 3/2$ :  $C = 1.875$  emu K/mol) and Ni<sup>2+</sup> ( $S = 1$ :  $C = 1.000$  emu K/mol) of 2.875 emu K/mol. The negative Weiss constant indicates antiferromagnetic behaviour. Again, both of these values could be affected by the presence of slight impurities.

The product of susceptibility ( $\chi$ ) and temperature (T) versus temperature appears in Figure 6.2. At higher temperatures, the data lie below the line denoting the spin-only Curie constant, indicating antiferromagnetic interactions. However, the plot rises to a sharp peak above the line at 152 K. This indicates some ferromagnetic behaviour, and is rather strange, given the peak itself is a sign of antiferromagnetism. Again this could be due to an impurity, and may not reflect the magnetism of the phase of interest, SrLaRuNiO<sub>6</sub>. As the temperature decreases, the data continue to slowly rise, until a rather sharp drop at about 85 K that continues below the Curie constant line. This could indicate antiferromagnetic ordering in the sample, which could be due to SrLaRuNiO<sub>6</sub>. It did not appear in the magnetic susceptibility graph perhaps due to the presence of impurity phases that dominated the signal. The derivative of  $\chi T$  with respect to T versus temperature graph or the so-called ‘‘Fisher heat capacity’’<sup>21</sup> is plotted in the inset of Figure 6.2. Again, a prominent lambda-like anomaly centred at 148 K is clear, which is most likely due to the presence of SrRuO<sub>3</sub>. Unfortunately, no other features are visible.

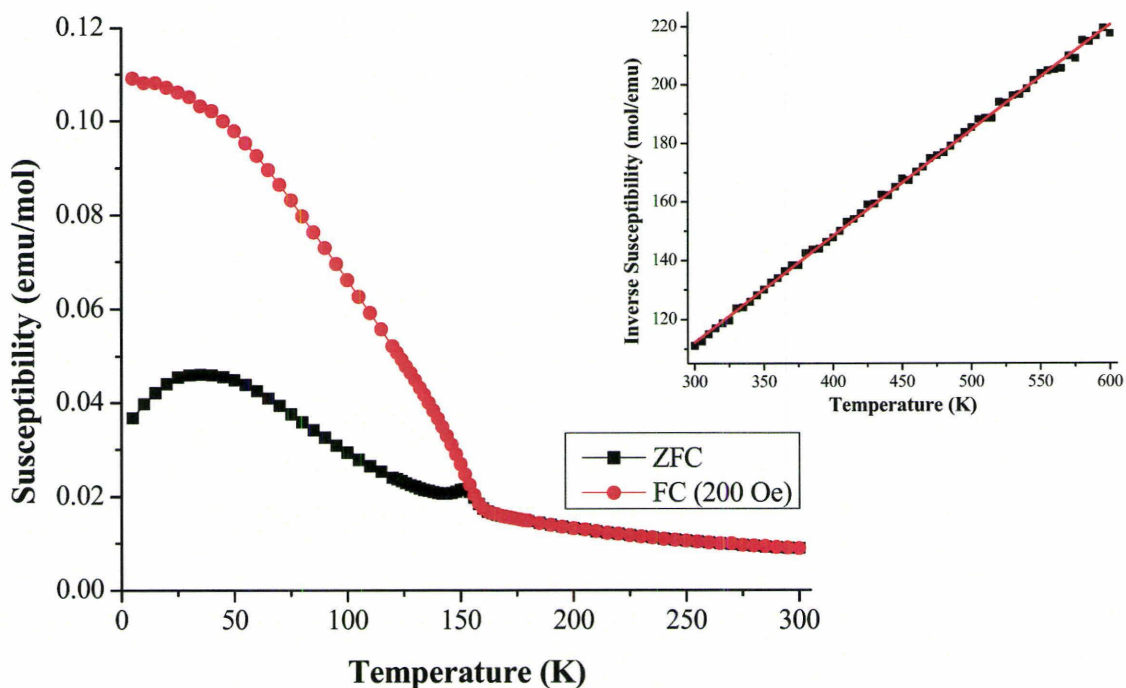


Figure 6.1. ZFC/FC magnetic susceptibility of SrLaRuNiO<sub>6</sub>. Inset – Inverse susceptibility plot for SrLaRuNiO<sub>6</sub>. The line is the fit to the Curie–Weiss Law.

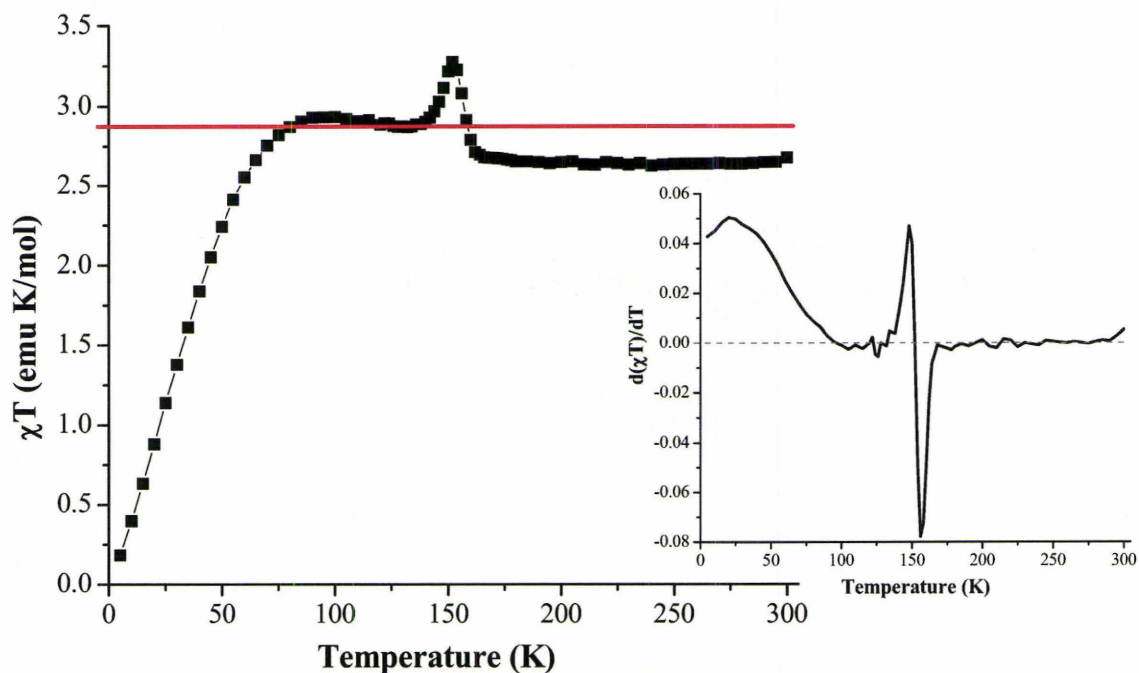


Figure 6.2.  $\chi T$  versus temperature plot for SrLaRuNiO<sub>6</sub>. The horizontal line denotes the spin-only Curie constant for this system. Inset – Fisher heat capacity for SrLaRuNiO<sub>6</sub>.

Magnetization data, sweeping the field from 0 to 5.0 T and back, at temperatures of 5, 50, 140, 160 and 250 K were collected, as seen in Figure 6.3. At low temperatures (5 and 50 K), there is some small hysteresis, but virtually no remanent magnetization. At higher temperatures (140, 160 and 250 K), the plots are clearly linear, indicating paramagnetic behaviour. This seems to indicate that a change in magnetic order occurs between 50 and 140 K, not at 152 K, as much of the previous magnetic data appears to imply.

Variable temperature powder neutron diffraction measurements were performed to elucidate the ordered magnetic structure of SrLaRuNiO<sub>6</sub>. Figure 6.4 displays a plot of low angle data at various temperatures, clearly indicating the presence of new magnetic reflections. These reflections could be indexed on a new unit cell with ordering vector,  $k = (1/2 \ 0 \ 1/2)$ . This magnetic structure has been seen in double perovskite compounds before.<sup>22-24</sup> Attfield and coworkers performed powder neutron diffraction experiments on the double perovskite, SrLaRuCoO<sub>6</sub>, with the same monoclinic  $P2_1/n$  symmetry, and  $(1/2 \ 0 \ 1/2)$  propagation vector for the magnetic unit cell.<sup>22</sup> In this study, the authors found equally good fits to the data from four different spin representations. Since the monoclinic cell distortion is so small,  $(h \ k \ l)$  and  $(h \ k \ -l)$  magnetic reflections are not well resolved, and the four models are indistinguishable from the data. In addition, refinements with all spin only at Co, all spin only on Ru or some intermediate combination gave equally acceptable fits to the experimental data. This reinforces the fact that there is a high degree of correlation between the two magnetic ions.

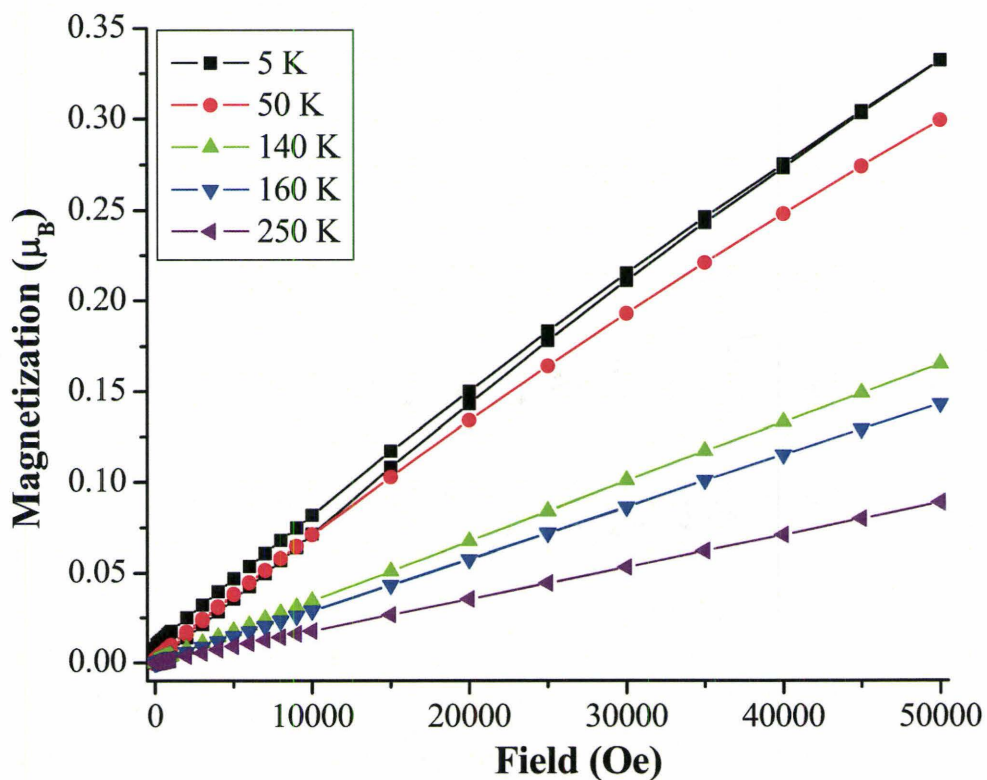


Figure 6.3. Magnetization curves recorded for SrLaRuNiO<sub>6</sub> at 5 K (black squares), 50 K (red circles), 140 K (green triangles), 160 K (blue inverted triangles) and 250 K (purple left arrowhead).

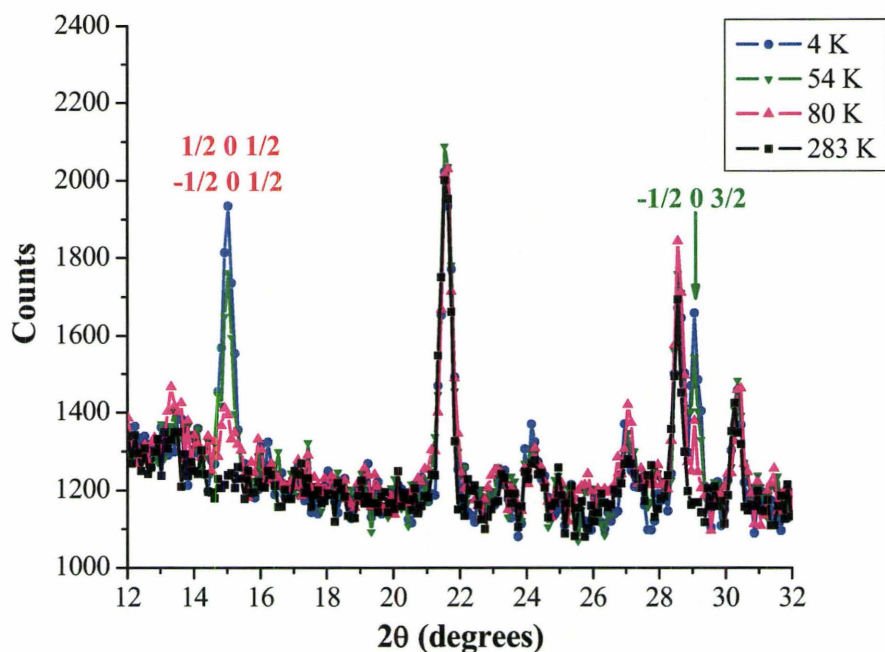


Figure 6.4. Powder neutron diffraction data for SrLaRuNiO<sub>6</sub> at 4 K (blue circles), 54 K (green inverted triangles), 80 K (pink triangles) and 283 K (black squares). The labelled peaks are the new magnetic Bragg reflections, indexed as indicated.

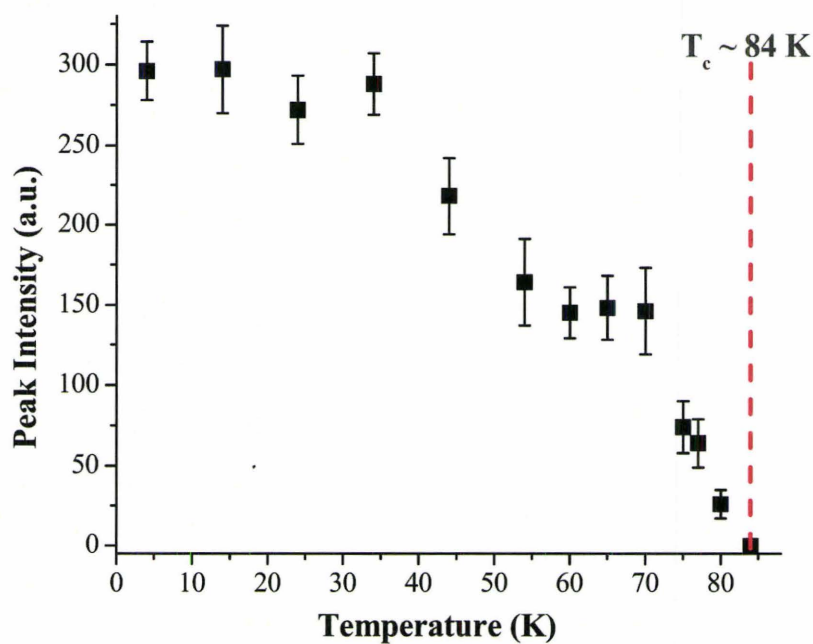


Figure 6.5. Temperature dependence of the magnetic peak indexed as  $(1/2\ 0\ 1/2) / (-1/2\ 0\ 1/2)$  in SrLaRuNiO<sub>6</sub>, indicating the critical temperature of  $\sim 84$  K.

Unfortunately, due to the pseudo-orthorhombic symmetry of the SrLaRuNiO<sub>6</sub> unit cell, as well as the high degree of correlation between the two different magnetic moments, a unique solution is not possible in this case either. However, the temperature dependence of the new reflections was interesting (Figure 6.5). The intensity of the reflections disappeared at 84 K, signalling the critical temperature of SrLaRuNiO<sub>6</sub>. What is interesting from this magnetic study is that the bulk magnetic data was completely overshadowed by the behaviour of SrRuO<sub>3</sub> and required a neutron diffraction experiment to demonstrate bulk antiferromagnetic order and determine the critical temperature for this order.

## 6.5 Conclusions

The compound, SrLaRuNiO<sub>6</sub> was synthesized, as well as structurally and magnetically characterized. Room temperature powder neutron diffraction confirmed *B*-site ordering of the Ru<sup>5+</sup> and Ni<sup>2+</sup> ions. Unfortunately, the presence of a small amount of ferromagnetic SrRuO<sub>3</sub> masked the bulk magnetic properties of SrLaRuNiO<sub>6</sub>. Despite this, variable temperature powder neutron diffraction data found that SrLaRuNiO<sub>6</sub> exhibits long-range antiferromagnetic order below 84 K. New Bragg reflections could be indexed to a magnetic unit cell with ordering vector (1/2 0 1/2). However, due to pseudo-orthorhombic symmetry of the unit cell and a high degree of correlation between the Ru<sup>5+</sup> and Ni<sup>2+</sup> magnetic moments, a unique structure could not be determined.

This chapter highlights the importance of neutron diffraction experiments in the investigation of magnetic properties. Often, magnetic susceptibility or magnetization

measurements are highly influenced by the presence of ferromagnetic compounds, even in minute quantities relative to the bulk of the sample. Accounting for and quantifying these contributions is often difficult. Variable temperature powder neutron diffraction measurements were critical in this study, not only in determining the nature of the long-range order, but the critical temperature for this order as well.

## 6.6 References

1. Bhalla, A. S.; Guo, R.; Roy, R. *Mat. Res. Innovat.* **2000**, *4*, 3-26.
2. Chen, D. Y.; Chien, F. Z.; Ling, D. C.; Tseng, J. L.; Sheen, S. R.; Wang, M. J.; Wu, M. K. *Physica* **1997**, *C282-7*, 73-76.
3. Ovchinnikov, S. G. *Physics-Uspekhi* **2003**, *46*, 21-44.
4. Philipp, J. B.; Majewski, P.; Reisinger, D.; Gepraegs, S.; Opel, M.; Erb, A.; Alff, L.; Gross, R. *Acta Phys. Polon.* **2004**, *A105*, 7-26.
5. Anderson, M. T.; Greenwood, K. B.; Taylor, G. A.; Poeppelmeier, K. R. *Prog. Solid St. Chem.* **1993**, *22*, 197-233.
6. Battle, P. D.; Gibb, T. C.; Jones, C. W.; Studer, F. *J. Solid State Chem.* **1989**, *78*, 281-293.
7. Kim, S. H.; Battle, P. D. *J. Solid State Chem.* **1995**, *114*, 174-183.
8. Fang, M.; Kato, M.; Yoshimura, K.; Kosuge, K. *J. Alloys Comp.* **2001**, *317-8*, 136-140.
9. Knapp, M. C.; Woodward, P. M. *J. Solid State Chem.* **2006**, *179*, 1076-1085.
10. Yoshii, K.; Ikeda, N.; Mizumaki, M. *Phys. Stat. Sol.* **2006**, *A203*, 2812-2817.
11. Sakai, C.; Doi, Y.; Hinatsu, Y. *J. Alloys Comp.* **2006**, *408-12*, 608-612.
12. Poirot, N. J.; Allancon, C.; Odier, P.; Simon, P.; Bassat, J. M.; Loup, J. P. *J. Solid State Chem.* **1998**, *138*, 260-266.
13. Rodriguez-Carvajal, J.; Fernandez-Diaz, M. T.; Martinez, J. L. *J. Phys.: Condens. Matter* **1991**, *3*, 3215-3234.
14. Fernandez, I.; Greatrex, R.; Greenwood, N. N. *J. Solid State Chem.* **1980**, *32*, 97-104.
15. Gateshki, M.; Igartua, J. M. *Mater. Res. Bull.* **2003**, *38*, 1893-1900.
16. Mulay, L. N. In *Theory and Applications of Molecular Paramagnetism*; Boudreaux, E. A., Mulay, L. N., Eds.; John Wiley & Sons: New York, 1976, p 494-495.
17. Shannon, R. D. *Acta Crystallogr.* **1976**, *A32*, 751-767.
18. Hill, R. J.; Howard, C. J. *J. Appl. Cryst.* **1987**, *20*, 467-474.
19. Shanker, R.; Singh, R. A. *Phys. Rev.* **1973**, *B7*, 5000-5005.

20. Cao, G.; McCall, S.; Shepard, M.; Crow, J. E.; Guertin, R. P. *Phys. Rev.* **1997**, *B56*, 321-328.
21. Fisher, M. E. *Philos. Mag.* **1962**, *7*, 1731-1743.
22. Bos, J.-W. G.; Attfield, J. P. *Chem. Mater.* **2004**, *16*, 1822-1827.
23. Bos, J.-W. G.; Attfield, J. P. *Phys. Rev.* **2004**, *B69*, 094434(1-6).
24. Bos, J.-W. G.; Attfield, J. P. *J. Mater. Chem.* **2005**, *15*, 715-720.

## Chapter 7

### Magnetic Studies of the Ordered Rocksalt Oxides, $\text{Na}_2\text{Cu}_2\text{TeO}_6$ and $\text{Na}_3\text{Cu}_2\text{SbO}_6$

This chapter summarizes the candidate's contributions to the manuscripts "Synthesis, Structure and Magnetic Properties of the Layered Copper(II) Oxide,  $\text{Na}_2\text{Cu}_2\text{TeO}_6$ ", published in the journal *Inorganic Chemistry* (*Inorg. Chem.* **2005**, *44*, 5042–5046) and "Electronic Structures and Low-Dimensional Magnetic Properties of the Ordered Rocksalt Oxides  $\text{Na}_2\text{Cu}_2\text{TeO}_6$  and  $\text{Na}_3\text{Cu}_2\text{SbO}_6$ ", published in *Physical Review B* (*Phys. Rev.* **2007**, *B76*, 104403). As part of a scientific collaboration, the candidate measured the magnetic properties of  $\text{Na}_2\text{Cu}_2\text{TeO}_6$ , analyzed the data and wrote the magnetic discussion for the *Inorg. Chem.* manuscript. For the *Phys. Rev.* journal article, the candidate entered into many detailed discussions of the magnetism with the corresponding author, as well as assisting with magnetic data collection, analysis and manuscript preparation.

Reproduced with permission from Xu, J.; Assoud, A.; Soheilnia, N.; Derakhshan, S.; Cuthbert, H. L.; Greedan, J. E.; Whangbo, M. H.; Kleinke, H. *Inorg. Chem.* **2005**, *44*, 5042–5046. Copyright 2005 American Chemical Society.

Reproduced with permission from Derakhshan, S.; Cuthbert, H. L.; Greedan, J. E.; Rahaman, B.; Saha-Dasgupta, T. *Phys. Rev.* **2007**, *B76*, 104403(1-7). Copyright 2007 by the American Physics Society.

## 7.1 Abstract

A new quaternary layered transition-metal oxide,  $\text{Na}_2\text{Cu}_2\text{TeO}_6$ , was synthesized by the Kleinke group at the University of Waterloo.<sup>1</sup> The structure is composed of  $\frac{2}{\infty} [\text{Cu}_2\text{TeO}_6]$  layers with the Na atoms located in the octahedral voids between the layers. Alternatively, it can be described as an ordered rocksalt oxide with one vacancy. The magnetic susceptibility shows Curie–Weiss behavior between 300 and 600 K with an effective moment of  $1.85(2) \mu_{\text{B}}$  per  $\text{Cu}^{2+}$  ion and a Weiss constant,  $\theta_{\text{c}}$ , of  $-87(6)$  K. A broad maximum at 160 K is interpreted as short-range one-dimensional antiferromagnetic (AF) correlations. This short-range order was analyzed in terms of an alternating chain model, with the surprising result that the stronger intrachain coupling involves a super-superexchange pathway with a Cu–Cu separation of  $>5 \text{ \AA}$ . The  $J_2/J_1$  ratio within the alternating chain refined to  $0.10(1)$ , and the spin gap is estimated to be 127 K.

The analogous compound,  $\text{Na}_3\text{Cu}_2\text{SbO}_6$ , was synthesized at McMaster University in the Greedan lab and its magnetic properties investigated.<sup>2</sup> Again, a broad peak in the magnetic susceptibility data (in this case, near 92 K) indicated dominant short-range, low-dimensional AF behaviour. The data fit very well to an AF-AF alternating linear chain model with  $J_1/k = -79$  K and  $J_2/J_1 = 0.39$ . High temperature data ( $> 300$  K) exhibited Curie–Weiss behaviour with  $\theta_{\text{c}} = -55(2)$  K. Recently, another group investigated both of these compounds and reported that an AF-ferromagnetic (F) linear chain model gives equally good agreement to the low temperature data and included analysis of heat capacity data that also supported the AF-F model.<sup>3</sup> However, Derakhshan *et al.* demonstrated that the Weiss constants derived from the high temperature

experimental susceptibility data are consistent with the  $J$  values obtained from the AF-AF model, and not the AF-F model.

## 7.2 Introduction

Ternary and quaternary compounds involving cuprates have been heavily investigated, as the  $\text{CuO}_2$  layers are responsible for the high- $T_c$  superconductivity observed in compounds such as  $\text{YBa}_2\text{Cu}_3\text{O}_7$  and related materials.<sup>4,5</sup> In contrast, the quaternary cuprate-tellurates and cuprate-antimonates have been relatively unexplored. The synthesis of  $\text{Na}_2\text{Cu}_2\text{TeO}_6$  represents the first compound of this structure type for cuprate-tellurates, as  $\text{Na}_3\text{Cu}_2\text{SbO}_6$  is for the cuprate-antimonates. Figure 7.1 shows the  $\text{Na}_3\text{Cu}_2\text{SbO}_6$  structure, which can be considered as an ordered rocksalt oxide. It basically consists of layers of edge-shared  $\text{CuO}_6$  and  $\text{SbO}_6$  octahedra, separated by  $\text{Na}^+$  ions in octahedral voids. One  $\text{Na}^+$  site is vacant in  $\text{Na}_2\text{Cu}_2\text{TeO}_6$ . The magnetic  $\text{Cu}^{2+}$  ions lie in planes of composition  $\text{Cu}_2\text{TeO}_6^{2-}$  or  $\text{Cu}_2\text{SbO}_6^{3-}$ , and due to site ordering with the  $\text{Te}^{6+}$  or  $\text{Sb}^{5+}$ , form a slightly distorted honeycomb lattice topology.

Magnetic oxides with an ordered rocksalt structure often exhibit low-dimensional behaviour due to either the topology of the cation ordering or to orbital ordering, especially with Jahn-Teller active ions. The distorted honeycomb magnetic lattice of copper ions is expected to exhibit strong magnetic fluctuations, characteristic of low-dimensional spin systems, due to the low co-ordination of the coppers. In addition,  $d^9$ - $\text{Cu(II)}$  centres are classic Jahn-Teller ions, resulting in a  $[4 + 2]$  coordination of the

copper ions. Consequently, the magnetic ordering of these compounds should be strongly affected by both this cation and orbital ordering.

Upon closer examination, there are five distinctive magnetic exchange pathways within the distorted honeycomb lattice of copper ions (Figure 7.2). Two such pathways ( $J_4$  and  $J_5$ ) are relatively long and involve fully occupied  $d_z^2$  orbitals, and as such, their contribution to the overall magnetism of the compound is negligible. The three most significant nearest-neighbour interactions are  $J_1$ ,  $J_2$  and  $J_3$ . Depending on the signs and relative magnitudes of these exchanges, 0, 1 or 2 dimensional magnetism may be possible (Table 7.1).

Table 7.1. Possible Dimensionalities of the  $\text{Cu}^{2+}$  Spin Correlations.

Relative Interaction Magnitudes	Magnetic Model
$J_2 \approx J_3 \gg J_1$	2D honeycomb
$J_1 = J_2 \gg J_3$	1D chain
$J_1 > J_2 \gg J_3$	1D alternating chain
$J_1 \gg J_2 \approx J_3$	0D dimer

Experimental magnetic susceptibility of the two compounds suggests a dominant dimeric or zero-dimensional interaction. Calculations confirm that  $J_1$  is the strongest exchange pathway, relative to  $J_2$  or  $J_3$ . Closer inspection indicates that a one-dimensional linear chain model provides a somewhat better fit.<sup>1,2</sup> However, there does exist some controversy regarding the sign of the second-neighbour interaction,  $J_2$ .

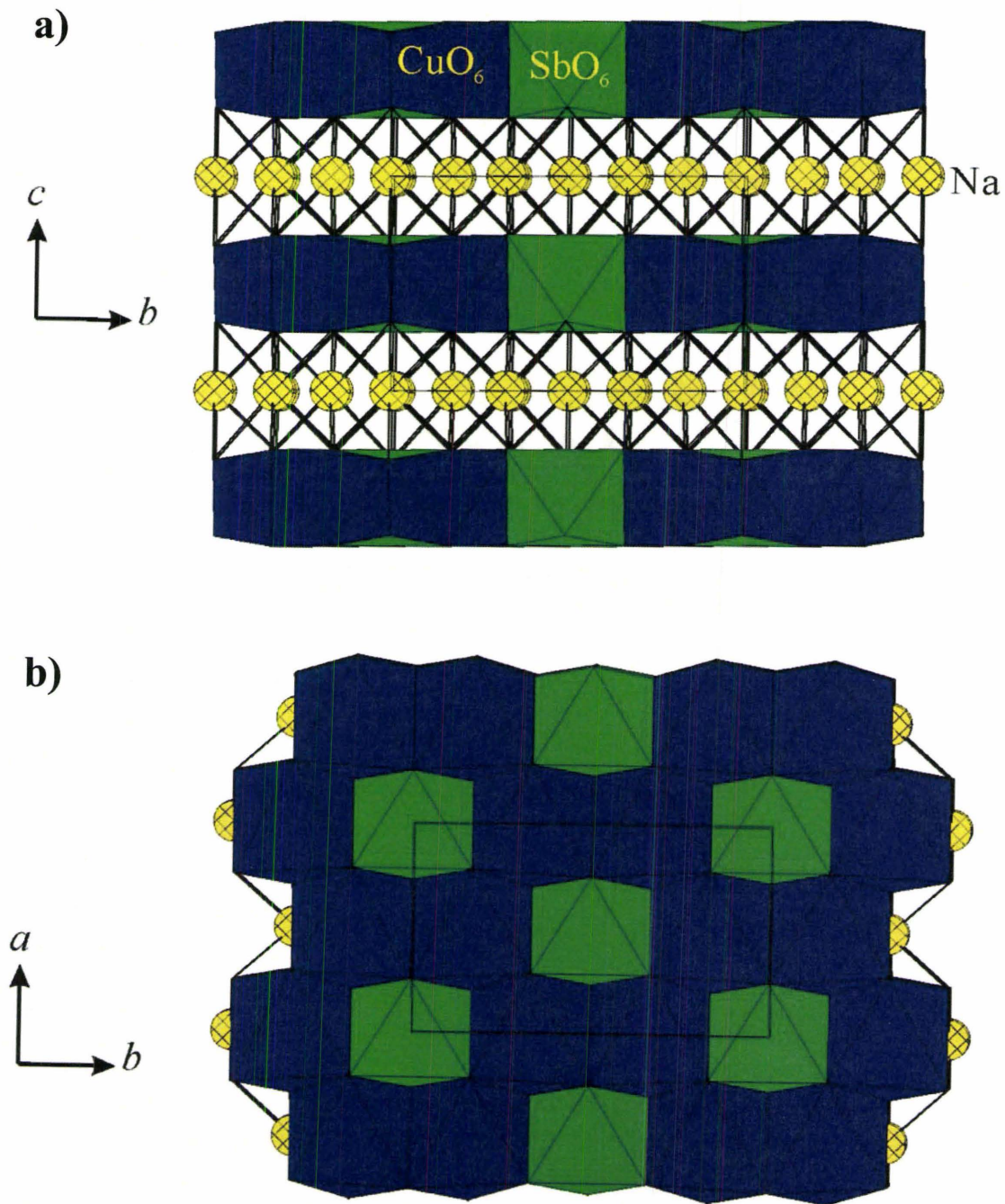


Figure 7.1. Edge-sharing octahedra in  $\text{Na}_3\text{Cu}_2\text{SbO}_6$ , viewed along a) the  $a$  direction and b) the  $c$  direction.  $\text{Na}_2\text{Cu}_2\text{TeO}_6$  would have one Na vacancy and Te in place of Sb.

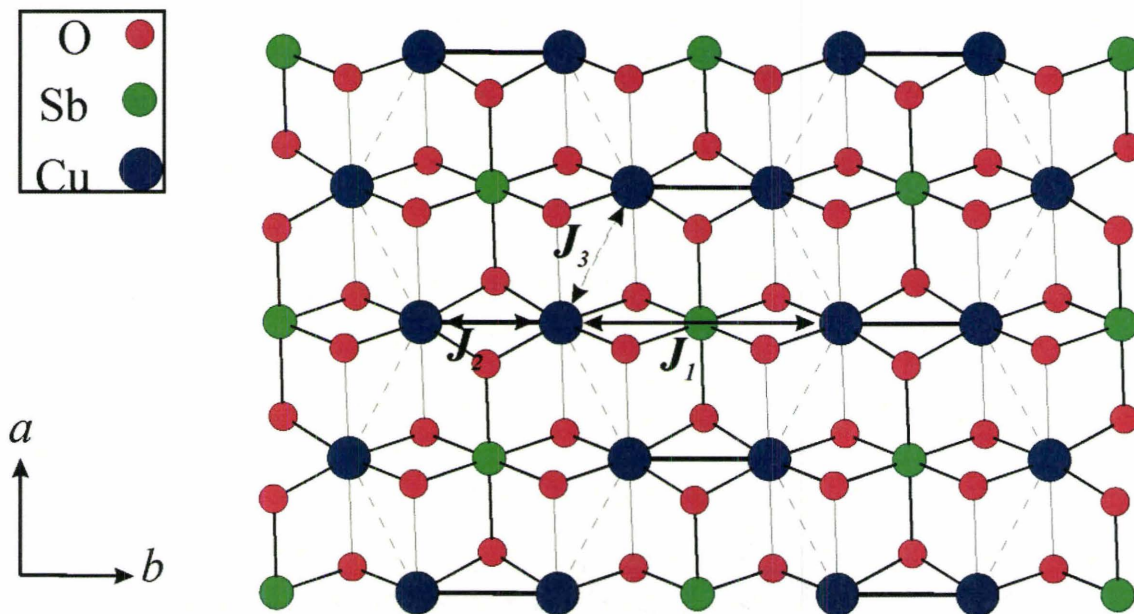


Figure 7.2. Schematic representation of the possible Cu–Cu interaction pathways in the  $ab$  plane of  $\text{Na}_3\text{Cu}_2\text{SbO}_6$ . The tellurate,  $\text{Na}_2\text{Cu}_2\text{TeO}_6$ , would look identical in this plane. The thick solid lines denote the shortest Cu–Cu contacts, the thin solid lines show Cu–O and Sb–O connectivity, and the dashed lines represent the shortest interchain Cu–Cu distance. The three magnetic interaction pathways, labelled  $J_1$ ,  $J_2$  and  $J_3$  are designated by double-sided arrows.

One group fit the low temperature magnetic susceptibility data for  $\text{Na}_2\text{Cu}_2\text{TeO}_6$  to an AF-AF alternating linear chain model, with  $J_2/J_1 = 0.10(1)$ .<sup>1</sup> A second group reinvestigated the magnetic properties and pointed out that distinguishing between an AF-AF and an AF-F model is very difficult, based only on the fit quality. In fact, the AF-F model does indeed provide an excellent fit, albeit with very different values for the fitting parameters (i.e.  $J_1/J_2 \sim -0.80$ , for both  $\text{Na}_2\text{Cu}_2\text{TeO}_6$  and  $\text{Na}_3\text{Cu}_2\text{SbO}_6$ ). In addition, their fits to low-temperature heat capacity data appear to support the AF-F model.<sup>3</sup>

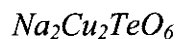
In an attempt to resolve this controversy, further calculations of the various exchange pathways was undertaken as well as a deeper analysis of the experimental magnetic data. The observed Weiss constants, derived from Curie-Weiss fits to high-temperature susceptibility data, were compared to the values predicted using the  $J$ 's obtained from the various fits to the low-temperature data.<sup>2</sup>

### 7.3 Experimental

#### *Magnetic Measurements*

Variable-temperature magnetic susceptibility data for  $\text{Na}_2\text{Cu}_2\text{TeO}_6$  and  $\text{Na}_3\text{Cu}_2\text{SbO}_6$  were collected using a Quantum Design MPMS SQUID magnetometer. Zero-field cooled (ZFC) and field cooled (FC) data were obtained over the temperature range of 5-300 K at an applied field of 750 Oe ( $\text{Na}_2\text{Cu}_2\text{TeO}_6$ ) and from 2-300 K at 1000 Oe ( $\text{Na}_3\text{Cu}_2\text{SbO}_6$ ). High temperature (300-600 K) susceptibility data were collected using an oven insert at 17500 Oe ( $\text{Na}_2\text{Cu}_2\text{TeO}_6$ ) and 1000 Oe ( $\text{Na}_3\text{Cu}_2\text{SbO}_6$ ).

## 7.4 Magnetic Results and Discussion



Examination of the high temperature magnetic susceptibility data of  $\text{Na}_2\text{Cu}_2\text{TeO}_6$  from 400 to 600 K (Figure 7.3) shows adherence to the Curie-Weiss law with a temperature independent (Pauli) paramagnetic term ( $\chi_{\text{TIP}}$ ):  $\chi = C/(T - \theta) + \chi_{\text{TIP}}$ . The fitting parameters found are  $\chi_{\text{TIP}} = 4.0(3) \times 10^{-4}$  emu/mol, the Curie constant,  $C = 0.855(8)$  emu·K/mol and the Weiss constant,  $\theta = -87(6)$  K. The Curie constant is consistent with a ‘spin-only’ effective magnetic moment,  $\mu_{\text{eff}}$ , of  $1.85(2) \mu_{\text{B}}$  per  $\text{Cu}^{2+}$  ( $S = 1/2$ ). This gives a Lande  $g$ -factor of  $2.14(1)$  for this compound, which is within the range expected for  $\text{Cu}^{2+}$ .

The zero-field cooled (ZFC) magnetic susceptibility from 5 to 600 K and field cooled (FC) susceptibility from 5–300 K of  $\text{Na}_2\text{Cu}_2\text{TeO}_6$  are shown in Figure 7.4. There is very little difference between the two curves, so for the purposes of discussion, the ZFC curve will be considered. At low temperatures (5–35 K), the curve shows a sharp increase in susceptibility that can be attributed to a paramagnetic impurity. The main feature of the curve is a broad maximum in the susceptibility, which is centered near 160 K. This is indicative of short range antiferromagnetic (AF) order in  $\text{Na}_2\text{Cu}_2\text{TeO}_6$ .

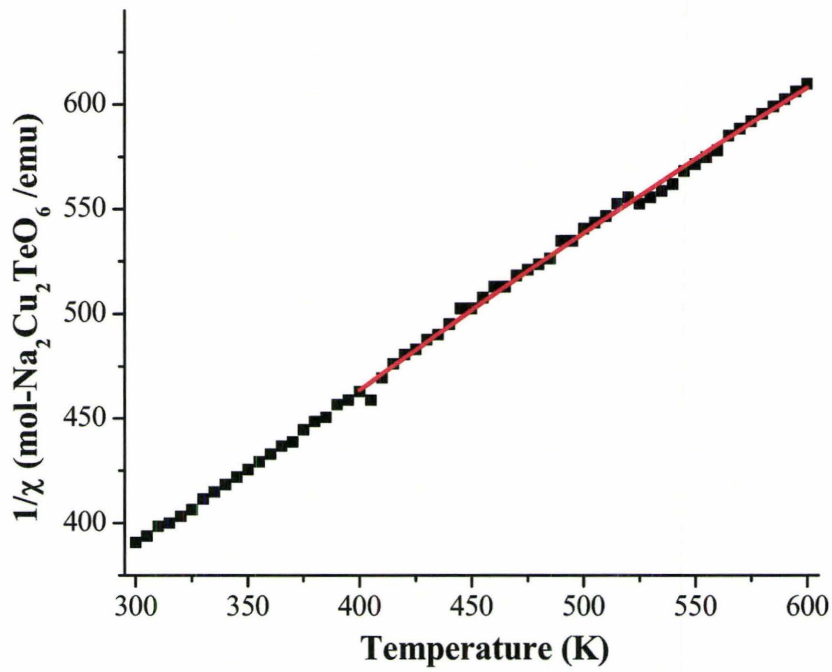


Figure 7.3. High temperature inverse magnetic susceptibility of  $\text{Na}_2\text{Cu}_2\text{TeO}_6$ . The fit to the Curie-Weiss law is the red line.

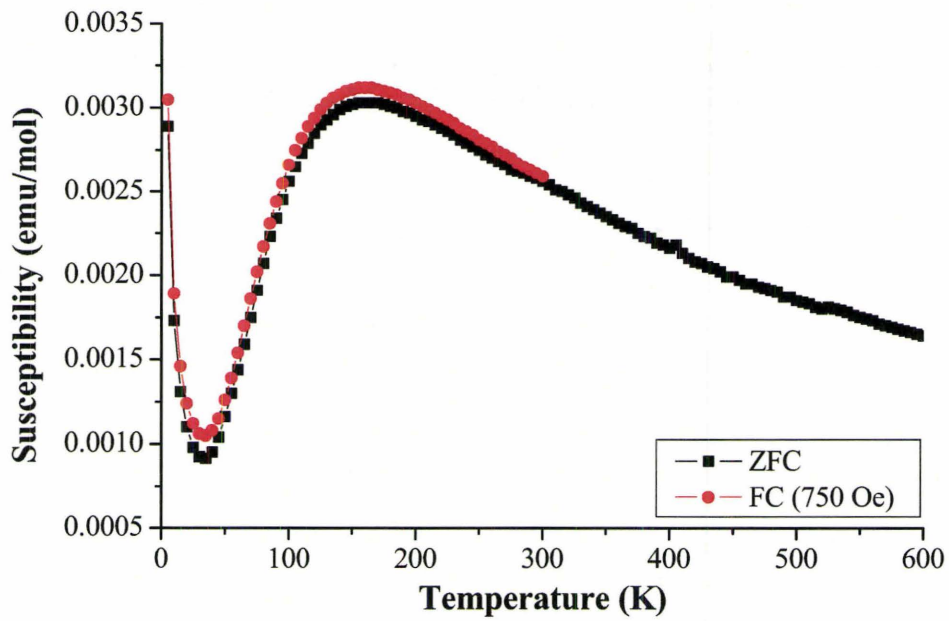


Figure 7.4. ZFC magnetic susceptibility (from 5 to 600 K) and FC susceptibility (from 5 to 300 K) of  $\text{Na}_2\text{Cu}_2\text{TeO}_6$ .

The  $\text{Cu}^{2+}$  ions lie in the  $ab$  plane (Figure 7.2). Also indicated on this Figure are three interaction pathways to consider. Two of these involve a linear chain along the  $b$ -axis,  $J_1$  and  $J_2$ , and one interchain pathway,  $J_3$ .  $J_1$  involves a super-superexchange pathway,  $\text{Cu-O-Te-O-Cu}$ , with a  $\text{Cu-Cu}$  distance of 5.817 Å and a  $\text{Cu-O...O}$  angle of approximately 139°.  $J_2$  corresponds to a  $\text{Cu-O-Cu}$  linkage with a considerably shorter  $\text{Cu-Cu}$  distance of 2.858 Å and a  $\text{Cu-O-Cu}$  angle of 91.3°. Finally,  $J_3$  also involves a  $\text{Cu-O-Cu}$  pathway with  $\text{Cu-Cu} = 3.214$  Å and a  $\text{Cu-O-Cu}$  angle of nearly exactly 90°.

The spatial dimensionality of the short range order depends on the relative magnitudes of the three exchange constants (Table 7.1). To aid in determining these, the method of magnetic dimer analysis was applied.<sup>6</sup> Here, the extended Huckel model is used to calculate the interaction between the magnetic orbitals,  $(\Delta e)$ , and the exchange constants are estimated from the expression,  $J \sim -(\Delta e)^2/U_{\text{eff}}$ . As  $U_{\text{eff}}$  is constant for a given magnetic ion, the trend in  $\Delta e$  is a semiquantitative representation of the trend in  $J$ . The magnetic orbitals are taken as the  $d_{x^2-y^2}$  orbitals of  $\text{Cu}^{2+}$ . The results are presented in Table 7.2. The Te orbitals were not included in the calculation of  $J_1$ .

Table 7.2. Relative Strengths of Cu–Cu Exchange Pathways in  $ab$  Plane of  $\text{Na}_2\text{Cu}_2\text{TeO}_6$ .

Pathway	$(\Delta e)^2$ (meV) <sup>2</sup>	Relative
$J_1$	10200	1
$J_2$	3320	0.33
$J_3$	130	0.01

Clearly,  $J_3$  can be ignored, thus eliminating the honeycomb lattice model. The small value of  $J_3$  can be understood in terms of the spatial relationship of the magnetic  $d_{x^2-y^2}$  orbitals, which lie in the  $\text{CuO}_4$  plane involving the short Cu–O distances. These planes are essentially parallel in the  $J_3$  dimer (Figure 7.2). The relatively large value of  $J_1$  may be attributed to the good overlap geometry of the Cu–O–O–Cu linkage. The Cu–O–Cu angle of  $90^\circ$  can explain the relatively small  $J_2$  value.

At this stage, an alternating chain model appears to be appropriate and as a first effort, the data were fit to the published function<sup>7</sup> beginning with  $J_2/J_1 = 0.3$ . In addition to the expression for the alternating chain, a Curie–Weiss term,  $C/(T - \theta)$  was included to account for the low temperature upturn as well as a temperature independent term (TIP). This model refined to  $J_2/J_1 = 0.10(1)$  (shown in Figure 7.5) which now suggested that a simple dimer (Bleaney-Bowers) model<sup>8</sup> should also be tried.

A fit was attempted using this model yielding a very similar result. The fitting parameters for the two models are compared in Table 7.3, suggesting that they are nearly equivalent.

Table 7.3. Comparison of the Fitting Parameters for the Simple Dimer (Bleaney-Bowers) Model and the Alternating Chain Model.

Model	g	$J/k_B$ (K)	$J_2/J_1$	C (emu·K/mol)	$\theta$ (K)	TIP (emu/mol)
Dimer	2.02(1)	-130.1(2)	0.0	0.010(3)	0.72(14)	0.00060(1)
Alternating Chain	2.03(1)	-134.6(3)	0.10(1)	0.0070(4)	1.2(2)	0.00066(2)

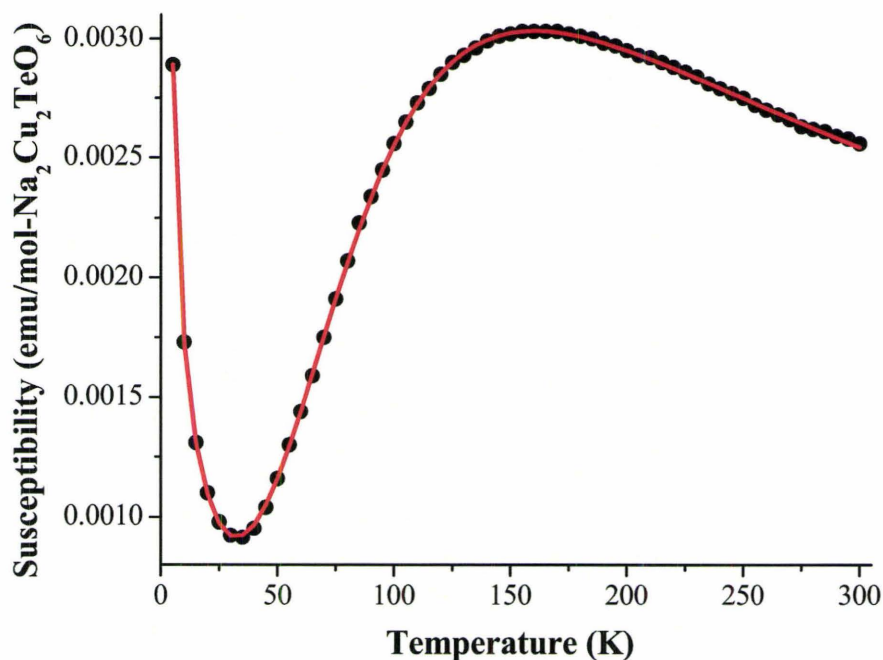


Figure 7.5. ZFC magnetic susceptibility of  $\text{Na}_2\text{Cu}_2\text{TeO}_6$  between 5 and 300 K (black circles). The solid line is the fit to the AF7AF alternating chain model, including a CurieWeiss and TIP term to model the upturn at low temperatures. Fitting parameters can be found in Table 7.3.

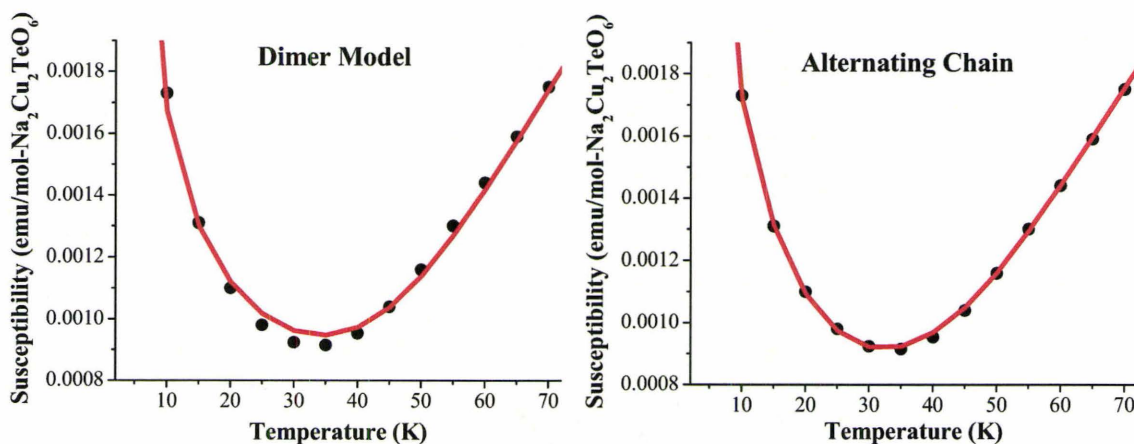


Figure 7.6. Comparison of the low temperature fits for the single dimer model ( $J_2/J_1 = 0$ ) [left] and the alternating chain model ( $J_2/J_1 = 0.10(1)$ ) [right].

However, a further test comparing the low-temperature fits to the experimental data for the two models (Figure 7.6) indicates that the alternating chain model appears to be slightly better. This is reasonable as only at low temperatures will the effect of a small but finite  $J_2$  be manifest.<sup>9</sup> In conclusion, the magnetic short-range order present in  $\text{Na}_2\text{Cu}_2\text{TeO}_6$  is best described as weakly one dimensional, an alternating chain with  $J_2/J_1 \sim 0.1$ , although the zero dimensional dimer model is nearly as good.

Finally, it is possible to estimate the so-called “spin gap”,  $\Delta$ , which is the effective energy difference between the ground singlet,  $S = 0$ , state and the lowest excited triplet state,  $S = 1$ , from the relationship<sup>10</sup>:

$$\Delta = J_1 (1 - J_2/J_1)^{3/4} (1 + J_2/J_1)^{1/4} \quad 7.1$$

to be 127 K. Thus, one would not expect long-range order to develop in this material at low temperatures.

#### *$\text{Na}_3\text{Cu}_2\text{SbO}_6$*

The high temperature inverse magnetic susceptibility data of  $\text{Na}_3\text{Cu}_2\text{SbO}_6$  from 310 to 600 K (Figure 7.7) fit very well to the Curie–Weiss law. The fitting parameters are  $C = 1.019(4)$  emu·K/mol for the Curie constant and  $\theta = -55(2)$  K for the Weiss constant. This Curie constant corresponds to an effective magnetic moment,  $\mu_{\text{eff}}$ , of  $2.02(1) \mu_{\text{B}}$  per  $\text{Cu}^{2+}$  ( $3d^9$ ,  $S = 1/2$ ). This is higher than spin only value of  $1.73 \mu_{\text{B}}$ , which is typical behaviour for  $\text{Cu}^{2+}$ . The negative value for the Weiss constant is indicative of predominant AF interactions.

Concerning the low temperature data (2-300 K), since there was no significant difference between the ZFC and FC data sets, only the ZFC data will be considered for

the purposes of discussion (Figure 7.8). The sharp increase in susceptibility at low temperatures (2-19 K) can be attributed to a paramagnetic impurity. A broad maximum in the susceptibility is present near 92 K, which is indicative of the low-dimensional, short range antiferromagnetic nature of the magnetism of this compound.

Due to strong similarities with the data for the tellurate, the AF-AF alternating chain model was applied in this case as well. A Curie-Weiss term was added to model the sharp upturn at low temperatures. This should not be confused with the Curie-Weiss fit of the high temperature data. As well, a temperature independent term,  $\chi_{TIP}$ , was added.

The following function was employed:<sup>7</sup>

$$\chi_M = \frac{Ng^2\mu_B^2(A + Bx + Cx^2)}{k_B T(1 + Dx + Ex^2 + Fx^3)} + \frac{C_{impurity}}{T - \theta_{impurity}} + \chi_{TIP} \quad 7.2$$

where  $g$  is the Landé  $g$ -factor;  $N\mu_B^2/k_B = 0.375$ ;  $x = |J_1|/k_B T$  and the constants are as follows (with  $\alpha = J_2/J_1$  and  $0 \leq \alpha \leq 0.4$ ):

$$A = 0.25$$

$$B = -0.12587 + 0.22752\alpha$$

$$C = 0.019111 - 0.13307\alpha + 0.50967\alpha^2 - 1.33167\alpha^3 + 1.0081\alpha^4$$

$$D = 0.10772 + 1.4192\alpha$$

$$E = -0.0028521 - 0.42346\alpha + 2.1953\alpha^2 - 0.82412\alpha^3$$

$$F = 0.37754 - 0.067022\alpha + 6.9805\alpha^2 - 21.678\alpha^3 + 15.838\alpha^4$$

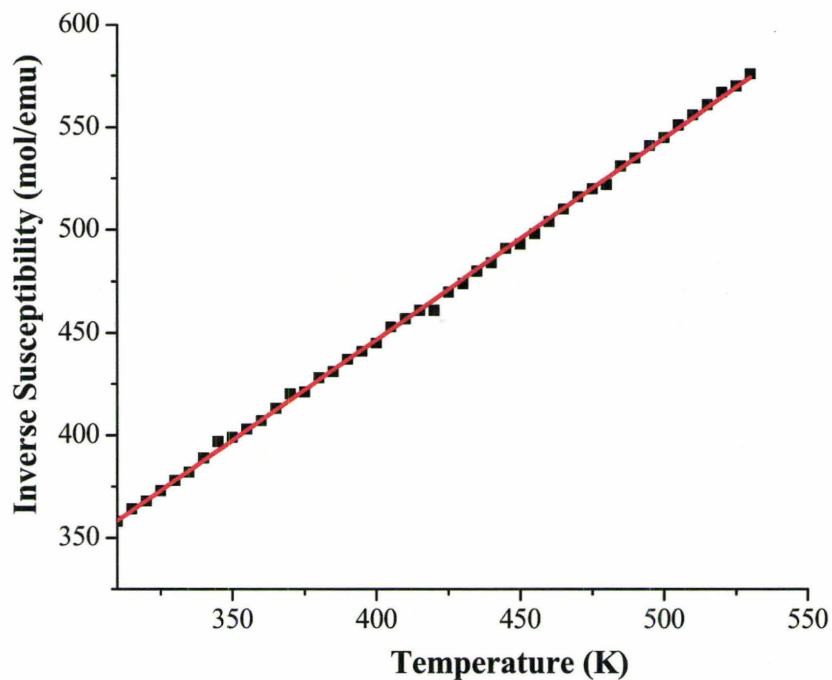


Figure 7.7. High temperature inverse magnetic susceptibility of  $\text{Na}_3\text{Cu}_2\text{SbO}_6$ . The fit to the Curie-Weiss law is the red line.

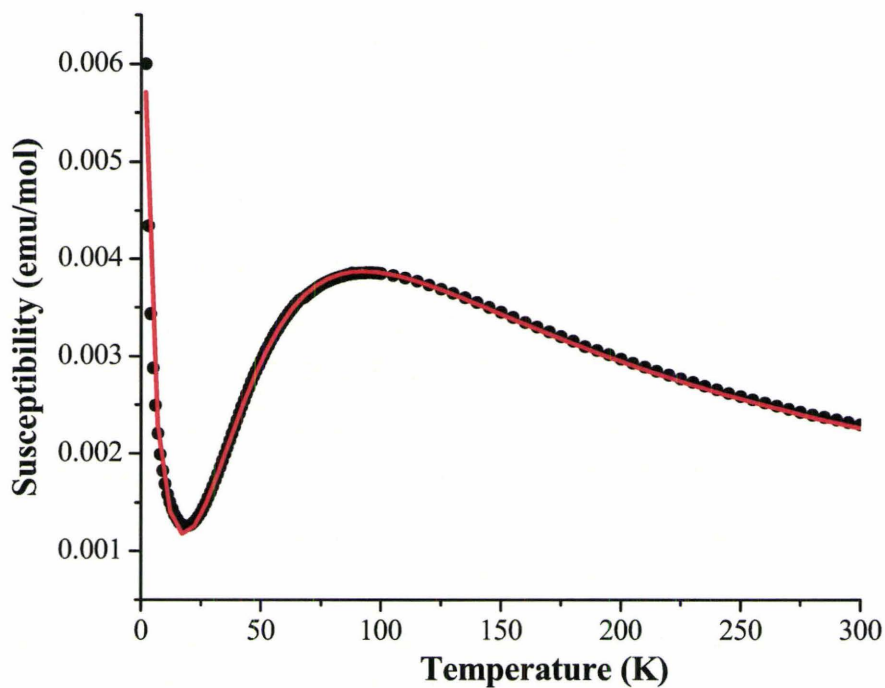


Figure 7.8. ZFC magnetic susceptibility of  $\text{Na}_3\text{Cu}_2\text{SbO}_6$  between 5 and 300 K (black circles). The solid line is the fit to the AF-AF alternating chain model, including a Curie-Weiss and TIP term to model the upturn at low T. Fitting parameters are in Table 7.4.

This is a general model, which includes the 0D dimer with  $\alpha = 0$  and simple 1D chain with  $\alpha = 1$ . The fit to the ZFC data is shown in Figure 7.8. The parameters are summarized in Table 7.4, which includes the results for the tellurate material for comparison.

Table 7.4. Obtained Values from the AF-AF Alternating Chain Model Fit to ZFC Susceptibility Data of  $\text{Na}_2\text{Cu}_2\text{TeO}_6$  and  $\text{Na}_3\text{Cu}_2\text{SbO}_6$ .

Compound	$g$	$ J_1 /k_B$ (K)	$\alpha$	$C$ (emu·K/mol)	$\theta$ (K)	$\chi_{\text{TIP}}$ (emu/mol)
$\text{Na}_2\text{Cu}_2\text{TeO}_6$ <sup>1</sup>	2.03(1)	-134.6(3)	0.10(1)	0.0070(4)	1.2(2)	0.00066(2)
$\text{Na}_3\text{Cu}_2\text{SbO}_6$	1.972(6)	-79.6(6)	0.39(1)	0.027(1)	-2.3(1)	0.00022

The values for the antimonate material are in good agreement with those obtained by Miura *et al.* for the same model.<sup>3</sup>

#### *Extended Huckel Tight Binding Magnetic Dimer Model*

At this stage, computational estimates of the various  $J$ 's are needed in order to interpret these results. In previous work on the tellurate material,<sup>1</sup> the extended Hückel, spin dimer analysis<sup>6</sup> was employed. In these computations the inter site hopping energy, ( $\Delta e$ ), is estimated using the *CAESAR* package.<sup>11</sup> Assuming that  $J \sim (\Delta e)^2/U_{\text{eff}}$  and that  $U_{\text{eff}}$  is constant, the relative magnitude of the various  $J$ 's can be determined. Calculations on the spin dimer model for the antimonate yielded the results shown in Table 7.5 which are compared with those reported for the tellurate.<sup>1</sup>

Table 7.5.  $(\Delta e)^2$  for the Various Exchange Pathways in  $\text{Na}_2\text{Cu}_2\text{TeO}_6$  and  $\text{Na}_3\text{Cu}_2\text{SbO}_6$  Calculated Using the Spin Dimer Model.

Pathway	$\text{Na}_2\text{Cu}_2\text{TeO}_6$		$\text{Na}_3\text{Cu}_2\text{SbO}_6$	
	$(\Delta e)^2$ (meV) <sup>2</sup>	Relative	$(\Delta e)^2$ (meV) <sup>2</sup>	Relative
$J_1$	10200	1	5224	1
$J_2$	3320	0.33	295	0.06
$J_3$	130	0.01	16	0.003

Note that in both compounds,  $J_1$ , which involves the longest Cu–Cu pathway is, nonetheless, the largest interaction by far. Second in magnitude is  $J_2$  of order  $\sim 0.1$  of  $J_1$ , while  $J_3$  is much smaller:  $\sim 0.01$  of  $J_1$ . Comparing the tellurate and antimonate phases the calculated  $J_1(\text{Sb})/J_1(\text{Te})$  ratio is 0.54 compared to the experimental ratio of 0.59, which is an acceptable agreement. However, the observed and calculated  $J_1/J_2$  ratios (“ $\alpha$ ” in Table 7.4 and “Relative” in Table 7.5) are in poor correspondence.

As mentioned, Miura *et al.*<sup>3</sup> have studied the magnetic behaviours of both  $\text{Na}_2\text{Cu}_2\text{TeO}_6$  and  $\text{Na}_3\text{Cu}_2\text{SbO}_6$ . They have pointed out, correctly, that it is very difficult to distinguish between the AF-AF and AF-F alternating chain models based solely on the fitting of the low temperature susceptibility data. Furthermore, it was argued that analysis of the magnetic component of the specific heat data can be used to discriminate between the two models and these data were interpreted in favour of the AF-F model with  $J_1$  and  $J_2$  of comparable magnitudes ( $\alpha \sim -0.8$ ). This approach is not without difficulty. In particular, the isolation of the magnetic contribution from the total specific heat can be problematic, as a good lattice match material is needed, given that the magnetic contribution to the specific heat extends to rather high temperatures. For this purpose

$\text{Na}_3\text{Zn}_2\text{SbO}_6$  was chosen, which is isostructural with  $\text{Na}_3\text{Cu}_2\text{SbO}_6$  but of course there is no static Jahn-Teller distortion at the  $\text{Zn}^{2+}$  site, which will influence the phonon spectrum and introduce some uncertainty into the subtraction procedure.

Apart from these potential experimental difficulties, it should be noted that neither computational method predicts a  $J_2$  that is of comparable magnitude to  $J_1$  with either sign for both materials. As well, there exists a rather simple experimental test that can distinguish between the AF-AF and AF-F linear chain models for these materials. By analysis of the high temperature susceptibility, the models can be compared to the mean field result for the Weiss temperature,  $\theta_c$ . In the high temperature regime ( $T > 300\text{K}$ ), the Curie-Weiss law describes the data very well. The relationship between the Weiss constant and the various exchange constants,  $J_m$ , is well-known and given by: <sup>12</sup>

$$\theta = \frac{2S(S+1)}{3k_B} \sum_{m=1}^N z_m J_m \quad 7.3$$

where  $\theta$  is the Weiss constant,  $z_m$  is the number of  $m^{\text{th}}$  nearest-neighbours of a given atom,  $J_m$  is the exchange interaction between  $m^{\text{th}}$  neighbours and  $N$  is the number of sets of neighbours for which  $J_m \neq 0$ . For both systems with  $S = 1/2$  and  $z_1 = z_2 = 1$  (i.e. neglecting the  $J_3$  contribution), the relationship is simplified to:

$$\theta = \frac{J_1 + J_2}{2k_B} \quad 7.4$$

In Table 7.6, the observed  $\theta$  values are compared with those derived from equation 4 and the  $J$ 's obtained from the fits to the low temperature data with both the AF-AF and AF-F linear chain models.

Table 7.6. Comparison of Observed and Calculated Weiss Constants ( $\theta$ ) for the AF-AF and AF-F Linear Chain Models for  $\text{Na}_2\text{Cu}_2\text{TeO}_6$  and  $\text{Na}_3\text{Cu}_2\text{SbO}_6$ .

	$\text{Na}_2\text{Cu}_2\text{TeO}_6$		$\text{Na}_3\text{Cu}_2\text{SbO}_6$	
	AF-AF	AF-F	AF-AF	AF-F
$J_1/k$ (K)*	-135	-136	-80	-83
$J_2/k$ (K)*	-14	108	-31	105
$\theta_{\text{calc}}$ (K)	-75	-14	-56	11
$\theta_{\text{obs}}$ (K)	-87(6)	-87(6)	-55(2)	-55(2)

\*Note that in Miura *et. al.*<sup>3</sup> the exchange Hamiltonian is written as  $J(S_i \cdot S_j)$  whereas, in Xu *et. al.*<sup>1</sup> and Derakhshan *et. al.*<sup>2</sup>  $-2J(S_i \cdot S_j)$  is used. Therefore, the  $J$  values quoted in <sup>3</sup> will be of the opposite sign and of twice the magnitude as those in <sup>1</sup> and <sup>2</sup>. The values in this table have been converted accordingly.

Clearly, the AF-AF linear chain model is in much better agreement with the observed Weiss temperatures for both materials. In fact, the value derived from the AF-F model for the antimonate is actually of the opposite sign to that experimentally observed.

## 7.5 Conclusions

The magnetic investigation of the new quaternary layered transition-metal oxide,  $\text{Na}_2\text{Cu}_2\text{TeO}_6$ , synthesized by the Kleinke group at the University of Waterloo, was an interesting examination of short-range, low-dimensional magnetic order.<sup>1</sup> The magnetic susceptibility shows Curie-Weiss behavior at high temperatures with a reasonable effective moment of  $1.85(2) \mu_B$  per  $\text{Cu}^{2+}$  ion and a Weiss constant,  $\theta_c$ , of  $-87(6)$  K, indicating dominant antiferromagnetic correlations. A broad maximum at 160 K is interpreted as short-range one-dimensional antiferromagnetic (AF) correlations. This short-range order was analyzed in terms of an alternating chain model, with the surprising result that the stronger intrachain coupling involves a super-superexchange pathway with

a Cu–Cu separation of  $>5 \text{ \AA}$ . The  $J_2/J_1$  ratio within the alternating chain refined to 0.10(1), and the spin gap is estimated to be 127 K.

The analogous compound,  $\text{Na}_3\text{Cu}_2\text{SbO}_6$ , was synthesized at McMaster University in the Greedan lab and its magnetic properties investigated.<sup>2</sup> Again, a broad peak in the magnetic susceptibility data (in this case, near 92 K) indicated dominant short-range, low-dimensional AF behaviour. The data fit very well to an AF-AF alternating linear chain model with  $J_1/k = -79 \text{ K}$  and  $J_2/J_1 = 0.39$ . High temperature data ( $> 300 \text{ K}$ ) exhibited Curie-Weiss behaviour with  $\theta_c = -55(2) \text{ K}$ , also indicating dominant antiferromagnetic interactions.

Another group investigated both of these compounds and reported that an AF-ferromagnetic (F) linear chain model gives equally good agreement to the low temperature data and included analysis of heat capacity data that also supported the AF-F model.<sup>3</sup> It is interesting to note that because the one antiferromagnetic interaction is so dominant (from calculations on these systems by all of the groups involved), the magnitude and even the sign of the second, less dominant pathway is extremely difficult to unambiguously determine. In fact, as previously mentioned, Miura *et. al.*<sup>3</sup> have pointed out that it is very challenging to distinguish between the AF-AF and AF-F alternating chain models based solely on the fitting of the low temperature susceptibility data alone. Only through experimental data fitting, combined with calculation and other experimental data, can more definitive conclusions be drawn.

It is in this way that Derakhshan *et. al.* demonstrated the Weiss constants derived from the high temperature experimental data could be used to distinguish between the

AF-AF model and the AF-F model.<sup>2</sup> On the basis of both analyses (low temperature susceptibility fitting, as well as high temperature Weiss constants), it can be concluded that the AF-AF alternating chain is the appropriate model for both compounds.

## 7.6 References

1. Xu, J.; Assoud, A.; Soheilnia, N.; Derakhshan, S.; Cuthbert, H. L.; Greedan, J. E.; Whangbo, M. H.; Kleinke, H. *Inorg. Chem.* **2005**, *44*, 5042-5046.
2. Derakhshan, S.; Cuthbert, H. L.; Greedan, J. E.; Rahaman, B.; Saha-Dasgupta, T. *Phys. Rev.* **2007**, *B76*, 104403(1-7).
3. Miura, Y.; Hirai, R.; Kobayashi, Y.; Sato, M. *J. Phys. Soc. Jpn.* **2006**, *75*, 084707(1-6)
4. Schneemeyer, L. F.; Waszczak, J. V.; Siegrist, T.; Dover, R. B. v.; Rupp, L. W.; Batlogg, B.; Cava, R. J.; Murphy, D. W. *Nature* **1987**, *328*, 601-603.
5. Vershinin, M.; Misra, S.; Ono, S.; Abe, Y.; Ando, Y.; Yazdani, A. *Science* **2004**, *303*, 1995-1998.
6. Whangbo, M. H.; Koo, H. J.; Dai, D. *J. Solid State Chem.* **2003**, *176*, 417-481.
7. Hall, J. W.; Marsh, W. E.; Weller, R. R.; Hatfield, W. E. *Inorg. Chem.* **1981**, *20*, 1033-1037.
8. Bleaney, B.; Bowers, K. D. *Proc. R. Soc. (London)* **1952**, *A214*, 451-465.
9. He, Z.; Kyomen, T.; Itoh, M. *Phys. Rev.* **2004**, *B69*, 220407.
10. Barnes, T.; Riera, J.; Tennant, D. A. *Phys. Rev.* **1999**, *B59*, 11384-11387.
11. Ren, J.; Liang, W.; Whangbo, M.-H. *Crystal and Electronic Structure Analysis using CAESAR*, 2005; <http://www.PrimeC.com/>
12. Smart, J. S. *Effective Field Theory of Magnetism*; Saunders: Philadelphia, 1966.

## **Chapter 8**

### **Conclusion**

## 8.1 Conclusions

New oxides with the “pillared perovskite” structure were synthesized and characterized. Based on the perovskite structure type, these new materials possess layers of discrete magnetic ions, separated by large distances connected by convoluted magnetic superexchange pathways. Nonetheless, through the diamagnetic pillaring unit, long-range magnetic order was observed for most of these compounds. The use of a multitude of techniques (such as powder X-ray diffraction, SQUID magnetometry, heat capacity measurements and variable temperature powder neutron diffraction) was required to elucidate as much information about these new substances as possible.

The candidate undertook a more definitive study of two previously known compounds ( $\text{La}_5\text{Re}_3\text{CoO}_{16}$  and  $\text{La}_5\text{Re}_3\text{NiO}_{16}$ )<sup>1</sup>, and the synthesis and characterization of a new family of compounds based on this structure type. An important result was the observation of a new magnetic structure for the Ni member – the first of its kind for any pillared perovskite material. In addition, the longer, more convoluted interplanar exchange pathway through the diamagnetic “pillar” was shown to play an important role in the overall magnetic ordering of these compounds.

As well, a new family of pillared perovskite compounds was synthesized and magnetically characterized. By varying the 3d transition metal, the effect of the spin quantum number  $S$ , on the resulting magnetism could be studied. One set of four new materials was realized through substitution of magnetic  $\text{Re}^{5+}$  within the perovskite layers with diamagnetic  $\text{Ta}^{5+}$ . There were significant synthetic challenges that arose in the investigation of  $\text{La}_5\text{Re}_{3-x}\text{Ta}_x\text{BO}_{16}$  ( $B = \text{Mn}, \text{Fe}, \text{Co}, \text{Ni}$ ), and detailed microscopic studies

to determine the extent of the  $\text{Ta}^{5+}$  substitution using SEM-EDS and TEM-EDS were undertaken. In addition, a  $\text{Nb}^{5+}$  compound ( $\text{La}_5\text{Re}_{3-x}\text{Nb}_x\text{MnO}_{16}$ ) was also synthesized and fully characterized by powder X-ray diffraction and SQUID magnetometry, as well as SEM-EDS and TEM-EDS, in an attempt to discern the extent of substitution on the  $A^{5+}$  site within the perovskite layers of these compounds. Despite these synthetic difficulties, pillared perovskite materials  $\text{La}_5\text{Re}_{3-x}\text{Ta}_x\text{BO}_{16}$  ( $B = \text{Mn, Fe, Co, Ni}$ ;  $x \sim 0.5$ ) were generated and analyzed using powder X-ray and variable temperature neutron diffraction, SQUID magnetometry and heat capacity measurements. The Ta-based system was very similar to the all Re-based pillared perovskites studied previously, with approximately the same critical temperatures for long-range magnetic ordering with the same  $B^{2+}$  ion, similar metamagnetic transitions and the same ordered magnetic structures. These data corroborated the idea that the longer interlayer superexchange pathway through the diamagnetic “pillar” is important in determining the overall magnetism of the pillared perovskite system. This series represents the first attempt at substitution of the  $A^{5+}$  cation in a pillared perovskite.

Continuing the theme of researching interesting, supposedly low-dimensional compounds that magnetically order, a lanthanum rhenium oxide based on the dimeric “pillar” of the pillared perovskites was investigated.<sup>2</sup> The material,  $\text{La}_3\text{Re}_2\text{O}_{10}$ , was synthesized for the first time as a phase-pure powder using conventional solid state methodologies. In this compound, there is one unpaired electron delocalized within the  $\text{Re}_2\text{O}_{10}^{9-}$  unit. Measurements of the magnetic properties showed that this material exhibits both short- and long-range order, with the former setting in at about 18 K.

However, the magnetic structure could not be determined by unpolarized powder neutron diffraction. Based on experimental fits of the susceptibility to a low-dimensional linear chain model, and theoretical investigations of the character of the metal–metal bonding orbitals and spin exchange interactions, the long-range structure was postulated to consist of antiferromagnetic 1-D chains which couple together antiferromagnetically. This investigation highlights the complementary relationship between experimental observation and theoretical calculations, as the insight gained through DFT modelling and EHTB spin dimer analysis led to a deeper understanding of the magnetic behaviour of  $\text{La}_3\text{Re}_2\text{O}_{10}$ .

The double perovskite,  $\text{SrLaRuNiO}_6$ , was also synthesized and its magnetic properties studied. Unfortunately, the presence of a small amount of ferromagnetic  $\text{SrRuO}_3$  impurity dominated the bulk magnetic data. However, low temperature powder neutron diffraction measurements were able to determine the critical ordering temperature for the material. This study showed the power of neutron diffraction in the investigation of magnetic materials, where interpretation of bulk magnetic data can be hampered by a ferromagnetic secondary phase.

The candidate also collaborated with other researchers, investigating the magnetic properties of the low-dimensional, ordered rock-salt oxides,  $\text{Na}_2\text{Cu}_2\text{TeO}_6$  and  $\text{Na}_3\text{Cu}_2\text{SbO}_6$ .<sup>3,4</sup> Interestingly, although the magnetic  $\text{Cu}^{2+}$  centres are arranged in a hexagonal “honeycomb” type array, the short-range magnetic order consists of an AF-AF alternating chain. These findings are still the subject of some controversy in the literature, as other experimental and theoretical groups researching the strengths of the

various superexchange pathways propose alternative models of the magnetic behaviour in these compounds.<sup>5,6</sup> The candidate's contribution has sparked much healthy debate and lively discussion regarding the nature of low-dimensional order within these materials.

Overall, this thesis reflects the candidate's extensive work on the synthesis of new transition metal oxide compounds and comprehensive magnetic characterization. Despite large distances between magnetic centres and convoluted magnetic superexchange pathways (often through diamagnetic centres), long-range order was observed in many of these systems. This body of work highlights the importance of continued research into the solid state synthesis of new materials and investigation of their magnetic properties. Often, interesting, unexpected and novel magnetic behaviour is observed, adding to the knowledge and understanding of the fascinating physical phenomenon of magnetism.

## 8.2 Future Work

There are some obvious extensions of this body of work, particularly in the area of pillared perovskites. As this is the first time substitution of the  $A^{5+}$  cation in a pillared perovskite was attempted, there are many opportunities for further research in expanding this structure type. Only the Mn member of the  $\text{La}_5\text{Re}_{3-x}\text{Nb}_x\text{BO}_{16}$  series was synthesized and partially characterized. As with the  $\text{La}_5\text{Re}_{3-x}\text{Ta}_x\text{BO}_{16}$  series, the dependence of the magnetism on the spin quantum number ( $S$ ) could be studied by changing  $B$  to Fe, Co or Ni. X-ray powder diffraction, SQUID magnetometry, variable temperature powder neutron diffraction and heat capacity measurements could all be performed to verify the structure and study the properties of these new compounds.

Another extension of the pillared perovskites could be substitution of a 4+ cation (such as  $\text{Ti}^{4+}$ ) within the perovskite layers. Without changing the starting stoichiometry, this would result in one extra electron in the pillared perovskite system, which would be expected to reside within the metal-metal bonded dimer 'pillars'. One extra, unpaired electron within the dimers would make them paramagnetic, and could have a significant impact on the resulting magnetic properties of the synthesized compounds. For example, the layers are normally coupled antiferromagnetically through the diamagnetic pillars. Once paramagnetic, would the dimers then participate in the coupling, so the layers are now coupled ferromagnetic with respect to each other?

Preliminary results of a series of  $\text{La}_5\text{Re}_{3-x}\text{Ti}_x\text{BO}_{16}$  ( $B = \text{Mn, Fe, Co, Ni, Mg}$ ) suggest that this is not the case. Again, synthetic studies (X-ray/neutron powder diffraction, SEM-EDS, TEM-EDS) indicate that only partial substitution of  $\text{Ti}^{4+}$  ( $x \sim 0.5$ ) within the perovskite layers occurs. However, magnetically, all compounds have about the same critical temperatures as their  $\text{La}_5\text{Re}_3\text{BO}_{16}$  analogues. Interestingly, it appears that the Mn member has the same magnetic structure by powder neutron diffraction as well. No magnetic peaks were visible in the other series' members, however, that may be due to poor sample crystallinity and weaker values of the moments, rather than the absence of any magnetism. Further study and refinement of this series should prove to be very interesting.

An expansion of the research involving the magnetically unusual lanthanum rhenium oxide,  $\text{La}_3\text{Re}_2\text{O}_{10}$  could be the successful solid-state synthesis of its osmium analogue,  $\text{La}_3\text{Os}_2\text{O}_{10}$ . All attempts at generating  $\text{La}_3\text{Os}_2\text{O}_{10}$  thus far have led to the

destruction of the quartz tube containing the reaction and a multitude of products along with the desired phase. The best oxidizing agent for this reaction has been  $\text{Ag}_2\text{O}$  and continued synthetic efforts to generate a pure phase compound could yield a positive result. Magnetic characterization of  $\text{La}_3\text{Os}_2\text{O}_{10}$  could generate some interesting and unexpected phenomena.

Much research has already been done in the area of Ru-based double perovskite compounds, however, one extension of this chemistry could be the substitution of other  $M^{2+}$  (such as Mn, Fe and Co) for  $\text{Ni}^{2+}$  in  $\text{SrLaRuNiO}_{16}$ . In addition, double perovskites are related to pillared perovskites. Both have layers of corner-shared octahedra, however, in the pillared perovskite, these layers are separated by edge-shared octahedral dimer ‘pillars’. In double perovskites, the layers are connected directly. Maintaining the same charges on the two metal sites (5+ and 2+) in the double perovskite should lead to octahedral site-ordering within the layers as well, and the newly generated compounds would serve as a more ‘condensed’ version of the pillared perovskites studied. The synthesis and magnetic characterization of double perovskites such as  $\text{SrLaReMO}_{16}$  ( $M = \text{Mn, Fe, Co, Ni}$ ) and  $\text{SrLaRe}_{0.5}\text{Ta}_{0.5}\text{MO}_{16}$  ( $M = \text{Mn, Fe, Co, Ni}$ ) would be a novel look at the ‘pillared’ perovskites without any pillars!

### 8.3 References

1. Cuthbert, H. L.; Greedan, J. E.; Cranswick, L. *J. Solid State Chem.* **2006**, *179*, 1938-1947.
2. Cuthbert, H. L.; Greedan, J. E.; Vargas-Baca, I.; Derakhshan, S.; Swainson, I. P. *Inorg. Chem.* **2007**, *46*, 8739-8745.
3. Xu, J.; Assoud, A.; Soheilnia, N.; Derakhshan, S.; Cuthbert, H. L.; Greedan, J. E.; Whangbo, M. H.; Kleinke, H. *Inorg. Chem.* **2005**, *44*, 5042-5046.

4. Derakhshan, S.; Cuthbert, H. L.; Greedan, J. E.; Rahaman, B.; Saha-Dasgupta, T. *Phys. Rev.* **2007**, *B76*, 104403(1-7).
5. Miura, Y.; Hirai, R.; Kobayashi, Y.; Sato, M. *J. Phys. Soc. Jpn.* **2006**, *75*, 847071(1-4)
6. Koo, H. J.; Whangbo, M. H. *Inorg. Chem.* **2008**, *47*, 129-133.